MODELLING OF LIGHT SCATTERING BY CIRRUS ICE CRYSTALS USING GEOMETRIC OPTICS COMBINED WITH DIFFRACTION ON FACETS

A THESIS SUBMITTED IN PARTIAL FULFILMENT OF THE REQUIREMENTS OF THE UNIVERSITY OF HERTFORDSHIRE FOR THE DEGREE OF DOCTOR OF PHILOSOPHY

By

Adrian Jonathan Miles Clarke
School of Physics, Astronomy and Mathematics

in collaboration with

The Met Office

December 2005

Contents

List of Figures

Abstract

A new 3D model of light scattering applicable to dielectric faceted objects is presented. The model combines Geometric Optics with diffraction on individual facets yet maintains the low computational expense of standard Geometric Optics. The current implementation of the model is explained and then applied to the problem of light scattering by ice crystals in cirrus clouds. Accurate modelling of the scattering properties of such crystals is crucial to better understanding of cirrus radiative properties and hence to climate modelling and weather forecasting.

Calculations using the new model are compared to a separation of variables method and the Improved Geometric Optics method with encouraging results. The model shows significant improvements over standard Geometric Optics. The size applicability of the new model is discussed.

The model is applied to a range of crystal geometries that have been observed in cirrus including the hexagonal column, the hollow column, the droxtal and the bullet rosette. For each geometry the phase function and degree of linear polarization are presented and discussed.

Ice analogue crystals grown at the University of Hertfordshire have optical properties very close to ice but are stable at room temperature. The geometries of three ice analogue crystals are reconstructed and the single scattering properties of the reconstructions are presented.

2D scattering patterns calculated using the model are compared to laboratory photographs of scattering patterns on a screen created by an ice analogue hexagonal column. The agreement is shown to be very good. By applying the model to a range of geometries, it is shown that the results in the form of 2D scattering

patterns can potentially be used to aid particle characterization.

By combining the model with a Monte Carlo radiative transfer code, comparisons are made with aircraft radiance measurements of cirrus provided by the Met Office. The improvements over standard Geometric Optics are found to persist following a radiative transfer treatment.

Acknowledgements

The assistance of the following people is gratefully acknowledged:

- The supervisory team: Dr. Evelyn Hesse (Principal Supervisor), Dr. Zbigniew Ulanowski, Dr. Anthony J. Baran and Prof. Paul H. Kaye
- Bill Liley (SEM images, chapter 6)
- Xian-Wei Liu (SEM images, chapter 7)
- Charles Parfitt (Ice analogue preparation)
- My wife Susannah and our whole family

This project has been supported by the following organisations:

- The Engineering and Physical Sciences Research Council (PhD studentship)
- The UK Meteorological Office (CASE studentship)
- The UK Aerosol Society (C.N. Davies award)

Photography Credits:

- All of the optical microscopy images used in this thesis are courtesy of Z. Ulanowski

Acronyms

APF *Analytic Phase Function*

CPI *Cloud Particle Imager*

DDA *Discrete Dipole Approximation*

DLP *Degree of Linear Polarization*

FDTD *Finite Difference Time Domain*

GO *Classical Geometric Optics*

IGO *Improved Geometric Optics*

IWC *Ice Water Content*

LIDAR *LIght Detection And Ranging*

MKA *Modified Kirchhoff Approximation*

RADAR *RAdio Detection And Ranging*

RTDF *Ray Tracing combined with Diffraction on Facets*

SDC *Spatial Double Centred*

SDF *Size Distribution Function*

SEM *Scanning Electron Microscopy*

SID *Small Ice Detector*

SVM *a generalisation of the Separation of Variables Method to nonspherical particles*

WMO *World Meteorological Organisation*

Commonly Used Symbols

α, β, γ	Euler angles
ε	Permittivity
η	% of rays incident on a slit or facet that are deflected by more than 1°
θ	Polar or scattering angle
$\theta_i, \theta_r, \theta_t$	Angles of incidence, reflection and refraction/transmission
λ	Wavelength
μ	Permeability
τ	Optical depth
υ	Velocity of light in a medium
ϕ	Azimuthal angle
ω	Single scattering albedo
$C_{ext}, C_{abs}, C_{sca}$	Extinction, absorption and scattering cross sections
c	Velocity of light in a vacuum
D_e	Mean effective diameter
$\boldsymbol{E}$	Electric vector
g	Asymmetry parameter
$\boldsymbol{H}$	Magnetic vector
$\boldsymbol{I}$	Stokes vector
I, Q, U, V	Stokes parameters
$\vec{k}$	Unit vector in the direction of propagation of a ray
L	Characteristic length of a geometry
n, n_r	Real part of the refractive index
n_i	Imaginary part of the refractive index
P_{11}	Phase function, an element of the scattering matrix
$-P_{12}/P_{11}$	Degree of linear polarization
r	Characteristic radius of a geometry
$\perp$	Perpendicular subscript
$\|\|$	Parallel subscript

Chapter 1

Introduction

Up to 30% of the Earth's surface is regularly covered by cirrus cloud [1]. As a result cirrus plays a major role in the balance of radiation between the Earth, the atmosphere and space. The study of cirrus is crucial to the future success of climate models and weather forecasting. Although studied for many years, there is still a large uncertainty over the radiative properties of cirrus clouds. This lack of understanding means that the current treatment of cirrus in climate models has room for improvement. Cirrus are high altitude clouds composed of ice crystals. Determining the shape and size of the ice crystals in cirrus and how they are formed are areas of ongoing research as this project will discuss. These areas are very important in enabling accurate modelling of the crystal and cloud properties. Equally important is the need for an accurate yet flexible computer model of light scattering which can be readily applied to many shapes and sizes of crystals to investigate their radiative properties. The advances in computing power in recent years have helped the field of light scattering to advance yet there is still a lack of such a model for intermediate to large sizes of ice crystals.

For spherical and near spherical particles one can gain an exact solution from Lorenz-Mie theory, a separation of variables technique. However, ice has a predominantly hexagonal structure and so numerical, near exact and approximate computational techniques must be relied upon.

T-matrix is a largely analytic exact technique that can be used for hexagonal columns with size parameters up to around twenty [2]. It is computationally demanding and so cannot be applied to scatterers of larger size parameter at this

time. If such implementation becomes possible, it will be the method of choice. Some success has been gained at intermediate size parameters using a generalization of the separation of variables method to nonspherical particles [3, 4]. Results from this method are considered in chapter 4. Other techniques exist but all involve more significant approximations and none allow flexible computation for larger sizes where most cirrus ice particles are classified. Traditionally the Geometric Optics method which is sometimes referred to as ray tracing has been used for such crystals. It provides rapid computation yet is very flexible in terms of the crystal geometries that can be considered. However, the accuracy provided by Geometric Optics is limited for all but the largest crystals. There have been many attempts to improve the Geometric Optics method. For example, the *Modified Kirchhoff Approximation* (MKA) [5] calculates far fields from Geometric Optics results and lead to the development of the *Improved Geometric Optics* (IGO) method [6], though the latter is computationally expensive.

A new model has been proposed which modifies Geometric Optics rays as they interact with crystal facets. A deflection is introduced to take into account diffraction caused by the facet acting as an aperture. This method maintains the flexible and computationally inexpensive advantages of Geometric Optics while producing much improved results. Following the work of Hesse and Ulanowski [7, 8] where *Ray Tracing combined with Diffraction on Facets* (RTDF) was introduced in a two-dimensional case, a three-dimensional version is now presented.

The 3D version allows rapid computation of scattering results at intermediate to large size parameters for any dielectric faceted objects, although this project concentrates on ice found in cirrus. The model has much promise as it shows a marked improvement over Geometric Optics in irradiance and linear polarization results. Further improvements beyond the remit of this thesis may yet be implemented. In the forthcoming chapters the RTDF model will be explained, tested against existing approximations and experiment, applied to a range of geometries and compared to aircraft radiance measurements taken from examples of cirrus clouds.

Verification of such a model is very difficult because of the lack of exact theory calculations to make comparisons with. One alternative is to make comparisons to laboratory experiments. Using ice crystals in the laboratory poses many difficulties, particularly if the geometry of the crystal is to be modelled for use in scattering calculations. Ice analogue crystals grown at the University of Hertfordshire [9] work around many of the problems because while they have optical properties very close to real water ice they are stable at room temperature. This

makes them ideal for applications such as laboratory scattering experiments and the calibration of in-situ cloud probes [10]. Photographs of scattering patterns created by an ice analogue hexagonal column provide the experimental verification in this discussion. More complex ice analogue crystals will be considered and their geometries reconstructed to allow more detailed study.

To create scattering results that can be compared to laboratory photographs, it is necessary to create 2D light scattering patterns that represent scattering on a screen. Given the rapid and flexible computation offered by ray tracing based models, such patterns can be created for even very complex nonspherical crystals. 2D scattering patterns provide much more information than azimuthally averaged scattering data such as a phase function. In contrast to standard Geometric Optics, the new model can produce 2D scattering patterns for fixed orientations as well as averaged random orientations. It has been shown that such spatial scattering patterns of single orientations can be used to distinguish between particle geometries and so aid in particle characterization in a range of scientific fields [11]. In the case of cirrus ice, the concept has been implemented in particle instruments such as the *Small Ice Detector* (SID) [12]. Such instruments measure the light scattering from particles and can distinguish between spherical and nonspherical particles as well as classifying nonspherical particle geometries. The RTDF model could potentially be used as a very useful tool in the further development of light scattering based in-situ particle instruments. This is not confined to the field of atmospheric science as there are many possible industrial applications. Particle characterization and other potential applications for the new model will be discussed in the forthcoming chapters.

The discussion will proceed as follows. The background to the project and fundamental elements of diffraction and light scattering theory that are relevant will be discussed in chapter 2, *"Background and Fundamentals"*. The model will be introduced and the current implementation explained in chapter 3, *"The Diffraction on Facets Model"*. There will also be a discussion of the size applicability of the model and some initial demonstrations of the effect of the model in chapter 3. The model will then be applied to the case of the hexagonal column in chapter 4, *"Testing the Model using Hexagonal Columns"*. This will include dissections of the phase function and degree of linear polarization as well as comparisons to a separation of variables method and IGO. Chapter 5, *"Application of the Model to a Range of Crystal Geometries"*, will consider types of crystal geometries that are found in cirrus. The single scattering properties of examples of each geometry calculated using the RTDF model will be presented

and discussed along with an explanation of the place of the geometry within the study of cirrus. The reconstruction of the geometries of examples of ice analogue crystals will be discussed in chapter 6, *"Ice Analogue Geometry Reconstruction"*. This will include the single scattering properties calculated using the RTDF model as well as comparisons of maximum dimension, projected area and volume to *Cloud Particle Imager* (CPI) measurements. Chapter 7, *"2D Scattering Patterns"*, will introduce the 2D scattering pattern form for presenting the results of calculations. This form will be used to make comparisons to laboratory photographs of ice analogue light scattering patterns. It will also provide the basis for a study to show how the new model could be used as a potential aid in particle characterization. In chapter 8, *"Comparisons to Aircraft Radiance Measurements"*, the model will be used in conjunction with a radiative transfer code to make comparisons to aircraft radiance measurements provided by the Met Office. Conclusions will be provided in chapter 9. Three appendices are included. The first, *Appendix A*, provides conventions and definitions used in the forthcoming chapters to avoid confusion with other texts. The second, *Appendix B*, provides a list of publications arising from this project. The third, *Appendix C*, provides a reproduction of a journal paper written as a result of this work. For reference, lists of acronyms and symbols used throughout the thesis are included between the *Acknowledgements* and this chapter.

Chapter 2

Background and Fundamentals

In this chapter the background to the project will be discussed and aspects of theory and mathematics that are relevant will be presented. Section 2.1 will provide an overview of computational methods used to solve the problem of light scattering by a particle. One of these methods, Geometric Optics, is crucial to the project. Section 2.2 will discuss some of the theory used within Geometric Optics, all of which is used directly within the new RTDF model. The RTDF model differs from Geometric Optics because it considers the phenomenon of diffraction at each crystal facet. Section 2.3 provides some definitions and descriptions of diffraction. This is followed by elements of diffraction theory that are relevant to the discussion in section 2.4. With this knowledge, methods based upon Geometric Optics that use diffraction to offer enhanced accuracy and wider size applicability will be discussed in section 2.5, including the RTDF model. Some aspects of general light scattering theory will be presented in section 2.6. Finally, an overview of the study of cirrus will be given in section 2.7 to help establish the merits of the project in the wider scientific world.

2.1 Solving the Light Scattering Problem

Light scattering is the process of absorption and reradiation of electromagnetic energy from obstacles, or scatterers, that light may encounter.

When a particle such as an ice crystal is illuminated by a light source, the incident electric field induces both an internal field within the crystal and a scattered field outside it. The scattered field is the fraction of the incident field that has been reradiated by the scattering particle.

All matter is made up of discrete electrically charged particles in the form of protons and electrons. The incident electric field sets the electric charges within the particle into oscillatory motion. This induces dipole moments throughout the particle. The motion of charged particles generates electromagnetic radiation in all directions that can be referred to as the scattered radiation. During the process, some energy can be converted into other forms such as thermal energy and it is said that this energy has been absorbed.

One of the challenges in the study of light scattering is to generate solutions to the electromagnetic wave equations for a given system so that the scattered electric field is known at some desired points in space. To perform such calculations for anything other than the most simple particle cases can be extremely time consuming, if possible at all. The amount of energy that is absorbed by the particle, the amount of radiation scattered in different directions and the effect that the scattering process may have on the radiation are all factors directly affected by the size, shape and composition of the particle.

Many methods have been developed for solving the light scattering problem for particles and crystals of different size, shape and composition. The field of light scattering has many applications, most noticeably in Astronomy, Atmospheric Science and Materials Science.

A solution to the problem for spherical particles was found independently by Gustav Mie (1869-1957) and Ludvig Lorenz (1829-1891). It was published by Mie in 1908. Now referred to as Lorenz-Mie theory, the solution is a separation of variables method that solves the spherical wave equation using boundary conditions that are applied at the surface of the scatterer. A detailed discussion of the solution is available in most general light scattering textbooks, for example Bohren and Huffman [13] or Stratton [14]. A discussion of different formulations

of the theory is available along with FORTRAN codes in Barber and Hill [15]. In the case of cirrus ice, all of the scatterers that are likely to be encountered will be nonspherical in nature. In the past, Lorenz-Mie theory has been used to obtain a first order description of the scattering by nonspherical particles but its application as a solution to such scatterers is inadequate. The differences in scattering properties between spherical and nonspherical particles can be significant, as shall be discussed in section 5.5.

Separation of variables methods can in theory be applied to any geometry where it is possible to formulate a coordinate system that coincides with the particle surface. For example, Asano and Yamamoto [16] obtained a solution to the problem of an arbitrary spheroid. In the case of cirrus ice, a separation of variables method cannot be used in general because it is not possible to formulate a coordinate system around the hexagonal structure of the crystals. Some success has been gained at intermediate size parameters using *a generalisation of the Separation of Variables Method to nonspherical particles* (SVM) [3, 17]. It is however only applicable to long columns with aspect ratios of at least $L/2r = 3$. Results from this method [4] will be used in sections 3.4 and 4.3.

The closest to an exact method that exists for nonspherical particles is the T-matrix method. Originally developed by Waterman [18], the method is a largely analytic technique. The incident and scattered fields are expanded into vector spherical wave functions, the coefficients of which are related by a transformation matrix or T-matrix. When applied to a sphere, the T-matrix equations reduce to those of Lorenz-Mie theory. The great advantage of the T-matrix is that once known it allows any scattering properties of the scatterer to be determined because the elements of the matrix depend only on the properties of the scatterer. The computation of the T-matrix is much simpler for geometries with axial symmetry and for smaller sizes. However, in theory it can be applied to any geometry even up to larger sizes. It has been applied to hexagonal columns up to size parameters of around twenty [2] but the computational demands mean that it cannot be applied to hexagonal crystals of larger size parameter at this time. If implementation becomes possible for increasingly more complex and larger crystals, it will become the method of choice. The definition of the size parameter, a quantity that will be frequently used in the coming chapters, can be found in appendix A.1.

The *Finite Difference Time Domain* (FDTD) method is a numerical technique that was pioneered by Yee [19]. In this method, the space in which a scatterer resides is divided into a grid of points. The scatterer is represented by assigning

appropriate values of permittivity, permeability and conductivity to the grid points that coincide with the volume of the particle. The finite difference approximation allows Maxwell's time-dependent curl equations to be evaluated at a finite number of points in time and space, the points in space being the grid of points. The computation of the solution involves a series of time iterations where the electromagnetic variations in time and space are calculated in response to an incident plane wave. Once a stable field has been found at all the grid points, the iterations stop and the solution has been found.

The advantage of FDTD is that it can be applied to any geometry due to the grid system, as opposed to the application of boundary conditions at the particle surface. There are, however, a number of disadvantages. Because one cannot create a spatial grid that extends to infinity, it is necessary to apply a special absorbing boundary condition at the extremities of the grid. This introduces an approximation that is not present in methods such as T-matrix where the radiation condition is fully satisfied. The second disadvantage is the staircasing effect that can be a problem for some geometries. By dividing space into finite volume elements, at the boundaries of a particle one will find that the element is partly inside and partly outside the particle. This can be minimized by choosing coordinate systems that are as close as possible to the geometry of the particle. Finally, the main disadvantage of FDTD is that it is very computationally demanding. In the case of cirrus ice, FDTD can realistically be applied to hexagonal columns of size parameters up to around twenty [20].

Another numerical method, the *Discrete Dipole Approximation* (DDA), was formulated in 1973 by Purcell and Pennypacker [21] who used it to study interstellar dust grains. In the DDA, a scattering particle is divided up into a number of dipoles or polarizable points. In this way, any particle geometry can be modelled. Each dipole is excited by a combination of the incident electric field and the scattered fields from all the other dipoles. A system of linear equations can be formulated which results in the field due to each dipole, and hence the whole scattered field, being calculable. The main disadvantage of the method is that a large amount of computer time is required to gain convergence as the number of dipoles (and hence crystal size) increases. As a result, the method is generally applied to scattering particles significantly smaller than those to be discussed in this thesis. A popular DDA code is publicly available called DDSCAT [22].

Other techniques exist but all involve approximations and none allow flexible computation for larger sizes where most cirrus ice particles are classified. The method commonly used for large and intermediate size crystals is the Geometric

Optics method. In this method, the assumption is made that a plane wave can be represented by a collection of independent parallel rays. The path of each ray is traced through the scatterer as it interacts with the particle surfaces obeying Snell's law and the Fresnel equations (to be discussed in section 2.2.2). A Monte Carlo approach is usually adopted, selecting random initial points of incidence for the rays. The scattering properties, including in some cases polarization properties, are obtained by collecting outgoing rays in angular bins. The method does not consider internal diffraction or internal edge effects. For very large crystals this does not restrict the accuracy significantly because the effects are not significant. The method also has no size dependency. In this form, Geometric Optics is sometimes referred to as *pure ray tracing.*

The term *Classical Geometric Optics* (GO) refers to pure ray tracing results that are combined with an external diffraction pattern. The external pattern is usually calculated using Fraunhofer diffraction at an aperture of equal area to the projected area of the particle. This introduces some size dependency and accounts for effects external to the crystal. Diffraction is still not considered in the ray tracing part of the calculation. There have been many GO implementations, most notably in terms of this investigation the implementation by Macke et al. [23], which shall be discussed in more detail later in this section.

Use of the GO method is limited by crystal size. The approximation is only valid for large size parameters where the distance between ray-facet interactions and the dimensions of the facets are very much greater than the wavelength of the incoming light. GO provides its most accurate results at large size parameters. Comparisons between GO for spheres and Mie theory found that the GO results were reasonably accurate, although only for size parameters greater than several hundreds [24]. A comparison to T-matrix for ice spheroids at a wavelength of 3.7 μm found even better agreement, with phase functions down to a size parameter of 60 differing little [25]. The authors noted that similar comparisons to spheres did not succeed however, indicating that the nonsphericity of the spheroids was an assisting factor. The method has also been applied to large stochastically deformed spheres [26].

The great advantage of the GO method is that it can be applied to almost any geometry. Numerous authors have applied it to the problem of hexagonal ice columns (for example, [27]), some of whom extend their discussion to oriented hexagonal crystals [28, 29, 30]. The motivation for many such studies is to try to explain the origins of certain atmospheric halo effects. Using GO it has been shown that regular particle shapes such as circular cylinders and spheroids that

are much larger than a wavelength are not good approximations for hexagonal columns, particularly at visible wavelengths [31]. This emphasizes the need to develop models able to handle such geometries. Note that at strongly absorbing infrared wavelengths cylinders can be used in place of hexagonal columns because particle geometry becomes much less important [32]. This will be discussed in section 4.4.2. The possibility that impurities such as soot particles could affect the scattering properties of hexagonal columns has also been investigated [33]. More complex geometries that are likely to be present in cirrus such as bullets, rosettes and hollow columns have been studied by various authors, for example [23, 34, 35]. More examples from the literature where the scattering properties of complex geometries that are likely to be found in cirrus have been calculated will be discussed in chapter 5.

In the development of the RTDF model the GO code written by Andreas Macke was used [23]. This implementation of the GO method for crystal geometries is based on the work of Rockwitz [30] where the scattering results for hexagonal columns are generated from ray tracing combined with a far field diffraction pattern. In this case, an equal area rectangular aperture is used. The method was limited to convex crystal shapes (i.e. multiple external reflections were not supported). Macke extended the method to concave particles and introduced diffraction at a circular rather than a rectangular aperture for simplicity reasons [34]. To account for polarization in the Macke code [23], the scheme for Stokes vector calculation outlined in Muinonen et al. [36] was adopted.

Section 2.5 will discuss methods that are based upon GO that offer improved accuracy and lower size applicability by considering internal diffraction, internal edge effects or by introducing exact theory components.

2.2 Geometric Optics Theory

2.2.1 The Geometry of the Problem

By using spherical polar coordinates, any position in space can be defined by a polar angle, θ, an azimuthal angle, ϕ and a distance from the origin, r. This is shown in figure 2.1a. Some texts use the convention given here while others exchange θ and ϕ. In this thesis the convention that θ is the polar angle will be adopted because it will be shown later that when considering a phase function,

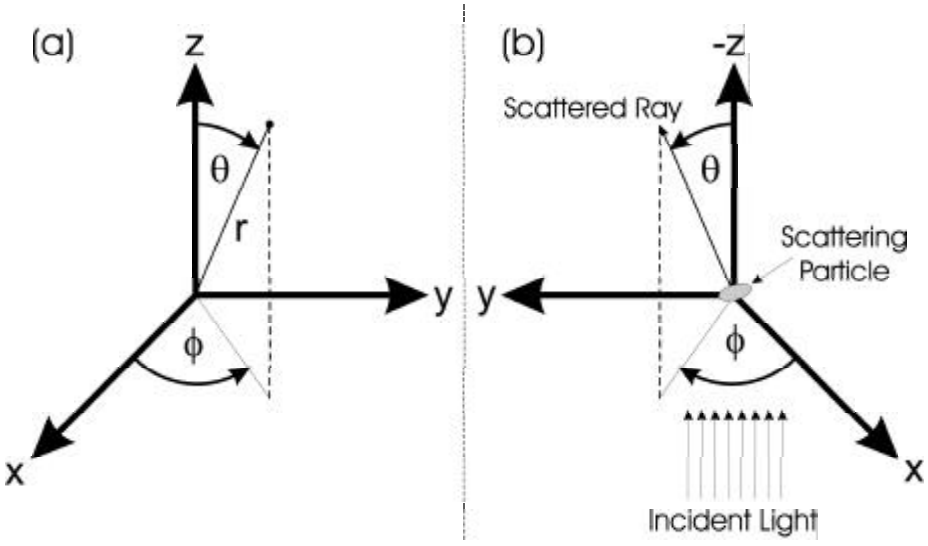

Figure 2.1: (a) The standard definition of spherical polar coordinates. (b) The geometry of the light scattering problem used throughout this thesis.

the scattering angle that is plotted on the x-axis is the same as the polar angle and the phase function scattering angle is normally referred to as θ.

Using only the angles θ and ϕ in figure 2.1a, it is possible to define any direction emanating from the origin. This is illustrated in figure 2.1b. It shows a light scattering event following the conventions that are adopted by the GO and RTDF model codes and also for the remainder of this thesis. A scatterer is located at the origin. Light is incident upon the scattering particle, light initially travelling in the negative z direction. Scattered light is collected in the far field. In the case of ray tracing models it leaves the scatterer in the form of a ray. The direction of the ray can be defined by the polar angle θ which is measured from the -z direction and the azimuthal angle ϕ, measured from the positive x-axis in an anticlockwise direction when looking in the -z direction.

In a scattering event, one can define the *scattering plane* as the plane that contains the incident ray, the scattering particle and the scattered ray. This term will be used repeatedly in the coming paragraphs.

It is standard practise to study scattering properties against θ only (for example, a phase function) and so normally scattering results for each value of θ are averaged over the azimuthal angle ϕ. In standard GO implementations, this is indeed the case. As a result not all of the information is retained when the direction of an outgoing ray is determined. For the majority of the results

presented here, the same standard format of results will be adopted. However, an extension to 2D scattering patterns where both scattering angles are retained will be discussed in chapter 7. Particularly important in that chapter is the absolute direction of the x and y axes, also relevant for fixed orientation studies. The convention adopted in this thesis is as follows. If one were to travel alongside an incident ray in the RTDF codes, one would find the positive x-axis pointing to the left with the positive y-axis pointing downwards.

2.2.2 Refractive Index, Snell's Law and the Fresnel Equations

The effect of a plane boundary such as a crystal facet interrupting the propagation of a light ray will now be described. Following the interaction with a plane boundary, incident light will spawn two components, one reflected and one refracted (also referred to as transmitted). The incident light and the boundary normal form a plane known as the *plane of incidence*. The reflected and transmitted light components will both fall in this plane. Consider the situation in figure 2.2 where there are different media on either side of a plane boundary. The plane of incidence lies on the page while the dotted line represents the boundary normal. A beam of light approaches the boundary in medium 1 which has a refractive index of n_1. Upon interaction the light beam will be partly transmitted into medium 2 (refractive index n_2) with some change in direction and partly reflected back into medium 1. The law of reflection simply states that the angle of reflection equals the angle of incidence, $\theta_i = \theta_r$. The direction of the transmitted component is described by the angle of refraction, θ_t. It is governed by the refractive indices of the two media, n_1 and n_2. The angle of refraction can be found using the law of refraction, also known as *Snell's law*, which is given in equation 2.1.

$$n_1 \sin\theta_i = n_2 \sin\theta_t \tag{2.1}$$

There is some debate over who first discovered the law of refraction. It was discussed as early as the first century A.D. by Ptolemy, though without accuracy. It is certain that Willebrord Snell (1580-1626) formulated the law in 1621, but he did not publish it. It was described independently by Descartes in his publication on Dioptrics ("the part of optics that deals with refraction") in 1637. When it was later discussed by Christiaan Huygens in 1703, it was referred to as

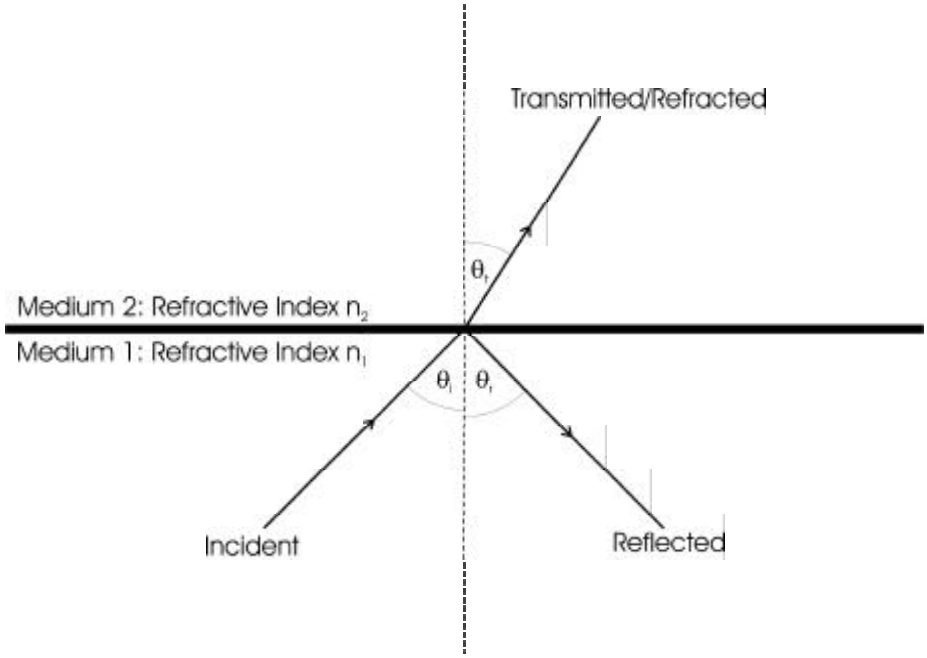

Figure 2.2: A diagram of a light ray incident upon a plane boundary.

Snell's result and has been credited to Snell ever since. Interestingly, in French it is still referred to as "la loi de Descartes".

Referring back to figure 2.2, there is another case that can occur. When light is passing between media and there is a decrease in the refractive index, if the incident angle θ_i is greater than a critical angle given by $\theta_{crit} = \arcsin \frac{n_2}{n_1}$ then *total internal reflection* occurs. This is where there is no transmitted component, and all of the light is reflected back into medium 1.

Critical to Snell's law is the concept of the refractive index of a material. The absolute refractive index of a medium is a complex quantity of the form $n = n_r + in_i$. The imaginary part, n_i, describes the absorption of light by the material. When considering ice at visible wavelengths, n_i is very small and is often neglected totally. This leads to the real part n_r being used independently. This is the case in the discussion up to this point where the values n_1 and n_2 have been used. When the imaginary part n_i is not zero, θ_t becomes complex and is therefore no longer simply an angle of refraction. A detailed description of the mathematics of this can be found in Born and Wolf [37, chapter 14]. The GO code by Macke and hence the RTDF model takes this and the attenuation of light as it passes through the material into account in its calculations.

The refractive index can be defined as in equation 2.2 where c is the velocity of light in a vacuum and v is the velocity of light in the medium. When the imaginary part of the refractive index is non zero, v represents the complex phase velocity.

$$n = \frac{c}{v} \tag{2.2}$$

The absolute refractive index therefore gives a measure of the velocity of light in the medium. It is influenced by the chemical composition of the particle. The fundamental electromagnetic properties of the material are consolidated in n. One can write n in terms of the permittivity (ε) and permeability (μ) of the material, as shown in equation 2.3. When considering non-magnetic substances such as ice, μ is effectively unity. The refractive index is wavelength dependent which leads to, for example, the dispersion of white light into a rainbow of colours when incident on a glass prism.

$$n = \sqrt{\varepsilon\mu} \tag{2.3}$$

The change in direction upon refraction is caused by different portions of the incident wavefront meeting the boundary at different times, leading to the change of velocity turning the wavefront direction towards (away) from the boundary normal for transition from a lower (higher) to a higher (lower) refractive index.

The laws of reflection and refraction describe the directions of the reflected and transmitted components following an interaction with a boundary between two media, but it is also necessary to consider their amplitudes. These are defined by the Fresnel formulae. If A is the amplitude of the electric vector of the incident light and r and t are the amplitudes of the reflected and transmitted components, one can write the Fresnel formulae as shown in equations 2.4-2.7. All of the vectors have been resolved into components parallel ($||$) and perpendicular ($\perp$) to the plane of incidence.

$$t_{||} = \frac{2n_1 \cos\theta_i}{n_2 \cos\theta_i + n_1 \cos\theta_t} A_{||} \tag{2.4}$$

$$t_{\perp} = \frac{2n_1 \cos\theta_i}{n_1 \cos\theta_i + n_2 \cos\theta_t} A_{\perp} \tag{2.5}$$

$$r_{||} = \frac{n_2 \cos\theta_i - n_1 \cos\theta_t}{n_2 \cos\theta_i + n_1 \cos\theta_t} A_{||} \tag{2.6}$$

$$r_{\perp} = \frac{n_1 \cos\theta_i - n_2 \cos\theta_t}{n_1 \cos\theta_i + n_2 \cos\theta_t} A_{\perp} \tag{2.7}$$

In the case of total internal reflection, the magnitudes of the reflected and incident amplitudes are equal. These formulae again assume a real refractive index. When considering a complex refractive index, the value of θ_t becomes complex and this can simply be substituted into the stated Fresnel equations to yield the form used in the Macke code. A more mathematical description is again available from Born and Wolf [37, chapter 14].

The consideration of complex refractive indices in the GO and RTDF codes will have very little effect for ice at visible wavelengths because, as already stated, the imaginary component is very small. However, it does mean that the models can be applied to ice at infrared wavelengths where absorption is more significant. The RTDF model will be used to make near infrared comparisons to IGO (to be discussed in section 2.5) in section 4.4.2 and to aircraft radiance measurements in chapter 8.

2.2.3 Scattering Cross Sections

The concept of a cross section value is widely used in nuclear physics as an indication of the probability that an event will occur. In light scattering, the descriptions of cross sections that follow are not restricted to use within GO but are discussed here rather than in section 2.6 due to their specific use within the GO model.

Cross section values have units of area. In the field of light scattering, there are three cross section values that are regularly discussed. The first is the extinction cross section, denoted by C_{ext}. It defines the total attenuation of incident light due to scattering and absorption. The units of area can be understood if it is explained that the total energy that is attenuated is equal to the amount of energy from the incident beam falling on an area the size of the cross section value. Mishchenko et al. [38] define the extinction cross section as follows:

> The product of the extinction cross section and the incident monochromatic energy flux is equal to the total monochromatic power removed

by the particle from the incident beam.

The other two cross sections commonly used are the scattering cross section (C_{sca}) and the absorption cross section (C_{abs}). They have almost identical definitions to the extinction cross section except that they deal with the attenuation of the incident light due to scattering or absorption only, as appropriate. Since extinction is equal to the sum of scattering and absorption and this extends to the cross section values, one can write equation 2.8.

$$C_{ext} = C_{sca} + C_{abs} \tag{2.8}$$

Generally, C_{ext}, C_{sca} and C_{abs} are functions of the orientation of the particle, its size, morphology and refractive index as well as the polarization state and wavelength of the incident light. The cross section values are useful in that they provide an overview of a scattering process and describe the effect the scattering particle has on the incident light. Cross section values are calculated in both the Macke GO code [23] and the RTDF model. In these models the concept of cross sections is also used to obtain the phase function from the separately calculated contributions of ray tracing and external diffraction in the following way. One can define a cross section value for each of the two components. The diffraction scattering cross section, C_{sca}^{dif}, represents the amount of scattering of the incident beam that is due to the external diffraction. The ray tracing scattering cross section, C_{sca}^{ray}, represents the amount of scattering of the incident beam that is due to ray tracing. The sum of these cross sections will be equal to the total scattering cross section. The combination of the two phase functions is a simple addition but weighted by their individual scattering cross sections. The final phase function is given by equation 2.9 where P_{dif} and P_{ray} are the diffraction and ray tracing phase functions respectively.

$$P(\theta) = \frac{C_{sca}^{dif} P_{dif} + C_{sca}^{ray} P_{ray}}{C_{sca}^{dif} + C_{sca}^{ray}} \tag{2.9}$$

By definition, the ray tracing extinction cross section is equal to the geometric cross section of the particle. In other words, the amount of energy removed by ray tracing is equal to the amount of energy incident directly on the scatterer. Therefore in the non-absorbing case the ray tracing scattering cross section C_{sca}^{ray} is equal to the mean projected area of the scatterer, denoted by C_{geo}.

From Babinet's principle it is known that a diffraction pattern is the same for an obstacle and an aperture of equal size and shape (this will be discussed in section 2.3). Therefore, the energy removed from the incident beam of light due to diffraction will also be equal to the mean projected area of the scatterer, so C_{dif} is also equal to C_{geo}. Given this non-absorbing situation, equation 2.9 simplifies because the cross sections and hence the weightings are equal. The fact that the total value of C_{ext} in the GO regime is twice rather than one times the mean projected area of the scatterer is often referred to as the *extinction paradox*. However, the paradoxical nature is removed by, as discussed above, taking into account Babinet's principle and the fact that light passing by the scatterer outside its physical boundaries is also removed from the incident beam through diffraction.

For an absorbing material there will also be extinction due to absorption, C_{abs}. This will be at the expense of scattering due to ray tracing. This means that the final phase function will be weighted towards the diffraction phase function. The amount of absorption can be measured by recording the amount of energy that enters (E_{in}) and leaves (E_{out}) the scatterer through ray tracing. The ray tracing scattering cross section is then given by equation 2.10. Note that the extinction cross section of the ray tracing component does not change and so $C_{ext} = 2C_{geo}$ still holds.

$$C_{sca}^{ray} = C_{geo}\frac{E_{out}}{E_{in}} \tag{2.10}$$

The scattering and extinction cross sections can be used to define the *single scattering albedo*. It is represented by the symbol ω and is given in equation 2.11.

$$\omega = \frac{C_{sca}}{C_{ext}} \leq 1 \tag{2.11}$$

The single scattering albedo provides a measure of the probability that an interaction will result in scattering rather than absorption. This quantity is widely used in radiative transfer applications and will be used in chapter 8.

2.3 What is Diffraction?

Many authors have offered definitions for the phenomenon of diffraction. Palmer and Rogalski [39] stated that:

> The deviation of a wave from rectilinear propagation, which can occur whenever a region of the wavefront is obstructed, is called *diffraction*.

This is similar to the definition offered by Hecht [40], who emphasizes the fact that it is a wave phenomenon first, an optical phenomenon second:

> The phenomenon of *diffraction* is the deviation from rectilinear propagation that occurs when light advances beyond an obstruction... The effect is a general characteristic of wave phenomena occurring whenever a portion of a wavefront, be it sound, a matter wave, or light, is obstructed in some way.

It has become common to use the term diffraction for the most general possible case of the definition by Hecht, that any scattering problem is actually a diffraction problem. It will be shown in section 2.4.2 that diffraction theory can be formulated to help solve scattering problems for arbitrary geometries.

Fowles [41] defines the diffraction of light by describing an example:

> If an opaque object is placed between a point source of light and a white screen, it is found that the shadow that is cast by the object departs from the perfect sharpness predicted by geometrical optics. Close examination of the shadow edge reveals that some light goes over into the dark zone of the geometrical shadow and that dark fringes appear in the illuminated zone. This smearing of the shadow edge is closely related to... the spreading of light after passing through a very small aperture such as a pinhole or narrow slit... The collective name given to these departures from geometrical optics is *diffraction*.

The first known reference to the phenomenon of diffraction appears in the work of Leonardo da Vinci (1452-1519). The first accurate description of diffraction came in 1665 in a book by Francesco Maria Grimaldi (1618-1663), which was not published until after his death. He is responsible for the name diffraction, referring to the phenomenon by the Latin word *diffractio* which loosely means "breaking up". However, he was unable to explain the phenomenon. Interestingly, he was the first to consider the possible wave nature of light. He even investigated the interaction between two beams of light in an experiment reminiscent of the famous two slit experiment by Young (see below), although he failed to observe interference fringes.

Christiaan Huygens (1629-1695) was the first true proponent of the wave theory of light and was able to derive the laws of reflection and refraction from his wave formulation. In describing how light propagates, Huygens stated what has since become known as Huygens's principle:

> Every point on a wavefront may be considered as a centre of a secondary disturbance which gives rise to spherical wavelets, and the wavefront at any later instant may be regarded as the envelope of these wavelets [37].

However, the approach ignores most of the secondary wavelet, retaining only that portion common to the envelope. Although Huygens's principle explains deviation from rectilinear propagation, it does not explain the light and dark fringes that Fowles described. Hence, using this theory for the propagation of light alone cannot fully explain diffraction.

In the discussion of light propagation, Thomas Young (1773-1829) added the principle of interference around the turn of the century. He stated that:

> When two undulations, from different origins, coincide either perfectly or very nearly in direction, their joint effect is a combination of the motions belonging to each [40].

Young demonstrated his interference principle using the famous two slit experiment, although in its original form he did not use slits at all. He passed sunlight through a pinhole to create a spatially coherent source that illuminated two further pinholes. The pattern on a screen that resulted from the light passing

through the two pinholes was found to show bright and dark fringes. The light from the two pinholes was exhibiting interference.

Augustin Jean Fresnel (1788-1827) used Young's interference principle to help explain diffraction. In 1818, he modified Huygens's principle by adding that the secondary wavelets mutually interfere. This combination of ideas has become known as the Huygens-Fresnel Principle:

> Every unobstructed point of a wavefront, at a given instant, serves as a source of spherical secondary wavelets (with the same frequency of that of the primary wave). The amplitude of the optical field at any point beyond is the superposition of all these wavelets (considering their amplitudes and relative phases) [40].

The Huygens-Fresnel principle therefore offers an explanation for the phenomenon of diffraction, including the observed interference fringes.

In 1882, Gustav Kirchhoff (1824-1887) derived the observed diffraction theories of Fresnel from first principles resulting in the Kirchhoff Diffraction Theory [42]. Rigorous solutions to some diffraction problems have since been found but in most cases due to mathematical complexity it is necessary to use time consuming numerical computations or approximate methods. The theory of Huygens and Fresnel is adequate for the treatment of the majority of problems. The mathematics of the Kirchhoff Diffraction Theory will be discussed in section 2.4.

An interesting quirk of diffraction is that diffraction due to an aperture will provide the same pattern as diffraction due to a complimentary obstacle, that is an obstacle of the same size and shape as the aperture. This is known as Babinet's principle, after it was discovered by the French physicist Jacques Babinet (1794-1872). This is an extremely useful result. It explains why diffraction at an equal area circular aperture can be used as the external diffraction pattern in the Macke GO code. The obstacle of the scattering particle is replaced with the equal cross sectional area aperture. The use of the actual cross section shape as the aperture is only restricted by the computational expense in performing the calculation.

2.4 Diffraction Theory

2.4.1 The Kirchhoff Diffraction Integral

The Kirchhoff diffraction theory was the first mathematical explanation for the observed diffraction phenomena derived from first principles. The theory has two main components, the Kirchhoff diffraction integral and the Kirchhoff approximation. In this section the derivation of the scalar Kirchhoff diffraction integral will be discussed, following Born and Wolf [37]. The vector case can be found in the literature, for example Jackson [42]. In section 2.4.2, the Kirchhoff approximation will be considered.

The aim is to express the solution of the homogeneous wave equation at an arbitrary point in a field, a point denoted here by P. One could also say that the optical disturbance at P is to be evaluated. The method Kirchhoff developed uses Green's theorem to relate a field (electric or magnetic) inside a closed volume ν to the values of the field and its normal derivative on an enclosing surface, S. Green's theorem, a vector form of Gauss's theorem, is given in equation 2.12. It requires that U and V have continuous first and second order partial derivatives within and on the surface S. A derivation is available in the literature, for example Kreyszig [43].

$$-\iint_S \left(U\frac{\partial V}{\partial n} - V\frac{\partial U}{\partial n}\right) \mathrm{d}S = \iiint_\nu \left(U\nabla^2 V - V\nabla^2 U\right) \mathrm{d}\nu \tag{2.12}$$

The inward surface normal is given by n. Consider that the function U is a monochromatic scalar wave. It therefore satisfies the time independent wave equation. If V is also a solution to the time independent wave equation, the volume integral vanishes at all points and so equation 2.13 is obtained.

$$\iint_S \left(U\frac{\partial V}{\partial n} - V\frac{\partial U}{\partial n}\right) \mathrm{d}S = 0 \tag{2.13}$$

Suppose that one defines $V = e^{ikq}/q$ where q is the distance from P. This presents a problem because at P, $q = 0$ and so there is a singularity. This can be averted by removing the point P from the integration in equation 2.13. This is achieved by creating an integral over a small sphere of radius ρ that

surrounds P and by making it a component of the enclosing surface. One can then let $\rho \to 0$. By expressing this sphere integral in spherical coordinates and integrating over a full solid angle, one finds that the contribution simplifies to just $4\pi U_P$, where U_P is the disturbance at the point P.

The *integral theorem of Kirchhoff* is then given by equation 2.14.

$$U_P = \frac{1}{4\pi} \iint_S \left(U \frac{\partial}{\partial n} \left(\frac{e^{ikq}}{q} \right) - \frac{e^{ikq}}{q} \frac{\partial U}{\partial n} \right) \mathrm{d}S \tag{2.14}$$

The Kirchhoff diffraction integral allows the calculation of the optical disturbance at any point in a volume if the field and its first derivative at all places on an enclosing surface are known.

2.4.2 The Kirchhoff Approximation

Unfortunately, the values of U and $\partial U/\partial n$ at all points on an enclosing surface are not normally known, unless the problem has been solved by another method. Kirchhoff worked around this problem by introducing the *Kirchhoff approximation*.

Figure 2.3 shows two possible applications of the Kirchhoff approximation. In case (a), light is incident on an aperture in surface 1. The light will create a diffraction pattern somewhere between surfaces 1 and 2, a region where the point P from the last section may exist. Case (b) gives an equivalent situation that is familiar because it resembles a light scattering event. This is the application of the suggestion in section 2.3 that the term diffraction can be applied to a scattering problem because of the mathematical solution. Within surface 1 there is a scattering particle that will produce a scattering pattern between the surfaces 1 and 2. The two cases are analogous.

Kirchhoff made two assumptions in developing the approximation.

Assumption 1 *The field and the first derivative of the field are zero everywhere on Surface 1, except in any openings.*

Assumption 2 *In any openings on Surface 1, the field and the first derivative*

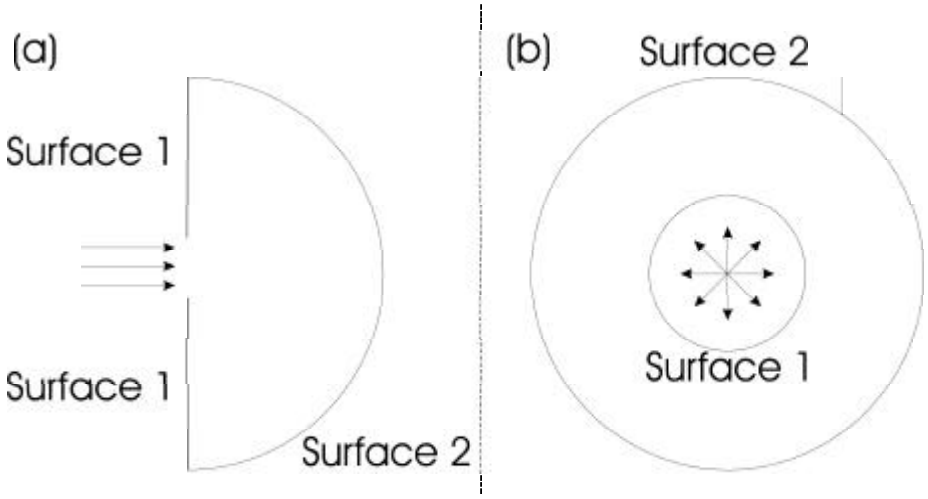

Figure 2.3: The Kirchhoff approximation can be used to solve cases such as these: (a) Light incident on an aperture in surface 1 that will create a diffraction pattern in the region between surfaces 1 and 2. (b) Light scattering from a particle that is located within surface 1 that creates a scattering pattern in the region between surfaces 1 and 2.

of the field are equal to the values that would exist due to the incident wave in the absence of a screen or scatterer.

These two assumptions greatly simplify the problem. Considering surface 1, one now needs only to know the incident field over the diffracting surface. In case (a) this is the diffraction aperture, in case (b) the particle surface. Surface 2 still poses a problem. A further assumption can be made that the surface is at a very great distance. The integral over surface 2 will then vanish if the evaluation of the optical disturbance at some point P is performed at some time when the emanating waves due to the diffraction event have not yet arrived at the surface.

Given these assumptions it is possible to calculate the optical disturbance at any point beyond an aperture if the incident field at the aperture is known. Likewise, the scattering by a particle can also be calculated at any point in space if the field on the surface of the scatterer is known. This provides the motivation for methods such as the *Modified Kirchhoff Approximation* (MKA) [5] and the IGO method [6], both of which will be discussed in section 2.5. Briefly, using ray tracing it is possible to obtain values for the scattered field at the particle surface. Using the Kirchhoff approximation, these results can be transformed to the far field. The MKA [5] provides a less computationally demanding method

than implementing the full Kirchhoff approximation, although there is nothing other than computational constraints preventing the implementation of the full approximation. The IGO uses a different exact theory technique, the *electromagnetic equivalence principle* [44] to transform the ray tracing results on the particle surface to the far field.

2.4.3 Diffraction by a Half-Plane

Using rigorous electromagnetic theory, it is possible to solve the problem of diffraction at a half-plane. A full mathematical derivation is available in Born and Wolf [37, chapter 11]. The solution provides a platform on which the RTDF model is built, something that will be explained in chapter 3. In this section there is a brief description of how one can determine the paths of energy flow lines passing a half-plane. The description follows that given in Hesse and Ulanowski [7]. For more details, referring to the quoted literature is recommended. Only the case of H-polarization will be considered. The E-polarization case follows an equivalent method and can be found in Hesse and Ulanowski [7].

Consider a perfectly conducting half-plane at $y = 0$, $x > 0$. Incident light travels in the negative y direction before interacting with the half-plane. The incident field is given by equation 2.15.

$$H_z^{(i)} = \sqrt{\frac{2}{\mu_0}} e^{-ikr\cos(\theta-\alpha_0)} \tag{2.15}$$

Here, μ_0 is the permeability of free space, k is the wave number and α_0 is the angle between the direction of propagation and the positive x-axis. Equation 2.15 is expressed in terms of polar coordinates, hence the use of r and θ.

The complete field after interaction with the half-plane can be written in terms of Fresnel integrals. This is shown in equation 2.16 where $F[a] = \int_a^\infty e^{i\xi^2} \mathrm{d}\xi$ is the complex Fresnel integral. More information on Fresnel integrals is available in any optics text, for example Hecht [40, chapter 10]).

$$H_z = \sqrt{\frac{2}{\pi\mu_0}} e^{-\frac{1}{4}i\pi} \left\{ e^{-ikr\cos(\theta-\alpha_0)} F\left[-\sqrt{2kr}\cos\frac{1}{2}(\theta-\alpha_0)\right] + e^{-ikr\cos(\theta+\alpha_0)} F\left[-\sqrt{2kr}\cos\frac{1}{2}(\theta+\alpha_0)\right] \right\} \tag{2.16}$$

The direction of the time averaged Poynting vector indicates the direction of energy flow. It is defined in equation 2.17.

$$\left\langle \vec{S} \right\rangle = \frac{1}{2}\mathrm{Re}\left(\vec{E}\times\vec{H}^*\right) = \frac{1}{2}\mathrm{Re}\left(E_y H_z^*, -E_x H_z^*, 0\right) \tag{2.17}$$

By combining the complete field expression (equation 2.16) with Maxwell's first equation in free space with the time factor suppressed one can obtain expressions for E_x and E_y . They are given in equations 2.18 and 2.19.

$$E_x = -\frac{1}{ik}\sqrt{\frac{\mu_0}{\varepsilon_0}}\frac{\partial H_z}{\partial y} \tag{2.18}$$

$$E_y = \frac{1}{ik}\sqrt{\frac{\mu_0}{\varepsilon_0}}\frac{\partial H_z}{\partial x} \tag{2.19}$$

Having calculated values for H_z, E_x and E_y, the Poynting vector is now known. One can calculate the energy flow lines as they pass the half-plane using the differential equation given in equation 2.20.

$$\frac{\mathrm{d}x}{\mathrm{d}y} = \frac{\langle S\rangle_x}{\langle S\rangle_y} \tag{2.20}$$

Such calculated energy flow lines will be discussed in section 3.2.1 which covers the first stage of the development of the RTDF model.

2.5 Light Scattering Models based upon Geometric Optics

An exact analytical solution for the scattering of hexagonal crystals is unlikely to ever be derived due to the inability to formulate a coordinate system at the particle surface that would allow boundary conditions to be implemented. As discussed in section 2.1, GO is the method of choice for intermediate to large sizes where most cirrus ice crystals are classified, and also for more complex geometries.

For lower size parameters one can use any of the exact or numerical techniques such as T-matrix or FDTD described in the previous section. Above the size applicability of these methods there exists a gap before the GO method offers acceptable results. Bridging this gap is important to ensuring accurate treatment of the scattering properties of scatterers in many fields. To extend the size applicability of the exact and numerical methods upwards is most desirable, but is governed overwhelmingly by the progress of computational capacity and even with the rapid advances in computation in recent years is likely to take decades. The alternative is to extend the size applicability of GO downwards. Many attempts have been made to improve the GO method both in its standard size applicability range and at reduced size parameters. The focus of these improvements is either to introduce diffraction to the ray tracing component or to introduce exact theory components. A brief overview of the models that use GO as a base shall be given in the paragraphs that follow.

Some years ago Keller put forward a model called the Geometrical Theory of Diffraction [45]. In addition to the standard GO rays, it introduces diffracted rays that are created when incident rays strike edges and corners of boundary surfaces and in certain other cases. The method was shown to reproduce diffraction from various apertures well. In terms of GO modelling, it could have provided an alternative to combining ray tracing results with an external diffraction pattern because the complete scattering pattern was considered by ray tracing.

The Heisenberg uncertainty principle has been used several times in ray tracing methods for the treatment of diffraction at apertures. Coffey et al. [46] outlined a system where the distance from an aperture edge that a ray strikes is taken to be the uncertainty in the ray's position. An uncertainty in the momentum can then be determined and from this a maximum deflection angle can be calculated.

They note that Likeness [47] proposed a probability density function to represent the deflection angle as a normal distribution with rays most likely to travel straight ahead on passing an aperture but with a standard deviation equal to the maximum deflection angle determined from the uncertainty principle. An almost identical method was described in Freniere et al. [48]. This modelling of diffraction at an aperture using a ray tracing technique could in principle replace the external Fraunhofer diffraction calculation that is used in standard GO. There would however be an increase in computational expense to obtain likely similar results.

The need for the addition of an external diffraction pattern in the GO model stems from the explanation of the extinction paradox, that light passing by the crystal outside of its physical boundaries is also scattered (see section 2.2.3). In any case, pure ray tracing alone is size independent and strongly underestimates forward scattering. While the treatment of pure ray tracing can provide information regarding effects such as halos, it is flawed due to the size independence. Introducing a physical optics component is a crucial part in making the GO method a useful tool. Summing external diffraction with the ray tracing component introduces some size dependency but better improvements can be achieved. The following three examples (Borovoi and Grishin, Ravey and Mazeron, Muinonen) are all different approaches that use Kirchhoff's diffraction theory in their treatment of diffraction.

A novel approach was considered by Borovoi and Grishin [49]. Their method modifies the standard ray tracing procedures so that it considers bundles of rays that are taking the same parallel paths through the crystal. These bundles are referred to as beams and each carries with it a Jones matrix which ensures that interference can later be considered. The physical optics correction is introduced by transforming these beams as they reach the surface of the scatterer to the far field. The mechanism of far field transformation simply considers that the outgoing beam will spread and undergo interference. The authors assume that this can be modelled using Fraunhofer diffraction at the aperture of the beam shape incident on the final crystal surface, a calculation derived from Kirchhoff's diffraction theory. This method offers rapid computation, but it was found in discussions [50] that it failed to reproduce certain scattering features that are predicted by the RTDF model and that have been observed in the laboratory (see chapter 7). One possible explanation for this is that Borovoi and Grishin do not consider diffraction effects inside the crystal.

A rigorous theoretical treatment of diffraction could use the Kirchhoff approx-

imation (see section 2.4.2) to transform scattering properties on the surface of the scatterer to the far field through the Kirchhoff diffraction integral [14]. An implementation of this as an improvement to GO ray tracing would require the inclusion of phase tracing to evaluate the fields correctly on the scatterers surface. This would then allow the Kirchhoff integral to be applied.

Ravey and Mazeron [51] introduced a physical optics correction to GO by using a method related to the Kirchhoff approximation to transform fields on a particle surface found through standard ray tracing techniques to the far field. The method used was specifically for large spheroids.

Muinonen took the idea further by introducing a *Modified Kirchhoff Approximation* (MKA) [5]. The method is applicable to more general shapes. Rays are traced in the normal manner until they reach the point of exiting the crystal. They are then transformed to the far field through a simplified version of the Kirchhoff approximation. The simplifications are that the amplitudes on the particle surface are summed without regard to phase, that the Kirchhoff diffraction integral is applied to circular apertures equal in area to the facets rather than the more complicated shapes of the facets themselves and finally that the external diffraction is calculated from Fraunhofer's theory assuming a size distribution of circular projected areas equal to the distribution of real projected areas for random averaged orientations. The complete Kirchhoff approximation could have been applied but it would have been prohibitively computationally expensive.

One of the limitations of the MKA is that it was developed specifically for applicability to random orientations. This eliminates its direct use for particles which adopt a preferred orientation or for studying fixed orientations. It is, however, applicable to size parameters as low as 10 for satisfactory results. This is a size parameter region that is significantly lower than those to which GO methods could previously be applied.

A significant improvement was found when the *Improved Geometric Optics* (IGO) method was first put forward by Yang and Liou [52]. The model was later extended to three dimensions [6]. The model again uses a standard ray tracing technique to find the electric field on the surface of the scatterer. This surface field is calculated by using the Fresnel formulae and by taking into account the phase and the area illuminated by the individual wavelets (this is an important difference when comparing to, for example, the MKA). The field can be expressed in the form of the tangential electric and magnetic currents and is

then mapped to the far-field using rigorous electromagnetic theory in the form of the equivalence principle [44]. This improves on the approximate physical optics correction of the MKA. This method by definition will be significantly more computationally expensive than GO, but can be used at low size parameters (down to 20 for reliable phase functions and scattering efficiencies when compared to FDTD) and will provide improved results. In the author's own words, the method can be classed as a hybrid method due to the approximate ray tracing component coupled with the exact EM theory component. At size parameters above around 100, IGO provides asymmetry parameters equal to standard GO results. Results calculated with IGO will be used in section 4.4.

The subject of this thesis, the RTDF model, offers an improvement to GO using a different approach. It attempts to improve the ray tracing both inside and as rays exit the crystal using a physical optics correction that has been derived using exact theory calculations for diffraction by a half-plane. This method allows rapid computation (computation times not significantly longer than standard GO) but with much improved results. The model was first introduced by Hesse and Ulanowski [7] and then compared to SVM for the two dimensional case [8]. Following the work included in this thesis, it has been extended to three dimensions [53]. A description of the development of the model will be given in chapter 3.

2.6 Selected Aspects of Light Scattering Theory

2.6.1 The Amplitude Scattering Matrix

The consideration of light incident on a boundary between two media as discussed in section 2.2.2 is crucial for the ray tracing codes. However, it is also necessary to be able to describe a more general scattering event using electromagnetic theory. This can be achieved using the *amplitude scattering matrix*. One can relate the electric vectors of the incident (subscript i) and scattered (subscript s) waves to each other by resolving them into their components parallel ($||$) and perpendicular ($\perp$) to the scattering plane and using the two by two amplitude scattering matrix, as shown in equation 2.21.

$$\begin{pmatrix} E_{s\perp} \\ E_{s||} \end{pmatrix} = \frac{e^{ik(z-r)}}{ikr} \begin{pmatrix} S_2 & S_3 \\ S_4 & S_1 \end{pmatrix} \begin{pmatrix} E_{i\perp} \\ E_{i||} \end{pmatrix} \tag{2.21}$$

The amplitude scattering matrix depends upon the directions of incident and scattered light as well as the composition and orientation of the scattering particle. The scattered fields and the matrix components are functions of θ and ϕ and so scattering in all directions can be described by the matrix. The matrix can then fully describe the scattering event, including providing information about polarization and, pertinent to the discussion later, phase. Simplified problems (such as the case of a sphere) can lead to simplifications of the matrix, by setting elements to zero or reducing the number of independent elements. The subject of the amplitude scattering matrix is covered in more detail in any good text on light scattering theory, for example [13, 54].

2.6.2 The Stokes Parameters and Mueller Matrices

The form of the amplitude scattering matrix is useful only from a theoretical point of view because it is not possible to measure the electric field associated with a beam of light in the laboratory. However, one can measure the irradiance of a beam of light (the energy flux per unit area) and, using a series of linear and circular polarizers, the complete state of polarization. This information can be expressed in the form of the *Stokes parameters*. They can be determined easily using simple experimental techniques.

To introduce the four parameters, consider an experiment where a beam of light is incident upon a detector. Various polarizers are placed between the source and the detector to investigate the polarization of the beam. Linear polarization is measured parallel (horizontal) and perpendicular (vertical) to a horizontal scattering plane. The first parameter, I, is the irradiance measured by the detector with no polarizer present. The second parameter, Q, is found by measuring the irradiance when there is first a horizontal polarizer in the beam and then a vertical polarizer. Q is given by the difference in the irradiances and reflects the tendency of the beam to be horizontally ($Q > 0$) or vertically ($Q < 0$) polarized. The third parameter, U, indicates the tendency of the beam to be polarized at $45°$ ($U > 0$) or $-45°$ ($U < 0$). It is determined in a similar way to Q but using linear polarizers at $45°$ and $-45°$. Finally, the parameter V indicates the tendency of a beam to be right ($V > 0$) and left ($V < 0$) circularly

polarized and is found using both right and left handed circular polarizers.

The mathematical definitions of the Stokes parameters are shown in equations 2.22-2.25 in terms of the components of the electric fields parallel and perpendicular to the scattering plane where a '*' indicates a complex conjugate. Further discussion of the derivation can be found in many optics and light scattering texts, for example [13, 37, 38, 40, 54].

$$I = E_{||}E_{||}^{*} + E_{\perp}E_{\perp}^{*} \tag{2.22}$$

$$Q = E_{||}E_{||}^{*} - E_{\perp}E_{\perp}^{*} \tag{2.23}$$

$$U = E_{||}E_{\perp}^{*} + E_{\perp}E_{||}^{*} \tag{2.24}$$

$$V = i\left(E_{||}E_{\perp}^{*} - E_{\perp}E_{||}^{*}\right) \tag{2.25}$$

The Stokes parameters are usually given in the form of a column vector of four terms called the *Stokes Vector*, shown in equation 2.26.

$$\mathbf{I} = \begin{bmatrix} I \\ Q \\ U \\ V \end{bmatrix} \tag{2.26}$$

A Stokes vector is always defined with respect to a reference plane. In the case of light incident on a boundary between two media (as in section 2.2.2), the obvious choice for the reference plane would be the plane of incidence. A series of such interactions, such as would occur if Stokes vectors assigned to rays were traced through a crystal, would lead to a different reference plane for each interaction. To ensure that the polarization state of the light maintains the correct physical meaning, one needs to make a transformation from one reference plane to another. This process is commonly referred to as *rotating the Stokes vector*. It is achieved by applying a rotation matrix $L(\zeta)$, as given in equation 2.27, where the rotation is anti-clockwise by an angle ζ when looking in the direction of propagation.

$$\mathbf{I}' = L(\eta)\mathbf{I} = \begin{bmatrix} 1 & 0 & 0 & 0 \\ 0 & \cos 2\zeta & \sin 2\zeta & 0 \\ 0 & -\sin 2\zeta & \cos 2\zeta & 0 \\ 0 & 0 & 0 & 1 \end{bmatrix} \mathbf{I} \tag{2.27}$$

One can describe how the polarization and intensity of a beam of light is changed by a given system by using a Mueller matrix. A Mueller matrix allows the calculation of a transmitted Stokes vector from an incident Stokes vector. The ray tracing code by Macke [23] uses Stokes vectors to describe the polarization state and intensity of each ray. To illustrate the mechanics of this consider a ray striking a facet in the Macke code. A ray leaving such an interaction can be described by the final Stokes vector, $\mathbf{I}_f$. This can be related to the incident Stokes vector, $\mathbf{I}_i$, using the Mueller matrix, M (equation 2.28).

$$\mathbf{I}_f = M\mathbf{I}_i \tag{2.28}$$

The Mueller matrices that describe the change from the incident ray to the reflected and transmitted rays are given in equations 2.29 and 2.30 respectively.

$$M_r = RLM_i \tag{2.29}$$

$$M_t = TLM_i \tag{2.30}$$

The Mueller matrix for reflection is denoted by M_r and for refraction (transmission) by M_t. L is a rotation to the new plane of incidence and is equivalent to that given in equation 2.27. M_i is a Mueller matrix that transforms the initial Stokes vector to the point immediately before the interaction. For example, light undergoing refraction for the second time in a crystal has already undergone one refraction event. In the Macke code [23] and the RTDF model, M_i for the incident light is set to a unity matrix so that the initial Stokes vector remains unchanged before the first interaction. The initial Stokes parameters for a ray are given by $I = 1, Q = 0, U = 0, V = 0$. These parameters represent unpolarized light which is often referred to as *natural light* because light incident on the Earth from the Sun has this form. R and T are the Fresnel reflection and refraction matrices which derive from the Fresnel coefficients which are given

using the same notation as in section 2.2.2 where they were defined. They are shown in equations 2.31 and 2.32 respectively.

$$R = \frac{1}{2}\begin{bmatrix} r_{||}r_{||}^* + r_\perp r_\perp^* & r_{||}r_{||}^* - r_\perp r_\perp^* & 0 & 0 \\ r_{||}r_{||}^* - r_\perp r_\perp^* & r_{||}r_{||}^* + r_\perp r_\perp^* & 0 & 0 \\ 0 & 0 & 2Re(r_{||}r_\perp^*) & 2Im(r_{||}r_\perp^*) \\ 0 & 0 & -2Im(r_{||}r_\perp^*) & 2Re(r_{||}r_\perp^*) \end{bmatrix} \tag{2.31}$$

$$T = \frac{1}{2}\begin{bmatrix} t_{||}t_{||}^* + t_\perp t_\perp^* & t_{||}t_{||}^* - t_\perp t_\perp^* & 0 & 0 \\ t_{||}t_{||}^* - t_\perp t_\perp^* & t_{||}t_{||}^* + t_\perp t_\perp^* & 0 & 0 \\ 0 & 0 & 2Re(t_{||}t_\perp^*) & 2Im(t_{||}t_\perp^*) \\ 0 & 0 & -2Im(t_{||}t_\perp^*) & 2Re(t_{||}t_\perp^*) \end{bmatrix} \tag{2.32}$$

2.6.3 The Scattering Matrix

It follows from the discussion of the amplitude scattering matrix and the Stokes parameters that one should be able to describe a complete scattering event by the use of a Mueller matrix that relates the incident Stokes vector to the scattered Stokes vector. This Mueller matrix is called the *scattering matrix*, sometimes referred to as the *phase matrix*. It is shown in equation 2.33.

$$\mathbf{I}_s = \begin{bmatrix} P_{11} & P_{12} & P_{13} & P_{14} \\ P_{21} & P_{22} & P_{23} & P_{24} \\ P_{31} & P_{32} & P_{33} & P_{34} \\ P_{41} & P_{42} & P_{43} & P_{44} \end{bmatrix} \mathbf{I}_i \tag{2.33}$$

It is important to note that the scattering matrix does not include any information regarding the phase of a wave. This means that such a system cannot be used to investigate interference effects. If one were writing a ray tracing program to investigate such effects, the amplitude scattering matrix would need to be used rather than the sixteen element scattering matrix.

If the sixteen elements of the scattering matrix are functions of the polar (θ) and azimuthal (ϕ) angles then the matrix provides a complete description of

a scattering event in terms of irradiance and polarization. Although there are sixteen quantities listed, there are only seven independent variables. Given a collection of randomly oriented particles in a volume, the scattering matrix of the total system is just the sum of the individual scattering matrices attributed to the individual particles. This is because the scattering matrix deals with relating Stokes parameters which can be simply summed. This of course is under the proviso that no multiple scattering takes place within the system.

The scattering matrix can be simplified in certain cases. For example, consider a collection of randomly oriented identical particles. If the particle geometry has a plane of symmetry, then the scattering medium can be described as *macroscopically isotropic and symmetric*. In this situation, the total scattering matrix is invariant with respect to the choice of scattering plane and depends only on the polar angle, θ. The structure of the scattering matrix is then given by equation 2.34 [38, 54]. As well as eight of the matrix elements becoming zero, $P_{21} = P_{12}$ and $P_{43} = -P_{34}$. The same matrix applies if the particles do not have a plane of symmetry but there are equal numbers of the particles and their mirror particles.

$$\mathbf{I}_s = \begin{bmatrix} P_{11} & P_{12} & 0 & 0 \\ P_{12} & P_{22} & 0 & 0 \\ 0 & 0 & P_{33} & P_{34} \\ 0 & 0 & -P_{34} & P_{44} \end{bmatrix} \mathbf{I}_i \tag{2.34}$$

Individual elements of the scattering matrix can be used to calculate specific scattering properties. There are two elements of the scattering matrix that are of particular importance to this investigation, with a third that is of interest. The first and most important quantity is the matrix element P_{11}, often referred to as the *phase function*. The phase function gives the angular distribution of the scattered irradiance. In the most general case, P_{11} will be a function of θ and ϕ. It is normal practise to normalise the function over all space using the normalisation condition given in equation 2.35.

$$\frac{1}{4\pi}\int_{4\pi} P_{11}(\theta,\phi)\, d\Omega = \frac{1}{4\pi}\int_0^{2\pi}\int_0^{\pi} P_{11}(\theta,\phi)\sin\theta d\theta d\phi = 1 \tag{2.35}$$

The function normally referred to as the phase function is a function of only θ. It is obtained by averaging over the azimuthal angle ϕ. One can obtain the

normalization condition that is used as standard for $P_{11}(\theta)$ by evaluating the integral over ϕ in equation 2.35 between the stated limits of 0 and 2π. The result of this is shown in equation 2.36.

$$\frac{1}{2}\int_0^{\pi} \langle P_{11}(\theta)\rangle \sin\theta d\theta = 1 \tag{2.36}$$

For convenience, the brackets indicating the averaging over ϕ will be omitted for the remainder of the thesis. The factor $\sin\theta$ takes into account that as the polar angle θ changes, a 1° polar angle bin represents a different surface area on an enclosing sphere of unit radius in which emanating rays can be collected. This solid angle interval is smallest for the bins at 0° and 180° and largest for the 90° bin.

One can define from the phase function an important quantity known as the *asymmetry parameter*. It is usually denoted by the lower case letter g. It is defined in equation 2.37. In this case, P_{11} is again averaged over all azimuthal angles.

$$g = \frac{1}{2}\int_0^{\pi} P_{11}(\theta)\sin\theta\cos\theta d\theta \tag{2.37}$$

The important addition is the $\cos\theta$ factor. The asymmetry parameter gives a measure of the degree to which a phase function scatters in the forward or backward directions. The asymmetry parameter can take a value between -1 and 1. If more light is scattered in the forward direction, $g > 0$. If more light is scattered in the backward directions, $g < 0$. If the scattering event leads to a phase function that is symmetric about 90° or that is totally isotropic then $g = 0$.

The second matrix element which is of importance to the discussion is P_{12}. To introduce how this matrix element will be used, consider a scattered light ray whose intensity and polarization state are defined by the Stokes parameters, I, Q, U and V.

One can define a quantity called the *degree of elliptical polarization*, denoted here by p_e. It represents the proportion of the scattered light that is polarized and is given in equation 2.38. It is equal to unity for fully polarized light.

$$p_e = \frac{\sqrt{Q^2 + U^2 + V^2}}{I} \leq 1 \tag{2.38}$$

The quantity can be split up into the *degree of circular polarization* and the *degree of linear polarization*, equations 2.39 and 2.40 respectively.

$$p_c = \frac{V}{I} \tag{2.39}$$

$$p_l = \frac{\sqrt{Q^2 + U^2}}{I} \tag{2.40}$$

When $U = 0$, the degree of linear polarization is often represented by the ratio given in equation 2.41.

$$p_l = -\frac{Q}{I} \tag{2.41}$$

For the case of incident natural light (Stokes vector $\mathbf{I}_i = [I_i, 0, 0, 0]$), the scattered Stokes parameters I_s, Q_s, U_s and V_s are given by equations 2.42-2.45, obtained by solving equation 2.33 for each.

$$I_s = P_{11} I_i \tag{2.42}$$
$$Q_s = P_{21} I_i \tag{2.43}$$
$$U_s = P_{31} I_i \tag{2.44}$$
$$V_s = P_{41} I_i \tag{2.45}$$

In the case of a macroscopically isotropic and symmetric medium as described above, the scattering matrix simplifies to equation 2.34. Consequently, $P_{31} = 0$ and so $U_s = 0$. The definition of p_l given in equation 2.41 can then be used. The scattering matrix simplification also leads to $P_{12} = P_{21}$. By using this fact and substituting equations 2.42 and 2.43 into equation 2.41, one obtains a definition for the *Degree of Linear Polarization* (DLP) in terms of scattering matrix elements that will be used throughout this thesis. It is given in equation

2.46.

$$p_l = -\frac{P_{12}}{P_{11}} \tag{2.46}$$

It is a very important quantity that gives the proportion of the scattered light that is horizontally ($p_l < 0$) or vertically ($p_l > 0$) polarized with respect to a horizontal scattering plane. The use of the negative sign is a widely adopted convention. DLP results will be used many times in the coming chapters. The assumptions used in the derivation of equation 2.46 are reasonable for all of the cases to be considered in this thesis.

The final matrix element that is of interest is P_{22}. The quantity P_{22}/P_{11} is unity at all scattering angles for spheres and as a result can be used as a test for sphericity. Using the matrix element P_{22} it is possible to define a quantity called the *linear depolarization ratio*. The term depolarization refers to a change in linear polarization. When conducting depolarization experiments, the incident light is completely linearly polarized, $p_l = \pm 1$. For nonspherical particles, the absolute value of p_l for the scattered light will decrease because the polarization state changes. This reduction in the absolute value of p_l could explain the origin of the term. The definition of the linear back scattering depolarization ratio, δ, is given in equation 2.47. It is a measure of the change in linear polarization at back scattering.

$$\delta = \frac{P_{11} - P_{22}}{P_{11} + P_{22}} \tag{2.47}$$

The linear back scattering depolarization ratio is practically applied in the LIDAR back scatter depolarization technique. It is a remote sensing technique allowing particle identification in the field. Initially it was thought that such a technique would enable differentiation between ice particles which would show a strong depolarization ratio and water droplets that would show zero depolarization ratio. This was found to be true and the technique was later extended when it was found that it could also provide information on the shapes and sizes of crystals in cirrus, especially when combined with other techniques such as RADAR. Although depolarization ratios will not be presented in this thesis, such results from the RTDF model have been compared to AIDA cloud chamber experiments in a concurrent collaboration [55]. The definition of depolarization used in the reference differs from that given above because it is measured at

176° in the experiment rather than at direct back scattering. Further discussion of depolarization ratios is available in the literature, for example [56] and [38, chapter 14].

2.7 The Study of Cirrus

Cirrus clouds are high altitude ice clouds that regularly cover up to 30% of the surface of the Earth [1]. Cirrus can be found all over the globe, though their frequency in different locations can be seasonal due to their existence being dependent on current weather conditions. Cirrus clouds are most frequently found in the Intertropical Convergence Zone, followed by midlatitude areas from 30° to 50° latitude. The definition of cirrus is the remit of the *World Meteorological Organisation* (WMO) which classifies clouds according to their morphological and visual daytime appearance. The system of classification varies little from that introduced by Luke Howard (1772-1864) in 1803, who was the first person to use the term cirrus. The three main types of meteorological cirrus are named cirrus, cirrostratus and cirrocumulus. They are defined by the WMO [57] as follows [58, chapter 1].

> *Cirrus*: Detached clouds in the form of white, delicate filaments or white or mostly white patches or narrow bands. These clouds have a fibrous (hair-like) appearance, or a silky sheen, or both.

> *Cirrostratus*: Transparent, whitish cloud veil of fibrous (hair-like) or smooth appearance, totally or partly covering the sky, and generally producing halo phenomena.

> *Cirrocumulus*: Thin, white patch, sheet or layer of cloud without shading, composed of very small elements in the form of grains, ripples, etc., merged or separate, and more or less regularly arranged; most of the elements have an apparent width of less than one degree.

These three types are further subdivided, details of which can be found in the above references. Cirrocumulus are responsible for some of the most photogenic examples of cirrus, although they are not very common [59].

There are two other forms of cirrus that are not currently included in the classification scheme. The first form, *subvisual cirrus*, is not fundamentally any different from normal cirrus apart from that examples are colder, thinner and made up of smaller ($< 50\mu$m) particles [58, Chapter 12]. The definition of subvisual cirrus is cirrus with an optical depth of less than 0.03 (see chapter 8 for more on the concept of optical depth). The second additional form, *contrail cirrus*, is formed by high altitude aircraft exhausts which shall be discussed in a moment. It would be possible to form several classification schemes for cirrus. Many important variables are not included in the standard classification scheme such as the cloud ice content, temperature, optical depth and altitude. Some of these factors became more important with the advent of satellite and multi-wavelength observation.

As mentioned in the introduction, cirrus are of vital importance to the Earth's radiation balance. Being usually found at high altitude in the upper troposphere and lower stratosphere (above about 8km), where temperatures are in general below $-30°$C, cirrus both trap outgoing radiation to create a greenhouse effect while also reflecting incoming radiation to create an albedo effect. The balance of these two effects, something that is wavelength dependent, determines how the cloud contributes to the climate. What makes cirrus such a vital research topic is the fact that the balance between the two effects is very sensitive to the properties of an individual cloud [60]. Cirrus becomes a complex issue due to the wide variety of crystal shapes and sizes that can be found in different clouds.

Cirrus clouds form due to the elevation of warm air to higher altitudes where it cools. As the warm air is elevated, the temperature falls well below 0°C and the moisture held within the warm air supercools. Ice does not form as easily as one might expect, only becoming common once cloud temperatures are around $-20°$C [61]. Ice nucleation, the commencement of ice formation, can be caused by a variety of processes. A more complete discussion can be found in the literature [61], with particular reference to cirrus available in the chapter by Demott [58, chapter 5]. A simple view of the nucleation process divides it into two main types, homogeneous and heterogeneous nucleation. Homogeneous nucleation is the spontaneous freezing of supercooled water or solution droplets below around $-40°$C. Heterogeneous nucleation can occur at warmer temperatures when solid aerosol particles such as soot and mineral dust in the atmosphere act as *Cloud Condensation Nuclei* and induce freezing.

Once ice nucleation has occurred, crystal growth proceeds readily because when supercooled water droplets and ice are both present, solidification of the water droplets occurs due to their metastable state. The mechanism by which this occurs, known as *deposition*, sees the water droplets diffusing to the ice crystals. The shape of cirrus ice crystals is based upon the hexagonal crystal system of ice. This leads to geometries such as hexagonal columns, plates and related geometries such as bullets and rosettes. There is some evidence that ice formed from its cubic crystal system can also form in the Earth's atmosphere [62], but it is very rarely observed. A cubic ice embryo could explain the tendency of ice rosette arms to grow with certain separation angles [63]. This will be discussed further in section 5.6.

The elevation of warm air in the atmosphere that causes the formation of cirrus can occur for several reasons. It can occur due to advancing weather fronts forcing warm air above cold air or due to air movements encountering hill and mountain ranges. Cirrus are the highest altitude clouds, so in the case of an advancing warm weather front they will be the first clouds observed caused by the front, normally around twelve hours in advance of any precipitation resulting from the front. The elevation can also take place due to convection, and this is the cause of much of the tropical cirrus that occurs. Cumulonimbus storm clouds move warm moist air to high altitudes through convection, resulting in a cirrus 'anvil' above the storm cloud. Tropical cirrus are particularly important to the Earth-atmosphere radiation balance because they can cover large areas of the Earth's surface and extend vertically for large distances [64]. This is in contrast to the thin patchy cirrus common to mid-latitudes.

An area of growing importance in the study of cirrus is that of condensation trails or *contrails*. Contrails are seen as visible clouds formed from the back of high altitude aircraft (although in some locations such as Alaska and Siberia they can be observed at ground level at airports when the temperature is very low). The exhaust trails from aircraft contain warm water vapour that freezes very quickly at high altitude. Contrails can persist for many hours and grow into a spreading cirrus cloud if the humidity in the surrounding atmosphere is high enough. More information on the formation of contrails can be found in the chapter by Schumann [58, chapter 11]. An example of a contrail was studied using aircraft based instruments as a part of the SUCCESS field campaign [65]. Contrails cover a very small fraction of the Earth at any one time compared to their natural cirrus cousins but there is evidence that the presence of contrails can have an immediate effect on the surface temperature of the Earth [66]. Aircraft exhausts can also have an indirect impact because they contain solid

particles such as soot that can act as cloud condensation nuclei, encouraging additional cirrus formation [67]. The impact of contrails on regional climate [68] and the effect of contrails in the context of general cirrus trends [69] have been investigated. The study of contrails is very much an area of ongoing research.

The first weather satellites were launched in the sixties and since then cirrus observations from above have been possible. Such observations introduced many challenges, one being that cirrus are defined by their visual appearance from the ground. The benefits however are great because cirrus can now be studied over large geographical areas at increasingly high resolutions. Remote sensing using satellites detects radiation scattered upwards from clouds. Observation of scattering at different wavelengths is advantageous. The widespread use of infrared channels to obtain for example cloud temperature is very useful in identifying cirrus, but also cloud altitude. Minnis [58, chapter 7] explains how it soon became clear that simultaneous observations over several spectral bands enabled greater discernment between cloud types and better retrieval of cloud properties.

The majority of ground based observations take the form of short wavelength RADAR, LIDAR and radiometers. Radiometers are used to identify the total amount of radiation received, most specifically in the infrared. In many ways this allows measurements similar to those taken from satellites but from the ground looking up. Short wavelength RADAR is used to identify and position clouds. LIDAR is similar to RADAR in its basic concept but it uses light rather than radio waves (LIght Detection And Ranging). It is useful in meteorological applications because of the large variations in scattering properties between hydrometeors. It is particularly suited to the study of cirrus due to the high dependence of the back scattering depolarization properties on the size, shape and orientation of ice crystals.

Numerous field campaigns have been launched to better understand the properties of cirrus. The first studies of cirrus were motivated by the advent of contrails from aircraft during the second world war and Weickmann used hand held slides coated in varnish to obtain impressions of ice crystals for later optical microscopy [70]. More recently, campaigns have been mounted that combine various types of simultaneous study including aircraft sampling and observation, balloon-borne sampling and observation, RADAR, LIDAR and satellite observation. These campaigns have given rise to many papers, for example FIRE I and II [71, 72, 73], SUCCESS [65], EUCREX [74] and CRYSTAL-FACE [75].

Aircraft based in-situ measurements have been obtained in many ways since Weickmann's initial particle sampling. Particle imaging is the major focus as particle collection for later study creates many practical problems. The *Cloud Particle Imager* (CPI) [76] uses a 1-million pixel CCD camera to obtain shadow images of cirrus particles and will be discussed further in chapter 6. Nephelometers have been used to measure scattering properties of crystals at the same time as imaging them. A probe developed at the University of Hertfordshire, the *Small Ice Detector* (SID), classifies ice crystals according to scattering properties [12]. The second generation of the probe is already in use in the field with the third currently in development (see section 7.4). One of the greatest challenges remains that small ice particles found in cirrus cannot in most cases be adequately detected with many of these systems. Impactor probes help to gain an idea of the size distributions of crystals by collecting them in oils or on coated slides and then imaging them. These techniques are the direct descendants of Weickmann's hand held slides. Balloon-borne sampling and observation provides the distinct advantage of vertical ascension through a cloud instead of along flight paths as in the case of aircraft.

Using all of the techniques described above, the scientific community has an emerging picture of the ice crystals that are found in cirrus. The variation of geometries observed in different clouds can be very large. Examples of crystal shapes sampled during the ICE field campaign can be seen in figure 1 of [34]. These are similar to those found from balloon-borne replicators during the FIRE II field campaign [77]. Both references show the spectrum of hexagonal columns, plates, bullets, rosettes and aggregates observed through a vertical slice of a cloud. They also highlight the small crystals near cloud top that resemble spheres due to the lack of resolution available and the hollow features on some crystals, which will be discussed later in section 5.3.

As shown in the references above [34, 77], the crystal geometries found at different altitudes within the same cloud are seen to vary greatly. One simple model of a cirrus cloud can be built up if an individual cloud is broken into layers. At the top of the cloud is a nucleation layer. This is where the ice crystals begin to form. This layer will include small particles that cannot accurately be classified at this time. They are likely to be small faceted objects such as droxtals (see section 5.5). Below this is a growth layer where the crystals grow to their maximum size in the cloud. Here and below crystals such as hexagonal columns, hexagonal plates, bullets and rosettes are found. Finally there is a sublimation layer at the bottom of the cloud where the crystals have fallen into drier air so begin to sublimate with some exhibiting rounded facet edges. By

this stage, likely crystals to be found are complex rosettes and aggregates. Using this model, a cloud in its early stages is unlikely to have a sublimation layer while a cloud having reached the end of its generating process will not have a nucleation layer. It is important to appreciate that this is only one simplified model of a cirrus cloud and that other scenarios such as deep convection in the tropics will have completely different vertical profiles of crystal size and shape. The scattering properties of some of the types of crystal geometries that are found in cirrus with references directing the reader to information regarding their formation will be discussed in chapter 5.

Just as the crystal geometry shows large variation, so does the crystal size. Accurate knowledge of crystal size is very important for understanding the properties of cirrus. Crystal sizes can range from below 50 μm where they are difficult to observe up to the millimetre scale. One of the first comprehensive studies of crystal dimensions in clouds was performed by Auer and Veal [78]. Since then, in-situ instruments have enabled more automated studies to take place. Heymsfield and Platt [79] found that the size spectra of cirrus crystals depend strongly on temperature. There have been many studies since looking at methods for inferring size distributions, for example [73]. In general however, smaller crystals are found near the cloud top leading to a gradual increase in size as one moves down through the cloud until reaching the complex aggregates and rosettes found in the lower layers of the cloud. The role of size and shape has been compared by Macke et al. [80], who found that average scattering properties (such as the asymmetry parameter) are more sensitive to crystal shape than to particle size distribution, particularly at visible wavelengths. They also found that the cloud optical depth depends on the crystal concentration rather than the crystal size. They did however note that their study used size distributions consisting of only one geometry and that there is likely to be some correlation between size and geometry, as one might expect from the simple cirrus layer model discussed above. This could lead to very different scattering properties.

Numerous authors have performed crystal growth experiments in the laboratory to provide further insight into the complex ice growth mechanisms and to attempt to create representative cirrus ice collections. Bailey and Hallett [81] investigated how ice crystal habits change with temperature between -20°C and -70°C. They found that as well as the temperature, the initial nucleation process had an impact on the resulting crystal habits. Ice nucleation experiments have been performed in the AIDA aerosol chamber [82] at Forschungszentrum, Karlsruhe. During some of the experiments, crystals were monitored using in-situ particle instruments that are usually aircraft-mounted [83]. Barkey et al.

[84] have measured size and shape distributions of plates and columns grown in a cloud chamber developed at the Desert Research Institute in Nevada. They have also obtained angular scattering properties of the crystals within the cloud chamber.

Laboratory experiments investigating the single scattering properties of ice crystals are very challenging because temperature and humidity need to be controlled, although results have been successfully reported [85]. An alternative in the form of ice analogues has been developed at the University of Hertfordshire. Single scattering properties have been obtained from such crystals which can be studied in much greater detail as they are stable at room temperature [9]. The use of an electrodynamic balance in this process allows non-contact single particle studies in certain fixed and random particle orientations. The use of the analogues allows the connection between individual crystals and their scattering properties to be studied in more depth. The ice analogues will be discussed further in chapter 6.

The role of aircraft in-situ probes in the identification and classification of cirrus particles has already been mentioned. Equally important are aircraft based radiance measurements, for example [86, 87, 88]. Such measurements allow further investigation of the composition of cirrus and provide an opportunity to validate cloud composition and light scattering models. Comparisons have been made between aircraft radiance measurements and a range of ideal crystal geometry phase functions using the GO approach [89]. However, such geometries were found not to be immediately representative. One can describe the scattering properties of cirrus reasonably well through an *Analytic Phase Function* (APF) that has been tested against aircraft and satellite data [90]. The analytic phase function is formed so that it is generally smooth and featureless, characteristics representative of cirrus in general. However, it would be advantageous to gain a better comparison to aircraft measurements using a light scattering model coupled with crystal geometries. The RTDF model has been used in conjunction with a radiative transfer code to compare with aircraft measurements to investigate the possibility of finding representative geometries for several cirrus cases, with particular interest paid to the University of Hertfordshire ice analogue crystals [91]. The contents of this reference, expanded on somewhat, can be found in chapter 8.

To conclude this brief overview of the study of cirrus, the phenomena for which the clouds are most famous will be considered. Cirrus are responsible through their ice crystal content for optical atmospheric phenomena known as *halos*.

These phenomena have been observed for centuries with Descartes (1596-1650) first suggesting an explanation in 1637 when he correctly identified that the 22 ° halo was caused by refraction through ice. Interestingly, he also described what would later be referred to as Snell's law (see section 2.2.2) and performed numerical ray tracing to investigate the formation of a rainbow.

The term halo is applied to any arcs or bright regions formed in the sky by light after it has interacted with ice crystals. The most common halo effects are the 22° halo, a large circle around the sun caused by randomly oriented hexagonal ice columns and the Parhelia (also known as Sundogs) which are bright spots either side of the sun near the 22° halo, formed from hexagonal ice plates with their cylinder axis aligned perpendicular to the horizon. The 46° halo, another circle seen around but much further from the sun is observed less often. It is also caused by randomly oriented hexagonal columns but differs from the 22° halo because it is caused by light refracting through one rectangular (prism) facet and one hexagonal (basal) facet, unlike the 22° case where two prism facets are involved.

When studying the azimuthally averaged scattering properties of perfect geometries calculated using GO, sharp peaks are frequently observed that represent halo features. In this thesis, several halo features will be encountered and shall be explained individually as they are encountered. For example, the 22° and 46° halos will be discussed more fully in chapter 4.

It is an interesting fact that halo effects are more common in Europe than rainbows [92], yet few people are able to bear witness to such an event. Possibly this is due to the fact that they can be more subtle than the dramatic rainbow, but it is likely that the main reason is that people are not aware of what they should be looking for.

Many authors have written about halo phenomena, for example Greenler [93]. Other examples include the numerous applications of GO to the subject that were referenced earlier in this chapter. Some have considered rare arcs such as the Parry arc [94] and those with unusual radii and positions [95, 96, 97]. In the polar regions, ice crystals form at lower altitudes and in high numbers and so it is there that the most dramatic and complex displays have been observed [92]. Under such conditions, it is possible to take radiance and polarization measurements of the phenomena while simultaneously sampling the crystals that are involved [98, 99]. Such polar studies have fuelled much of the present understanding of halos. It is however important to note that such low altitude

clouds of ice crystals are not classified as members of the cirrus family. Cirrus halos have been quantitatively studied, the observation of four 22° halos during the 1986 FIRE field campaign provided simultaneous ground based LIDAR and aircraft measurements [100]. Wonderful photographs of halos amongst many other atmospheric phenomena are available from various authors, for example [101]. An excellent website describing many atmospheric effects exists that offers descriptions of halos in some detail [102]. It offers a publicly available Monte Carlo ray tracing code that can predict halo displays, based upon the earlier work by Trankle and colleagues, for example [103]. Laboratory halos have been recreated using ice analogue crystals [104].

Given the extremely common nature of cirrus, it is perhaps surprising that more halo effects are not observed. Most of the halo effects that can be formed by cirrus are rarely, if ever, seen. Many rare halos such as the 46° halo are not often seen simply because the intensity generated by even a large number of crystals is too low. The halo is so large that the intensity is dispersed over too large an area. In other cases, the circumstances that lead to the halos, such as crystal geometry or orientation, are themselves rare.

Crystal size is very important to the successful creation of all halos. This was discussed by Mishchenko and Macke [105]. The authors used the T-matrix method to investigate how the halo peak of a circular cylinder developed as the crystal size increased to large size parameters, something that cannot be achieved with the more complex geometry of a hexagonal column. They estimated that well defined halos should be visible for ice crystal size parameters of the order of 100 and above. Rare halos that rely upon specific orientations are only likely to occur when larger crystals are present in low turbulence conditions because, as well as the Mishchenko and Macke [105] finding, such conditions are required for the specific orientations to occur (this will be discussed further in section 5.1). However, there is a problem if crystals are too big because larger crystals are most prone to exhibiting hollow features and facet deformation, both of which are regularly observed, for example [106, 107]. Both these factors can weaken and ultimately prevent halo effects forming. To replicate the halos predicted by ray tracing studies, crystals would need to be pristine. Konnen et al. [98] noted that Antarctic halos were not as sharp as predicted by pristine crystals. They suggested that the crystals responsible might have had basal facets that were not perpendicular to the long axis of the column and prism facets that did not have precise 60° separations. This was confirmed by observation. However, following further investigations they proposed an alternative theory citing Fraunhofer diffraction as the dominant cause of the halo smooth-

ing [99]. They maintain however that facet separation angles can cause a lesser amount of additional smoothing.

To summarise, for a halo to form, there need to be large numbers of crystals of the correct geometry and size present and, if applicable, in the correct orientations. It is essential that a significant number of the crystals are in a sufficiently pristine condition to avoid the effect being smoothed out by hollow features, rough surfaces and facet deformation. The halos that are more rare are naturally weaker in intensity either because they are spread out over large areas or because the conditions that lead to their formation are themselves rare. This means that conditions have to be perfect for rare halos to be observed.

Chapter 3

The Diffraction on Facets Model

3.1 What is Diffraction on Facets?

Diffraction on Facets (RTDF) is a computational light scattering model for dielectric faceted objects based upon the standard GO model. In addition to the usual Fresnelian interactions treated in GO, as rays meet crystal facets they are deflected to take into account diffraction caused by the facet acting as an aperture. The main aims of the model are to extend the applicability of GO towards lower size parameters while providing improved results for all size parameters usually associated with the GO model. Due to the nature of the RTDF model it can be stated that it tends to GO at very large size parameters. The crystal sizes to which the model can be applied will be discussed in more detail in section 3.5.

The current implementation of the model uses the Geometric Optics code by Macke [23] as a starting point. The code by Macke has a full treatment of polarization built in by associating a complete Stokes vector to each ray travelling through the crystal. This functionality has been preserved in implementing the new model making it possible to review several elements of the scattering matrix. In this study, our attention is restricted to the phase function (P_{11}) and the degree of linear polarization ($-P_{12}/P_{11}$).

In the following, the development and implementation of the model will be discussed. In developing the model in section 3.2, the question to be answered is "By what amount and in what direction should GO rays be deflected to best model diffraction?" The development is separated into three stages. Stages 1 and 2 essentially cover the work carried out by Hesse and Ulanowski [7] which resulted in a 2D model which was later tested against SVM for long hexagonal columns [8]. Stage 3 describes how the model was extended to three dimensions. In section 3.3 some key points concerning the implementation of the 3D model will be raised.

3.2 Developing the Model

3.2.1 Stage 1: Half-Plane Diffraction

The problem of half-plane diffraction can be solved using rigorous diffraction theory (see section 2.4.3). The upper panel of figure 3.1 shows the paths of average energy flow lines as they pass a semi-infinite half-plane. In the far field, the lines are deflected towards the half-plane. The deflection increases as the energy flow lines pass closer to the half-plane. Interestingly, the path of the lines as they pass the half-plane is quite complex with a small oscillation visible, most noticeable with lines passing at a greater distance from the half-plane. This can be seen in the lower panel of the same figure which gives a magnified view. Also shown in the lower panel is an initial movement away from the half-plane. After the flow lines have travelled some distance past the half-plane, they move back towards the half-plane and most importantly at large distances they gain a close to linear trajectory. This far field linear behaviour allows us to estimate the direction of the far field Poynting vector and hence a far field deflection angle for the energy flow lines can be calculated.

Figure 3.2 shows the far field deflection angles calculated using rigorous diffraction theory against the distance from the half-plane at which the energy flow line passes. If the GO rays can be used to represent the average energy flow lines, these deflection angles can be seen as the GO ray deflection angles that are required. It was found that equation 3.1 gives a reasonable fit to the rigorous theory deflection angles, where λ is the wavelength of the incident light, ϕ is the far field deflection angle and x is the distance of the energy flow line from the edge of the half-plane as it passes. Equation 3.1 is also plotted in figure 3.2

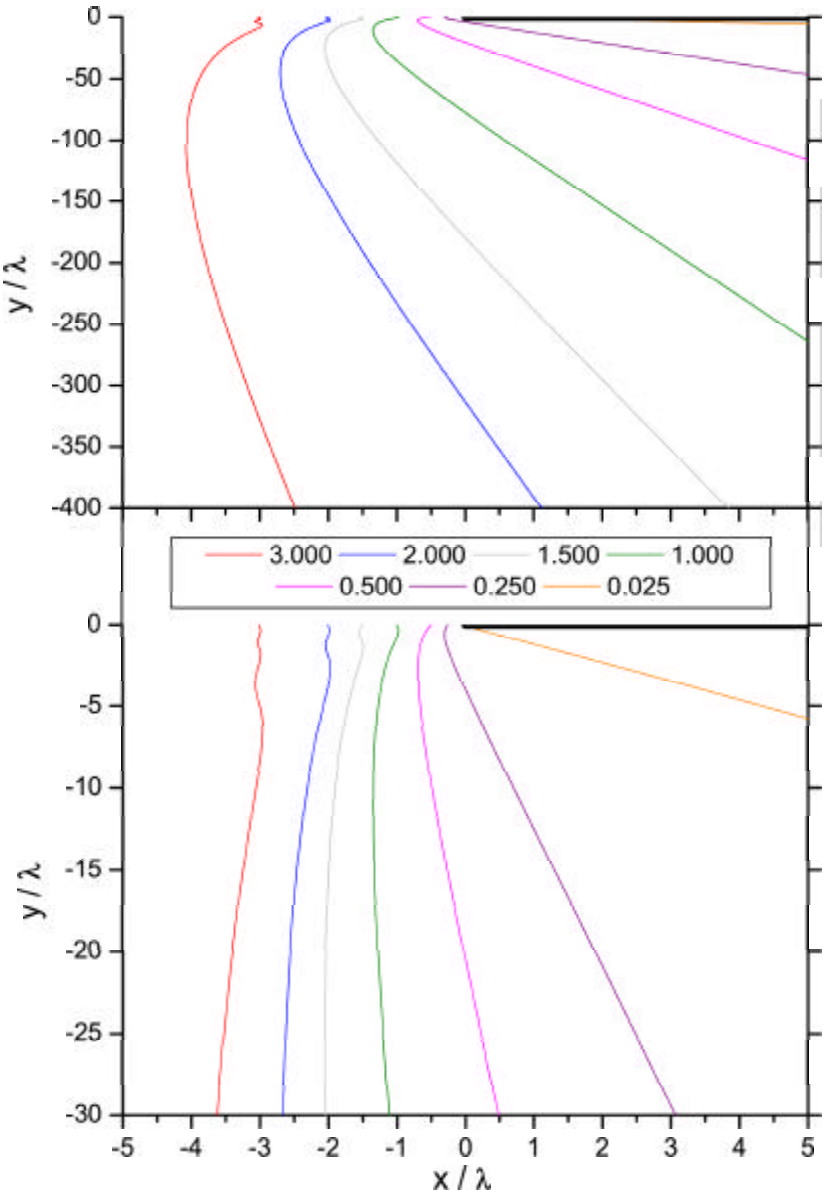

Figure 3.1: Energy flow lines incident perpendicular to a half-plane. The half-plane is shown as a thick black line with flow lines initially travelling in the negative y direction. The legend gives the distances in wavelengths from the half-plane edge for each traced flow line as they pass $y = 0$. Top: Overview. Bottom: Enlarged view of the near field behaviour of the energy flow lines.

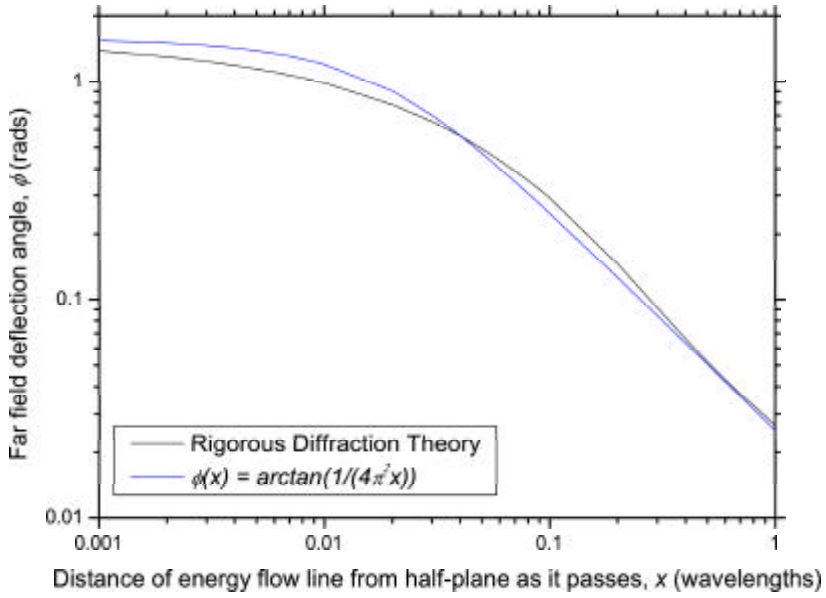

Figure 3.2: Far field deflection angles of energy flow lines passing the half-plane at a range of distances, x (measured in wavelengths).

for comparison.

$$\phi(x) = \arctan \frac{\lambda}{4\pi^2 x} \tag{3.1}$$

Further discussion of equation 3.1 is given in [7] where it is shown that an angular energy density in the far field calculated from equation 3.1 is identical to that derived by using asymptotic variants of the rigorous diffraction theory.

3.2.2 Stage 2: Slit Diffraction

To develop the treatment of a half-plane into a useful model it is necessary to consider a more complex situation, such as a slit. This problem cannot be solved in a closed form using exact theory but only in a series expansion with the solutions for each term rapidly becoming complicated [37, Section 11.8.3]. The computation for such a solution would be prohibitively expensive and in any case the closed form solution for the half-plane is more desirable. To extend

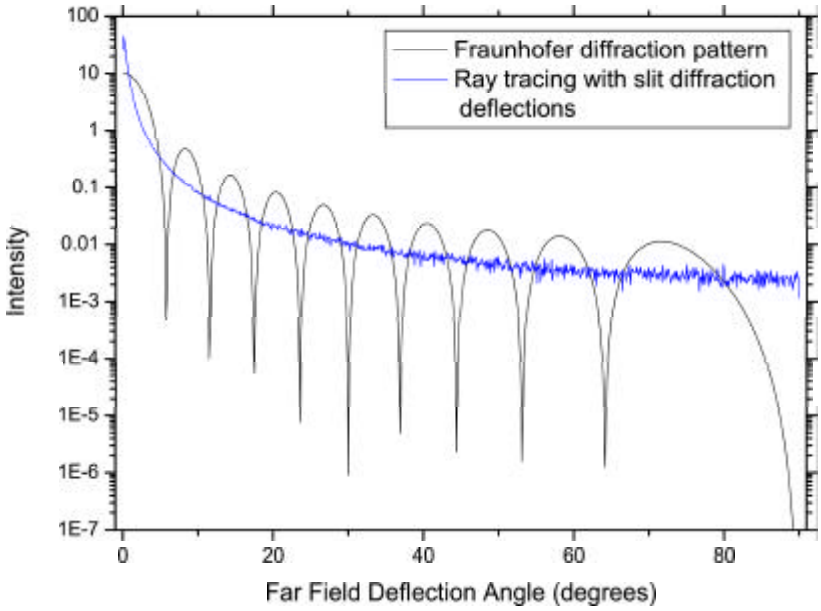

Figure 3.3: The angular intensity distribution of rays incident upon a slit deflected using equation 3.2 compared to the Fraunhofer diffraction pattern.

the half-plane result to a slit, the added complexity of the problem is due to the fact that there are essentially two interacting half-planes between which the rays pass. The rays incident on the centre of the slit need to pass undeflected.

Conveniently, it is possible to adapt equation 3.1 to give an acceptable result for diffraction at a slit. Equation 3.2 considers a slit of width $2a$. It gives a deflection angle of zero for the centre of the slit (when $x = a$) and reduces to equation 3.1 near the edges of the slit (when $x \to 0$ and $x \to 2a$). The expression is very versatile because it can be applied to slits of any size.

$$\phi(x) = \arctan\left(\frac{\lambda}{4\pi^2}\left(\frac{1}{x} - \frac{1}{2a - x}\right)\right) \tag{3.2}$$

In reference [7], it is shown that the far field angular intensity distribution calculated directly from equation 3.2 compares well with the Fraunhofer diffraction pattern. A similar result is shown in figure 3.3. A Monte Carlo ray tracing procedure was modified using equation 3.2 to deflect rays incident upon a slit. The

resulting intensity distribution, which is equivalent to the analytic calculation in [7], is shown in the figure compared to the Fraunhofer diffraction pattern.

It is important to note in the figure that the model does not predict the maxima and minima created by interference effects that are the signature of the Fraunhofer pattern. The model currently has no treatment of interference although some work towards a 2D test model has been completed [108]. Despite the lack of interference effects, the model shows broad agreement with the Fraunhofer pattern. Near a deflection angle of zero, the Fraunhofer pattern takes the shape of a smooth curving maximum. In contrast, the model rises to a sharp peak. This discrepancy is thought to be mainly due to the lack of interference effects in the model.

The application of the concept to a slit was implemented in a 2D code by Hesse and Ulanowski [7]. The GO code by Macke [23] was modified so that each ray reflected from or refracted through a facet was deflected towards the closest facet edge by the appropriate deflection angle. Because the 2D version only allowed scattering calculations for long columns with the column axis perpendicular to the incident light, all rays are confined to a plane by GO and so the only diffraction treatment required was a slit.

The equation for the deflection angles on a slit also includes a factor of $\cos\theta_i$ to account for rays incident at oblique angles, where θ_i is the angle between the incoming ray and the facet (slit) normal. The diffraction affecting oblique rays is actually the diffraction at the projection of the slit into the plane perpendicular to the direction of the incident ray. This modification is shown in equation 3.3. In the same equation the concept of the *effective wavelength* has been introduced. The wavelength that must be considered is actually the wavelength of the medium through which the outgoing ray travels. For example, a ray entering a crystal will need to use a wavelength value equal to the wavelength of the ray in the crystal medium, namely $\lambda_{eff} = \frac{\lambda}{n_r}$ where n_r is the real part of the refractive index of the crystal. Equation 3.3 is the final equation used in the 2D model. The 2D version was later tested against SVM [8].

$$\phi(x) = \arctan\left(\frac{\lambda_{eff}}{4\pi^2\cos\theta_i}\left(\frac{1}{x} - \frac{1}{2a-x}\right)\right) \tag{3.3}$$

As mentioned above, at large size parameters the model tends to the standard GO result. Diffraction on Facets only has a large effect on rays that strike close

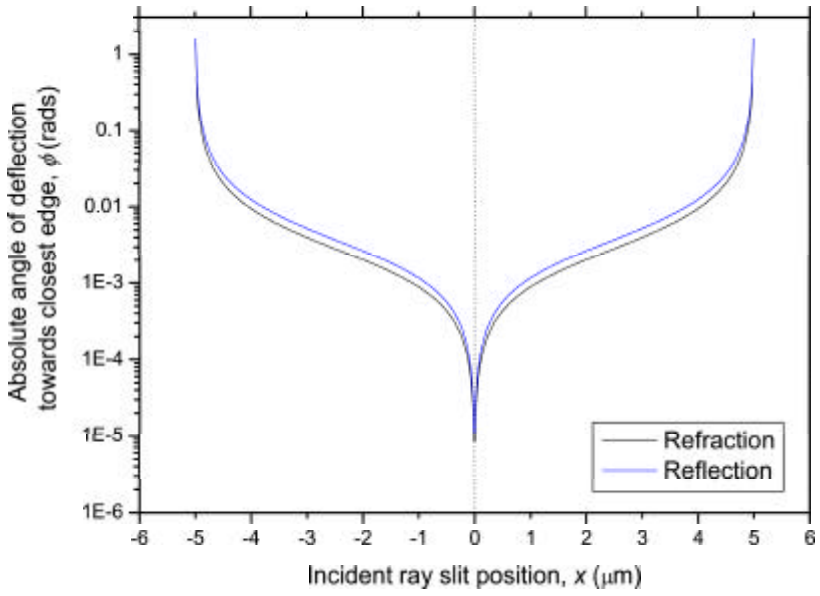

Figure 3.4: Deflection angles for rays incident on a slit of width 10 μm when enforcing RTDF rules at a wavelength of $\lambda = 0.55$ μm. Rays refract from air ($n_r = 1.0$) into ice ($n_r = 1.311$) and approach the slit at normal incidence.

to the edge of the facet (slit). As a result, at larger size parameters the proportion of rays being affected significantly by the model reduces and so the results move to the Geometric Optics result. Figure 3.4 shows the deflection angles for rays incident on a slit enforcing RTDF rules where the slit acts as a boundary between air and ice and the rays approach the slit at normal incidence. It shows the proximity of a ray to the slit edge required to deflect a ray significantly. The effect of the model for increasing sizes will be considered in section 3.5.

3.2.3 Stage 3: Facet Diffraction

The final stage to be considered is diffraction at a facet of arbitrary shape and orientation with respect to the incident ray. A rigorous theory solution to this problem of the form used in stage 1 is not possible. As a result, an approximation must be formulated that applies the rules that have already been discussed to this more complex case. The result for a slit from stage 2 can be used if it is assumed that any facet shape can be represented by two *effective*

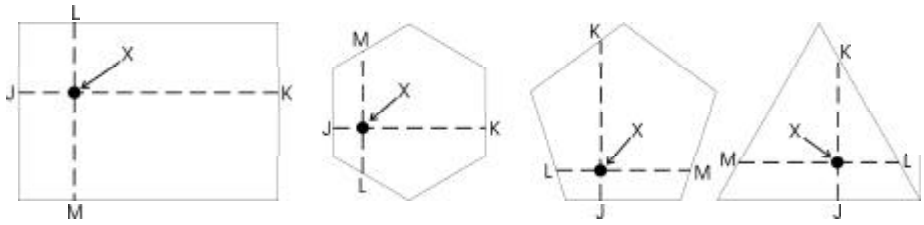

Figure 3.5: The use of effective slits to allow arbitrarily shaped facets to be considered. The point of intersection between the ray and facet is labelled X. The line segments $\overline{JK}$ and $\overline{LM}$ define the corresponding effective slits.

slits. These two slits can then be used as diffracting slits. Some examples are shown in figure 3.5 where the point X is the intersection point between ray and facet, the line segment $\overline{JK}$ is the first effective slit and $\overline{LM}$ is the second. The points J, K, L and M can all be found on facet edges. Consider a ray incident upon and then being reflected from one of the facets shown in the figure. The standard GO reflection procedure is performed before the outgoing (reflected) ray is deflected to take into account the diffraction caused by the facet. Two separate slit deflections are performed using the formula presented in the previous section, stage 2. The first slit deflection is towards the closest point, J, on the closest facet edge by forming an effective slit $\overline{JK}$. The second slit deflection is perpendicular to the first, in the direction of the closest facet edge along the line segment $\overline{LM}$. The mechanism used to locate the points J, K, L and M will be discussed in section 3.3.1. Note that by calculating the deflection angle for the ray in this way, an approximate solution is found for the three dimensional diffraction problem.

Reflected and refracted rays are first deflected towards J and then towards L. It is necessary for the deflection angle formulae to change here slightly from the two dimensional case for oblique incidence. The angle of incidence with respect to the facet normal is not sufficient to account for oblique incidence. The $cos(\theta)$ factor needs to be treated separately for the two slits so that the slit is correctly projected into the plane perpendicular to the incoming light. Equation 3.4 is the final deflection angle with this correction in place where $\vec{k_i}$ and $\vec{m}$ are unity vectors pointing in the direction of the incident propagation vector and along the effective slit being considered respectively. An arbitrarily shaped facet can be treated by the model using this technique, allowing crystals of complex shape to be considered.

$$\phi(x) = \arctan\left(\frac{\lambda_{eff}}{4\pi^2 \sin\left(\arccos\left(\vec{m} \cdot \vec{k_i}\right)\right)}\left(\frac{1}{x} - \frac{1}{2a - x}\right)\right) \tag{3.4}$$

3.3 Implementation of the Model

3.3.1 Defining the Effective Slits

The point J is always the point on any of the facet edges that is closest to X. The line segment from J to X is perpendicular to the facet edge upon which J lies. The point K is on the opposite facet edge to J falling on the extension of the line segment $\overline{JX}$. The points L and M lie on the line perpendicular to the line segment $\overline{JX}$ that passes though X. In the following, the convention that L is closer to X than M is adhered to. Consequently, the deflection using this effective slit will be towards L. J, K, L and M must all fall on facet edges.

The algorithm that is used to locate the points that define the effective slits will now be outlined. The points are located one at a time in the order J, K, L and then M. The algorithm uses the same mathematical procedure for each of the four points. The mathematics is based upon the the equation of a line and the intersection of two lines.

Consider a line segment in space denoted by $\overline{AB}$ that is defined by two points, A and B. The positions of the two points are defined by their position vectors with respect to the origin, $\overrightarrow{OA}$ and $\overrightarrow{OB}$ respectively. One can define a vector that joins the two points as $\vec{u} = \overrightarrow{OB} - \overrightarrow{OA}$. A third point, P, lies somewhere on the line of infinite length $\overleftrightarrow{AB}$ also defined by the points A and B. The location of P can be written in terms of $\vec{u}$. This is shown in equation 3.5 where $\overrightarrow{OP}$ is the position vector of P with respect to the origin and s is a scalar value. If $0 < s < 1$ then P lies on the line segment between A and B.

$$\overrightarrow{OP} = \overrightarrow{OA} + s\vec{u} \tag{3.5}$$

Now consider that the point P is not an arbitrary point on the line defined by A and B but the unknown intersection point with a second line. The second line is defined by a point C and the point P. The point C is defined by a position

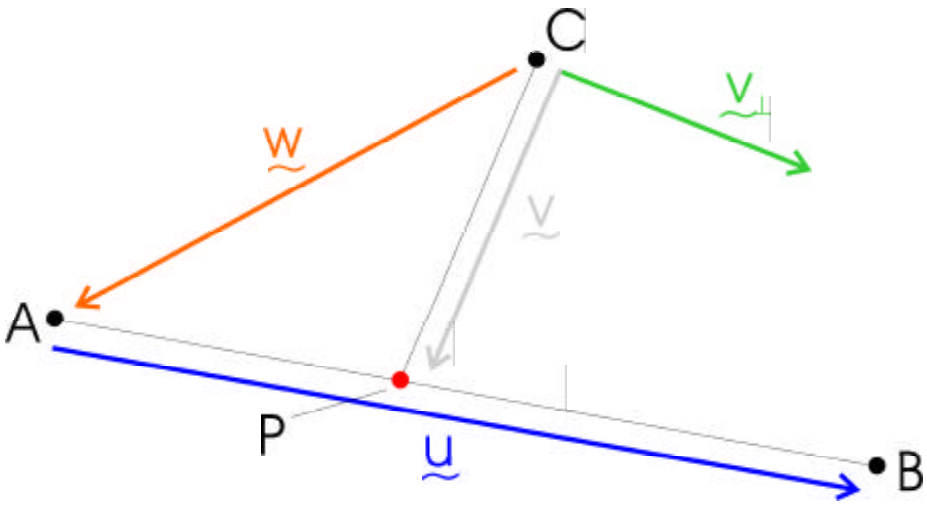

Figure 3.6: A diagram of the line intersection problem discussed in the text.

vector $\overrightarrow{OC}$ with respect to the origin. One can define a vector that joins C and P as $\vec{v} = \overrightarrow{OP} - \overrightarrow{OC}$. A vector can also be defined that joins C and A as $\vec{w} = \overrightarrow{OA} - \overrightarrow{OC}$. This situation is illustrated in figure 3.6.

If the vectors $\vec{u}$, $\vec{v}$ and $\vec{w}$ are known then the scalar value s and hence the exact location of P on $\overleftrightarrow{AB}$ can be determined as follows. The scalar product of two vectors that are perpendicular to each other is equal to zero. For example, the scalar product of the vector $\vec{v}$ and some vector $\vec{v}_\perp$ that is perpendicular to it is equal to zero, equation 3.6.

$$\vec{v}_\perp \cdot \vec{v} = 0 \tag{3.6}$$

By inspecting figure 3.6 one can write the vector $\vec{v}$ in terms of $\vec{u}$ and $\vec{w}$ as $\vec{v} = \vec{w} + s\vec{u}$. Substituting this into equation 3.6 gives equation 3.7.

$$\vec{v}_\perp \cdot (\vec{w} + s\vec{u}) = 0 \tag{3.7}$$

Solving equation 3.7 for the scalar quantity s gives equation 3.8.

$$s = -\frac{\vec{v}_\perp \cdot \vec{w}}{\vec{v}_\perp \cdot \vec{u}} \tag{3.8}$$

Equation 3.8 means that if the location of an intersection point P is sought then a solution can be found given the vectors $\vec{u}$, $\vec{v}_\perp$ and $\vec{w}$. The vector $\vec{v}_\perp$ can be any vector that is perpendicular to $\vec{v}$ so that the perpendicular condition given in equation 3.6 is fulfilled.

The current implementation of the RTDF model uses equation 3.8 to identify the four points J, K, L and M on a facet by defining $\vec{u}$, $\vec{v}_\perp$ and $\vec{w}$ according to the specific case at hand within the constraints of the derivation above. Given the support for facets of arbitrary shape, it is necessary to not only calculate the exact location of the four points but first the facet edges on which they lie. This does not interfere with the solution currently being discussed because the test for whether a point lies on a facet edge is given by the condition $0 < s < 1$, provided that the vector $\vec{u}$ defines the facet edge that is being tested. This fixes the first vector. Note that an intersection point with the line $\overleftrightarrow{AB}$ of which the facet edge is a segment will always be found because all of the points considered are coplanar. The case of parallel lines provides an exception, but this case is detected and dealt with in the implementation.

Figure 3.7 illustrates the definitions of the three vectors for identifying the four points on a hexagonal facet, although the rules hold for a facet of arbitrary shape. The black circles represent points whose locations are known. These include the ray-facet intersection point, X, the points that define the facet edges and points that have already been calculated. The red circle highlights the point that is sought. There follows a brief description of each case.

Point J Figure 3.7a. The two intersecting lines are the edge being tested (defined by $\vec{u}$) and the line segment $\overline{XJ}$ which is defined by the vector $\vec{v}$. By definition, J is the point on a facet edge closest to X. This means that $\overline{XJ}$ is perpendicular to the facet edge on which J lies. Hence $\vec{u} = \vec{v}_\perp$. The final vector $\vec{w}$ is shown in the figure. In this case, multiple facets are expected to offer candidate points for J although the point is fixed by finding the candidate point offering the smallest distance from X to J. This is the only step in locating the four points that can have any such ambiguity (except when considering adjacent coplanar facets, see section 3.3.2).

Point K Figure 3.7b. The point K is the intersection of the line $\overleftrightarrow{JX}$ with a facet edge. The edge being tested is defined by $\vec{u}$. Extending the line segment $\overline{JX}$ gives the segment $\overline{JK}$ which is defined by the vector $\vec{v}$. Due

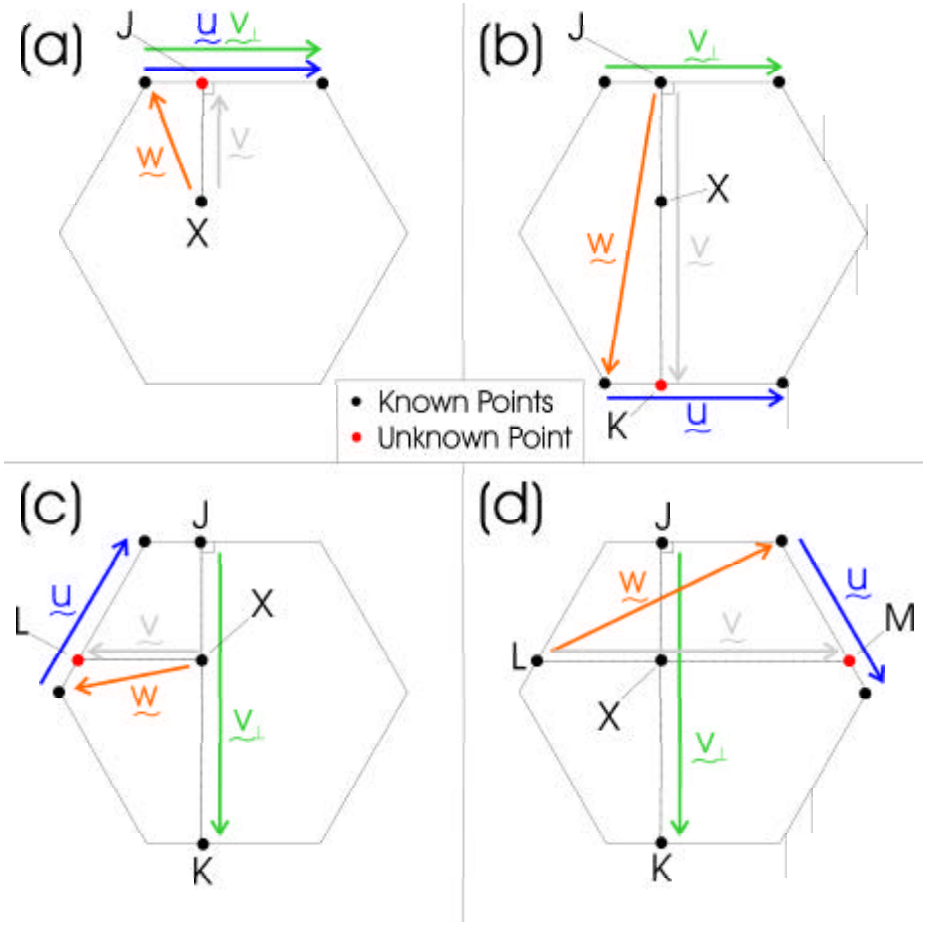

Figure 3.7: A diagram showing the use of the solution to a line intersection problem in defining the effective slits in the RTDF model. A hexagon is shown but an arbitrary facet shape can be used.

to the fact that $\overline{JK}$ is perpendicular to the facet edge on which J lies, one can use the facet edge as $\vec{v}_\perp$. The final vector $\vec{w}$ is shown in the figure.

Point L Figure 3.7c. The two intersecting lines are the edge being tested ($\vec{u}$) and the line segment $\overline{XL}$ defined by the vector $\vec{v}$. This case is similar to that for point J except that $\overline{XL}$ is not necessarily perpendicular to the facet edge. As a result, the perpendicular condition is fulfilled by the first effective slit $\overline{JK}$ which is represented by the vector $\vec{v}_\perp$ and by definition is perpendicular to $\overline{XL}$. The final vector $\vec{w}$ is shown in the figure.

Point M Figure 3.7d. The two intersecting lines are the edge being tested ($\vec{u}$)

and the line segment $\overline{LM}$ defined by the vector $\vec{v}$. This case is similar to that for point K except that, as in figure 3.7, the perpendicular condition is fulfilled by the effective slit that has already been defined by the line segment $\overline{JK}$, represented by $\vec{v}_{\perp}$. The final vector $\vec{w}$ is shown in the figure.

Two methods are currently employed to implement the mathematics to locate the four points J, K, L and M. The first searches through all of the facet edges for each point in turn, testing to see if the desired point is to be found on the edge using the condition $0 < s < 1$. This method allows any regular or irregular polygon to be considered. However, because each point only exists on one facet edge it is not a very efficient process. If regular shapes such as rectangular and hexagonal facets are being considered, a rapid technique uses symmetry relations to determine the facet edges on which K, L and M are found once the point J has been determined.

3.3.2 Adjacent Coplanar Facets and Concave Facets

If the RTDF model is to be applied to arbitrary crystal geometries, there are several situations that may arise that need to be considered.

Using the Geometric Optics code by Macke [23] it is not possible to consider a concave facet such as the irregular facet shown in figure 3.8a. This is due to the manner in which the code determines whether a ray strikes inside or outside the boundary edge of a facet. To consider such complex facets it is necessary to split them into convex facets that are adjacent and coplanar, illustrated in figure 3.8a using the dotted lines. A practical example can be found in Macke [23] where a hexagonal tube is considered. A ray striking the end of the tube cannot be adequately handled unless the hexagonal ring is separated into six quadrilaterals. This is shown in figure 3.8b. Breaking the ring up like this is perfectly acceptable for the case of GO but when considering RTDF an alternative must be sought. Using edges between the coplanar quadrilaterals will create deflections of the sort not originally intended by the RTDF concept. Another example of such unintended deflections is found when considering the 4-1 bullet rosette that will be discussed in section 5.6. One side of the geometry exhibits four coplanar adjacent pentagons formed because four individual bullets are used to construct the crystal. This is illustrated in figure 3.8c.

An alternative system was created to handle such cases. At the beginning of an

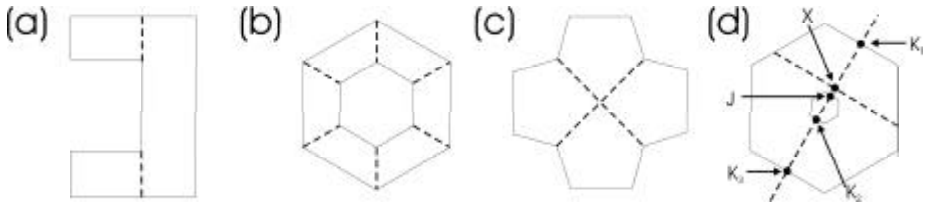

Figure 3.8: Examples of adjacent coplanar facets.

execution run, facets are tested against each other to detect adjacent coplanar facets. These facets are recorded in such a way that the edges between them can be neglected when determining the effective slits used by the RTDF model. This enhancement was implemented using replacement subroutines so it must be turned on using an option variable. This method of implementation was chosen because the algorithm used is likely to increase execution times somewhat and so should only be used when necessary. The system has been used in section 5.6 for the case of the 4-1 bullet rosette. It is also applied in section 5.4 where hexagonal tubes of the form used by Macke are investigated. Using the system, the end facets formed using a hexagonal ring split into six quadrilaterals is treated as a standard hexagonal ring in terms of the RTDF model yet the GO constraint on concave facets is not an issue.

As a result of concave facet support it is necessary to consider that candidate points for K, L and M (see sections 3.2.3 and 3.3.1) may be found on several facet edges whereas for convex facets there is no such ambiguity. For example, figure 3.8d shows the end of a hexagonal tube that has been struck by an incident ray at the point X. The dashed lines indicate the effective slit directions associated with RTDF. The closest point on a facet edge, J, is clearly defined. The location of the point K according to the algorithms that locate the point (outlined in section 3.3.1) is ambiguous. There are three candidates, K_1, K_2 and K_3. This is rectified by adding the condition that the hitting point X is always between J and K (and also between L and M). The correct candidate point is the closest to J within this constraint.

3.3.3 Polarization in the 3D Model

In section 2.6.2, the concept of the Stokes vector was introduced and the process of rotating the Stokes vector in GO briefly explained (page 52). The Stokes vector of a plane wave is always defined with respect to a reference plane in-

cluding the propagation vector. In a GO interaction, it is defined with respect to the plane of incidence which contains the incident ray and the normal of the plane struck by the ray. For the Stokes vector to maintain its physical meaning during several consecutive interactions it must be expressed with respect to each plane of incidence in turn. Consequently, the reference frame is rotated at each ray-facet interaction and the transformation from the old Stokes vector to the new Stokes vector is given by equation 2.27 from section 2.6.2. In the GO code, the components of the electric field vector parallel and perpendicular to the plane of incidence are used to define the Stokes vector. As a result it can be assumed that the perpendicular component of the electric field vector ($E_\perp$) of both incoming and outgoing rays lie within the plane of the facet during a reflection or refraction event. This leads to a standard rotation of the Stokes vector. However, this is not necessarily the case for an RTDF event because although $E_\perp$ lies in the plane of the facet during the reflection or refraction process, the deflection that RTDF introduces to the propagation vector can pull $E_\perp$ out of the facet plane if the orthogonality of the propagation vector and the components of the electric field vector are to be maintained.

A correction was applied within the RTDF model to rectify this. The correction applied was based upon a scheme outlined by Hovenier and van der Mee [109]. Initially, the GO process is allowed to occur as usual including the calculation of the GO perpendicular component of the electric field vector, $E_\perp^{GO}$, and the rotation of the Stokes vector. The RTDF deflection of the outgoing propagation vector is then performed including the calculation of the RTDF perpendicular component of the electric field vector, $E_\perp^{RTDF}$. It is now necessary to rotate the GO Stokes vector to become the RTDF Stokes vector. To help with this, one can define a reference vector, $\boldsymbol{h}$, as the vector product of the outgoing GO and the outgoing RTDF propagation vectors. Two rotations of the Stokes vector are then performed. The first rotates from $E_\perp^{GO}$ to $\boldsymbol{h}$ about the propagation vector of the outgoing GO ray. The second rotation is from $\boldsymbol{h}$ to $E_\perp^{RTDF}$ about the outgoing RTDF propagation vector.

3.4 Demonstrations of the Effect of Diffraction on Facets

In the following discussions, a wavelength of $\lambda = 0.55$ μm will be used for the incident light. Throughout this thesis when this wavelength is used, the

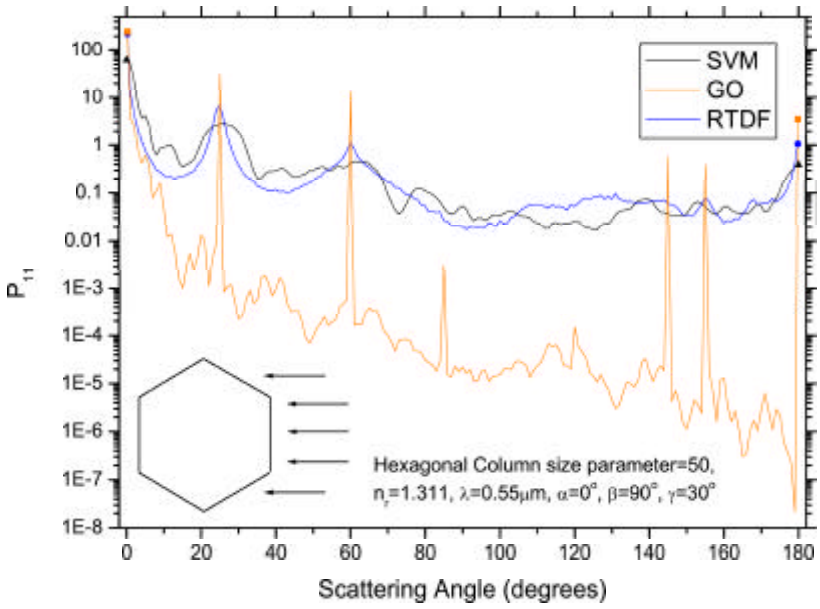

Figure 3.9: A demonstration of the RTDF model for a hexagonal column of size parameter 50 at a wavelength of $\lambda = 0.55$ μm at perpendicular incidence. SVM and GO results are plotted for comparison.

refractive index of the crystal will be taken to be $n_r = 1.311$ and $n_i = 3.11\text{x}10^{-9}$ [110].

An excellent demonstration of the effect that the RTDF model has is for hexagonal columns in a fixed orientation at perpendicular incidence. Figure 3.9 shows RTDF, GO and SVM results for an infinitely long hexagonal column of size parameter 50 at a wavelength of $\lambda = 0.55$ μm. All results presented in this document under the name GO were generated using the classical Geometric Optics code by Macke [23]. The orientation of the crystal is such that incoming rays travel perpendicular to the plane of one of the long facets, as shown in the figure. The RTDF and GO results were calculated using 500,000 incident rays. The SVM result is an average of results from a range of carefully selected size parameters to smooth out interference effects. The current version of the RTDF model does not include interference effects and so such action ensures a fair comparison.

The idea behind the method to smooth out interference is as follows. When considering light scattering by small particles, it is the effects caused by inter-

ference between light passing by the crystal without interaction and light passing through the crystal that dominates. In terms of GO, it is possible to calculate the phase difference between a ray that passes directly through a crystal and one that misses the crystal completely. Equation 3.9 gives the phase difference δ_p between rays passing by and through a crystal where the characteristic diameter of the crystal d is also the path length inside the crystal.

$$\delta_p = \frac{2\pi d}{\lambda_{eff}} - \frac{2\pi d}{\lambda} \tag{3.9}$$

Using the definition of the effective wavelength (section 3.2.2), this can be written in terms of a size parameter η and the real part of the refractive index, n_r, as shown in equation 3.10.

$$\delta_p = 2\eta\,(n_r - 1) \tag{3.10}$$

If the size parameter is varied around the desired value carefully, it is possible to create a spread of phase differences to cover a range of 2π (or one wavelength). By setting δ_p to 2π in equation 3.10, η gives the magnitude of size parameter variation required. This method will suppress the interference effects in the forward direction and act as an approximation that will lead to a similar effect at larger scattering angles where interference effects arise mostly due to rays taking different paths as they pass through the crystal. Given a hexagonal column at perpendicular incidence there are clear problems with this method. For example, the distance that a ray travels through the crystal depends upon where it enters the crystal. However, as an approximate method for smoothing interference effects it is most adequate.

The figure shows that the characteristic sharp spikes from Geometric Optics are widened in the RTDF results and compare very well with SVM. These results were generated using the 3D model codes but are very similar to those calculated using the original 2D version found in [8] where more details regarding such orientations can be found.

A second demonstration is provided in figure 3.10. In this case, a hexagonal column of finite length is considered. The aspect ratio of the column is defined using the quantity $L/2r$ which is further explained in appendix A.1. The figure

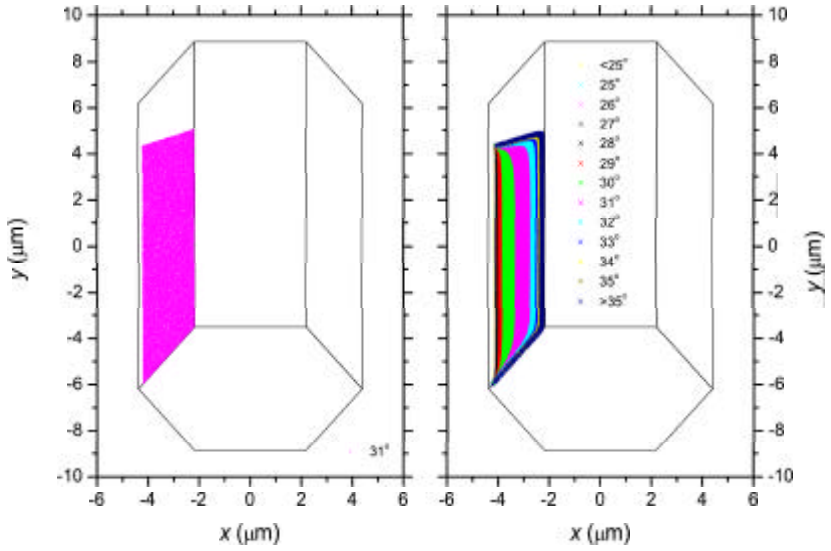

Figure 3.10: A demonstration of the RTDF model for a hexagonal column of size parameter 50 at a wavelength of $\lambda = 0.55$ μm tilted from perpendicular incidence by an angle of 45°. The crosses represent the locations of incident rays entering the crystal and the colours indicate the final scattering angle, given in the legend. Only the ray path discussed in the text is considered. Left Panel: GO. Right Panel: RTDF.

shows a hexagonal column tilted from incidence perpendicular to the column axis by an angle of 45°. The size parameter of the crystal is 50 with $L/2r = 2$. The figure shows the scattering angles resulting from rays entering the left prism facet that is exposed to the incident light and exiting the central prism facet on the underside of the column. This is achieved by placing a cross at the point that the incident ray enters the crystal whose colour corresponds to the eventual scattering angle. In the panel on the left hand side, the GO result is given. All of the rays following the ray path are scattered at an angle of 31°, as illustrated by the solid magenta area on the facet. Note that areas of the facet without any colour are where the rays leave the crystal through other facets. The panel on the right hand side provides the equivalent RTDF result. The large range of colours and hence scattering angles illustrates how the model spreads the rays incident upon a facet when compared to GO. Note that the scattering angle is a combination of the Snellian refractions and the RTDF deflections on both facets that are involved in the ray path.

3.5 Size Applicability Study

3.5.1 Upper Limit

As the new model is applied to increasing size parameters, the result tends asymptotically to the GO result. To explain this, consider a 2D Monte Carlo ray tracing system with rays incident on a slit. For a slit obeying GO rules, all the rays will pass through undeflected. For a slit obeying the rules of the new model, rays passing through the slit will be deflected as described in section 3.2.2. One can quantify the deviation of the model from GO by calculating a value κ. κ is the percentage of the slit that, when struck by a ray, will result in a deflection angle greater than some small angle ψ. In the following, we shall set $\psi = 1°$.

For very narrow slits, κ will be close to 100%. As the width of the slit increases, κ will drop rapidly because as shown in figure 3.4, only rays striking close to the slit edge are deflected significantly. As the slit increases in size to very large widths, the behaviour of the model will move towards that of two independent half-planes. This means that κ will approach 0% asymptotically for finite widths because there will always be an ever decreasing area of the slit that will deflect rays by more than 1°. This is shown in figure 3.11 where κ is plotted against the width of the slit. For comparison, the equivalent result for Fraunhofer diffraction at a slit is given where κ represents the percentage of the energy found at an angle greater than 1°. Both logarithmic and linear scales are included in the figure. Fraunhofer diffraction is included because as the width of the slit tends to infinity, Fraunhofer diffraction tends to a single point maximum at a deflection of 0° where $\kappa = 0$. This is an identical result to GO. One can state therefore that Fraunhofer diffraction tends to GO at large slit widths. Comparing the model to the Fraunhofer result illustrates how the model moves towards the GO result. In the figure, κ for both the model and the Fraunhofer case drops rapidly as the slit width increases to 500 μm. Above a slit width of around 750 μm, the RTDF case begins to approach the Fraunhofer case. This figure clearly shows how the RTDF model will have a small effect on a ray tracing calculation up to very large size parameters. Assuming that the slit width is the same as the characteristic radius of a particle, the figure shows calculations for size parameters up to near 43,000 at a wavelength of $\lambda = 0.55$ μm. The value of κ falls below 1% at a slit width of approximately 158 μm which corresponds to a size parameter of approximately 1,800 at $\lambda = 0.55$ μm. Crystal size in cirrus is

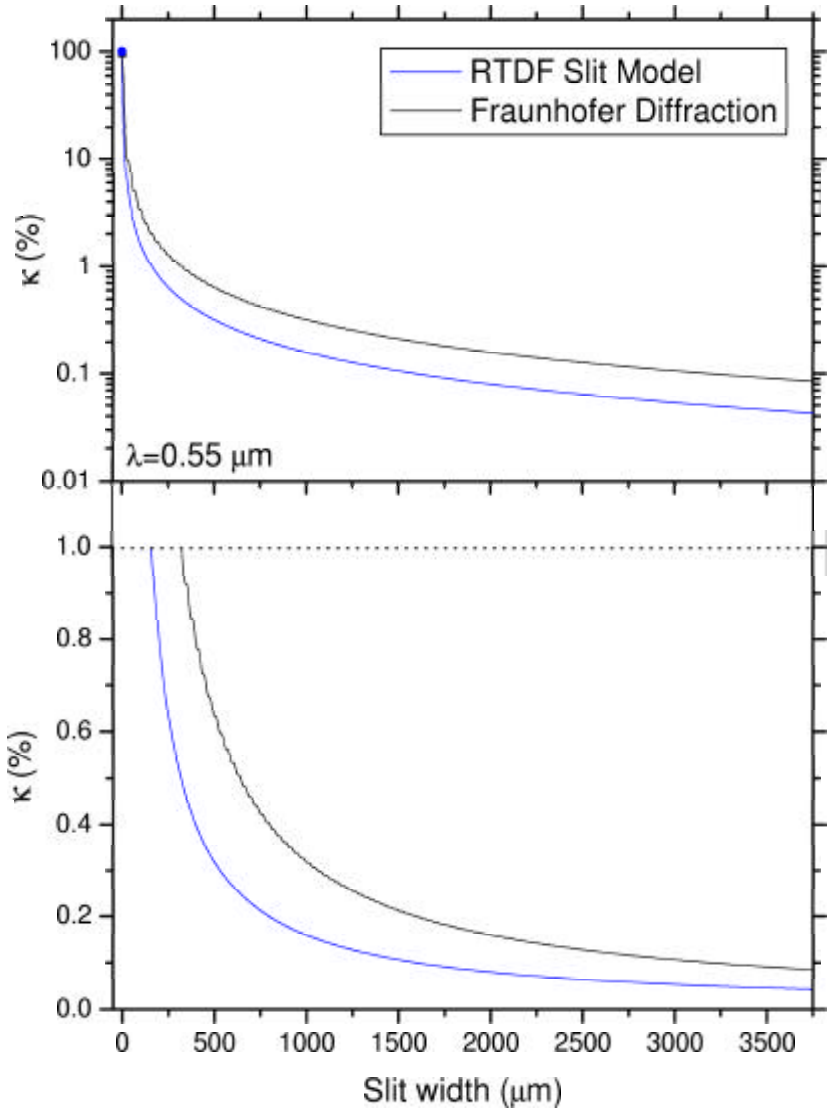

Figure 3.11: κ against increasing slit width for the RTDF slit model and Fraunhofer diffraction.

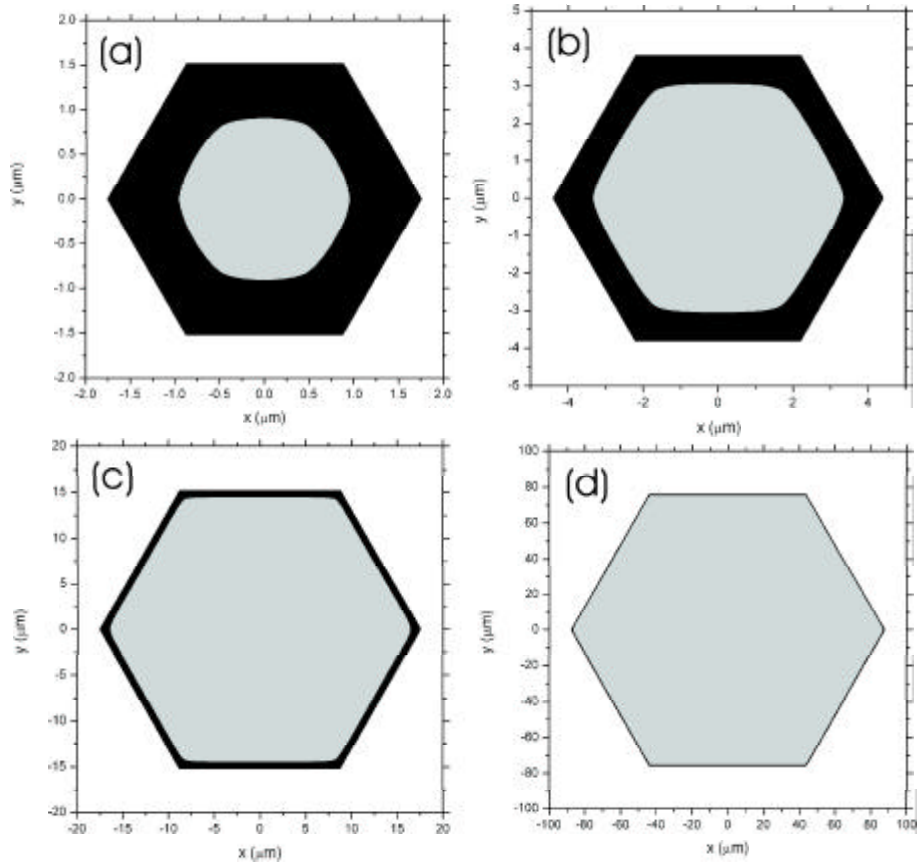

Figure 3.12: Illustration of the proportion of a facet that leads to RTDF behaviour (deflections of more than 1°, black shading) and approximate GO behaviour (deflections of less than 1°, grey shading). (a) Size parameter 20, RTDF 65.56% (b) Size parameter 50, RTDF 35.68% (c) Size parameter 200, RTDF 10.21% (d) Size parameter 1000, RTDF 2.14%.

often quoted in terms of a maximum dimension. The characteristic radius which determines the size parameter is usually less than the maximum dimension. For example, a rosette with a large maximum dimension is made up of constituent arms that have radii that are significantly smaller than the whole crystal. This means that the model will have an impact that can be considered significant for the majority of crystals found in cirrus [79].

Figure 3.12 shows how this result translates to rays reflecting from a hexagonal facet. Note that in this case two RTDF deflections will occur as described in section 3.2.3. In the following, the deflection angle considered will be the total deviation from the incident direction. The figure shows four hexagonal facets with radii of (a) 1.751 μm, (b) 4.377 μm, (c) 17.507 μm and (d) 87.535 μm

which would correspond to size parameters of 20, 50, 200 and 1000 respectively at a wavelength of $\lambda = 0.55$ μm. If a ray strikes the areas coloured black, it will be deflected by an angle greater than 1°. Those areas shaded grey will lead to behaviour more similar to GO. The percentage of each facet that leads to deflections greater than 1° varies in a similar fashion to the case of the slit, values for the figure were found to be (a) 65.56% (b) 35.68% (c) 10.21% (d) 2.14%. As the size of the facet increases, the area where rays are deviated significantly falls. The value for case (d) is in agreement with the slit discussion above.

The use of a Monte Carlo ray tracing method means that the result that is achieved using the model can depend upon the number of rays used due to statistical effects. In the case of averaging over random orientations, the number of orientations is important. In using the model, the general rule followed is that in the case of a fixed orientation, the number of rays is sufficient if the scattering property being studied has stabilised. In other words, adding more rays will not change the result. In the case of averaged orientations, the same rule is applied but to the number of orientations. As we move to higher slit widths (and also higher crystal sizes for the 3D model) achieving this stability in the result becomes harder. To give a complete model result for a very wide slit, it will require the same number of rays per unit of width as for a narrow slit. One reaches a point where this is computationally unreasonable, so placing an upper size limit on the use of the model that depends upon the computational resources of each individual user. In the theoretical case of a computer of unlimited power, the RTDF model will only ever asymptotically approach GO because if there are sufficient rays incident on a very large facet, some will always strike close to the facet edge where the half-plane behaviour persists.

When the result is averaged over many random orientations the effect of the model is not always as obvious. Figure 3.13 shows the RTDF phase functions for four hexagonal columns with no external diffraction compared to the equivalent GO result. The RTDF columns all have $L/2r = 1$ with size parameters of 50, 100, 150 and 200 at a wavelength of $\lambda = 0.55$ μm. The GO result is size independent due to the lack of external diffraction but was calculated using the size parameter 200 crystal. The movement of RTDF towards the GO result can be seen as the crystal size increases, particularly in the halo regions and near forward scattering. Although the signature sharp halo peaks of GO are already established in the size parameter 200 RTDF result, the phase function still exhibits noticeable differences, particularly near forward scattering and above 140°. This confirms the preceding discussion. However, due to the similarity

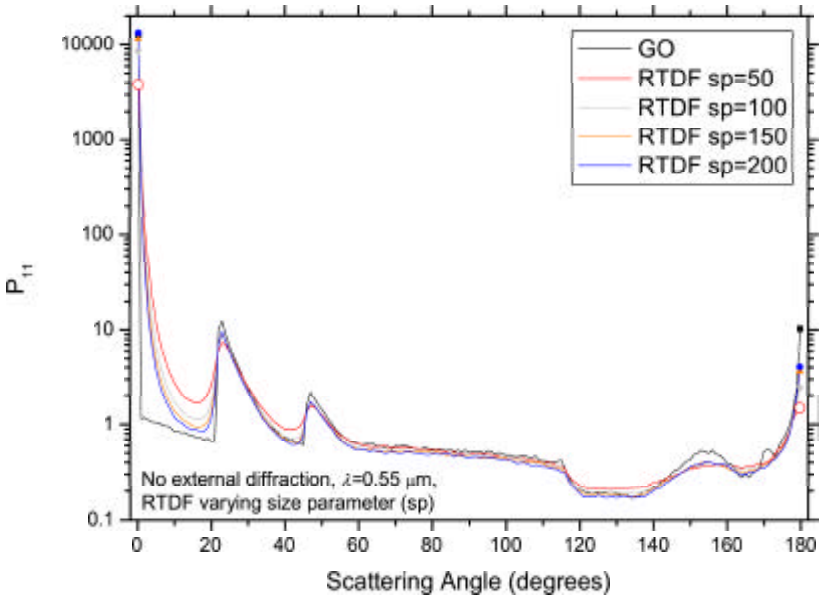

Figure 3.13: The RTDF phase functions for four hexagonal columns with size parameters of 50, 100, 150 and 200 at a wavelength of $\lambda = 0.55$ μm averaged over 50,000 orientations with 100 rays per orientation. Shown for comparison is the equivalent GO result. The results are pure ray tracing results so do not include any external diffraction.

with the GO result at the largest size parameter it is clear that the RTDF model has the most impact below size parameters of around 100. The results to be presented in the coming chapters will be confined to size parameters below this value, except in the case of the aggregate result in section 5.7 where the crystal size is defined in the literature.

To summarise, in theory there is no upper applicability limit for the RTDF model. At very large size parameters, the behaviour of the model will approach that of GO. Up to a size parameter of approximately 1,800 (below which one can classify the majority of cirrus ice particles) the RTDF model makes a clear impact because it deflects at least 1% of rays by at least 1° at each facet interaction. The percentage value grows strongly as the size decreases. Up to size parameters of 43,000 and above, the effect of the model modifying a standard ray tracing result can still be detected, albeit by a very small amount. The GO result will only ever be approached asymptotically because of the half-plane behaviour near the facet edges. In practise, an upper applicability limit

for the RTDF model is enforced at large size parameters by the computational constraints of individual users and the number of orientations and rays per orientation that are required to obtain a stable result for a given crystal geometry. The model has the most impact at size parameters below 100.

3.5.2 Lower Limit

It is much harder to determine a lower limit for the size applicability of the RTDF model. There are two lower limits to consider. The first is the limit below which there is no physical justification for using such a model. The second is the limit below which the quality of results is known to be poor. It has been found that the RTDF code runs without errors for inappropriately small crystals. Consequently, code stability is not an issue.

The ray tracing approximation holds when the distance between ray-facet interactions and the dimensions of the facets are very much greater than the wavelength of the incoming light. Let us consider light of wavelength λ incident upon a hexagonal column with $L/2r = 1$, taking many random orientations. If the phrase "very much greater than" can be translated as a crystal radius of 10λ then GO can be applied above size parameters of approximately 60, but even this is pushing the applicability boundaries. As discussed in section 2.1, GO was found to provide the most accurate results at size parameters of several hundreds when considering spheres [24]. At such sizes, "very much greater than" has significantly more validity. However, due to the lack of alternative methods GO is frequently used at size parameters as low as 50 for cirrus ice particles. In addressing the first lower limit discussed above, one expects that the introduction of a physical optics correction within the crystal by using the RTDF model removes some of the restrictions associated with standard GO. It allows the model to be used at size parameters much smaller than the standard GO regime. In this way, the use of RTDF at size parameters down to at least 50 can be justified, and in part down to sizes closer to the boundary with numerical and exact methods. It is certain that somewhere between that boundary and the GO regime the lack of interference effects and the ray tracing nature of the model will create a lower limit below which use of the RTDF model cannot be justified. Unfortunately, this limit is near impossible to quantify reliably. As a result, the applicability of the model can only really be assessed by finding the second limit described above.

The limit below which the RTDF results are known to be poor is unfortunately also very difficult to quantify. Exact and numerical methods are not available to cover the size parameter range from 50 downwards to assess the degradation of the reliability of the RTDF results. The only method that covers such a range is IGO [6], discussed in section 2.5. To recap, IGO is a hybrid method that uses Geometric Optics to evaluate the scattering on the surface of the particle before making a transformation to the far field using exact theory. The exact theory component makes IGO computationally demanding compared to models such as GO and RTDF. IGO has been applied to crystals much smaller than those in the usual applicability range of GO. IGO phase functions have been found to compare reasonably well to FDTD down to size parameters of around twenty [6].

Figure 3.14 provides the IGO [111] and RTDF phase functions for hexagonal columns of size parameters 30 and 12 at a wavelength of $\lambda = 0.55$ μm. The reader may like to refer to figure 4.6 on page 107 which provides an equivalent comparison for a size parameter of 60. In figure 4.6, the comparison to IGO is good with the shape of the RTDF profile matching in all areas except the forward scattering, back scattering and halo regions. The apparent intensity shift is a normalisation effect and will be discussed in the text that accompanies the figure, section 4.4.1. As will be discussed later, the lack of agreement at forward and back scattering is likely partly explained by the lack of interference effects in the model. A part of the halo discrepancy may have a similar origin. At a size parameter of 30, the shape agreement at larger scattering angles is equally as good as at a size parameter of 60 although the treatment in the halo regions has deteriorated further. The IGO result agrees with common knowledge and observation that as the crystal size reduces, the halo gradually disappears. RTDF exhibits a similar trend but through a reduction in the halo peak rather than a change of the halo shape, as seen in IGO. A size parameter of 12 offers less agreement, especially between 40° and 175°, although the comparison of the width and shape of the 22° halo appears to have improved. The quality of the result across the full angular range suggests that application of the RTDF model at such small size parameters is inappropriate. These results would suggest that the RTDF model can be applied at size parameters as low as 30 because the comparison is of equal quality to that found at larger size parameters but that crystals smaller in size would be pushing the size applicability limit. A more complete range of IGO data over the size parameters between 12 and 30 is not publicly available at this time.

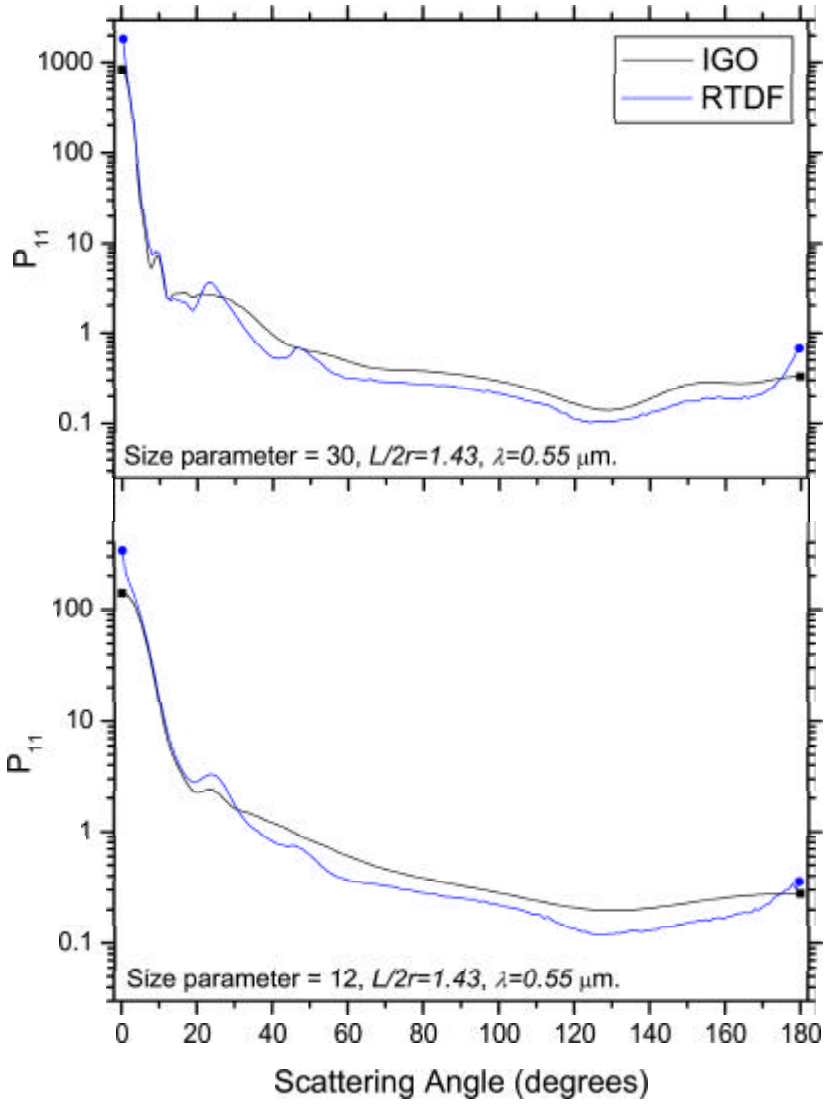

Figure 3.14: The phase functions for two hexagonal columns calculated using IGO and RTDF at a wavelength of $\lambda = 0.55$ μm. Top: Size parameter = 30, $L/2r = 1.43$. Bottom: Size parameter = 12, $L/2r = 1.43$.

Chapter 4

Testing the Model using Hexagonal Columns

Ice crystals in cirrus have a structure that is predominantly hexagonal in nature. The well known 22° halo is created due to this hexagonal structure by refraction of light through two prism facets. The case of a hexagonal column has been well studied. In this chapter, results for a hexagonal column calculated using RTDF averaged over random orientations will be presented and compared to GO, SVM and IGO. In section 4.1, the phase function due to GO and RTDF will be dissected and the ray origins of features explained. Section 4.2 will provide a similar discussion for the degree of linear polarization. Comparisons to SVM will be made in section 4.3 before comparisons to IGO at both visible and infrared wavelengths in section 4.4. The closely related geometry of the hexagonal plate will be discussed in the next chapter.

The calculations in sections 4.1 and 4.2 were performed on a standard desktop PC. In this case the RTDF calculation increased the computation time by only 27% when compared to GO. This illustrates the negligible increase in computational expense introduced by the model, maintaining the accessibility of the code to researchers with everyday computational resources.

All of the GO and RTDF phase functions and degrees of linear polarization that follow are calculated over 50,000 averaged random orientations with 100 incident rays per orientation unless explicitly stated. This rule extends throughout the

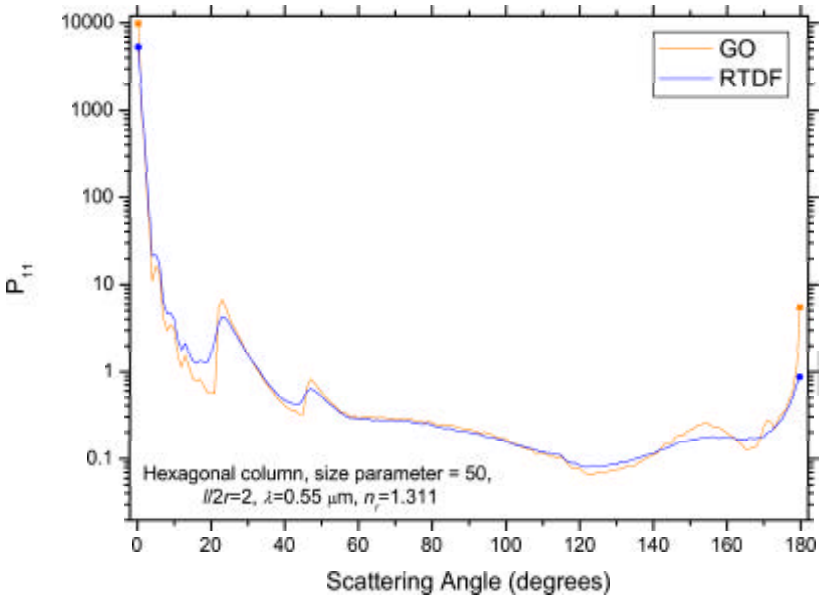

Figure 4.1: The phase function (P_{11}) for a hexagonal column of size parameter 50 with an aspect ratio $L/2r = 2$ calculated using RTDF and GO.

rest of the thesis for all crystal geometries.

4.1 Phase Function

Figure 4.1 shows the phase function generated by a hexagonal column calculated using the RTDF model. The equivalent GO result is plotted for comparison. The column has a size parameter of 50 at a wavelength of $\lambda = 0.55$ μm with an aspect ratio $L/2r = 2$. One can see that the RTDF model smooths out the P_{11} profile across the angular range. It reduces the 22 ° and 46 ° halo peaks, smoothing the shape of the halos. The forward and back scattering peaks are also reduced in intensity. GO features between 120 ° and 170 ° are significantly less prominent. The effect of the RTDF model depends upon the size and shape of the crystal in question but these smoothing and dampening effects are common when comparing to GO.

The codes that implement the RTDF model allow all of the ray paths to be

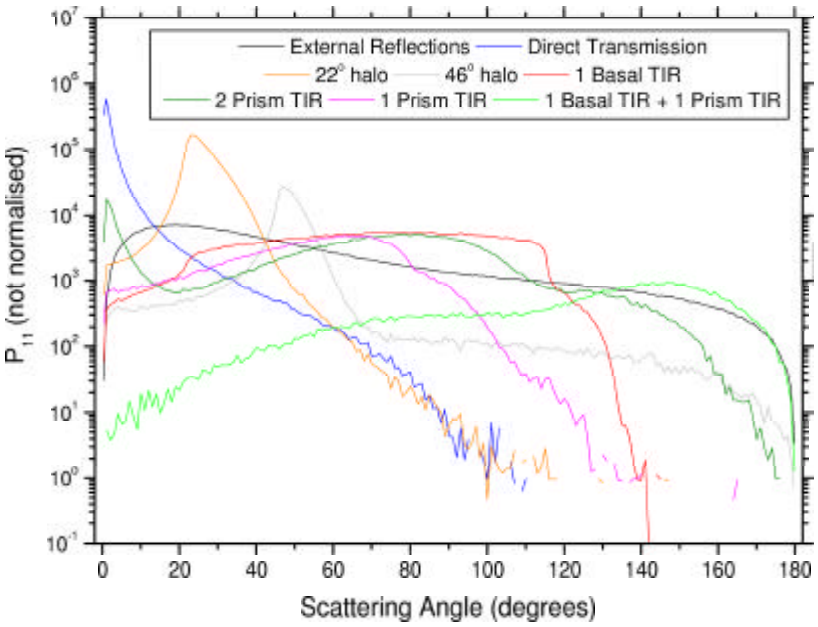

Figure 4.2: The phase function (without normalisation) for a hexagonal column of size parameter 50 with an aspect ratio $L/2r = 2$ calculated using RTDF and broken into contributing ray path types. The most important ray path types are shown and discussed in the text.

recorded and analysed individually. This allows the identification of scattering features in terms of their ray origins. Figure 4.2 shows eight of the main ray path types from an equivalent case to figure 4.1 plotted individually. The results are calculated using the RTDF model using the same hexagonal column as in figure 4.1 but using four times as many random orientations. This helps to make the profiles of the weaker ray path types smoother. The radiances of individual rays have been collected in each of the angular bins with no normalisation. As a result, figure 4.2 shows accurately how the ray paths compare to one another. It must be remembered that there is a large contribution from the external Fraunhofer diffraction pattern that is not included here, particularly within a few degrees of forward scattering. Also, there are many more possible ray paths that are not included in figure 4.2. Including them all would be impractical. Those chosen highlight the main points. There follows a brief explanation of the features that can be seen in figure 4.1 using figure 4.2 where appropriate.

Across the whole angular range is a strong background caused by external re-

flections from facets. This feature is a strong contributor to the scattering of the hexagonal column. It offers a very low contribution at direct forward scattering due to a grazing incidence case being required, which is unlikely to occur. It then rises quickly to a maximum at around 20° before decreasing at a reasonably constant slow rate until back scattering where it gives a low contribution due to a requirement for perpendicular or basal incidence.

The forward scattering point in GO is due to refraction through parallel facets, *direct transmission*. In the RTDF result, this peak is spread to as large a scattering angle as 100° but it is only the dominant ray contribution out to around 14°.

The 22° halo is caused by refraction through two prism facets separated by an angle of 60°. It is formed because such a refraction event has a minimum deflection angle of approximately 22° when considering GO. For GO, the peak begins at 22° and extends as far as 45°. The effect of RTDF is to spread the peak in both directions but primarily forwards. The RTDF 22° halo peak is present at forward scattering and becomes the dominant feature at 14°, taking over from the direct transmission peak. The RTDF 22° halo provides a trace contribution out to 100°. Between 14° and 22°, GO is dominated by the external reflections.

The 46° halo is a result of refraction through one prism and one basal facet. The facet separation angle in this case is 90°. Like the 22° halo case, a minimum angle of deflection exists of approximately 46°. The GO profile of the halo starts at the halo angle of 46° and reduces to zero at around 68°. The RTDF effect is similar to the 22° halo, spreading the halo forwards to a weak forward scattering contribution and taking over from the 22° halo as the dominant contribution a few degrees forward of where it occurs for GO at about 42°. A signal from the RTDF 46° halo is seen at as large a scattering angle as back scattering, although it falls very quickly to low levels above 60°.

Between 60° and 110° the GO and RTDF results appear to differ little. There is a curving decrease, beginning at around 80°. This is due in part to the steady reduction of the external reflection contribution. However, it is mainly as a result of a decrease in rays refracting into the crystal, totally internally reflecting once and then exiting the crystal, with all of the interactions occurring at prism facets (path "1 Prism TIR" in figure 4.2 and below). Such interactions cannot produce scattering above 110° or below 25° for GO. This can be verified using Snell's law and the condition for total internal reflection (see section 2.2.2). The effect

of RTDF is to spread the contributions forwards as far as forward scattering but backwards by only a few degrees. Evidence of this in the phase function is hard to discern, but can clearly be seen in figure 4.2.

Ray paths including combinations of only refractions and total internal reflections are important because a total internal reflection does not reduce the intensity of a ray. This makes them as strong as halos when comparing individual rays leaving the crystal. Another important case is when the total internal reflection is from one of the basal facets (path "1 Basal TIR"). This creates a feature in the degree of linear polarization that will be discussed in the next section. This ray path provides the largest scattering contribution between around 90° and 116° above which it cannot scatter, verifiable using the same method as the previous case. A weak signal can be found at larger scattering angles due to RTDF spreading. The drop in scattering at 116° can be seen in both the phase function and figure 4.2.

The combination of the two single total internal reflection paths being removed results in the minimum in the phase function from 116° onwards. The RTDF result is higher than the GO result between 116° and 140° because of rays undergoing total internal reflection twice within the crystal. Such rays provide a bimodal scattering pattern. In terms of GO, they rise to a broad peak at approximately 80°. There is then a sharp drop to a minimum at approximately 116° before rising to form a wide peak of lower intensity that extends to back scattering, centred at approximately 150°. The first peak is due to ray paths involving two total internal reflections from prism facets (path "2 Prism TIR"). The second is caused when one of these is from a basal facet (path "1 Basal TIR + 1 Prism TIR"). In the case of RTDF, the minimum at 116° is considerably smeared out resulting in increased scattering. This provides the positive shift in the RTDF phase function between 116° and 140°.

The rest of the scattering range is a mix of complicated internal reflecting and total internal reflecting ray paths. The GO maximum at 155° is formed by rays entering and leaving the same facet, undergoing several total internal reflections while inside the crystal. Above a scattering angle of 166°, such ray paths are rare and their disappearance results in the minimum in this scattering range. Due to RTDF smearing, the minimum is only visible in the GO result. The GO maximum at 171° arises because ray paths involving up to ten total internal reflections scatter in a very narrow angular window centred here. Again, RTDF smooths the feature. From 173° onwards, the phase function increases to the back scattering peak, formed by many different ray paths that involve internal

and total internal reflections. Some of the ray paths are very complicated. The RTDF model spreads the peak, moving intensity forwards and resulting in a reduced signal at back scattering.

The asymmetry parameters for the results shown in figure 4.1 are $g_{GO} = 0.807$ and $g_{RTDF} = 0.816$. On first glance, this result is puzzling. The strongest contribution to the asymmetry parameter is found at forward scattering. If this peak is spread out by applying the RTDF model, then one intuitively would expect that the asymmetry parameter would reduce. However, this is not the case. In fact it is a common result that the RTDF model increases the asymmetry parameter by a value of the order of 0.01. By studying the change in the asymmetry parameters for a range of specific features as one moves from GO to RTDF, it can be shown that the strong features at forward scattering and in the halo regions do result in a reduction of the asymmetry parameter but only by a small amount. It is balanced by an increase from more complex ray paths that are scattered at angles greater than 90°. It is the case that, when spread out, scattering features at angles less than 90° generally move intensity to larger scattering angles while features at greater than 90° move it to smaller scattering angles. The important factor in determining the change in the asymmetry parameter from GO to RTDF is not how much intensity is moved but by what angular distance the intensity is shifted. More complex ray paths involve more facet interactions and so have a greater smoothing effect because the RTDF ray deflections are cumulatively larger. These ray paths are the dominant type at scattering angles larger than 90° and so there is greater angular movement per unit irradiance in this angular range than at, for example, the forward scattering point. Due to the tendency of intensity to shift forwards from this angular region, the asymmetry parameter increases.

This is a very important point when considering the potential applications of the RTDF model. Solar reflectivity studies have found asymmetry parameters of as low as 0.7 being required for particles in models to fit the data from measurements [60, 71, 112]. Calculations for hexagonal columns using GO tend to give asymmetry parameters of 0.8 or above, as the example above has confirmed. As will be demonstrated in the IGO comparisons in section 4.4, the tendency of RTDF to reduce the forward and back scattering peaks when compared to GO is a move in the right direction. However, due to the effect explained above the RTDF model does not offer an improvement over GO asymmetry parameters when considering the solar reflectivity predictions. It is apparent that the slightly higher accuracy found using GO in this case is artificial and due to the unrealistic large forward and back scattering peaks predicted by GO. The

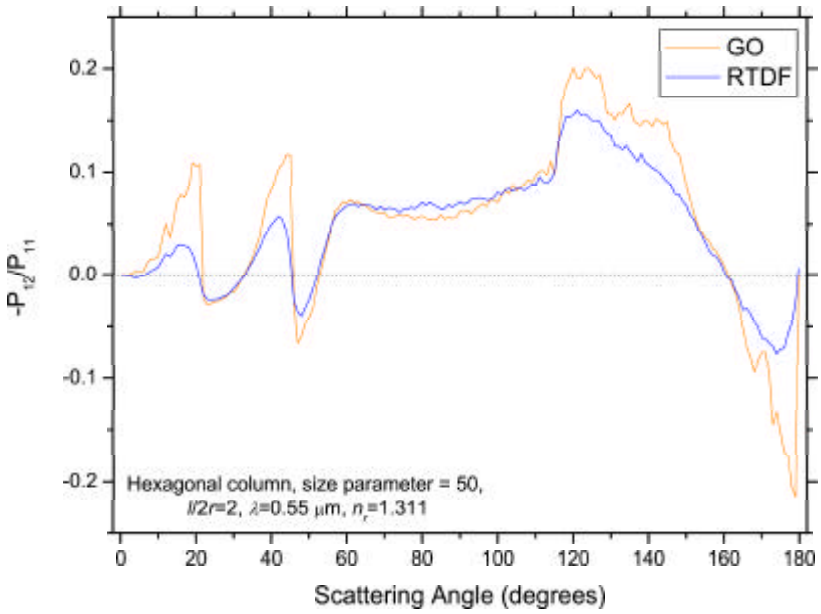

Figure 4.3: The degree of linear polarization $(-P_{12}/P_{11})$ for a hexagonal column of size parameter 50 with an aspect ratio $L/2r = 2$ calculated using RTDF and GO.

asymmetry parameter is determined mainly by the contributions at direct forward and back scattering where interference effects are important, something the RTDF model does not currently have. This will be discussed further when the IGO asymmetry parameter is considered in section 4.4.1.

4.2 Degree of Linear Polarization

The *Degree of Linear Polarization* (DLP) is dominated by two competing groups of ray paths. First, the external reflections from crystal facets make a positive contribution to the DLP (corresponding to a tendency to polarization perpendicular to the scattering plane). Second, the halos and rays paths including only odd numbers of total internal reflections and/or internal reflections make a negative contribution to the DLP (corresponding to a tendency to polarization parallel to the scattering plane).

Figure 4.3 shows the DLP (defined here as $-P_{12}/P_{11}$) for the case described in the previous phase function section. The RTDF model reduces the absolute values of the DLP across the profile. Figure 4.4 provides the $-P_{12}$ equivalent to figure 4.2 where the ray path types are individually plotted using 200,000 orientations. Normally the DLP is normalised by dividing by the normalised phase function. This is not appropriate here, so the raw $-P_{12}$ values are plotted to indicate the strength and direction of linear polarization for each ray path with respect to one another. The lower pane of the figure provides a zoom view to magnify the contributions of ray paths that while important are much smaller than the halos and external reflections. There follows an equivalent discussion to that for the phase function given in the previous section.

GO shows very weak linear polarization at forward scattering due in part to the very strong value of the phase function. In addition, rays scattered directly forwards exhibit low polarization because the scattering plane which acts as the reference plane for the Stokes vector is not defined. The incident and scattered rays travel in close to the same direction. By choosing a random reference plane at this point the result of zero polarization is obtained, as has been predicted theoretically [54]. Although not shown in figure 4.4, it should be noted that the external diffraction component is also not polarized. Up to a scattering angle of 20° the external reflections dominate, helping the DLP to rise to a maximum at 21°. In this region the RTDF model shows a significant reduction. Within the first six degrees of forward scattering, a negative signal is visible. It is created by the spreading of the negatively polarizing direct transmission ray path into regions where the phase function is not so overwhelming and the scattering plane can be defined. The positively polarizing external reflections then take over but tempered by the forward spreading of the negatively polarizing 22° halo peak. This results in the reduction in the absolute DLP values for RTDF between 10° and 20° when compared to GO.

Halo ray paths (two refractions through the crystal) result in negative polarization, as shown in figure 4.4. As a result, the contribution from the 22° halo feature in both GO and RTDF is strongly negative. This counteracts the positive external reflection background to give a small negative peak. It is reduced in magnitude slightly by the RTDF model. As the scattering angle increases, the effect of the halo trails off in the GO result and the profile rises to a second strong peak dominated by external reflections. The RTDF result reduces this peak by a mixture of the backward spreading of the 22° halo and the forward spreading of the 46° halo. The transition between each one dominating occurs at the same angle as for the phase function, at around 42°. The 46° halo is

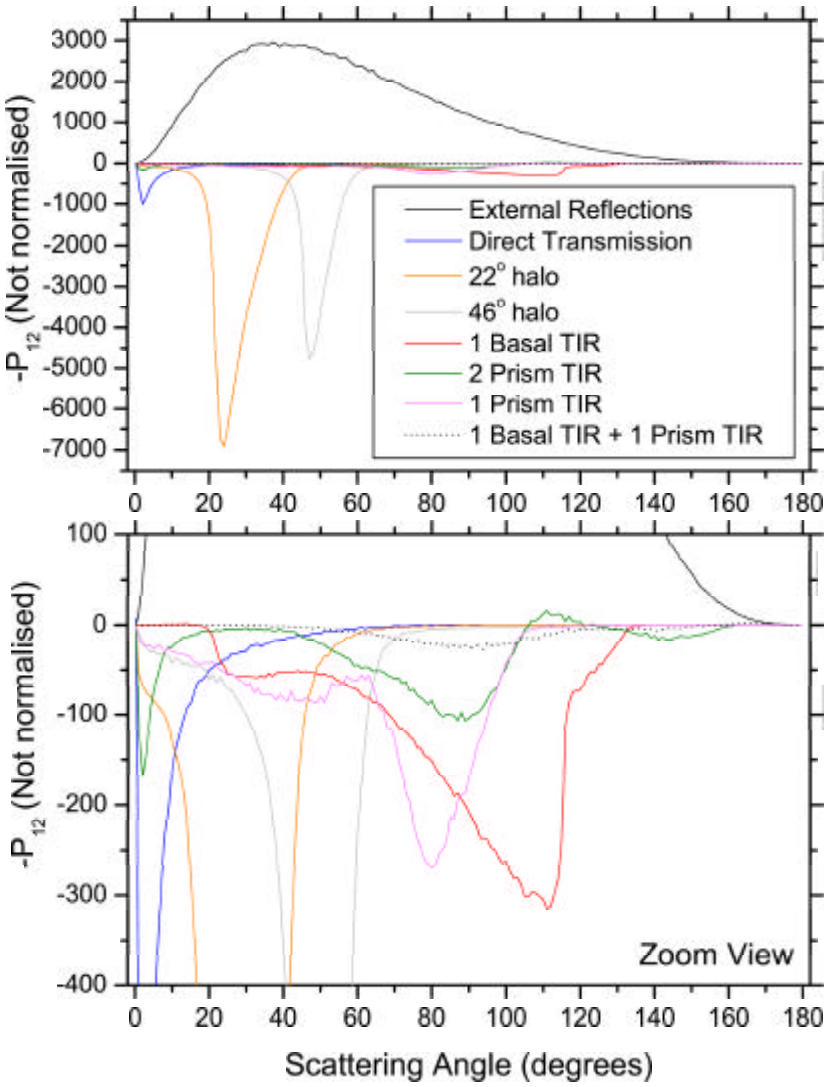

Figure 4.4: The scattering matrix element $-P_{12}$ (without normalisation) for a hexagonal column of size parameter 50 with an aspect ratio $L/2r = 2$ calculated using RTDF and broken into contributing ray path types. The most important ray path types are shown and discussed in the text.

noticeably reduced by RTDF, although both GO and RTDF peaks are larger in magnitude than the 22° case due partly to the reduced phase function value.

Between 60° and 110° the discussion is very similar to that of the phase function. The ray paths that control the DLP in this angular range are those that involve rays entering the crystal, undergoing one total internal reflection and then exiting the crystal, where all of the interactions are with prism facets. In the case of GO, these contributions are strongest between approximately 65° and 95° where their negative contribution reduces the DLP signal, though this is not clear in the DLP because the external reflections still dominate. Between 80° and 110° the negative contributions reduce gradually. This results in an increase in the DLP. The smoothing caused by RTDF helps to temper the increase.

GO and RTDF show the strongest change in linear polarization at 116°. As discussed for the phase function at this angle, rays entering the crystal that undergo a single total internal reflection from a basal facet before exiting cannot be scattered above 116°. The strong negative contribution by this ray path stops abruptly at this scattering angle because it is a maximum deflection angle, as shown in figure 4.4. This results in the sudden increase in the DLP that can be seen in figure 4.3.

As is the case for the phase function, above 140° the complex ray paths involving internal reflections begin to dominate the DLP. Above 160°, the external reflections begin to decrease in strength quite sharply. The *neutral point* (N_P), the point at which the DLP crosses the x-axis near back scattering, does not move for RTDF compared to GO at a value of approximately 160°. In theory, one can distinguish between columns ($157° < N_P < 165°$) and plates ($140° < N_P < 160°$) using the position of the neutral point [113]. The lack of movement of the neutral point suggests this concept still holds using RTDF.

The strong negative DLP near back scattering for GO shows the continued dominance of the negatively polarizing complex ray paths involving odd numbers of internal reflections. The RTDF result is significantly reduced due to the forward shift of scattering from this angular range, also a contributing factor to the reduction compared to the GO feature between 120° and 160°. The DLP returns to close to a theoretical zero for both models at back scattering because the scattering plane is not defined, as was the case at forward scattering.

4.3 Comparison to SVM

As discussed in section 2.1, exact methods such as T-matrix and numerical methods such as FDTD cannot be applied at sizes where GO and RTDF are normally considered acceptable. The closest method to exact theory that can be used for comparison is a variation of SVM. The SVM method used here [4] is an approximation for finite cylinders based on an exact numerical SVM code for hexagonal cylinders of infinite length [3]. The code does not provide satisfactory results for orientations close to basal incidence due to the approximation involved. This means that in making comparisons to the GO and RTDF codes, the crystal orientations must be restricted to include only reliable orientations.

Figure 4.5 shows the phase function and degree of linear polarization for a long hexagonal column calculated using SVM, GO and RTDF. The GO and RTDF results are calculated using 50,000 averaged random restricted orientations with 100 incident rays per orientation. The column has a size parameter of 50 with $L/2r = 10$. The orientation restrictions are such that the long axis of the column is at least 12.96° from the direction of the incident light. A consequence of this restriction is the lack of the 46° halo and the back scattering peak in the SVM profile. The same features appear suppressed in the GO and RTDF results. Although the SVM data is not as smooth as one would like, the RTDF phase function provides a better comparison than standard GO as it widens the 22° halo peak, reduces both forward and back scattering and smooths the profile across the angular range. The degree of linear polarization shows similar improvements, particularly in the halo region and above 160 °, although discrepancies still remain.

The SVM comparison is not ideal but until the size applicability range of methods such as T-matrix are increased, it is the only comparison with a computational method that can in any way be described as exact.

4.4 Comparison to IGO

In this section, the IGO method discussed in section 2.5 and used to investigate the lower size applicability limit of the RTDF model in section 3.5.2 will be revisited. Using publicly available IGO data [111], comparisons will be made to GO and RTDF for hexagonal columns at both visible and near infrared

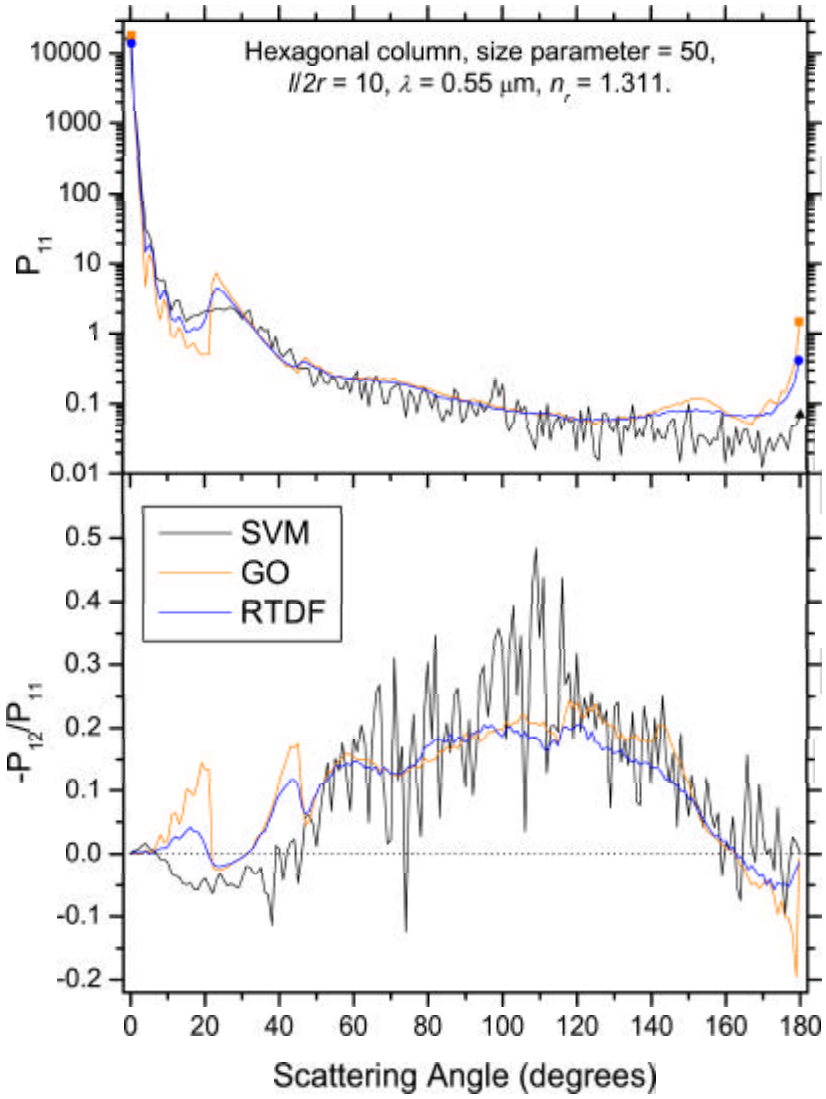

Figure 4.5: Phase function and degree of linear polarization for a long hexagonal column of size parameter 50 and aspect ratio $L/2r = 10$. Calculations were made using SVM, GO and RTDF at a wavelength of 0.55 μm. Random orientations are restricted so that the long axis of the column is at least 12.96° from the incident light to comply with the approximation involved in the SVM method.

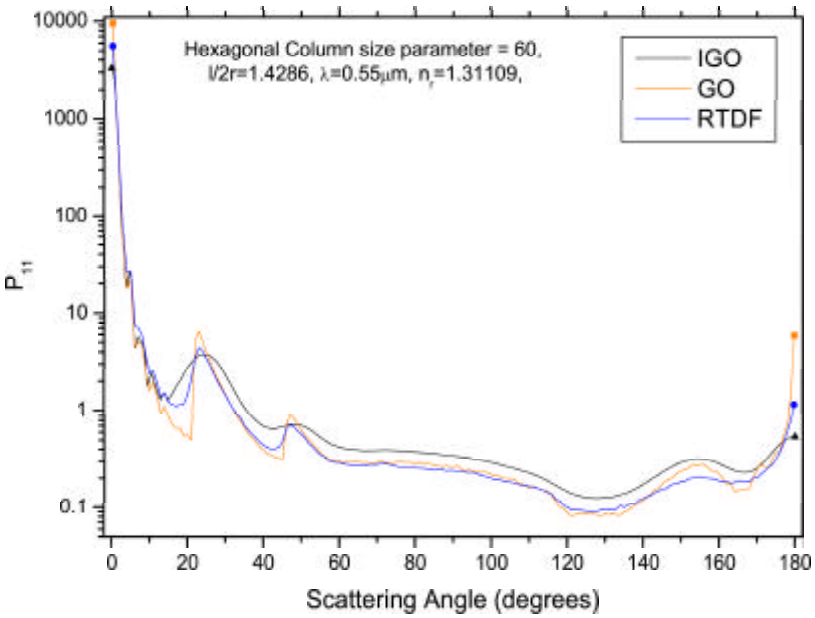

Figure 4.6: A phase function comparison between RTDF, GO and IGO for a hexagonal column at a visible wavelength of 0.55 μm. The column has a size parameter of 60 and an aspect ratio $L/2r = 1.4286$.

wavelengths. This model allows comparisons for averaged random orientations without restrictions. The far field transformation used by IGO introduces an exact theory component and phase dependency which separates the model from standard ray tracing codes. IGO uses standard ray tracing up to the surface of the scatterer, in contrast to the RTDF model which introduces a diffraction treatment for all of the facets.

4.4.1 Visible Wavelengths

Figure 4.6 compares results from GO, RTDF and IGO for a hexagonal column at a visible wavelength of 0.55 μm. The column has a size parameter of 60 and aspect ratio $L/2r = 1.4286$. The IGO profile appears to be of higher intensity across much of the angular range when compared to the other two models, though this is a consequence of the normalisation. The forward and back scattering peaks predicted by IGO are much reduced, leading to the discrepancy over the side scattering regions. Renormalising over a less complete angular

range would resolve this, although such action has not been taken here because the forward and back scattering comparisons are important. The forward and back scattering peaks predicted by RTDF are significantly reduced compared to standard GO, providing a better comparison to IGO.

Interestingly, the asymmetry parameter predicted by IGO is consistent with the solar reflectivity predictions mentioned in section 4.1, having a value of $g = 0.71$. This is significantly lower than for the other two models due to the drop at forward scattering. This raises questions over the asymmetry parameters generated by the SVM code as they are found to be generally higher than both GO and RTDF, albeit over a restricted orientation range. If the IGO results can be relied upon then the solar reflectivity consistency would suggest that the crucial treatment of forward and back scattering in RTDF, though a significant improvement over GO, is an area that restricts the accuracy of the model. Furthermore, it suggests that caveats should be placed upon the use of asymmetry parameters from RTDF in applications such as climate modelling at this time. It has been shown that by introducing phase tracing and a ray based far field approximation which includes physical optics effects into a two dimensional version of the RTDF model, the treatment at forward and back scattering for fixed orientations can produce results that compare much better with exact SVM calculations for cylinders of infinite length than GO and the current version of RTDF [108]. It may be possible in the future to apply this to the model for averaged orientations, although it represents a significant undertaking.

Setting aside the apparent intensity shift in the side scattering regions, the shape of the IGO profile is reproduced well by RTDF between 60° and 160°. A particular improvement over GO is found at 155°. IGO provides halo peaks that are smooth and rounded to a much greater extent than RTDF, the IGO shape resembling the 22° halo in the SVM result discussed above. At larger size parameters, IGO results become more similar to GO with sharper halos. As the crystal size decreases, the halo becomes more smooth. As shown in section 3.5.2, a similar effect is seen in RTDF but does not occur as quickly. This suggests that the shape of the IGO and SVM halos exhibit greater smoothing as a result of the exact theory components, perhaps due to interference effects.

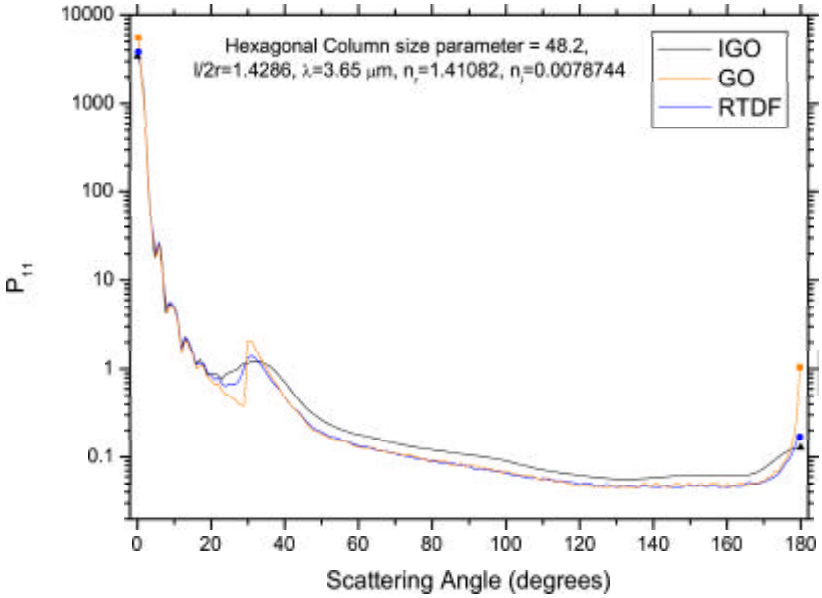

Figure 4.7: A phase function comparison between RTDF, GO and IGO for a hexagonal column at an infrared wavelength of 3.65 μm. The column has a size parameter of 48.2 and an aspect ratio $L/2r = 1.4286$.

4.4.2 Infrared Wavelengths

As the wavelength considered increases, the effect of absorption becomes more important. In section 2.2.2, it was explained how the amount of absorption is determined by the imaginary part of the complex refractive index, a wavelength dependent quantity. Compared to visible wavelengths, the imaginary part of the refractive index is much increased at infrared wavelengths. Section 2.2.2 also made reference to the changes that a complex refractive index makes to Snell's law and the Fresnel equations. These adjustments do not have a large impact on the scattering properties of a particle when compared to the effects caused by the attenuation of light within the material. The effect of this attenuation will be demonstrated in the forthcoming paragraphs.

Figure 4.7 shows GO, RTDF and IGO results for a hexagonal column at an absorbing wavelength of $\lambda = 3.65$ μm. The components of the refractive index are taken to be $n_r = 1.41082$ and $n_i = 0.00787$, following the values used to produce the IGO results [111]. The GO and RTDF results are calculated using

50,000 averaged random orientations. The column has a size parameter of 48.2 and aspect ratio $L/2r = 1.4286$. The first thing to note about the three model phase functions is that they exhibit less features. The 46° halo has disappeared. The 22° halo is much flatter in the IGO result. It is smaller in intensity in the GO and RTDF results compared to the results at 0.55 μm. As a consequence the halo appears flatter, particularly for RTDF. The forward scattering point is reduced for both GO and RTDF due to the attenuation of rays refracting through parallel facets. The RTDF result is now close to IGO. A similar effect can be seen at back scattering.

As the crystal size increases, one would expect these effects to be emphasised because energy is increasingly absorbed rather than scattered due to the increased distances that rays have to travel through the crystal. This can be seen in figure 4.8 which shows results for two larger hexagonal columns at the same wavelength. The first has a size parameter of 99.5 and an aspect ratio $L/2r = 2.3789$. The 22° halo is further smoothed. The forward and back scattering points for RTDF have been reduced to below the IGO levels, although the forward scattering point is close in value. The comparison to IGO across much of the angular range is excellent. The second column has a size parameter of 150.7 and an aspect ratio $L/2r = 4.2827$. The reduction in the forward scattering point has continued. The 22° halo can hardly be seen in the IGO result. The halo size for GO and RTDF is much reduced, the difference between the ray tracing based models being much less. At back scattering, the IGO result drops away while GO and RTDF are in the closest agreement so far observed at this scattering angle. As for the first column, a very good comparison to IGO is exhibited at most scattering angles. In both cases in figure 4.8, the normalisation shift compared to IGO has disappeared because the results from the models across the angular range are in better agreement.

Figures 4.7 and 4.8 have shown that as the absorption increases due to an increase in crystal size, the phase functions become flatter and increasingly featureless. This can also be seen as the wavelength is increased for a crystal of constant size. A consequence of this is that at infrared wavelengths where there is increasing absorption, the geometry of a crystal becomes less important because characteristic scattering features of any given geometry are smoothed out. It has been shown that circular cylinders can be used in the place of hexagonal columns at strongly absorbing wavelengths [32].

It remains the case that the treatment of scattering at forward and back scattering in the RTDF model is likely to be much improved if interference effects can

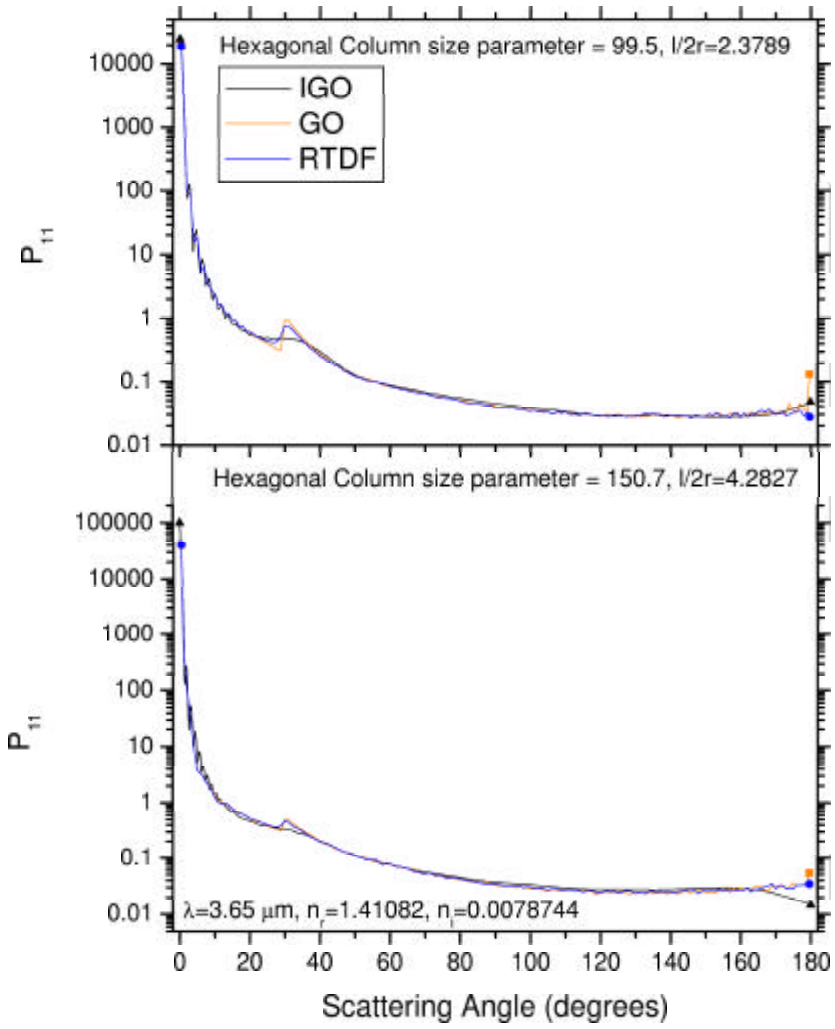

Figure 4.8: Phase function comparisons between RTDF, GO and IGO for two hexagonal columns at an infrared wavelength of 3.65 μm. Top: Size parameter of 99.5 and an aspect ratio $L/2r = 2.3789$. Bottom: Size parameter of 150.7 and an aspect ratio $L/2r = 4.2827$.

be introduced. Improved comparisons to IGO at forward and back scattering as the wavelength or crystal size is varied do not indicate optimum crystal size or wavelength applicability regions for RTDF.

The RTDF results at $\lambda = 3.65$ μm have shown that the model can be applied at near infrared wavelengths, offering comparisons to IGO of comparable quality to those at visible wavelengths. This justification of the use of the model will be important in chapter 8 where the model will be used to compare to aircraft radiance measurements, some of which are in the near infrared at a wavelength of $\lambda = 1.61$ μm.

Chapter 5

Application of the Model to a Range of Crystal Geometries

The case of the hexagonal column has been well studied and is the most fundamental geometry that can be studied for ice crystals that are representative of those in cirrus. There is a wide variety of increasingly complex geometries that have also been observed in cirrus. The RTDF model maintains the flexibility of GO in terms of the geometries that it can be applied to. This will be exploited in this chapter where RTDF results for a range of geometries will be presented. There will be a short discussion of each geometry to illustrate its relevance to the field.

5.1 Hexagonal Plates

A hexagonal plate is essentially a hexagonal column whose length is less than its diameter. Hexagonal plates are regularly observed in cirrus and are responsible for the *parhelia*, enhanced brightness of the 22° halo horizontally to both sides of the sun that are commonly known as *sun dogs*. They are more commonly observed independently of the complete halo because they are caused by falling hexagonal plates adopting a preferential orientation where their largest

projected area is perpendicular to the direction of fall. This results in ray paths concentrating at 22° on either side of the sun. Such preferential orientations can occur for any crystal geometry whose projected area varies with orientation. The phenomenon is restricted to low air turbulence and a certain crystal size range. If the crystal is too small then the orientation can still be considered random, the smallest being subject to Brownian motion. If the crystal size is too large, turbulence due to the air flow around the crystal results in pitching and tumbling. In between the two one finds a region where the orientation stabilises. This size range depends upon the particle shape, particle size, fall velocity and the viscosity of the air. One can define the size range in terms of the *Reynolds number*, a dimensionless quantity that describes fluid flow with respect to a solid. It is denoted by R_e and defined in equation 5.1 where v_p is the particle fall velocity, d the particle diameter and ν the kinematic viscosity of the fluid.

$$R_e = \frac{v_p d}{\nu} \tag{5.1}$$

Stable atmospheric particle orientations occur for plate like particles in the range $1 < R_e < 100$, which corresponds to plates with a diameter of between 0.15 mm and 1.5 mm [114]. This converts to crystals with size parameters above around 800 at 0.55 μm, which falls in the GO domain where halo effects are strong. The particle size range required for stable orientations is therefore large compared to the crystals of various geometries that will be discussed in this chapter.

In section 5.6, it will be demonstrated using RTDF that bullet rosettes adopting preferred orientations can scatter light very differently to those in random orientations. The same is true for a hexagonal plate. The preferred orientation scattering of a hexagonal plate which is in such a position with respect to the sun and the observer that it can contribute to a sun dog will be similar to that of a hexagonal column at perpendicular incidence, identical in the case of GO results. To study the scattering characteristics of a hexagonal plate more generally, a comparison to a hexagonal column in the averaged random orientation case is more appropriate.

Figure 5.1 shows the phase function and degree of linear polarization for hexagonal crystals of size parameter 50 with aspect ratios of $L/2r$ =2, 1, 0.5 and 0.1. The crystal with an aspect ratio of 2 is a hexagonal column identical to that considered in sections 4.1 and 4.2. An aspect ratio of 1 corresponds to the

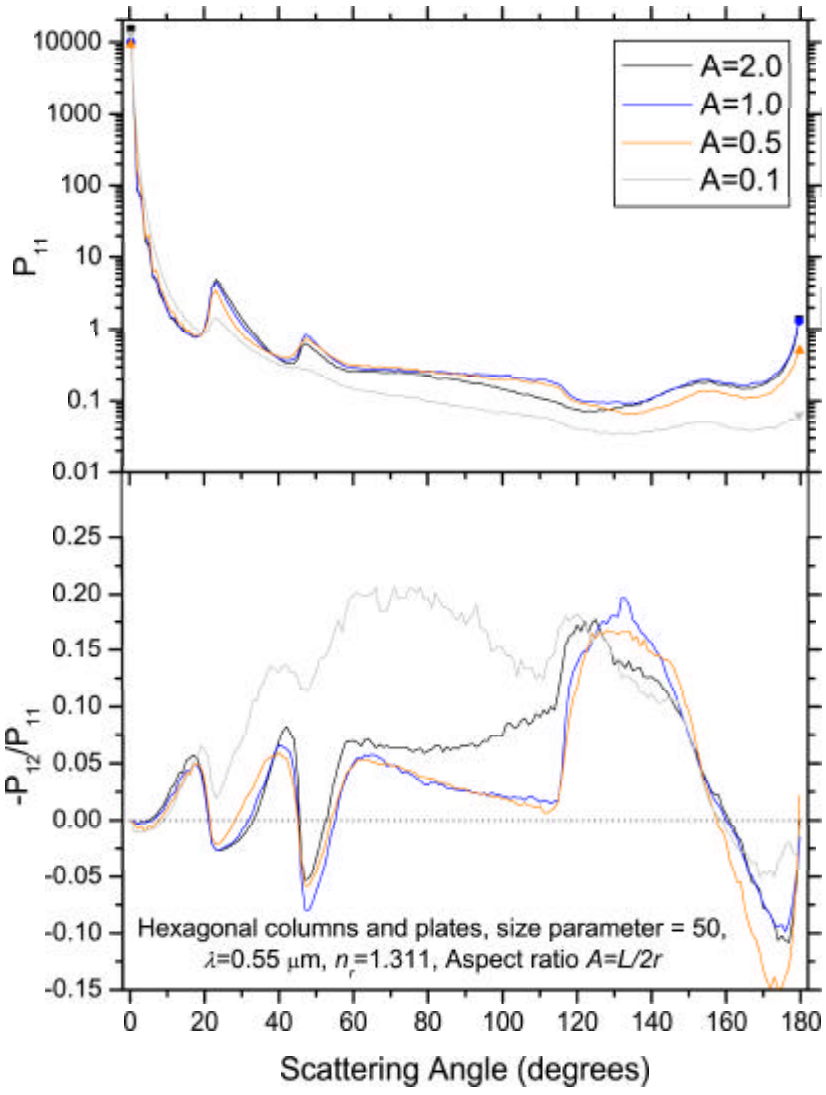

Figure 5.1: Phase function and degree of linear polarization for hexagonal crystals of size parameter 50 at $\lambda = 0.55$ μm. Aspect ratios $A = L/2r$ of 2 (Column), 1 (Borderline column/plate), 0.5 (Medium thickness plate) and 0.1 (thin plate).

borderline case between a column and a plate. A plate of medium thickness is represented by an aspect ratio of 0.5 and a thin plate by 0.1.

As the aspect ratio falls, the areas of the prism facets reduce and so the 22° halo reduces in intensity and exhibits less negative polarization. The 46° halo increases in prominence as the aspect ratio reduces from the column to the borderline case. This is due to the increasing importance of the basal facets. It then reduces slightly for the thick plate before being drastically reduced for the thin plate. This is because the areas of the prism facets are very small for the thin plate, reducing the probability of the 46° halo ray path.

In the phase function, from 80° to 120° there is an increase in intensity for the borderline and medium thickness plate when compared to the column. A reduction in the same angular range in the DLP also extends forwards to the 46° halo. The reason for these changes is that the negatively polarizing ray paths that involve internal reflections from the basal facets become much more prominent. This also makes the jump in the DLP at 116° more severe, the angle above which the ray path cannot scatter.

Above 120° the borderline case is seen to behave in a similar fashion to the column. The medium thickness plate shows a reduction in the phase function in this region. This is a normalisation effect because of changes to the phase function elsewhere. This is supported by the fact that the shape of the phase function in this angular range does not change when compared to the column or the borderline crystal. The enhanced DLP signal at 173° is due to the polarization component remaining reasonably unchanged while the phase function falls.

The neutral point N_P for the medium thickness plate moves forwards by a few degrees compared to the column and the borderline crystal, again suggesting that the plate or columnar nature of a crystal can be determined from the location of N_P. A more complete study over size parameters would be necessary to fully verify that the findings of Macke apply to RTDF [113].

The thin plate is quite distinct from the other crystals. The phase function exhibits less features and scatters more light forwards of 20°. This is because ray paths such as the 46° halo and those involving multiple internal reflections are rarely observed. Rays are much more likely to refract through the two parallel basal facets. The increase in scattering forwards of 20° is caused by this increase in direct transmittance. The forward scattering point becomes

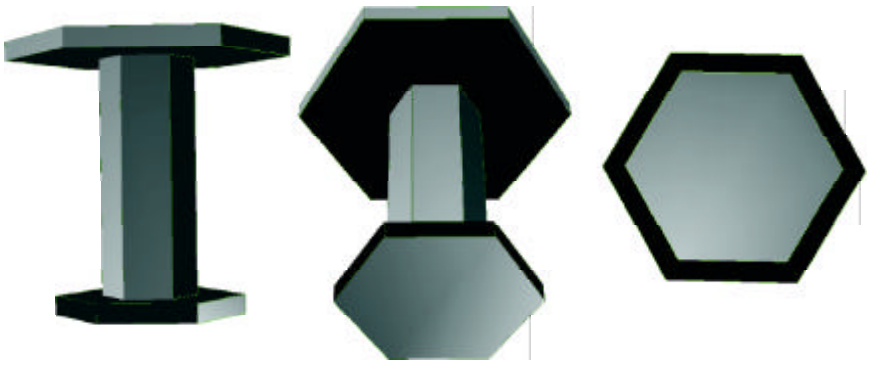

Figure 5.2: The capped column considered in section 5.2 shown in three orientations.

stronger and is then spread due to RTDF. This is confirmed in the DLP where there is a strong negative signal from the two refractions. The lack of internal reflection ray paths changes the DLP across the profile for the thin plate. The positively polarizing external reflections dominate which leads to a significant increase in the DLP at side scattering compared to the column, with a much weaker negative signal near back scattering.

5.2 Capped Columns

A capped column is a combination of a column and one or two plates where the plates literally cap the column at the ends. This geometry was included in the Magono and Lee classification scheme of ice crystals as CP1a "Column with plates" [115]. A photograph of an excellent example of such an ice crystal can be found in figure 1f of Libbrecht [116]. Although this particular example was found in a natural snowfall, it illustrates the existence of such crystals in nature. The GO properties of such crystals have been studied by Macke [34] and Takano and Liou [35]. Bruintjes et al. [117] investigated double plate crystals in the atmosphere, a related geometry where the plates are separated by only a small

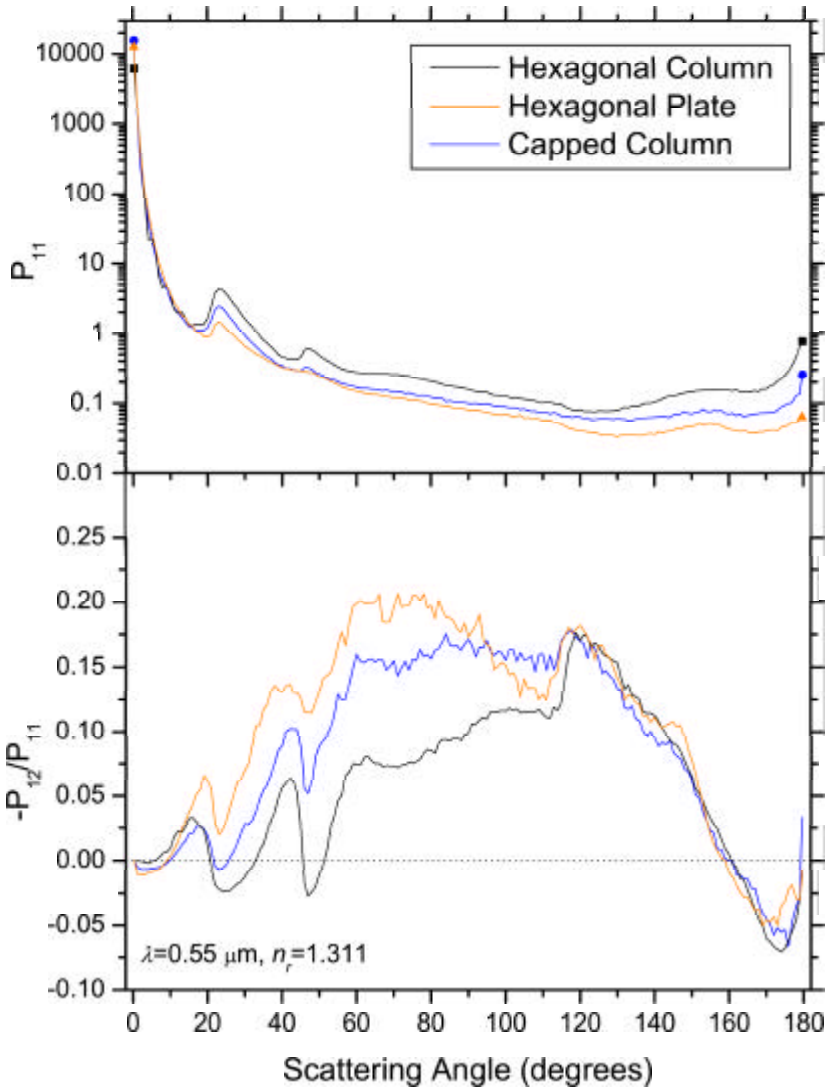

Figure 5.3: Phase function and degree of linear polarization for a capped column compared to that of a column and a plate at $\lambda = 0.55$ μm. Hexagonal column: Size parameter = 50, $L/2r = 2.5$. Hexagonal plate: Size parameter = 100, $L/2r = 0.1$. Capped column: As column, capped with two thin plates the first of which is the same as the comparison plate. The second has a radius of one and half times the first.

distance.

A model of an example of the capped column geometry is shown in figure 5.2 in three orientations. Figure 5.3 gives the phase function and degree of linear polarization for the same crystal compared to a column and a plate. All calculations are made using RTDF. The column has a size parameter of 50 and an aspect ratio $L/2r = 2.5$. The plate has a size parameter of 100 and an aspect ratio of $L/2r = 0.1$. The capped column is made up of the column that has just been described, capped at one end by the plate being used for comparison and at the other end by a plate with a radius one and a half times the first.

In both the phase function and the DLP the capped column profile can be found between the column and the plate. The large radii of the plates that are present in the capped column makes them very important. Rays incident on the particle in a random orientation are likely to interact with the plates in some way. The scattering of the capped column between 20° and 110° demonstrates this because it more closely resembles that of the plate. The capped column shows how scattering from a composite crystal can resemble that of its constituent parts. At the same time it illustrates that by adding more constituent parts, even if they are of a similar form to those already present, the scattering pattern can and in most cases will be changed.

5.3 Hollow Columns

In this section, deformed hexagonal columns that have depressions at both ends will be considered. These hollow columns are sometimes referred to as 'hopper' crystals. When the deformation is strong, they are sometimes called 'hollow sheaths'. The existence of such crystals is dependent on both temperature and ice supersaturation levels. Heymsfield and Platt [79] found that hollow columnar crystals were common in cirrus, particularly near cloud top where they dominated. When there was no convection within the cloud or at low temperatures, the crystals were more widespread in the cloud. These crystal habit findings are commensurate with other authors, for example Weickmann [70]. Photographs of hollow columns from Weickmann's work can be found in Parungo [107]. An image of a replica of a hollow column collected from a cirrus cloud is provided in figure 1A of Heymsfield [106]. Such hollow crystals have been used as a possible explanation for some rare small angle halo phenomena [118].

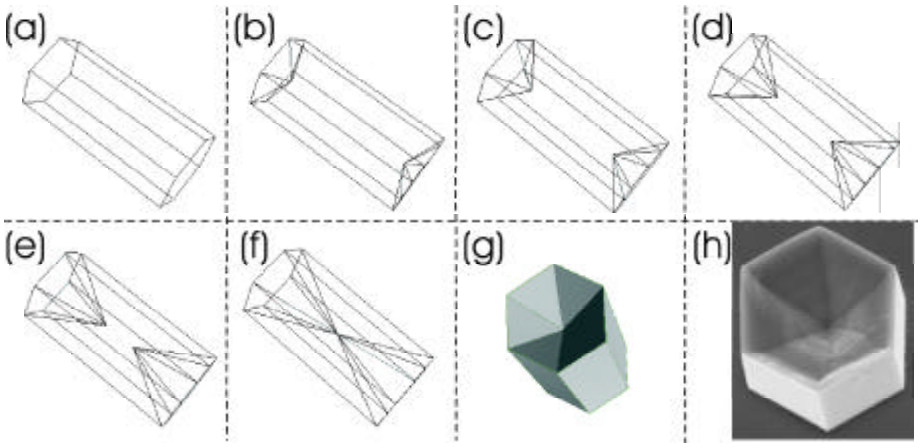

Figure 5.4: A variety of hollow columns showing the following indentations from each end, measured as a percentage of crystal length. Skeletal views: (a) 0 %, (b) 10 %, (c) 20 %, (d) 30 %, (e) 40 %, (f) 50 %. Full view: (g) 20 %. Ice analogue 'hopper' crystal: (h) Courtesy of Z. Ulanowksi.

The formation of hollow features occurs when supersaturation levels are sufficiently high [58, chapter 3]. As the supersaturation level increases, crystal growth accelerates and the comparatively slow ordered growth that results in pristine solid prisms becomes less common. The growth of the crystal proceeds by deposition on the existing facets and being at the extremities there is more rapid growth at the edges of each facet than at the centre. Once a small indentation has been formed the process exhibits positive feedback. The local supersaturation near the facet edge falls due to deposition and is replenished by vapour from both the surrounding air and from near the facet centre. This impedes the growth at the facet centre in favour of the facet edges. Over time, this results in the hollow features currently being discussed. The relationship between high supersaturation levels and deformation was demonstrated by Bailey and Hallett [81] who grew ice crystals in the laboratory and observed that between -42° and -50° hollow ends began to develop at ice supersaturation levels of 40%. As the ice supersaturation increased, the crystals became sheaths. Images of laboratory grown ice columns with hollow ends can be found in figure 3 of Libbrecht [116].

Some examples of models of hexagonal columns with hollow ends are shown in figure 5.4(a-g). The perfect triangular facets that form the depressions at the crystal ends may look idealized. However, the ice analogue crystals that will be discussed in chapter 6 have been seen to form such indented ends, as shown in the *Scanning Electron Microscopy* (SEM) image in figure 5.4h. Although

this does not guarantee that these facets form in cirrus ice, it indicates that crystal growth processes in general can create such facets. The GO scattering properties of this geometry have been discussed by Takano and Liou [35].

The scattering properties calculated using RTDF for the crystals shown in figure 5.4(a-f) are presented in figure 5.5, illustrating the effect of increasing severity of indentation. The results for a standard hexagonal column of the same size are plotted for comparison. The size parameter of the column was taken to be 50 at a wavelength of $\lambda = 0.55$ μm with aspect ratio $L/2r = 2$. The letters shown in the legend correspond to the labels in figure 5.4.

As the indentation becomes more profound there is a decrease in the phase function at back scattering and above 140° due to internal ray paths at these scattering angles being removed. There is also an increase at forward scattering and a smoothing of the inner edge of the 22 ° halo feature. These results indicate that modelling crystals perfectly rather than considering hollow areas could lead to significant errors in scattering properties, particularly for methods reliant on back scattering such as LIDAR. The 46° halo is seen to disappear for the hollow columns as the ray path responsible is impossible once the basal facet is removed. This could provide a contributing factor to the scarcity of observed 46° halos because even a small deformation breaks the halo signal into contributions from the triangular facets. The scarcity of the 46° halo is most clearly evident in the DLP where the negative polarization peak is only present for the perfect column.

The 22 ° halo becomes less prominent for both the phase function and the DLP as the indentation is increased due to the necessary ray path being obstructed by the triangular facets that form the hollow areas of the crystal. The slow degradation of the inner edge of the halo feature in the DLP around 15° suggests that polarimetry could be used to identify varying degrees of imperfections where hexagonal columns are present. In section 2.7 it was suggested that one of the reasons for the lack of observed halos, particularly the 22° halo, was the prevalence of hollow features in crystals which may dilute the effects. The phase functions in figure 5.5 show that it is not until the 50% hollow column that the halo is fully obscured. This indicates that some degree of imperfections at the ends of columns would still allow 22° halos to exist as long as a high enough proportion of the crystals present have sufficiently large solid portions. It has been observed in the field that crystals exhibiting some hollow structure can be the norm rather than the exception in halo producing clouds [100]. The same authors suggest that it is the complexity and diversity of cirrus particle shape

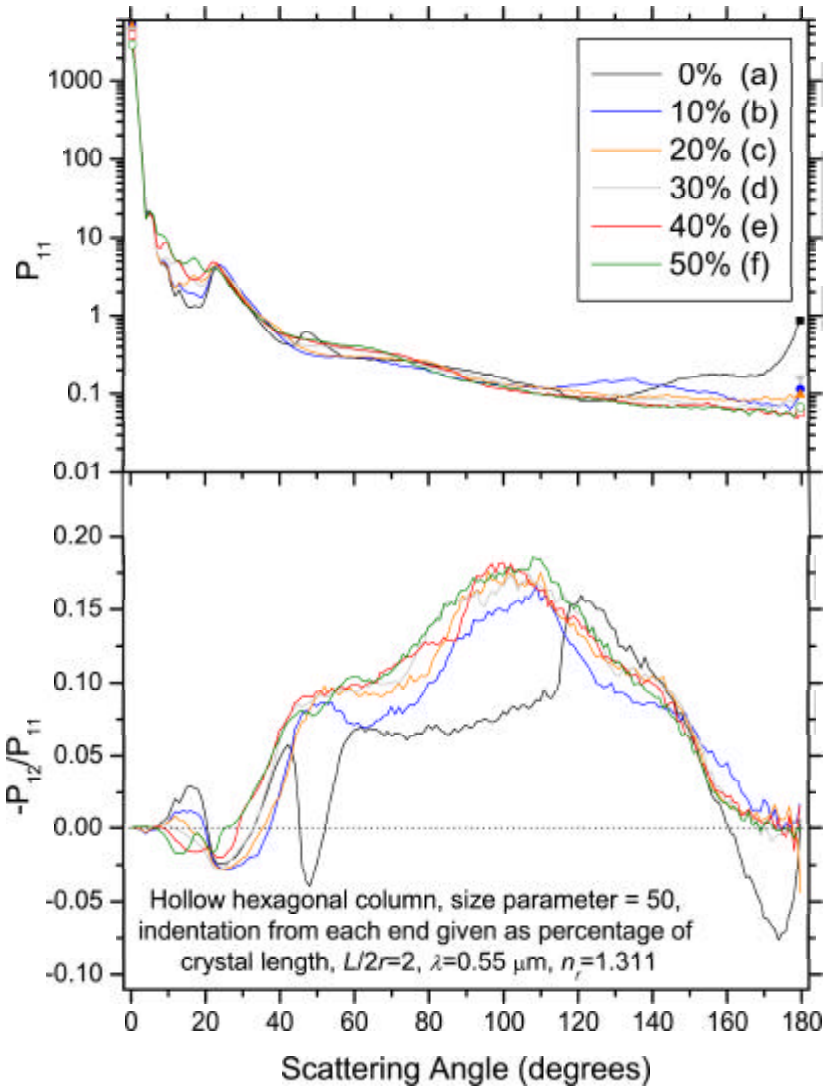

Figure 5.5: Phase function and degree of linear polarization for a hollow hexagonal column of size parameter 50 and $L/2r = 2$ at $\lambda = 0.55$ μm with increasing indentation. Labels (a-f) correspond to figure 5.4. The indentations from each end are measured as a percentage of crystal length.

that limits halo formation, rather than the hollow features alone.

Crystal Label	Indentation	Prism Angle	Halo Angle
b	10%	65.21	24.68
c	20%	47.27	16.15
d	30%	35.82	11.73
e	40%	28.43	9.13
f	50%	23.41	7.44

Table 5.1: The five hollow columns studied in section 5.3 will produce small angle halos due to rays interacting with a prism facet and a neighbouring triangular facet. The prism and halo angles for the five crystals are given for the case of $n_r = 1.311$, along with crystal labels and indentation values that correspond to those in figures 5.4 and 5.5.

The triangular facets in the hollow crystals allow new halo ray paths to exist, most notably rays refracting through a prism facet and its neighbouring triangular facet (and vice versa). Considering GO, light refracting through such facets are subject to a minimum deviation angle. This leads to a scattering maximum near the angle of minimum deviation, also known as the *halo angle*. One can predict the halo angle for a given ray path if the angle between the facets (the *prism angle*) and the refractive index of the medium is known. Equation 5.2 gives the relationship between the prism angle σ, the halo angle δ and the refractive indices inside and outside the crystal, n_{prism} and n_0 respectively. The equation can be derived by applying Snell's law twice and calculating the extreme case for the angle between the incident and exiting ray. Test cases for the equation are the 22° and 46° halos for an ice crystal. The former has a prism angle of 60° which gives a halo angle of 21.92°. The latter has a prism angle of 90° which gives a halo angle of 45.95°.

$$\delta = 2 \arcsin\left(\frac{n_{prism}}{n_o} \sin\left(\frac{\sigma}{2}\right)\right) - \sigma \tag{5.2}$$

The halo angles due to prism-triangular facet interactions for the various indentations considered in the case above are given in table 5.1 using a refractive index of $n_r = 1.311$ for ice. Referring back to figure 5.5, these halos can all be found in the phase function profiles at the predicted halo angles, although the 24.68° halo is difficult to identify due to its proximity to the 22 ° halo. They can also be seen in the DLP results by their negative nature but it is their effect of the overall shape rather than specific peaks that can be identified. As

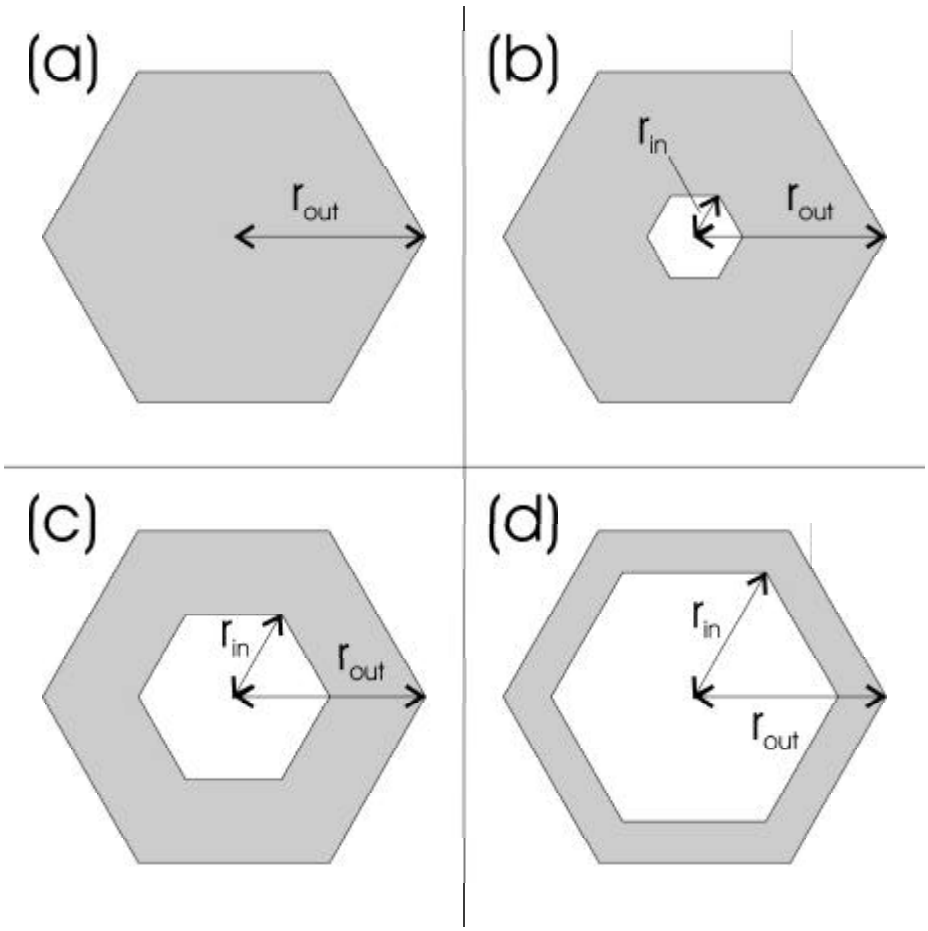

Figure 5.6: Cross section views of four hexagonal tubes. (a) $r_{in} = 0$, hexagonal column (b) $r_{in} = 0.25 r_{out}$ (c) $r_{in} = 0.50 r_{out}$ (d) $r_{in} = 0.75 r_{out}$.

mentioned above, it is possible that ray paths such as these can explain some halos at unusual angles that are observed in the atmosphere [118].

5.4 Hexagonal Tubes

Sometimes referred to as hollow columns [23], hexagonal tubes are the more extreme case of the hollow ended columns discussed above. They are also contained in the ice crystal classification scheme by Magono and Lee [115]. Hexagonal tubes are important because they share similarities with hollow columns where not all of the basal facet is indented. These more complex hollow columns will not be considered in this thesis. The presentation of results for hollow

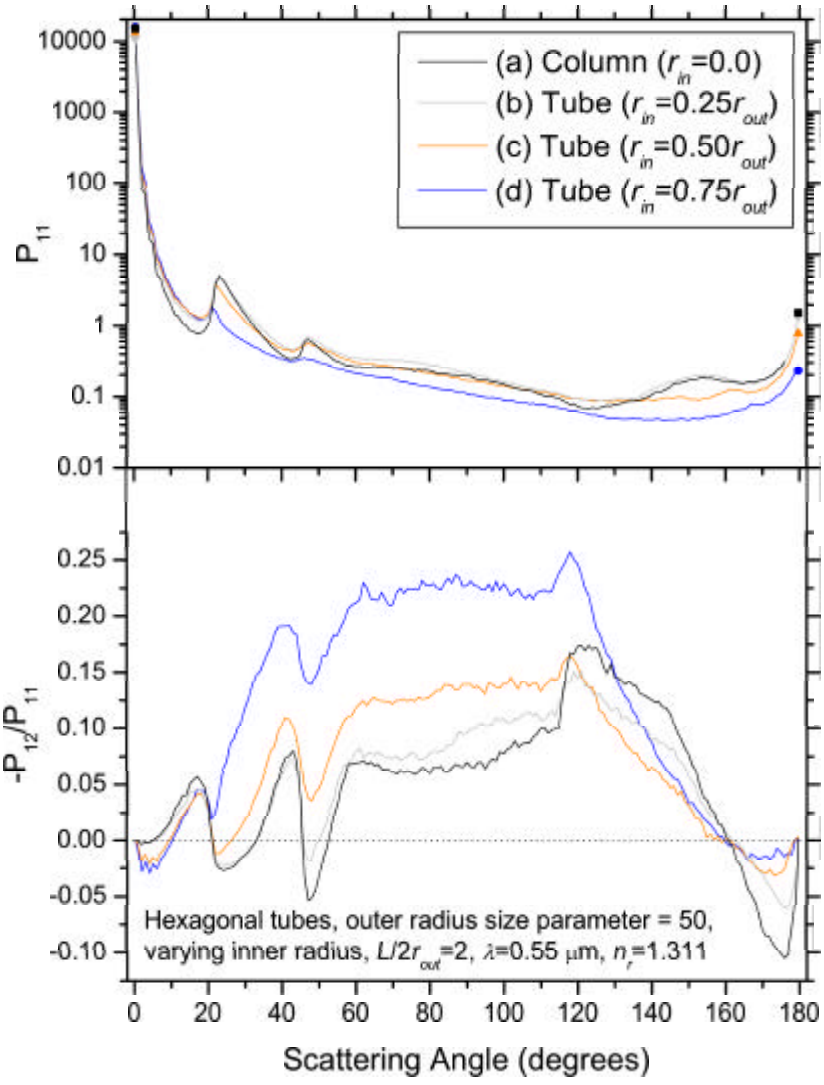

Figure 5.7: Phase function and degree of linear polarization for hexagonal tubes of outer radius size parameter 50 and $L/2r = 2$ at $\lambda = 0.55$ μm with various values of inner radius. Labels (a-d) correspond to crystal diagrams in figure 5.6.

columns in the last section and for hexagonal tubes in this section illustrates the ability of the RTDF model to handle them. Study of geometries such as hexagonal tubes and the more complex hollow columns using RTDF required the addition of support for coplanar adjacent facets, as discussed in section 3.3.2.

The hexagonal tube is defined by an outer and inner radius. The cross sections of four hexagonal tubes are shown in figure 5.6. The outer radius is the same as that for a solid column and is constant for all four cases in the figure. The inner radius, r_{in}, defines a hexagonal column of air within the solid column. Case (a) in figure 5.6 has $r_{in} = 0$. This is a standard hexagonal column. The other three cases have r_{in} defined in terms of the outer radii, r_{out}. The r_{in} values are (b) $0.25r_{out}$, (c) $0.50r_{out}$ and (d) $0.75r_{out}$.

Figure 5.7 shows the phase function and DLP for the four cases in figure 5.6. The RTDF results for hexagonal tubes vary little in terms of ray features from the hexagonal column. As the radius of the hollow centre increases, the halos and internal reflection ray paths are greatly reduced resulting in a reasonably featureless phase function for the most extreme case and a strongly positive DLP as the external reflections dominate. In the GO phase function and DLP for hexagonal tubes presented by Macke [23], a sharp peak at exactly 120° is highlighted and is caused by a 'light-guide' effect with rays internally reflecting several times from the inner and outer prism facets. This effect is totally smoothed out using RTDF.

5.5 Droxtals

Small crystals are very important to the radiative properties of cirrus [119]. It is often the case that small crystals below 50 μm are classified as ice spheres when detailed information regarding their geometry is not available. In-situ imaging instruments such as the CPI [76] are unable to classify these crystals definitively because they do not have the necessary resolution at these very small sizes [10]. It has been suggested that at cloud top crystals form from supersaturated water droplets at cold temperatures so quickly that the crystals do not have time to reach an equilibrium state for the development of normal hexagonal or rectangular facets [120]. As a result it could be that small crystals are more accurately represented by faceted objects such as droxtals [121] which have been observed in arctic ice fog [120]. A droxtal can be defined as a 20 faceted

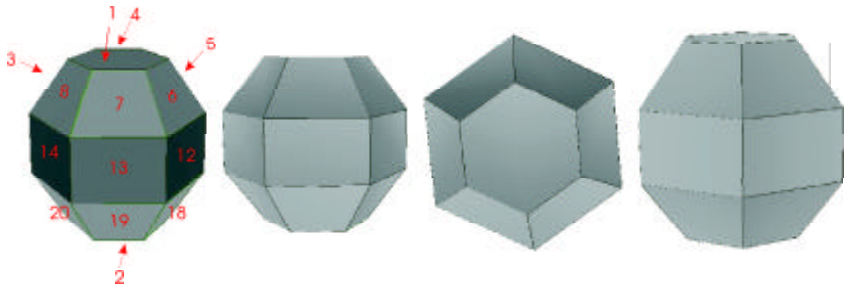

Figure 5.8: An example of a droxtal shown in four orientations. (Left to Right) Overview with facet labels, side view 1, top view, side view 2.

crystal formed from 2 hexagons, 6 rectangles and 12 trapeziums (according to the British definition of a trapezium, known elsewhere as a trapezoid). Figure 5.8 shows an example of a droxtal in four orientations. The facets are numbered in one of the orientations to assist the discussion as it proceeds. Facets 1 and 2 are the hexagonal facets. Facets 3 to 8 are the upper trapezium facets. Facets 9 to 14 are the rectangular facets. Facets 15 to 20 are the lower trapezium facets. According to the geometrical definition of a droxtal given by Yang et al. [121], all of the crystal points lie on a circumscribing sphere. IGO calculations have been published for very small droxtals [121] and very large droxtals [122], although in the latter case the crystal size is in the regime where IGO gives results very close to GO.

Classifying small crystals as spheres could have implications for the radiative properties of a model cloud. Figure 5.9 compares the phase function and DLP for a sphere of size parameter 50 at $\lambda = 0.55$ μm calculated using a Mie theory code [13] to that of an equivalent droxtal calculated using RTDF. The droxtal is formed so that the circumscribing sphere is identical to the calculation sphere and so that the sphericity is maximised by volume (the volume of the droxtal is as close as possible to its circumscribing sphere). It was found that maximising the sphericity by surface area gives very similar results. Both spheres and spheroids were considered but spheroids with realistic levels of deformation do not significantly change the results. A second form of Mie result is included, a size averaged result that is calculated in the same way as the size averaged SVM result in section 3.4 that minimises interference effects. Given the lack of interference effects in the RTDF model, it provides a more valid comparison.

The agreement between Mie theory and RTDF for the droxtal is good in the phase function in certain areas. However, note the difference in the 70 °-140 °

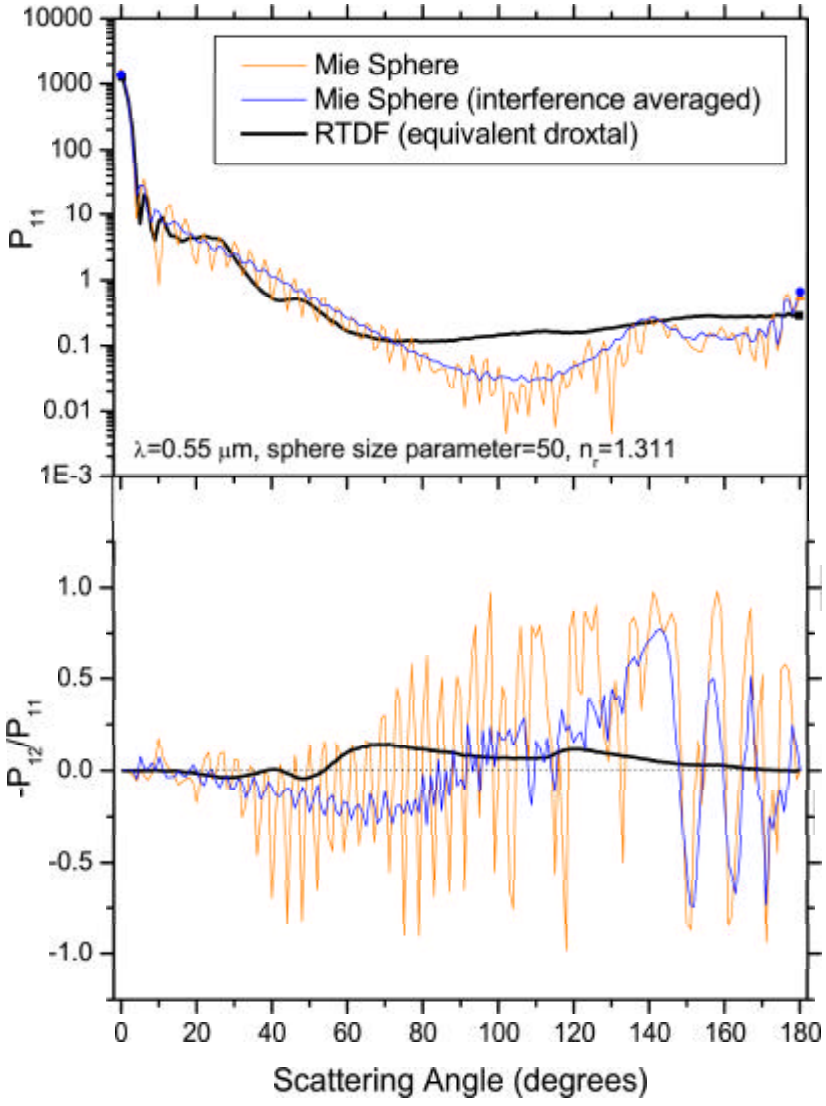

Figure 5.9: Phase function and degree of linear polarization for a Mie theory sphere of size parameter 50 at $\lambda = 0.55$ μm compared to an equivalent RTDF droxtal. The sphericity of the droxtal is maximised by volume. Also present is an interference averaged sphere result to allow the best possible comparison.

range. The DLP profile for the droxtal bears little resemblance to the sphere result, even exhibiting the wrong sign in regions where the phase function gives reasonable agreement. The figure illustrates how the scattering properties of a sphere can be very different from that of a droxtal-like crystal, particularly in the side scattering region. This could have implications for future particle instrumentation design because such differences could enable spheres and droxtal-like particles to be distinguished. The difference in scattering properties means that correct particle characterisation for small crystals could be very important for radiative transfer modelling [10].

The droxtal geometry by Yang [121] uses the radius of the circumscribing sphere and two angles to define the positions of the crystal points. By varying the two angles, the angle between the trapezium facets and the hexagonal and rectangular facets respectively will alter. One should not disregard the possible existence of noteworthy amounts of more elongated or flattened droxtals where the crystal points do not all lie on a circumscribing sphere. For example, by constructing the facet angles from crystal directions and adopting preferred orientations, the droxtal can be used to explain halos of unusual radii [123]. The authors referred to the crystals as 'pyramidal' crystals, a term also used by Goldie et al. [96] who used flattened droxtals to help explain a concentric ring halo display. Clearly the angle of the trapezium facets defines the angular position of any halos that are created.

One can predict the possible halo angles for the droxtal considered above using the halo angle formula discussed in section 5.3, equation 5.2. There are seven theoretical halo ray paths that involve two refractions through the crystal. They are summarised in table 5.2 which provides the prism angle, halo angle, and a list of the combinations of interacting facets that create each halo. The facets are labelled using the numbering system introduced in figure 5.8. Note that these halo angles are only valid for a droxtal with sphericity maximised by volume and hence for the given prism angles only. The seven halos will exist to some degree for any droxtal-like crystal following the ray paths listed in the table but the prism angles and consequently the halo angles will change.

Figure 5.10 shows the phase function for an equivalent case to figure 5.9 except that the circumscribing sphere has a size parameter of 100 rather than 50. The larger resulting droxtal creates halo peaks that are more prominent. The angles corresponding to the halo angles are marked and labelled to correspond to table 5.2. Halo A is clearly visible. Halo B is a smaller peak but can still be identified. Halos C and D appear to have combined given their angular

Halo Label	Prism Angle	Halo Angle	Facet A	Facet B
HALO A	34.01	11.08	9	6 or 18
	-	-	10	7 or 19
	-	-	11	8 or 20
	-	-	12	3 or 15
	-	-	13	4 or 16
	-	-	14	5 or 17
HALO B	48.97	16.85	3	17 or 19
	-	-	4	18 or 20
	-	-	5	15 or 19
	-	-	6	16 or 20
	-	-	7	15 or 17
	-	-	8	16 or 18
HALO C	55.99	19.97	1	15,16,17,18,19 or 20
	-	-	2	3,4,5,6,7 or 8
HALO D	60.00	21.92	9	11 or 13
(22° halo)	-	-	10	12 or 14
	-	-	11	9 or 13
	-	-	12	10 or 14
	-	-	13	9 or 11
	-	-	14	10 or 12
HALO E	65.51	24.85	9	5,7,17 or 19
	-	-	10	6,8,18 or 20
	-	-	11	3,7,15 or 19
	-	-	12	4,8,16 or 20
	-	-	13	3,5,15 or 17
	-	-	14	4,6,16 or 18
HALO F	90.00	45.95	1	9,10,11,12,13 or 14
(46° halo)	-	-	2	9,10,11,12,13 or 14
HALO G	91.77	48.75	3	5 or 7
	-	-	4	6 or 8
	-	-	5	3 or 7
	-	-	6	4 or 8
	-	-	7	3 or 5
	-	-	8	4 or 6
	-	-	15	17 or 19
	-	-	16	18 or 20
	-	-	17	15 or 19
	-	-	18	16 or 20
	-	-	19	15 or 17
	-	-	20	16 or 18

Table 5.2: The prism angle, halo angle and involved facets for the seven droxtal halos for a droxtal with sphericity maximised by volume at a wavelength of $\lambda = 0.55\ \mu$m ($n_r = 1.311$).

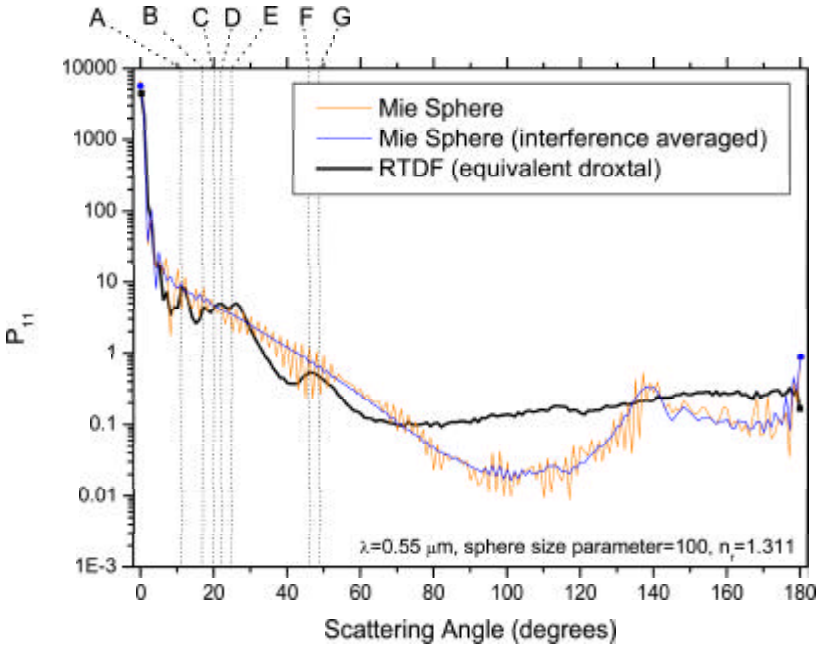

Figure 5.10: The phase function for a Mie theory sphere of size parameter 100 at $\lambda = 0.55$ μm compared to an equivalent RTDF droxtal. The sphericity of the droxtal is maximised by volume. Also present is an interference averaged sphere result to allow the best possible comparison.

proximity with Halo D being the most dominant. Halo E can be seen at a slightly larger scattering angle than expected. It should be noted that the halo angle is the angle of minimum deviation so the fact that halos can appear with small backward shifts in location should not be a surprise. The strong halo F is clearly visible with the weaker halo G helping to widen its peak.

As mentioned above, if the geometry of the droxtal is modified then some of the halo angles will change. The seven halos will however all still exist. Halos D and F will not change position because the angles between the facets involved (the rectangular and hexagonal facets) will remain constant. The angular positions of the other five halos depend upon the sphericity of the droxtal. It is therefore possible to explain almost any unusual angle halo phenomena using droxtal like crystals by choosing the correct trapezium facet angles. Consequently, further studies into the reasons for the formation of such crystals and subsequently the likely or most common trapezium facet angles would be of assistance in halo studies. Better understanding of droxtal formation would have implications for

the important smaller droxtal like crystals mentioned at the beginning of this section.

5.6 Bullets and Rosettes

Alongside hexagonal columns, *rosettes* have been described as a primary cirrus crystal habit [124]. They are most common in the mid to lower regions of cirrus clouds, away from the crystal formation levels at cloud top [79] and at temperatures above -40° [77]. Rosettes are collections of hexagonal arms growing outwards from a common growth centre. Rosettes form from frozen water droplets that grow through vapour deposition. If the temperature is low enough then the geometry may develop into a collection of columnar crystals growing outwards. The columns may appear conical or pyramidal in shape at the end pointing towards the growth centre because of competition for water vapour. Images of rosettes formed from hexagonal columns with pyramidal or conical extensions can be found in the literature, for example [61, chapter 2] and [107, 124]. When one of these arms detaches it is known as a *bullet*. This can happen when a rosette enters a region where ice saturation has not been reached. The GO studies by Macke used bullets formed from a combination of a hexagonal column and a hexagonal pyramid of the same cross section [23, 34]. They looked similar to figures 5.11a and 5.11b. Bullets of this form are also common in other studies, for example [35, 97].

One can create rosettes from model bullets by connecting them together at their pointed ends, a geometry type whose GO scattering properties have been considered by various authors [23, 35]. This formation process is actually in reverse because as already stated, bullets in nature form following detachment from a rosette. Iaquinta et al. [125] suggested a bullet formed from ten facets with pentagons forming the head. A model of such a bullet can be seen in figures 5.11c and 5.11d. By using such bullets as rosette building blocks, rosettes can be formed that exhibit a tendency for arms to have their long axes approximately 70° apart. Kobayashi et al. [63] found from measurement of crystals that rosettes in nature have a tendency towards arm separation angles of 70°. The authors explained that this angle corresponds to a rosette forming from a cubic ice embryo. Figures 5.11(e-h) show examples of rosettes constructed using the Iaquinta bullets. It has been found that rosettes most frequently consist of three or four bullets [61] but can contain large numbers of arms.

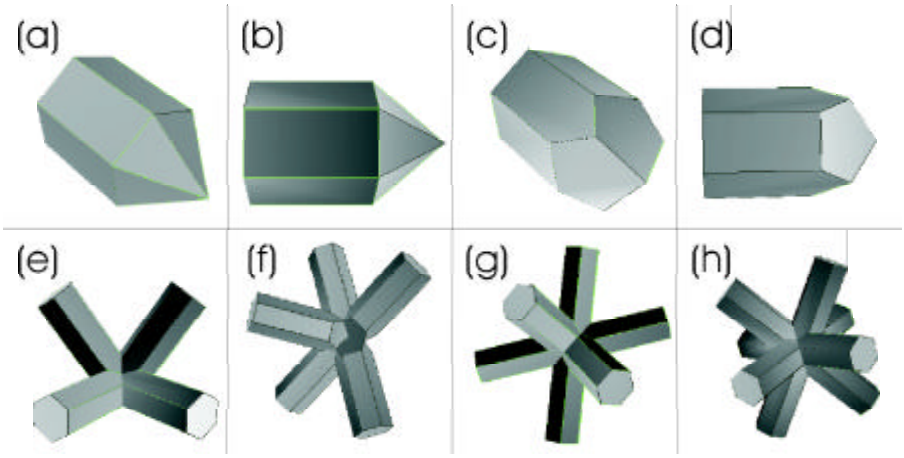

Figure 5.11: A selection of models of bullets and rosettes. (a,b) Bullet as used by Macke. (c,d) Bullet as used by Iaquinta. (e) Iaquinta 4 arm rosette (4-1). (f) Iaquinta 5 arm rosette (5-1). (g) Iaquinta 6 arm rosette (6-1). (h) Iaquinta 8 arm rosette (8-1).

To investigate the scattering properties of bullets and rosettes, figure 5.12 gives the phase function and DLP for an Iaquinta bullet of size parameter 50 with $L/2r = 2$ (L excluding the bullet head) at $\lambda = 0.55$ μm. It is compared to an equivalent hexagonal column (size parameter 50 and $L/2r = 2$) and an 8-1 rosette constructed using the bullet. The rosette geometry is shown in figure 5.11h, as defined in the literature [77, 125].

The results confirm the findings of Macke [34] that a rosette with several arms exhibits scattering properties very close to the individual bullet of which it is composed. The bullet and the rosette noticeably smooth the feature created by the column between 116° and 140° as different internal ray paths are possible. The 46° halo is noticeably smoothed first by the bullet due to one basal facet being removed and then further by the added complexity of the rosette. The fact that the scattering of a rosette so closely resembles that of its constituent bullets would indicate that the scattering properties of a rosette are dominated by the single scattering from individual bullets and that multiple scattering between the arms offers a less significant contribution. The result is emphasised by the complexity of the 8-1 rosette. In the case of rosettes with many short arms, this may not be the case because multiple scattering between arms is more likely. A rosette with arms that do not extend far from the crystal centre will be considered in chapter 6.

The calculations in figure 5.12 assumed that the crystals were oriented randomly

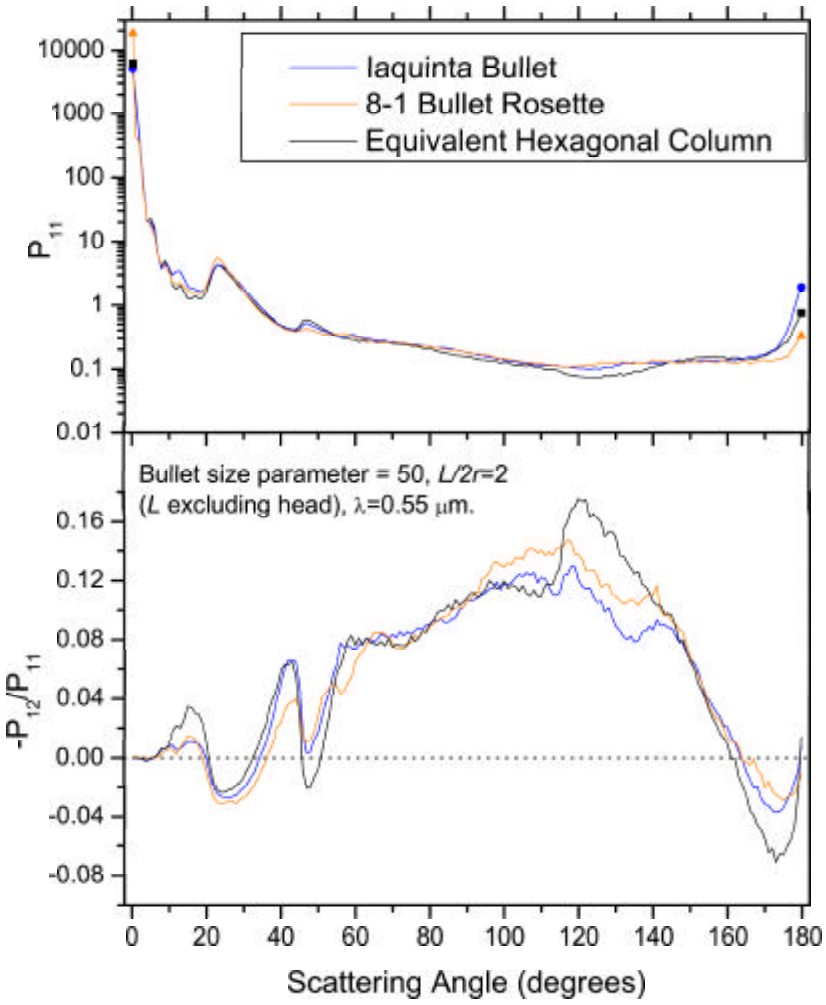

Figure 5.12: The phase function and degree of linear polarization for an Iaquinta bullet of size parameter 50 with $L/2r = 2$ (L excluding the bullet head) compared to an equivalent hexagonal column and an 8-1 rosette (see figure 5.11h). The wavelength is $\lambda = 0.55$ μm.

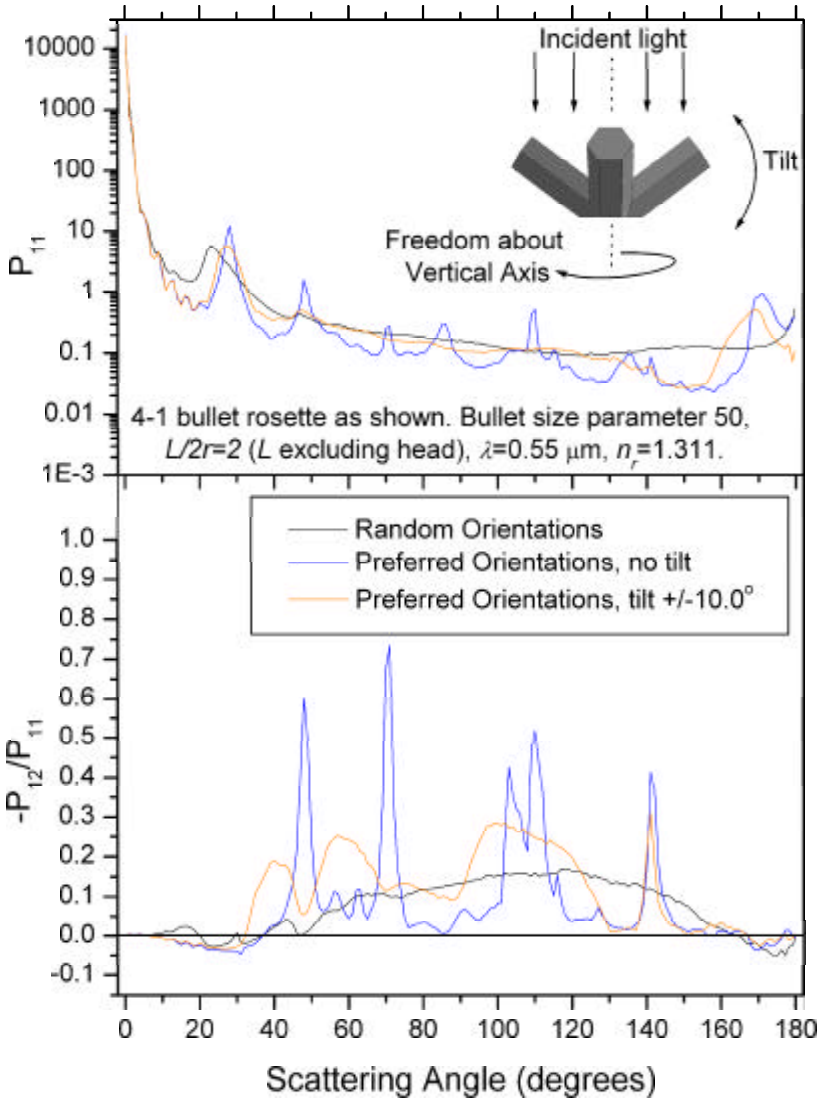

Figure 5.13: The phase function and degree of linear polarization for a 4-1 rosette (see figure 5.11e) constructed from Iaquinta bullets of size parameter 50 and $L/2r = 2$ (L excluding the bullet head) at a wavelength of $\lambda = 0.55$ μm to investigate the effect of crystal orientation. Three cases are considered: Random orientations, preferred orientations and preferred orientations with tilt. For the second and third cases, the solar position is taken to be overhead.

with respect to the incoming light. However, as discussed in section 5.1, particles of a certain size tend to align themselves as they fall except in the most turbulent conditions. The desired alignment is so that the crystal has its greatest possible projected area perpendicular to the direction of fall. For droxtals (section 5.5) or columns with aspect ratios close to unity an averaged orientation calculation is appropriate as the projected area does not exhibit large variation across orientations. For crystals such as longer columns and bullet rosettes a preferred orientation may be more appropriate.

Figure 5.13 provides both preferred and averaged orientation scattering results for the 4-1 rosette that is shown in figure 5.11e. The preferred orientation was found by calculating the cross sectional area for many orientations and selecting the largest via an automatic process. The crystal was then allowed to move freely about the axis in the direction of fall. This is illustrated in the figure. In the results it is assumed that the sun is directly overhead, but any solar position could be used. A third case is considered in the figure where the crystal adopts the preferred orientation but then oscillates through some tilt angle to model natural behaviour due to slight turbulence or instability.

The scattering results change quite significantly for random orientations compared to preferred orientations. Correct use of crystal orientation is therefore very important in modelling work. The use of tilts markedly smooths out peaks in the preferred orientation phase functions although the features are still present at large tilts. A marked difference from the random case persists indicating that modelling of such oscillations is also important. It should be noted that changing the solar position will result in changes to the scattering properties for the preferred orientation cases but the principle of these findings will still hold.

The rosettes considered above were all simplified so that all of the arms were the same length. In considering the scattering of rosettes, it must be remembered that in nature there is almost infinite variability in terms of arm length and the combinations of separation angles.

5.7 Aggregates

As crystals fall through a cirrus cloud, they are susceptible to aggregation. In the lower regions of clouds once crystals have grown to their fullest extent one

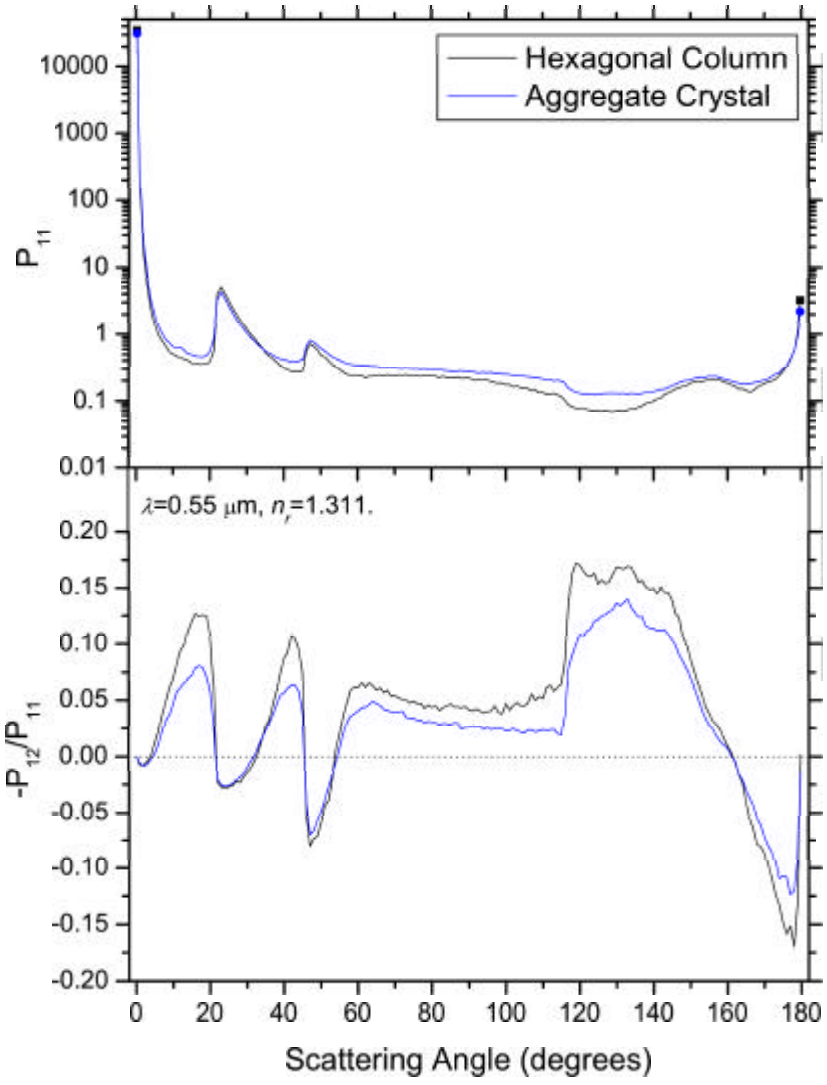

Figure 5.14: The phase function and degree of linear polarization for an ice aggregate model (shown in figure 5.15) compared to a hexagonal column of size parameter 444 and $L/2r = 1.4855$ at a wavelength of $\lambda = 0.55$ μm.

finds larger crystals formed from individual crystals joining together. There are two types of aggregate. The first is an amalgamation of smaller crystals that has no clearly defined growth centres (see below). The second type is an aggregate of rosettes where the constituent rosettes can be discerned, so providing clearly defined growth centres [124].

A discussion of crystal aggregation in cirrus can be found in Kajikawa and Heymsfield [126]. They found that the number of larger aggregates increased as the temperature increased (as the cloud base became closer) for all the cirrus cases that they considered. The process of aggregation depends on many factors. There appears to be a relationship between the crystal size and the probability of two crystals aggregating. Also important is the terminal velocity of the crystals, itself a function of crystal size. After a collision between two particles, it takes a finite time for the crystals to form a physical join and so conditions have to allow contact to exist for a period if aggregation is to be successful. The process of aggregation is complex, and the reader is referred to the literature for a more involved discussion.

Yang and Liou [127] formed a model of an aggregate by using a collection of hexagonal columns and thick plates in close proximity. They include an image of an ice aggregate of the first type discussed above. The aggregate scattering results they provide are calculated using a version of the IGO where a surface roughness factor is introduced to the ray tracing part. The surface roughness component randomly tilts the facet normal during each ray-facet interaction. In some cirrus modelling cases such treatment may be appropriate. The reference provides SEM images of rough ice crystals grown in the laboratory to illustrate the potential existence of rough crystals in cirrus. The phase function due to a rough ice analogue crystal has been measured experimentally [104]. The Macke GO code and hence the RTDF model has a surface roughness capability built in but it has not been used to calculate the scattering properties of the aggregate that is considered in this section. The process washes out halo effects and GO features due to its random nature and does not allow a proper evaluation of the RTDF result. Furthermore, it does not represent the size dependence of diffraction in a systematic way.

Figure 5.14 provides the phase function and degree of linear polarization for an aggregate crystal very similar to the aggregate used in the literature [127] compared to a hexagonal column of size parameter 444 and $L/2r = 1.4855$ at $\lambda = 0.55$ μm whose length and radius are average values for the constituent crystals of the aggregate. The aggregate is composed of eight large hexagonal

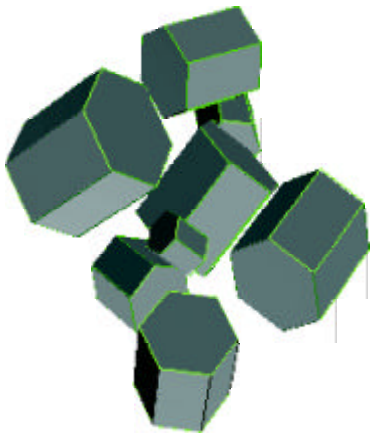

Figure 5.15: The aggregate model discussed in section 5.7.

columns and thick plates, as shown in figure 5.15. The smallest size parameter included is above 200, well into the GO regime. Because the aggregate is made up of a collection of hexagonal crystals, the scattering properties are very close to that of its constituent particles. Note the strong GO nature of the result for both the column and the aggregate due to the large size of the crystals involved. Even large aggregates are not normally associated with atmospheric halos and so this result is not satisfactory. If it can be shown that the majority of aggregates in cirrus exhibit rough surfaces, the surface distortion could solve this problem. However, by definition the constituent crystals in an aggregate are fixed together. Consequently, there is room for a more adequate model of atmospheric aggregate geometries exhibiting actual connections between crystals. Such models could then take into account surface roughness to better represent cirrus ice if necessary.

Chapter 6

Ice Analogue Geometry Reconstruction

The study of theoretical light scattering results in cirrus such as those from the RTDF model goes hand in hand with the study of crystal growth and development. Ulanowski et al. [9] have developed ice analogue crystals that have very similar optical properties to ice but that are stable at room temperature. The crystals are sodium fluorosilicate grown from solution. Sodium fluorosilicate has a refractive index that is negligibly different from that of ice at visible wavelengths. Examples of these analogue crystals have enabled realistic laboratory halos which resemble real ice halos to be seen for the first time [104]. The ice analogues were grown in order to determine the single scattering properties of ice crystals experimentally because exact models do not exist, as discussed earlier. This presents an opportunity to make comparisons to the RTDF model, although to do so it is necessary to have knowledge of the crystal geometry. Since the crystals are stable at room temperature, their shape can be studied in great detail using both optical microscopy and SEM. Consequently it has been possible to reconstruct the geometries of a selection of the crystals and create 3D models. In this chapter the method adopted for geometry reconstruction will be discussed (section 6.1) and three crystals that have been reconstructed will be introduced (section 6.2).

A significant advantage of the ice analogues is that the crystals can be used as calibration tools for in-situ particle instruments such as the CPI. A short

discussion of the role of the geometry reconstruction in this area including a brief explanation of the instrument will be given in section 6.3.

An explanation of some modifications required by the RTDF model to consider ice analogue reconstructions will be discussed in section 6.4 and the scattering properties of the crystals introduced in section 6.2 will be presented in section 6.5. At this time, geometry reconstructions of the type discussed here have not been used to make comparisons between the laboratory scattering properties of ice analogue crystals and the RTDF model. However, this is likely to occur in due course. Comparisons have been made using an ice analogue hexagonal column and this will be discussed in detail in chapter 7.

6.1 Mechanics of Reconstruction

Initially it was hoped that partial three dimensional geometries could be quite accurately reconstructed using two or more SEM images with the crystal in slightly different orientations, using standard stereo imaging techniques. However, it was found that the positions of the camera with respect to the crystal could not be determined accurately enough. The optical microscopy images did not present an alternative because they were not of a high enough magnification. Determining the locations of the individual crystal points was therefore ruled out, a task that in any case would have been prohibitively complicated for the more complex crystals.

Many of the ice analogue crystals that resemble cirrus ice have very complex geometries. The common factor between the crystals is an inherent hexagonal structure. This was exploited in the reconstruction process. Crystals were reconstructed using multiple examples of perfect hexagonal columns. SEM images clearly show some of the arms of rosettes are not perfect hexagonal columns, but using such columns was considered an acceptable approximation. A code was written to enable many columns to be placed in the same crystal with much greater control over the rotation and translation of individual arms than for example in the bullet rosette codes which only allow the construction of a collection of predetermined crystal geometries. The resulting code also generates a 3D visualisation of the crystal using Apple's now legacy format Quickdraw3D. This enables fast verification of changes made to the crystal in the input file. The Quickdraw3D technology has also been used to generate the images of crystal models throughout this thesis.

Several ice analogue crystals were reconstructed using this code. The rosette arms were oriented correctly using SEM and optical microscopy images at different orientations as a guide. Relative column sizes were estimated using measurements taken from optical microscopy images. The final reconstructed geometry was scaled to the correct size using an average scale value taken from as many dimension measurements as possible from the optical microscopy images.

Uncertainties were unfortunately introduced due to the human element of reconstructing the geometries using such a process but the results are encouraging as the reconstructions appear to faithfully reproduce the crystals. Examples can be seen in figures 6.1 and 6.2. An interesting point found during this work was that in many cases columns seen on opposite sides of crystals were in fact the same column growing straight through the centre, even in the most complex of crystals such as Gros48. Gros48 is shown in figure 6.1.

6.2 The Reconstructed Crystals

In this study three reconstructed crystals were used. In the following the laboratory names will be used to avoid confusion in future work.

The first crystal is a germ rosette called Gros48. Gros48 is a very compact and complicated germ or budding rosette. The reconstruction of Gros48 contains fifteen hexagonal columns. Figure 6.1 contains a variety of images of Gros48. Figure 6.1a is an SEM image of the crystal which compares well with the reconstruction shown in figure 6.1b. The column that is exposing its basal facet most in the SEM image has a cross section that is not a perfect hexagon. Although opposite rectangular facets appear parallel, the edge lengths of the hexagonal facet are not all the same. Hexagons exhibiting this asymmetry have been referred to as *scalene* hexagons in previous literature [81], a term usually applied to a triangle with three sides of unequal length. The same reference illustrates that such scalene effects exist in ice. An image of Gros48 obtained using optical microscopy is shown in figure 6.1c. Figure 6.1d will be discussed in the next section.

The second crystal considered is a relatively simple three arm rosette called Ros172. An SEM image is shown in figure 6.2a with the reconstruction in figure 6.2b. An alternative view of the crystal using optical microscopy is shown in figure 6.2c. This was in fact the first crystal that was reconstructed and so the

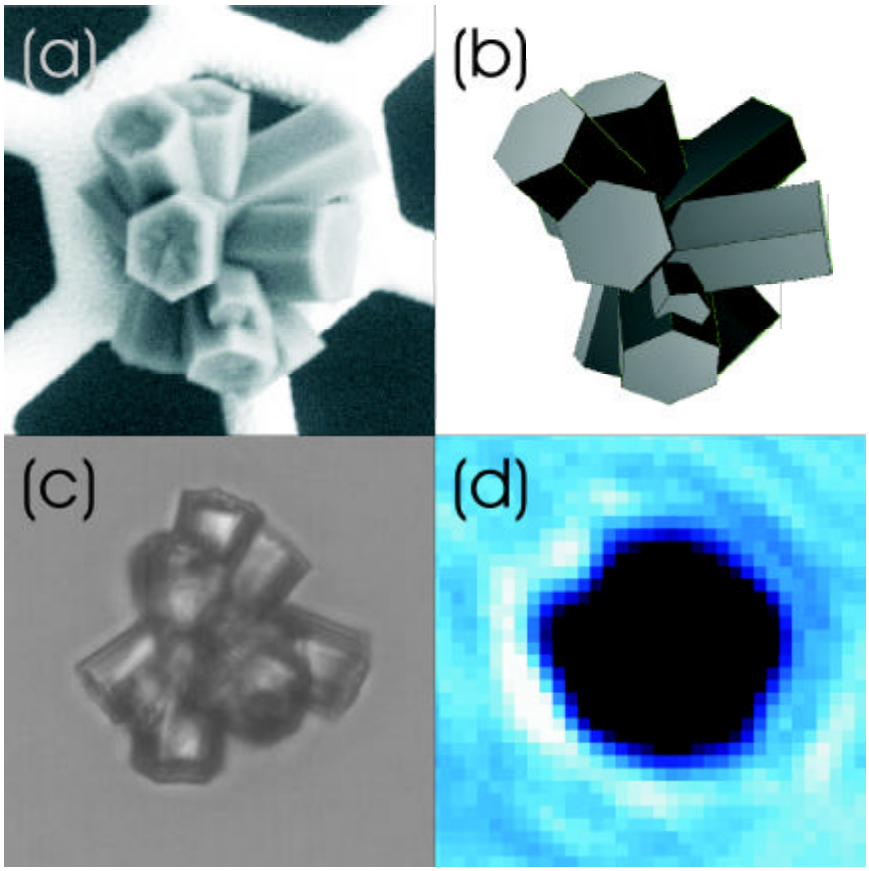

Figure 6.1: The ice analogue crystal Gros48. (a) SEM. (b) The reconstructed geometry. (c) Optical microscopy. (d) CPI image.

test case for the codes involved. The orientations and lengths of the crystal arms are well defined. It is clear from the SEM image that the ends of the rosette arms are not pristine, the end facing out of the page boasting an irregular deformity pattern. The ends that are side on appear to show depressions, noticeable from the apparently curved nature of the ends of the rectangular facets.

The third crystal is a more open rosette called Ros52. This crystal was reconstructed after interest following an experiment using an electrodynamic balance [128] and a laser diffractometer [129] at the University of Hertfordshire. Unfortunately, it was not possible to retrieve the crystal after the experiment and so it was not possible to obtain SEM images of the crystal. The reconstruction proceeded using optical images such as the one shown in figure 6.2d which compares well with the reconstruction in figure 6.2e. Video footage of the crystal captured while it was in the electrodynamic balance was also used to aid the

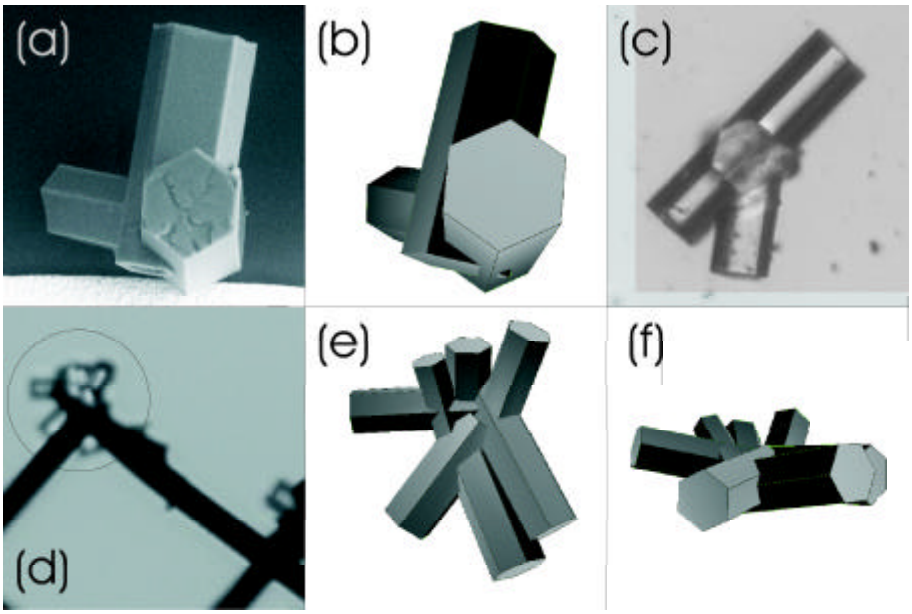

Figure 6.2: The ice analogue crystals Ros172 and Ros52. (a) Ros172 SEM. (b) Ros172 reconstruction. (c) Ros172 optical microscopy. (d) Ros52 optical microscopy, (e) Ros52 reconstruction. (f) Ros52 reconstruction, illustrating the flatness of the crystal.

reconstruction. The video clearly showed that the arms of the rosette almost fall in one plane, so giving a reasonably flat crystal. The reconstruction allows us to study this from any angle, and the flat nature of the crystal is demonstrated in figure 6.2f. The reconstructed geometry includes seven columns.

Values for the maximum dimension, average projected area and volume of the three crystal reconstructions are given in table 6.1. The values given for the projected area and volume were calculated using the methods that will be briefly described in the next section. The maximum dimension is defined here as the largest distance that can be measured in a straight line within the crystal. This quantity, though not the same as the maximum dimension for a specific orientation as used by in-situ particle instruments, offers a demonstration of the size of the crystal.

There are no error values quoted in the table because it would be misleading to quote errors relating to the method of calculation for the maximum dimension,

projected area and volume. They would not reflect the error in the reconstruction process, which is very difficult to quantify. Once the reconstructed geometry is defined, the maximum dimension is a fixed value. The average projected area is obtained by using sufficient orientations to produce a stable value and so by definition the calculation carries no error to two decimal places. The volume calculation of the reconstructed crystal carries a possible staircasing error in the method that it uses, to be explained briefly in section 6.3. The error was found to be of the order of 0.1% or less for the three cases considered. These errors are of little consequence when compared to the errors inherent in the geometry modelling process. The perfect hexagonal column approximation will likely create errors on the volume of the reconstructed geometry compared to the volume of the actual crystal Gros48 of the order of between 5% and 10%. This is an estimate because without more detailed information about the extent of the scalene column features it is very difficult to quantify an error. The human error involved in aligning the columns necessitates large error tolerances. It is estimated that the orientations of the columns are correct to within 5° on average. The sizing of the columns is another large source of error. An error value on the radii or lengths of the individual columns means little given the perfect hexagonal column approximation. The overall size of the crystal is scaled using an average scale value found from dimensions measured using optical microscopy. These measurements were taken from crystal edges that were as close to perpendicular to the direction of observation as possible. They were made by electronically examining the images. The error on each of these values is estimated to be ± 2.25 μm.

Crystal	Max. Dim. (μm)	Avg. Proj. Area (μm^2)	Volume (μm^3)
Gros48	35.06	2323.28	22025.00
Ros172	189.00	1184.11	540797.00
Ros52	47.00	1364.24	6097.00

Table 6.1: Values for the maximum dimension, average projected area and volume of the three reconstructed ice analogue geometries. See section 6.3 for a brief description of the methods used to obtain the values.

6.3 Reconstruction Comparisons to CPI measurements

The CPI is an instrument that captures in-situ digital images of cloud particles and can be used to measure particle size, shape and concentration [76, 130]. The instrument casts shadows of particles on to a one million pixel CCD using a 25 ns pulsed laser diode to prevent blurring due to particle motion. A signal from particle detection lasers that are directed across the particle flow triggers the imaging laser.

The ice analogue crystals offer an opportunity to test the performance of the CPI and the post processing techniques used to detect particle geometry, projected area and volume. Some examples of ice analogue crystals were imaged using the CPI, including Gros48 and Ros172. To make comparisons to the CPI results, it was necessary to be able to find the volumes of the models as well as the projected areas for several orientations that coincided with already held CPI images. The projected areas could easily be determined using the original GO code. The volume posed more of a difficulty as the overlap of individual columns in the centres of rosettes was in some cases great and very complicated (for example, Gros48). The volume of each individual column was calculated in its position in the crystal by dividing it up into volume elements and recording the positions of the centres of the elements. These were then all recorded without duplication and summed to find the volume of the crystal as a whole.

The results of these comparisons have been included in a conference publication. The poster is available online [10]. It was found that when crystals were in good focus in the CPI images, the typical average size errors were only a few percent. Under poor focus, the sizes were significantly overestimated by the CPI. Interestingly, Gros48 produced a quasi-spherical CPI image despite its strong nonspherical nature. This is shown in figure 6.1d. Without prior knowledge, it is not clear that the CPI image shows a rosette. This adds to the discussion in section 5.5, where it was suggested that crystals below 50 μm in size should not automatically be classified as spheres because there is evidence that they are in fact faceted geometries such as droxtals, or in this case germ rosettes. Gros48 with its maximum dimension of around 35 μm is not far below the 50 μm threshold. It is feasible that smaller crystals are droxtal-like with germ rosettes developing as the size increases. In section 6.5 the scattering properties of the reconstructed crystals will be considered and a comparison can then be made between Gros48 and the droxtal properties discussed in section 5.5.

6.4 RTDF Modifications for Reconstructed Crystals

The crystals that have been reconstructed are effectively collections of hexagonal columns that overlap in space. This is in contrast to the geometries discussed in chapter 5 where the geometries are defined as individual closed crystals. For such overlapping collections of crystals there are a number of points that need to be addressed in the RTDF model.

The first is that overlapping crystals will lead to facets inside the crystal that have the same medium on either side. The GO code by Macke [23] does not include support for such facets. Because the RTDF model is built upon the GO code, it too lacks this feature. There are two ways to remedy this situation. First, one could modify the reconstructed geometries so that these internal areas of facets are removed, creating a standard crystal geometry. This is an unattractive proposition as the process to complete this for a crystal like Gros48 would be incredibly difficult. The second option is to modify the RTDF code so that whether a ray is inside or outside the crystal is always known, and more importantly how far into the crystal the ray is. This is achieved by counting rays into and out of each overlapping crystal. This means that when an internal facet is encountered it will be recognised as such. For all of the internal facet interactions, no RTDF deflections are performed and the rays pass straight through with no refraction deflection or reflection. These modifications were implemented by Hesse [131].

The second point to address is the definition of the effective slits in the RTDF model (see section 3.3.1). Let us consider the treatment of Gros48. Being a collection of hexagonal columns, the majority of the rectangular facets will extend from one side of the crystal, through the crystal centre and out of the other side. Using the model code in its standard state, this will lead to the effective slits being defined incorrectly with some being found to be longer than they should be. For example, consider a ray striking a rectangular facet on one of the columns protruding from Gros48. As standard, the code will find one slit across the column and a second along the length of the column. The slit along the length of the column will cover the full length of the column. However, this is incorrect. The slit should be considerably shorter, only covering the length of the column until it enters the central core of the crystal. This was corrected using a simple method where each effective slit is tested to see if it intersects another crystal facet or facet edge. If such an intersection is found, the effective

slit is shortened appropriately.

6.5 Scattering Properties of Reconstructed Crystals

Figure 6.3 shows the single scattering properties of Gros48. Shown for comparison are the scattering properties of an equivalent droxtal (with a diameter equal to the Gros48 maximum dimension given in section 6.2) and a hexagonal column with a length equal to the Gros48 maximum dimension and a radius of 7 μm. This radius value is chosen because all of the columns within Gros48 have radii equal or close to it. The droxtal is formed so that its sphericity is maximised by volume [121].

The phase function of Gros48 for averaged random orientations still exhibits the 22° halo, as one might expect given the nature of the crystals construction. However, it is slightly reduced and less pronounced due to an increase in scattering either side of the halo, when compared to a standard column. The 46° halo has been smoothed out totally. The forward scattering point has been reduced while there is a significant increase in the 2°-20° region. Side scattering has been increased over a wide angular range and the back scattering peak has disappeared.

The phase function of the droxtal shows increased scattering compared to a hexagonal column above around 100°. This is similar to the response of Gros48 in this angular range. In section 5.5, it was found that one could distinguish between spheres and droxtals at scattering angles between 80° and 130° because of the strong signal from the droxtal and the low scattering by the sphere. The same idea extends to Gros48, with an even larger signal between 90° and 110°.

The droxtal phase function exhibits five halos as opposed to the standard two for a hexagonal column. The origins of these were explained in section 5.5. As discussed in that section, the location of these halos depends upon the sphericity definition of the droxtal and so the halos will move or may not be formed at all for less regular small quasi-spherical crystals. However, given that some low angle halos will be formed, the increase in scattering for Gros48 in the 2°-20° region compared to a hexagonal column suggests a similarity between Gros48 and all droxtals that have close to spherical characteristics.

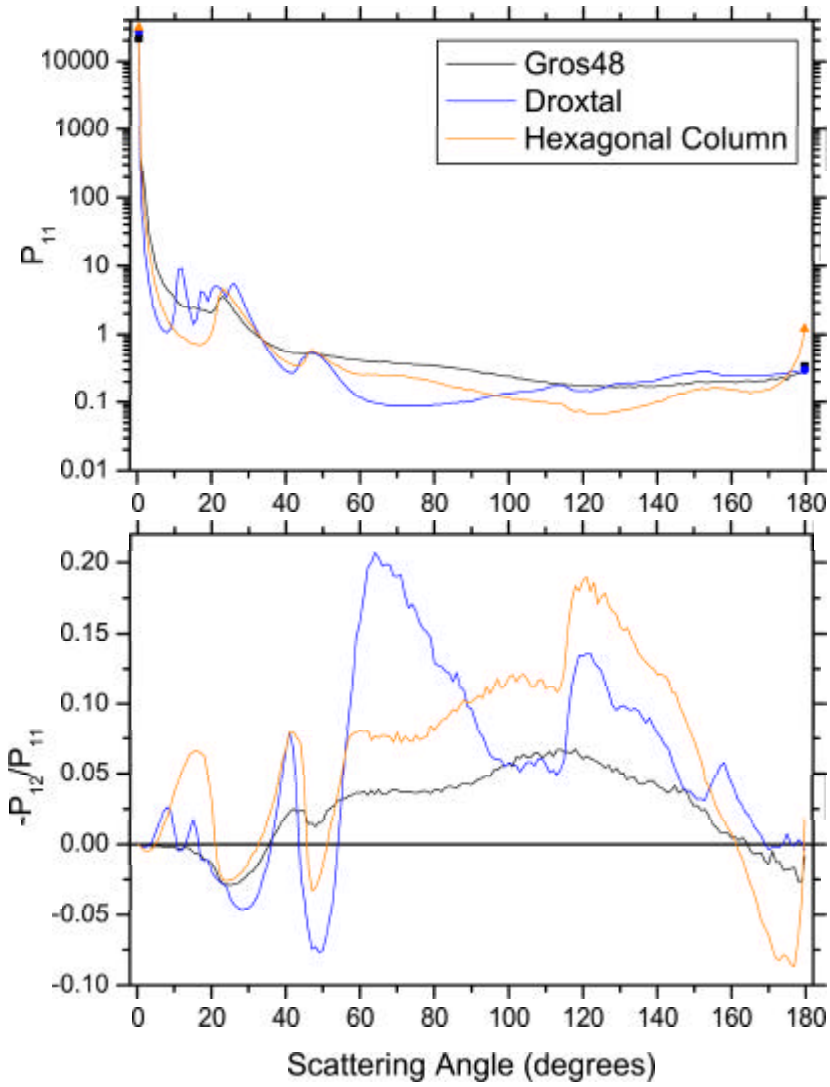

Figure 6.3: The phase function and degree of linear polarization for the reconstructed geometry Gros48 compared to an equivalent droxtal of radius 35.06 μm (sphericity maximised by volume) and a hexagonal column of length 35.06 μm and radius 7 μm.

The DLP for Gros48 shows more similarity to the hexagonal column than to the droxtal. Again, given the nature of the crystal construction, this is not surprising. Across the profile the DLP for Gros48 is less polarizing than the droxtal or the hexagonal column with all features being smoothed out to some extent. The 22° halo is similar to the hexagonal column, though considerably wider in nature. This causes the very low polarization forward of the 22° halo, a significant difference when compared to the hexagonal column. The smoothing out of the 46° halo is confirmed by only a very small negative polarization contribution. The strong feature at 116° is present for both the droxtal and the hexagonal column. It is caused by ray paths involving transmission through the crystal via one total internal reflection not being possible above 116°, so suddenly removing their negatively polarizing effect above 116° (see section 4.2). It is not present for Gros48, therefore the strong positive polarization due to external reflections that provides the positive jump observed for hexagonal columns and droxtals is smoothed out significantly. The neutral point has not moved, indicating that the crystal is a column-like rather than plate-like crystal, according to the discussion in section 5.1. Finally, the strong negative polarization peak at back scattering observed for hexagonal columns is lessened significantly. The strongly negatively polarizing internally reflecting ray paths involving perpendicular prism and basal facets that are responsible occur less often due to shorter prism facet lengths and the increased complexity of the crystal.

The lack of similarity between the DLP for Gros48 and a droxtal illustrates the importance of improved knowledge of the crystal geometries at smaller sizes in cirrus. Modelling smaller crystals as droxtals may be equally as incorrect as using spheres, depending on the scattering properties being studied and the particular cirrus case at hand.

Figure 6.4 compares the scattering properties of Ros52, Ros172 and a hexagonal column of Ros52 maximum dimension length and radius 4.2 μm. This value is the average radius of columns within Ros52. It should be noted that all of the reconstructed crystals in this chapter are larger in size than the crystals studied in chapter 5. As larger crystals are considered, diffraction becomes less important and so increasingly GO-like scattering features are observed. Gros48 did not resemble GO patterns for a hexagonal column due mainly to the complexity of the crystal but also because it is the smallest of the three crystals.

One can see that the phase functions of Ros172 and Ros52 are both very similar to that of a hexagonal column, boasting 22° halos that are sharp, resembling the GO result for a hexagonal column in chapter 4. In the case of Ros52, there

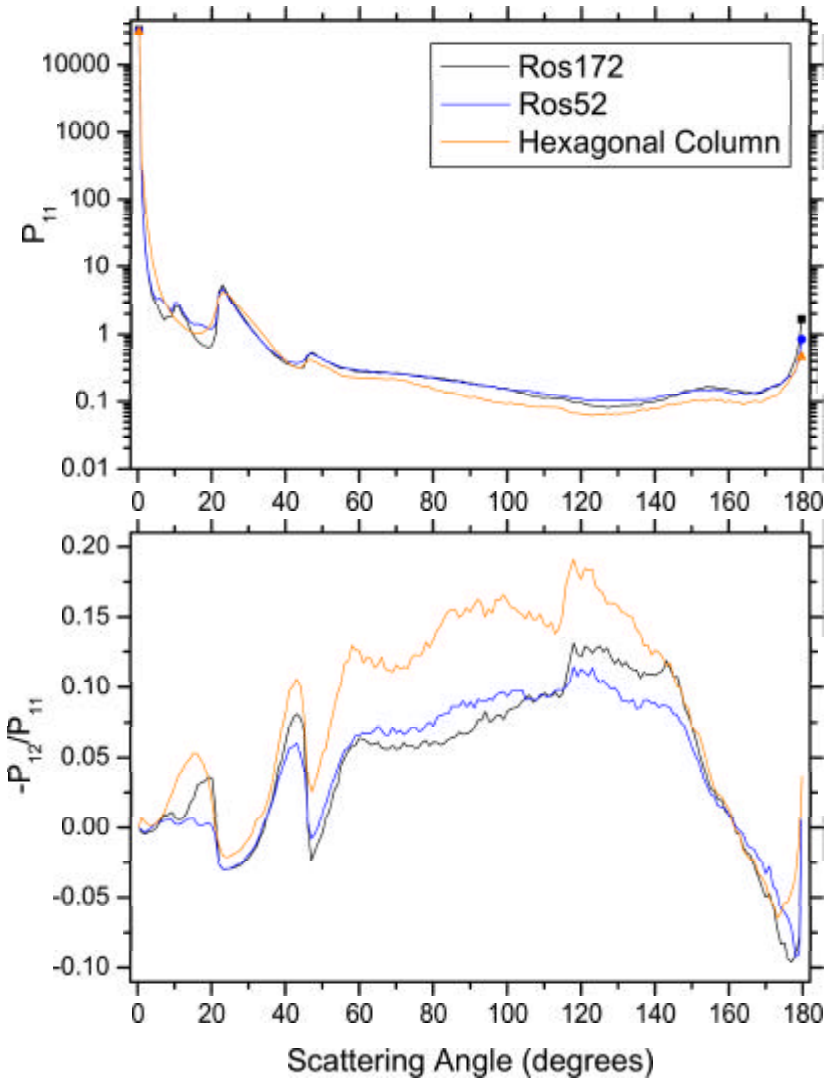

Figure 6.4: The phase functions and degrees of linear polarization for the reconstructed geometries Ros52 and Ros172 compared to a hexagonal column of length 47 μm and radius 4.2 μm.

is some spread of the halo towards forward scattering. The 46° halos exhibit the familiar rounding due to the RTDF model. Both crystals show a small angle halo peak at around 10°. This is created by rays refracting through two rectangular facets that are separated by around 30°, each contributing facet being a part of a different arm. Just as prism facets separated by 60° give a minimum refraction deviation of 22°, facets separated by 30° give a minimum deviation of 9.66° (see section 5.3). It is interesting that the feature is present for crystals of different geometries, which may indicate a tendency of the ice analogue crystals to grow arms at certain separations. A halo peak at 9° has been observed experimentally using collections of ice analogue crystals [104]. Equally possible is that the reconstruction halos are just coincidence and a consequence of the geometry reconstruction method. There would need to be a significantly wider survey of ice analogue crystals to investigate this.

There is slightly increased side and back scattering for both crystals compared to the hexagonal column. The hexagonal column chosen has quite a large aspect ratio and as a result the 46° halo is significantly smoothed.

The degree of linear polarization results for Ros172 and Ros52 also closely resemble the hexagonal column. The 10° halo is again visible, with a small negatively polarizing contribution. The spread of the 22° halo for Ros52 towards forward scattering results in neutral polarization up to near 20°, similar although not as severe as the equivalent effect seen for Gros48. The weaker 46° halo for the hexagonal column is confirmed and the overall smoothing of the polarization for the reconstructed crystals is clearly visible.

The similarity between the scattering properties of Ros52, Ros172 and a hexagonal column is as a result of the use of hexagonal columns in the reconstruction of the geometries. The reasonably simple and open nature of these rosette examples allows single scattering from the crystal arms to dominate, particularly in the case of Ros172. This is in contrast to Gros48, although as shown in figure 6.3, the hexagonal column nature still persists in many features in the degree of linear polarization.

The three reconstructed crystals introduced here will be used in chapter 8 where the RTDF model will be used alongside a radiative transfer code to make comparisons to aircraft observation data. An attempt will be made to assess the degree to which such geometries are representative of cirrus ice geometries. These single scattering properties will be referred back to from that chapter.

Chapter 7

2D Scattering Patterns

All of the angular intensity distributions that have been considered so far have been in the form of a phase function. Phase functions are functions of one variable, the polar angle θ. In producing this standard form of scattering result, there is an averaging over the azimuthal angle ϕ that leads to some information regarding scattering direction being lost. One of the benefits of using a ray tracing based method is that it is computationally reasonable to preserve both the θ and ϕ angles. Having such information not only provides a full description of the scattering but also allows the scattering patterns to be projected in two dimensions on to a virtual screen or an array of sensors at some distance. This is something that can be recreated in the laboratory or in principle incorporated into an instrument. In this chapter, results generated by the RTDF model that are in this 2D scattering pattern form will be presented.

In the first part the model results will be compared to an experiment involving an ice analogue hexagonal column in fixed orientations. As shown in earlier chapters, the fundamental task of testing the model is not simple. There are no light scattering models that one could call exact that can be applied in the size applicability range of the RTDF model. Verifying the model by comparing to laboratory results is an alternative. Performing light scattering experiments in the laboratory using individual real ice crystals is very difficult because temperature and humidity need to be controlled, although it is possible [85]. As discussed in chapter 6, the ice analogue crystals developed at the University of Hertfordshire provide a unique opportunity to study and reconstruct crystal geometries. Equally important from the current perspective is the ability to

perform a light scattering experiment for a fixed crystal orientation that can be both studied over some period of time and repeated.

Section 7.1 will include details of the laboratory apparatus used to obtain photographs of ice analogue light scattering patterns. The method used to create the 2D scattering patterns using the model which can be compared to the photographs will be described in section 7.2. Results will be presented in section 7.3. These will include comparisons for a hexagonal column in six orientations illustrating how the scattering patterns change from near perpendicular incidence to near basal incidence (section 7.3.1). There will also be two studies of orientation comparisons that are more in depth in sections 7.3.2 and 7.3.3.

In the second part of the chapter, it will be shown that the 2D scattering patterns can be more than just a model verification tool. They are potentially very useful in the development of in-situ particle characterisation instruments. This will be explained and demonstrated in section 7.4.

7.1 Laboratory Methods

The laboratory equipment was assembled as shown in figure 7.1. An ice analogue hexagonal column of length 61 μm and diameter 15 μm was mounted on a long 6 μm carbon fibre using high temperature epoxy. The carbon fibre was attached to a supporting arm which in turn was connected to a rotation stage. Using this support structure, the crystal was suspended in the beam of a 15 mW He-Ne laser of wavelength 612 nm. The inclusion of a rotation stage made it possible to vary the orientation of the crystal. The forward scattering pattern was projected onto a flat screen normal to the beam at a distance of 15 mm. The screen was transparent and so allowed the scattering pattern to be viewed from both sides. A Sony DSC-S75 digital camera was mounted behind the screen to photograph the resulting scattering patterns. A beam stop was placed on the screen to shield both the camera and the central region of the scattering pattern from the incident laser beam. Small circular apertures were placed between the lens and the screen to help remove light that is due to internal reflections from the two surfaces of the focussing lens that is positioned immediately in front of the laser. To minimise diffraction effects, more than one aperture is used with the second being larger than the first.

Figure 7.2 shows four images of the crystal that was investigated in the exper-

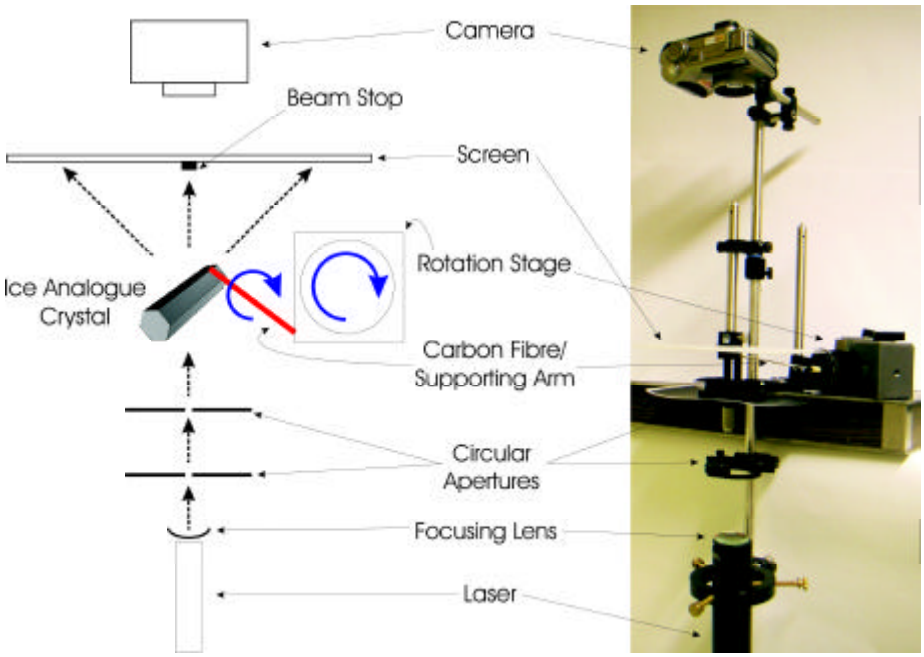

Figure 7.1: A photograph and a diagram of the laboratory apparatus used in the fixed orientation light scattering experiments.

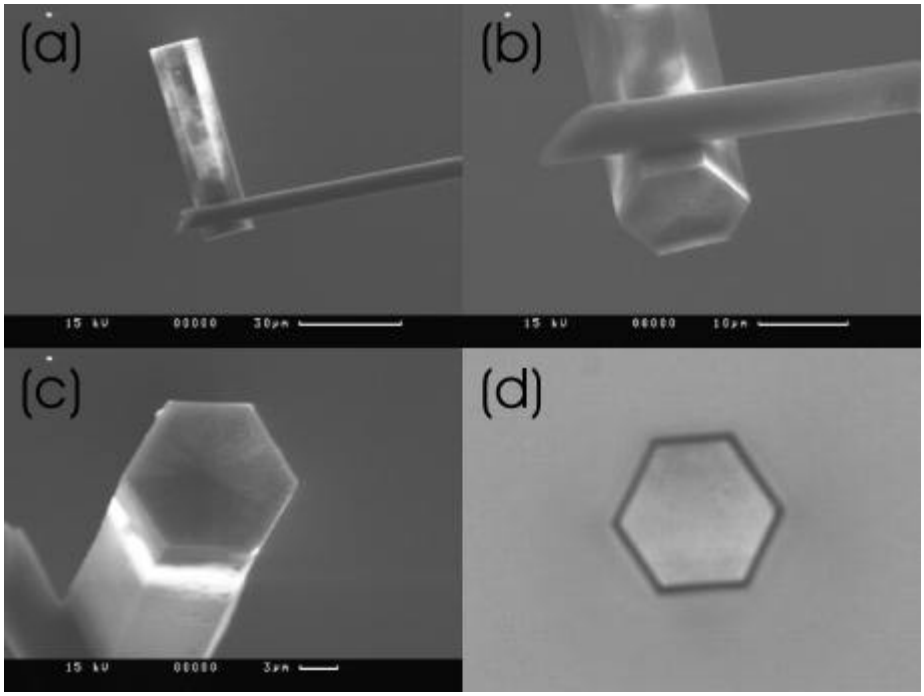

Figure 7.2: One optical microscopy and three SEM images of the crystal investigated in the experiment. (a) SEM side view showing the carbon fibre. (b) SEM end view. (c) SEM opposite end. (d) Optical microscopy end view.

iment. Figures 7.2(a-c) are SEM images. A nonconducting material such as the ice analogue column would normally be coated in a conductive metal to improve the image. However, in this case the images were taken without any coating. Such a coating would have allowed a detailed view of the crystal facets but it would also have meant that the crystal could not be used in scattering experiments again. The bright and dark areas in the SEM images are caused by inhomogeneous charge distributions building up on the surface of the crystal and so are an artefact of the SEM process. Figure 7.2a is a side view showing clearly the supporting carbon fibre. One can see that the crystal facets are well defined with no obvious rounding of the facet edges. The hexagonal facets at either end appear to be close to if not exactly perpendicular to the long axis of the column. One should note that this is not the case for the carbon fibre, which is attached at an angle of several degrees. Figures 7.2b and 7.2c show the ends of the crystal. The change in brightness across the facet suggests that the column ends may have slight indentations, similar to those discussed in section 5.3. This is further supported by the very slight curvature near the ends of the facet edges (noticeable in figure 7.2c on the left end of the upper facet edge of the hexagonal facet). Significant defects are not present, however. Figure 7.2b suggests that the cross section of the column may not be a perfect hexagon. This is confirmed by the optical microscopy image, figure 7.2d, which shows that the cross section is a scalene hexagon (see section 6.2).

To create RTDF results, it is necessary to model the geometry of the crystal. In the case of this experiment, the crystal is modelled as a perfect hexagonal column of length 61 μm and radius 7.5 μm. The images in figure 7.2 show that the column is not perfect, particularly the unequal lengths of the hexagonal cross section. This scalene nature should be noted but should not cause undue concern. The effect of this is likely to be small given that it is not a severe asymmetry. Any improvements that are possible from more exact geometry modelling are not likely to be great. From the SEM images it is known that the facets are well defined and that the deformities at the column ends are not severe so a perfect column is an acceptable approximation.

Having modelled the geometry of the crystal, it is now necessary to model the orientations of the crystal in the experiment so that the RTDF results can be generated. An analytical prediction of the orientation was sought, but found to not be possible due to the complexity of the problem. From figure 7.2a it is possible to see that the carbon fibre was attached to a prism facet near the end of the column at an angle of around 5° from perpendicular to the column axis. The carbon fibre lies parallel to the plane of the facet that it is attached

to. This is confirmed by the carbon fibre scattering arc, which is slightly curved in all of the photographs that follow. Using the rotation stage as the base, the supporting arm and carbon fibre were angled upwards by about 5° from the horizontal and this helped to counteract the irregularity of the orientation. The system was aligned carefully by hand and because of the 5° elevation it was possible to set the long axis of the column parallel with the laser beam when the crystal was at basal incidence. Because the carbon fibre was not perpendicular to the long axis of the column, making adjustments to the orientation using the rotation stage did not result in simply a tilt of the crystal. The scattering patterns show that the crystal also rotated around its long axis at least. The rotation was further complicated because the scattering pattern created by the carbon fibre is seen to move as the orientation changes, suggesting that it is not perfectly parallel to the supporting arm, resulting in a precession effect. This leads to the quality of the scattering patterns deteriorating because the crystal moves partially out of the laser beam after rotations too far outside of a $0° - 90°$ 'safe' angular range. As a result of this complex situation, the orientations of the crystal were modelled by finding the best fit Euler angles α, β and γ when considering the resulting light scattering patterns. For an explanation of Euler angles and Euler's rotation theorem, see appendix A.2.

Photographs were taken of light scattering patterns created by many crystal orientations. For example, a series of orientations was examined covering 90° from near perpendicular incidence to near basal incidence in 2° steps to allow an animation to be created for use in various presentations regarding this work. These photographs form the basis of the results that will be presented in a moment. Early attempts showed that long exposure times were required to capture some of the faint scattering features that were both visible to the eye and predicted by the model. As a result, photographs with such long exposure times were selected in which some brighter features are saturated. Given the red colour of the laser, the photographs appeared red on a black background. To ensure that the animation would display well on a presentation screen and that black and white reproductions of the images would be of an acceptable quality, the images were processed using a graphics package. First, the image was resampled in greyscale. Second, the image was inverted so that intensity increases from white to black. Third, a small 'gamma correction' was introduced which essentially creates a logarithmic intensity scale. A similar effect could have been achieved using an even longer exposure time as the aim was to ensure that the faint features were readily visible but longer exposure times were not possible with the camera used. The use of this effect was slight and so considered acceptable. Finally, to simplify the orientation modelling, the photograph was

rotated so that the main scattering arc was approximately symmetric about the vertical axis on the photograph. This then allows the approximation $\alpha = 0$. This simplification of the orientation removes much of the complication of the crystal orientation, leaving the trajectory of the main scattering arc to control β and the asymmetry of scattering features both on and away from the arc to control γ.

All of the resulting photographs had a resolution of 2048x1536 pixels and given that the camera was fixed in position it was possible to obtain a pixel to millimetre conversion value. Features visible on the long exposure photographs such as the edges of the screen were measured in the laboratory and compared to the number of pixels they cover on the photographs. An average was taken over all of the comparisons that were possible and it was found that 1 pixel on the photograph represented 0.111±0.001 mm on the screen. This made it possible to ensure that the distance scale on the photographs and the model results matched within experimental errors.

7.2 2D Scattering Patterns using RTDF

Modifications need to be made to the ray tracing codes and some data processing introduced to allow a comparison to the photographs. The first stage is to ensure that all of the information regarding the direction of a ray leaving the crystal is preserved. The direction in which a ray is travelling can be defined using a polar angle, θ and an azimuthal angle, ϕ (as explained in section 2.2.1). In generating a phase function, there is an averaging over the azimuthal angle and so ray tracing codes only record the polar angle, θ. The ray tracing codes are modified so that both angles are retained. The polar angle θ is sampled in the usual way using the scalar product of the forward direction (-z) with the direction of the ray, as given in equation 7.1 where $\vec{k} = (k_x, k_y, k_z)$ is a unit vector in the direction of propagation of the ray. The azimuthal angle ϕ is sampled using the scalar product of the x-axis (left if riding on a ray) and the projection into the x-y plane of the direction of the ray (equation 7.2). The angle ϕ is measured in an anti-clockwise direction from the positive x-axis when looking in the negative z direction. This convention matches standard practice (for example [38]) although unlike standard practice θ is measured from the negative z direction because that is the forward direction used in the ray tracing codes.

$$\theta = \arccos(-k_z) \tag{7.1}$$

$$\phi = \arccos\left(\frac{k_x}{\sqrt{k_x^2 + k_y^2}}\right) \tag{7.2}$$

Sampling rays using both θ and ϕ results in a significantly larger number of bins than before. As standard, θ is sampled using an array of 181 bins, covering $0° - 180°$. Sampling both θ and ϕ at the same resolution requires 65341 bins. This does not pose memory problems for the average machine but it could if the resolution were to be increased.

The bins are normalised using the standard expression for normalising scattering over all space, equation 7.3. This equation is identical to equation 2.35. Note that from this expression it is simple to average over ϕ to obtain the standard phase function normalisation expression using integration limits of $\phi = 0$ and $\phi = 2\pi$, as discussed in section 2.6.3.

$$\frac{1}{4\pi}\int_{4\pi} P_{11}(\theta,\phi)d\Omega = \frac{1}{4\pi}\int_0^{2\pi}\int_0^{\pi} P_{11}(\theta,\phi)\sin\theta d\theta d\phi = 1 \tag{7.3}$$

At this point, the scattering information is still held in angular bins. To compare to the photographs discussed above, this information needs to be projected onto a screen at some distance, r. Consider the point on the screen where a ray strikes. In spherical polar coordinates the position of this point is defined uniquely in space by the distance from the origin r_o, the polar angle θ and the azimuthal angle ϕ. The location can be expressed in Cartesian coordinates using the standard transformation formulae for moving from spherical polar coordinates to Cartesian coordinates given in equations 7.4, 7.5 and 7.6.

$$x = r_o \cos\phi \sin\theta \tag{7.4}$$

$$y = r_o \sin\phi \sin\theta \tag{7.5}$$

$$z = r_o \cos\theta \tag{7.6}$$

If the distance to the screen in the forward direction is r_s then r_s, r_o and θ can

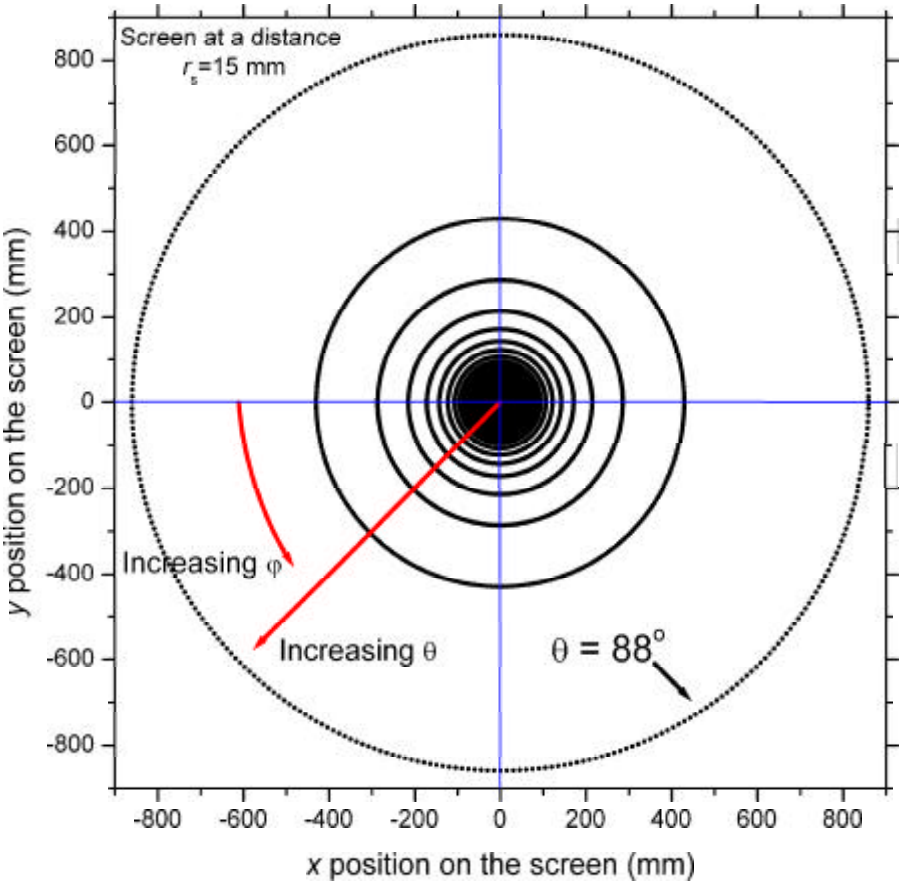

Figure 7.3: The positions of the centres of angular bins projected onto a screen at a distance of 15 mm. Illustrated are the directions of increasing θ and ϕ. The ring of points that is due to $\theta = 88°$ is marked.

be related to each other using $\cos\theta = \frac{r_s}{r_o}$. This all leads to the transformation equations 7.7, 7.8 and 7.9 which give the positions on the screen directly from the sampled angles θ and ϕ and the distance to the screen in the forward direction r_s. Conveniently, the z coordinate falls out as simply r_s as one would expect.

$$x = r_s \cos\phi \tan\theta \tag{7.7}$$

$$y = r_s \sin\phi \tan\theta \tag{7.8}$$

$$z = r_s \tag{7.9}$$

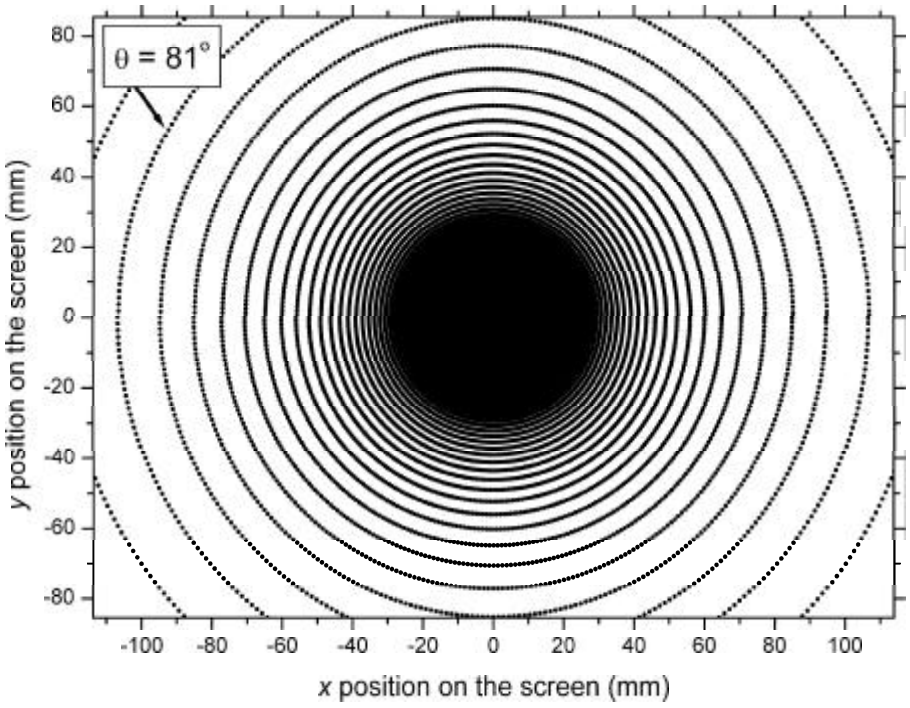

Figure 7.4: The positions of the centres of angular bins projected onto a screen at a distance of 15 mm. This plot has almost exactly the same dimensions as the range of a photograph taken using the laboratory apparatus shown in figure 7.1.

The transformation equations given above allow values from the angular bins to be projected onto a screen at some distance. However, this will lead to an irregular set of point values on the screen. Figure 7.3 shows the positions of the centre of the bins projected on to the screen out to $\theta = 88°$ in the forward direction looking from the direction of the incident light. The screen in this case is 1.8 m across which is unrealistic practically but at this size of θ one can see how the rings of points separate due to the factor $\tan\theta$. Also shown are the directions of increasing θ and ϕ. Using the laboratory apparatus shown in figure 7.1, the scattering photographs cover an area very close to that shown in figure 7.4. Here the points are much closer together even though up to $\theta = 81°$ are still being considered. Note how closely packed the points are in the forward scattering region.

This array of points on the screen does not allow the scattering pattern to be viewed in the same way as a photograph. It is necessary to have a regular grid of data points so that commercial software can be used to produce colour maps

of the changing intensity values. This was achieved by laying out a regular grid of data points over the area to be studied and calculating the intensity on the screen at those points using a linear interpolation method. The values of the interpolated points will be much more reliable near forward scattering where the data points created directly by the model are closely packed. The values are likely to be less reliable at larger angles, but for comparisons to photographs this should not be of too much concern.

In the case of comparisons to the experiment being considered, there is one final consideration. The camera was mounted behind the transparent screen and so in the results that follow the required model results are mirrored at the y-axis with respect to the transformations discussed above. If this reflection is not performed, the result will be from the point of view of the laser beam and not the camera.

It should be noted that all model 2D scattering patterns discussed in this document do not include external diffraction. The external diffraction component will mainly contribute to the forward scattering peak. Fraunhofer diffraction at a 15 μm slit (the diameter of the crystal in the current study) will produce a first minimum at an angle of less than 2.5°, which is covered by the beam stop. In any case, the low intensity interference features at larger scattering angles seen in the laboratory will be different from Fraunhofer diffraction patterns at a circular aperture. External diffraction will be omitted in section 7.4 for the same reasons.

7.3 Results

7.3.1 Six Example Orientations

Figures 7.5 and 7.6 show results for six crystal orientations from the experiment described above. The six orientations are labelled (a) to (f) and show the crystal orientation changing from near perpendicular incidence to near basal incidence. The best fit Euler angles that were used in the modelling to describe the orientation are given in the caption and follow the convention in section A.2. On the left hand side of each comparison is the laboratory photograph which has been processed as described in section 7.1. The blue arrows highlight a bright scattering arc that cuts the images from top to bottom. This is a

feature that appears on all of the photographs from this experiment. The arc is created by scattering from the carbon fibre and so can be disregarded when comparing to the model. At the forward scattering point there is an area of lower intensity which is caused by the beam stop. To the right of the photographs are the corresponding results from the RTDF model. Also shown in the RTDF frame are the results obtained from a pure ray tracing approach, marked in red. From a pure ray tracing approach one expects points of intensity, analogous to the GO sharp peaks observed in figure 3.9 where a fixed orientation phase function was being discussed. These points or spots of intensity are seen but they appear to change shape depending upon their location in the image. This is caused by the transformation on to the screen and interpolation once on the screen as described above. Some of the red pure ray tracing points near forward scattering (image centre) are literally points and as a result are not always easy to see on the background of the model result. On the right hand side of each comparison is a graphic showing the crystal orientation from the point of view of the incident light.

One can see that overall the agreement between the model and experiment is good for the six orientations. These are typical of the results from this experiment. The most important thing to note is the significant improvement over pure ray tracing. The introduction of diffraction on individual facets spreads out ray tracing points to form the scattering arcs and features that are visible on the photographs as well as allowing new ray paths that cannot exist in the framework of standard GO. The six orientations will now be discussed in turn. They are shown in figures 7.5 and 7.6. Over the coming paragraphs, bear in mind the lack of computational expense and the amount of flexibility that is associated with the model. Using the codes written to generate these model results it is possible to identify the origins of all scattering features. In the case of these six orientations it is not necessary to include such information to study the comparison between the model and experiment and so in the interests of brevity it will be omitted. Two orientation case studies will follow where all of the features will be identified in detail to illustrate the capabilities of the codes and to highlight the effect of the model. It is interesting to note as the discussion proceeds that the main scattering arcs visible are in fact conic sections which appear as ellipses ($\beta < 45°$), a parabola ($\beta = 45°$) or hyperbolas ($\beta > 45°$) depending upon the value of β. This is linked to the discussion of scattering by circular fibres available in Bohren and Huffman [13].

Orientation (a): $\alpha = 0°$, $\beta = 91°$ and $\gamma = 43°$. In orientation (a) the crystal is close to perpendicular incidence, the slight bend in the horizontal scattering arc

on the photograph illustrating that it is not exactly perpendicular incidence. The curved scattering arc on the model result that appears to be close to the location of the carbon fibre scattering arc is not related to the carbon fibre at all. RTDF stretches the forward scattering point along the length of the column which provides the near vertical feature by deflecting rays towards the column ends. It is curved in a similar way to the carbon fibre scattering arc because the carbon fibre is nearly perpendicular to the long axis of the column and lies parallel to the plane of one of the prism facets. If the carbon fibre were exactly perpendicular to the long axis of the column, the arc would lie in exactly the same position as the carbon fibre scattering arc.

Orientation (b): $\alpha = 0°$, $\beta = 73.5°$ and $\gamma = 40°$. In this orientation, the main scattering arc through forward scattering has become clearly bowed. The same six pure ray tracing features are visible and although their positions have changed, they have the same origins. A further two arcs have appeared, due to the influence of the basal facets. Note that the upper arc is faint on the photograph but can be seen as it passes through the carbon fibre scattering arc. The lower arc is more interesting. It is bright at points corresponding to three of the pure ray tracing features. The lower arc is not at all complete on the photograph and it is quite clearly broken up by interference structure. This is an effect that cannot be reproduced by the RTDF model currently. The interference structure in the photograph is something that can be observed in almost all photographs of scattering patterns included in this chapter. Despite this, the pattern predicted by the model looks much more realistic than the pure ray tracing result.

Orientation (c): $\alpha = 0°$, $\beta = 55.5°$ and $\gamma = 40°$. The main arc through forward scattering has curved even further, with the number of pure ray tracing points on it increasing. The upper arc has disappeared. If you were to watch an animation moving from orientation (b) to orientation (c) you would see the upper arc curve in on itself to form an ellipse before shrinking to nothing. An intermediate step between orientations (b) and (c) will be studied in more detail in section 7.3.2 as it presents an interesting first case study. The lower arc has moved further from forward scattering and the interference structure on the photograph has become more complicated. It is easier in this orientation to see that the bright points on the lower arc correspond to the pure ray tracing features, although the features are significantly larger in size on the photograph than is predicted by the model. This could be due to the interpolation method used in the model and it could also be connected to the lack of interference effects, which has already been mentioned.

Orientation (d): $\alpha = 0°$, $\beta = 37.2°$ and $\gamma = 35°$. The main arc through forward scattering has now curved over to form an ellipse. The interference effects on the photograph along the ellipse are clearly visible. The model reproduces the ellipse well. The apparent interference structure in the model above the ellipse is an artefact due to the transformation on to the screen at fairly large angles because the distance between actual angular bin data points on the screen increases. Below the ellipse in both the model and the experiment there are three faint arms, those in the photograph again heavily affected by interference.

Orientation (e): $\alpha = 0°$, $\beta = 18°$ and $\gamma = 30°$. The ellipse seen in orientation (d) now closes in towards being a tight circle. The comparison between model and experiment for this is good, although it is not easy to resolve the circle in the experiment. Another larger ellipse has formed in the model result although this is not reproduced in the experiment because the feature is not bright enough. In the experiment, the lower part of the ellipse is visible as an arc but it is exhibiting by far the most complicated interference structure yet seen in this discussion. Three bright spots on the arc correspond to three pure ray tracing points, with possibly a further two at the left and right extremities of the visible structure.

Orientation (f): $\alpha = 0°$, $\beta = 0°$ and $\gamma = 30°$. In this orientation, light is near to normally incident on a hexagonal facet. The large ellipse seen for the first time in orientation (e) has moved to form a tight circle surrounding forward scattering. This can be seen on the photograph as the six bright points connected by interference structure. As a result, it has come to resemble a six spoked wheel with bright scattering features forming the spokes. The model cannot reproduce the rim of the wheel at this precise orientation but at $\beta \pm 1°$ the ellipse is still visible (not shown). However, the spokes are reproduced well. The reason for this is that at this orientation the only pure ray tracing point is at forward scattering. All of the scattering seen in the RTDF result is due to rays refracting through both hexagonal facets and being deflected towards one of the facet edges, resulting in six spokes.

7.3.2 Case Study 1

In the first case study, the orientation is approximately $\alpha = 0°$, $\beta = 60.5°$ and $\gamma = 35°$, between (b) and (c) in figure 7.5. Figure 7.7c shows the crystal in the best fit orientation from the point of view of the incident light. Each facet has

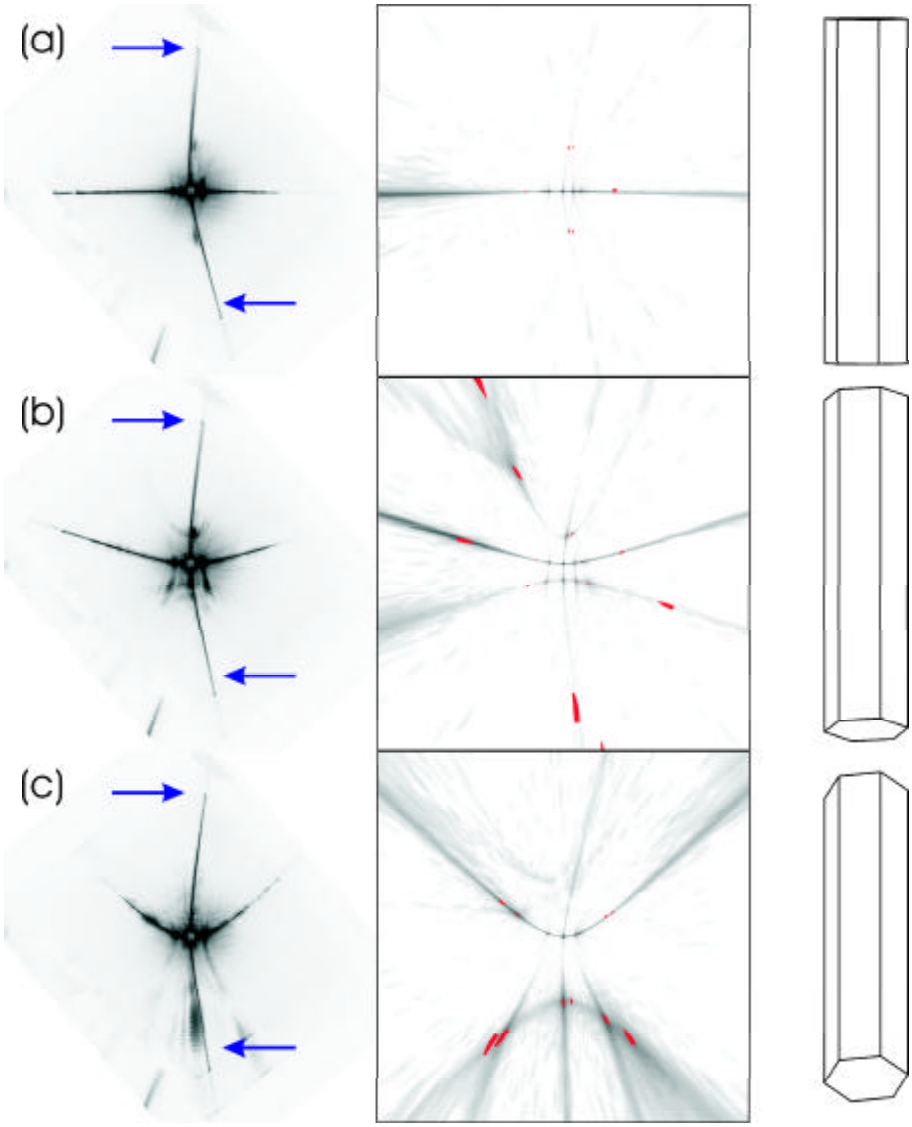

Figure 7.5: Results from the fixed orientation scattering experiment compared to pure ray tracing and the RTDF model. (a) $\alpha = 0°$, $\beta = 91°$, $\gamma = 43°$. (b) $\alpha = 0°$, $\beta = 73.5°$, $\gamma = 40°$. (c) $\alpha = 0°$, $\beta = 55.5°$, $\gamma = 40°$.

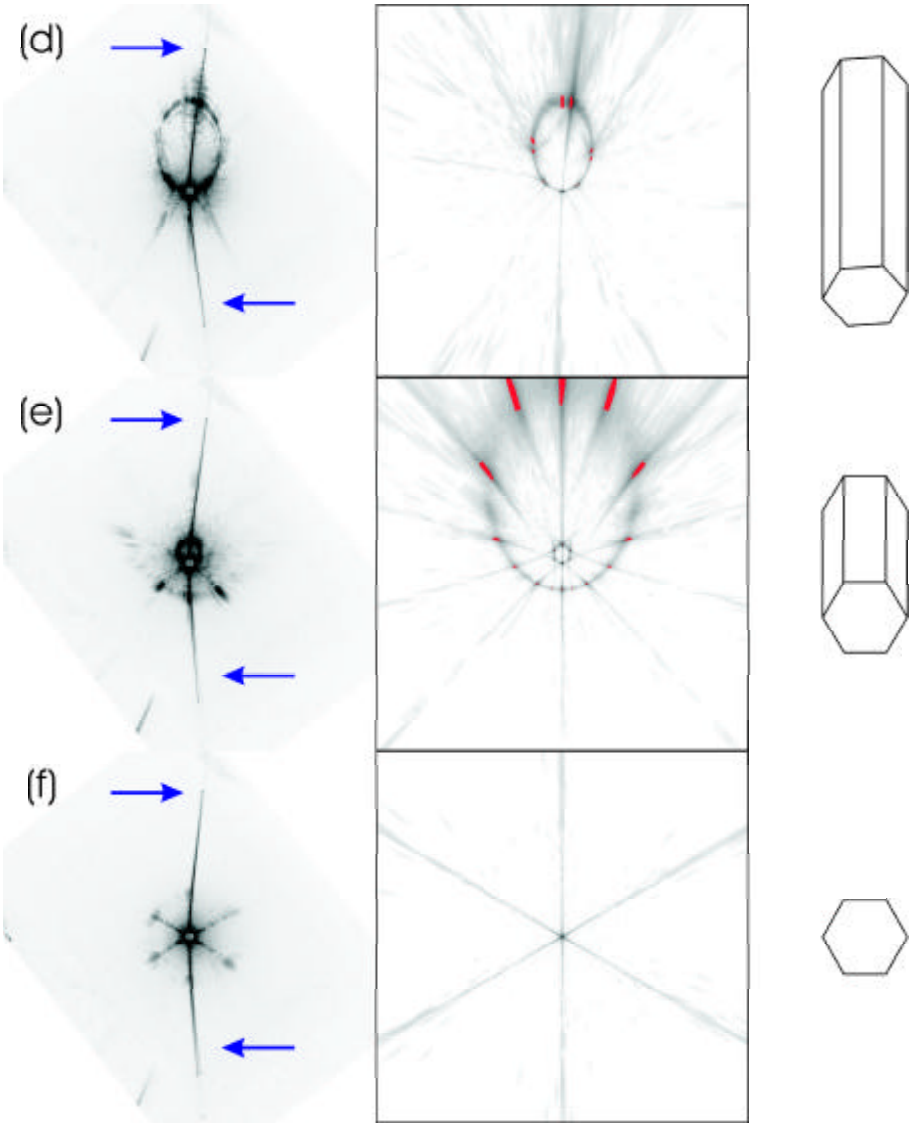

Figure 7.6: Results from the fixed orientation scattering experiment compared to pure ray tracing and the RTDF model. (d) $\alpha = 0°$, $\beta = 37.2°$, $\gamma = 35°$. (e) $\alpha = 0°$, $\beta = 18°$, $\gamma = 30°$. (f) $\alpha = 0°$, $\beta = 0°$, $\gamma = 30°$.

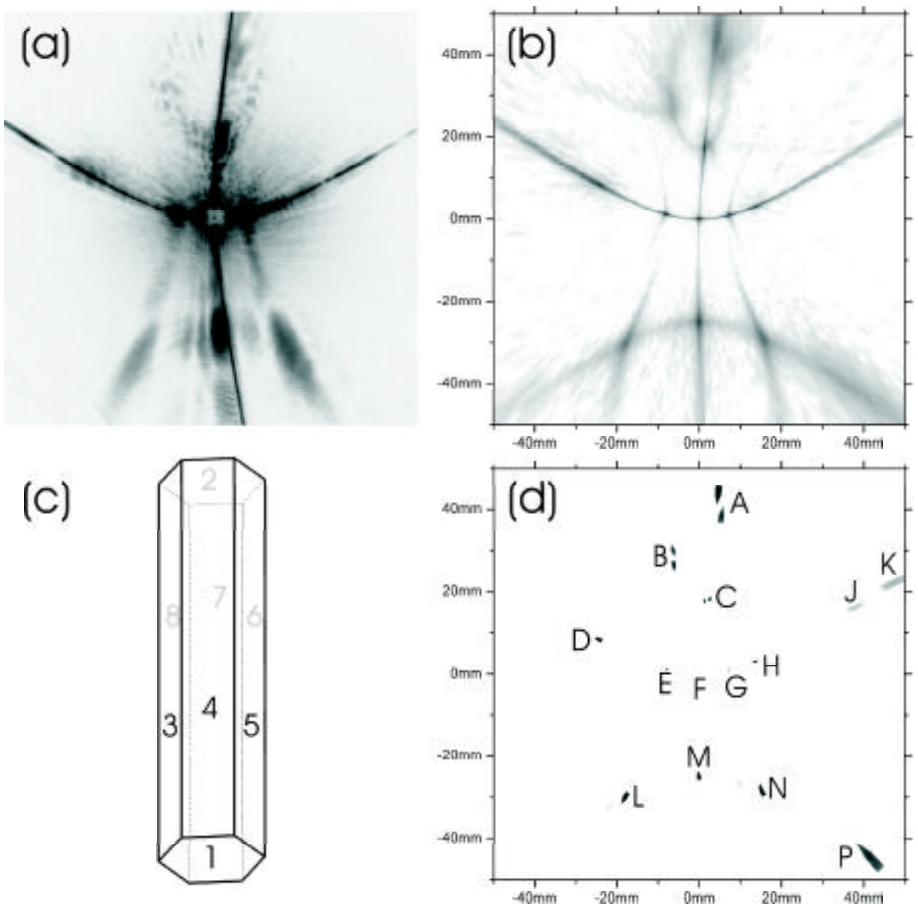

Figure 7.7: (a) Laboratory scattering pattern for a hexagonal column with orientation $\alpha = 0°$, $\beta = 60.5°$ and $\gamma = 35°$. (b) Equivalent RTDF result. (c) The orientation of the crystal from the point of view of the incident light. (d) Equivalent GO result.

been assigned a number with facets 1, 3, 4 and 5 exposed to the incident light. Figure 7.7a shows the laboratory photograph of the scattering pattern. The pattern appears slightly asymmetric because of the γ Euler rotation. Figures 7.7b and 7.7d show the equivalent results for RTDF and GO respectively. Note that the photograph in figure 7.7a again clearly shows interference fringes over much of the pattern.

Comparing the GO and RTDF results, the effect of the new model can be clearly seen. The RTDF scattering pattern takes a much more realistic appearance than the GO result when compared to the photograph in a similar fashion to the last section.

In the next few paragraphs the origins of the various GO features shown in figure 7.7d will be discussed while highlighting specific features that are enhanced by the new model. The GO points have been labelled for identification. All of the GO points are made up of contributions from several ray paths through the crystal. It will be stated that a given feature is caused by the dominant ray path on the understanding that there are likely to be small contributions from more complex paths.

Examining figure 7.7b it can be seen that the bright arc through forward scattering that is reminiscent of the conic section created by scattering by a circular fibre is recreated by RTDF. This arc includes bright spots at points E and G that represent refractions through prism facets. For E, rays enter through facet 3 and for G rays enter through facet 5. In both cases the rays leave the crystal through facet 7. There are external reflections from facets 5 and 3 at points D and H respectively, although they are not well defined in the photograph. The forward scattering peak at F is dominated by rays entering through facet 4 and leaving through facet 7, with no net deflection due to standard GO interactions. Also contributing to the arc are faint points at J and K. J is formed from rays entering through facet 3, internally reflecting several times and exiting facet 8. K is formed in a similar way except that the rays both enter and leave through facet 3. Finally there are two small faint features that contribute to the arc that are not labelled. Being near the centre of the image, the features are small and not visible in the figure but they are present in the raw data. Both are formed from several internal reflections with paths very closely related to J. The first is located between F and G where rays enter through facet 5 and eventually exit through facet 8. The second is located near E, found when moving in the direction of point D. Here, rays enter through facet 3 and exit through facet 6. In all cases along the scattering arc the bright GO spots are spread by the new model near horizontally to recreate the arc but also in a more vertical direction on the screen. This makes the pattern similar to the photograph, particularly in the case of the features above and below points E and G.

There are numerous features below the main scattering arc most of which are created by ray paths including an internal reflection or a total internal reflection from the basal facet 2. Point M is the exception, the feature being dominated by an external reflection from the basal facet 1. All of the features compare better with the photograph in the RTDF result than the standard GO result. The features at points L and N represent rays entering through facets 3 and 5 respectively. Some of the contributing ray paths are complicated, undergoing multiple internal reflections including one total internal reflection from the basal

facet 2. In both cases rays leave the crystal through facet 7. Point P is also due to complicated paths made up of multiple internal reflections. There are numerous entrance and exit facets for this feature with the only common facet interaction being the internal reflection from the basal facet 2. There are also two faint GO spots that are not labelled, both with complicated ray paths. To the left of point L is a spot formed from rays entering through facet 3 and exiting through facet 6. Between points M and N is a feature formed from rays entering through facet 5 and exiting through facet 8.

Above the main scattering arc is a very interesting collection of features. There are six features in total in the vicinity of points A, B and C with two located at each. The left hand feature at point C is perhaps the most familiar as it is dominated by refraction through facets 1 and then 7. Being the only feature on the screen at this orientation representing refraction through a basal facet and a prism facet, it is effectively the 46° halo. This was confirmed experimentally by tilting the crystal into other orientations where it was observed that the feature did not move below 46°. The other five points are created by rays entering facet 1, undertaking a complex path of internal reflections and then leaving the crystal through one of the prism facets. The upper and lower points at A are created by rays leaving through facets 4 and 3 respectively. The upper and lower points at B are from rays exiting through facets 5 and 6 respectively. The right hand point at C is formed by rays leaving through facet 8. There is also a similar ray path that contributes to the 46° halo spot that exits through facet 7.

In the photograph and RTDF result in figures 7.7a and 7.7b one can see a hollow elliptical feature connecting points A, B and C. This feature persists when varying the γ Euler angle. Explaining it in terms of ray tracing, the feature is created by rays entering the basal facet 1 and internally reflecting up the length of the column. RTDF then allows rays to exit through any prism facet at a wide range of angles, some of the ray paths including an internal reflection from the basal facet 2. This cannot be reproduced by GO where the ray paths are strictly confined to specific scattering angles to create the features at A, B and C. This hollow elliptical feature can be likened to a guided wave effect and given the complexity of modelling such effects (for example, Reisinger [132]) it presents another potential application of the RTDF model.

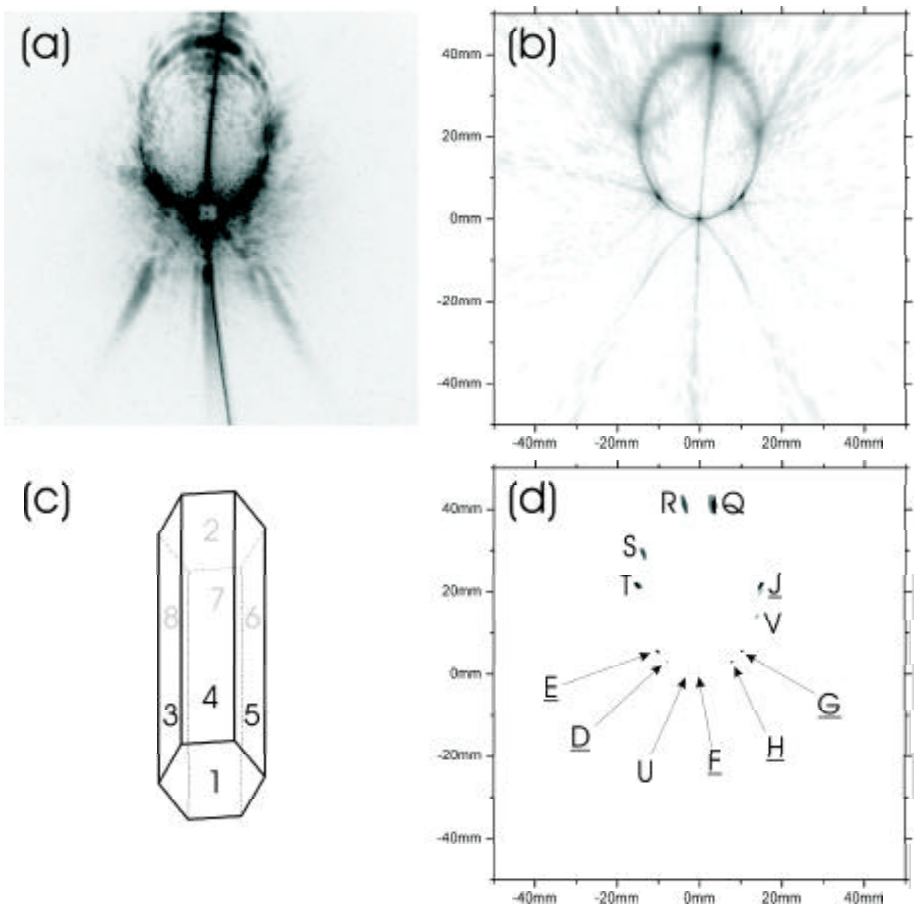

Figure 7.8: (a) Laboratory scattering pattern for a hexagonal column with orientation $\alpha = 0°$, $\beta = 35°$ and $\gamma = 34.5°$. (b) Equivalent RTDF result. (c) The orientation of the crystal from the point of view of the incident light. (d) Equivalent GO result.

7.3.3 Case Study 2

In the second case study, the orientation is approximately $\alpha = 0°$, $\beta = 35°$ and $\gamma = 34.5°$ and is shown in figure 7.8c. This orientation sits close to (d) and between (d) and (e) in figure 7.6. The laboratory photograph, RTDF result and GO result are shown in figures 7.8a, 7.8b and 7.8d respectively. Similar to the first case study, the photograph shows many interference fringes. The GO features have again been labelled, those features that are related in origin to features from case 1 being denoted by the same letter but underlined. These relationships will be explained below.

The scattering pattern is dominated by a large ellipse. By rotating the crystal from the first case study orientation to this orientation, it is possible to see that the ellipse is formed by the main scattering arc from the first case folding over. The RTDF result matches well with the laboratory photograph. Of particular interest are the three arms extending from the forward scattering point below the main scattering ellipse. There are no GO points that correspond to these features at this orientation. However, the RTDF result provides three such features. Although at first it appears that the RTDF features are a result of the forward scattering point being spread out by the model, this is not in the main the case. It is true for the very early part of the arms but in the regions close to where the features appear strongest in the photograph, the sources are new ray paths that are not visible elsewhere on the screen or indeed possible using GO. All three features are dominated by two refractions with rays entering a prism facet and leaving through the basal facet 2. From left to right, the entrance facet for the three features are 3, 4 and 5. In this way, the model at this orientation has reproduced a feature by creating a ray path that GO cannot create.

With respect to the forward scattering point on the scattering arc the points D and E have swapped places, as have G and H. Being refractions through two prism facets, E and G are formed by the ray paths that contribute to the 22° halo. In case 1, the points were at scattering angles of around 29° and 26° respectively and so it is not surprising that they move away from the forward scattering point given that the minimum scattering angle possible for the ray path is 22°.

The bright points that contribute to the large ellipse are as follows. Point Q is dominated by a reflection from facet 4. Points R, S and V are formed by complex ray paths entering through facet 5 and exiting through facets 3, 6 and 4 respectively. Point T is formed from a range of complicated ray paths with the only common feature being either an internal or total internal reflection from facet 7. Points $\underline{E}$ and $\underline{G}$ are identical in origin to the equivalent lettered features in case 1. Point $\underline{D}$ is formed by complex ray paths both entering and leaving the crystal through facet 5. It is related to point D because this type of ray path was a minor contributor in case 1. The dominant contributor to point D, the external reflection from facet 5, has moved past the screen boundary. The faint feature at point U is due to complex reflection paths entering the crystal through facet 5 and exiting through facet 8. In this way it is similar to the faint feature between F and G in case 1. The forward scattering point, $\underline{F}$ is in the main identical to F in origin save for a few of the minor ray paths not persisting. Point $\underline{H}$ is dominated by a reflection from facet 3 giving it a connection to point

H. It also includes the ray paths that created point K in case 1. There are two features at point $\underline{J}$. Both points include complex ray paths with rays entering through facet 3 and exiting through facet 8, just like point J. The upper point at $\underline{J}$ also includes a range of other complex ray paths that all have at least one interaction with the basal facet 2, in some cases as the refraction out of the crystal.

7.4 Particle Characterisation using 2D Scattering Patterns

In the preceding sections, the new model has been shown to create scattering patterns on a screen that compare well with laboratory photographs. The scattering patterns generated using RTDF offer a degree of realism that is not possible with standard GO. It has been previously shown that spatial or 2D scattering patterns of single orientations can be used to distinguish between particle geometries and so aid in particle characterization in a range of scientific fields [11]. In the case of cirrus ice, the concept has been implemented in particle instruments such as SID [12, 133]. Such instruments use a laser beam to illuminate particles as they pass through the instrument and an array of detectors then measures the light scattering. By studying the relative signals from these detectors it is possible to distinguish between spherical and nonspherical particles and also to classify nonspherical particle geometries. The RTDF model could potentially be used to further develop such in-situ particle instruments. To illustrate this, the model will now be applied to a range of crystal shapes, a process that benefits from the flexibility of the model with regards to particle geometry.

Consider an ideal particle characterisation instrument that has the ability to take in-situ images of 2D scattering patterns created by ice crystals in cirrus. The crystals pass through a chamber where they are illuminated by a laser of wavelength 550 nm. An array of sensors or a CCD captures an image of the resulting scattering pattern. To successfully characterise the geometry of a particle from such a pattern, one requires knowledge regarding the general characteristics of scattering patterns created by candidate geometries. In the following, figures 7.10 and 7.11 show how such general characteristics can be obtained from modelling results by comparing the scattering patterns from eight example geometries. All of the results presented use the same scatterer to screen

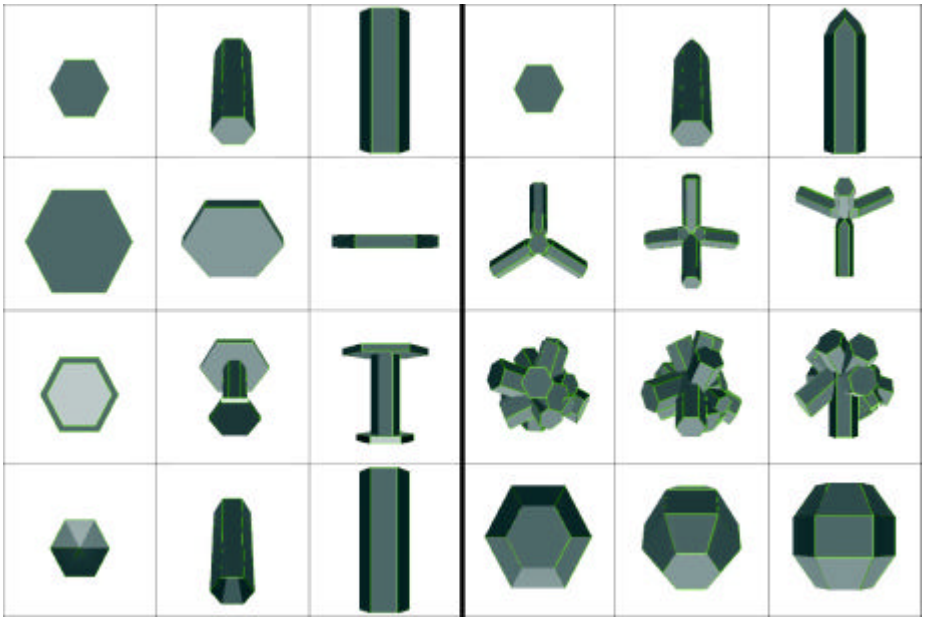

Figure 7.9: Illustrations of the eight geometries used in the particle characterisation discussion (not to scale). The three orientations shown for each geometry correspond to the scattering patterns in figures 7.10 and 7.11. The twelve boxes on the left correspond in layout to the twelve scattering patterns in figure 7.10. The twelve boxes on the right correspond to figure 7.11. Left side (top to bottom): Hexagonal column, hexagonal plate, capped column, hollow column. Right side (top to bottom): Bullet, bullet rosette, reconstructed germ rosette Gros48 and droxtal.

configuration as found in section 7.3. Each result shows a 100 mm square section of the screen. This means that the screen represents a large angular range of approximately 147° along the x and y axes.

The eight geometries to be considered in this study are shown in figure 7.9 in the three orientations that each crystal takes, corresponding to $\beta = 0°$, $\beta = 45°$ and $\beta = 90°$. The layout of the geometries and orientations in the left hand side of the figure correspond directly to the layout of the scattering pattern results in figure 7.10. In the same way, the right hand side corresponds to figure 7.11. All orientations are shown from the direction of the incident light. This figure can be used as a reference as the discussion proceeds.

Figures 7.10a, 7.10b and 7.10c show the 2D scattering patterns for a hexagonal column of size parameter $2\pi r/\lambda = 50$ with $L/2r = 2.5$ in the three orientations shown in figure 7.9. A range of orientations need to be studied because fixed

orientation 2D scattering patterns are strongly orientation dependent. One can see that the dominant feature in the patterns is the strong scattering arc through forward scattering appearing as a straight line in figure 7.10c. Rotating the crystal by decreasing the β Euler angle past the orientation in figure 7.10b, this feature turns into an ellipse (as shown in section 7.3.3) before disappearing when close to the orientation in figure 7.10a. The scattering arc provides a simple signature of a columnar shape. This simplicity combined with the fact that the shape of the scattering arc is determined by the crystal orientation means it is possible to infer information regarding the crystal orientation from the scattering pattern. In practise, the obvious application would be to identify crystals taking preferred orientations in cirrus, a phenomenon discussed earlier in section 5.6. This would only be possible if the ideal instrument were able to ensure that the natural orientation of a crystal were preserved in the sampling process.

The scattering patterns for a hexagonal plate are quite different from those for a column. Figures 7.10d, 7.10e and 7.10f show the scattering patterns for a plate of size parameter 100 with $L/2r = 0.1$. The hexagonal facets are oriented so that they face in the same directions as for the column cases (see figure 7.9). For the plate the dominant feature is the six spoked star seen in the first image. Figure 7.10e shows that as you move to more oblique angles of incidence, the star is gradually distorted. Only near to the third orientation does the feature change into a more complicated pattern of scattering. Note that the horizontal line in figure 7.10f which corresponds to refraction through prism facets is thinner with a different intensity distribution to the equivalent column orientation in figure 7.10c. If the hexagonal nature of the crystals is near to regular then the spokes of the star observed for the plate will form arcs relative to each other that are in predictable positions, even as the orientation changes. With this information one could distinguish between the scattering patterns produced by columns and plates in most cases. Ambiguity could arise for patterns very close to 7.10a or 7.10d but there is only a small probability of these orientations occurring. The weighting towards either geometry for such ambiguous cases could be estimated in post processing from the ratio of columns to plates identified at less contestable orientations. It is interesting to note that the six spoked star seen for the plate and also in figure 7.10a for the column cannot be reproduced using GO. In the cases of figures 7.10a and 7.10d the GO result would be restricted to a point at forward scattering.

It is not uncommon to observe capped columns, a combination of a column and one or two plates as discussed in section 5.2. Figures 7.10g, 7.10h and 7.10j

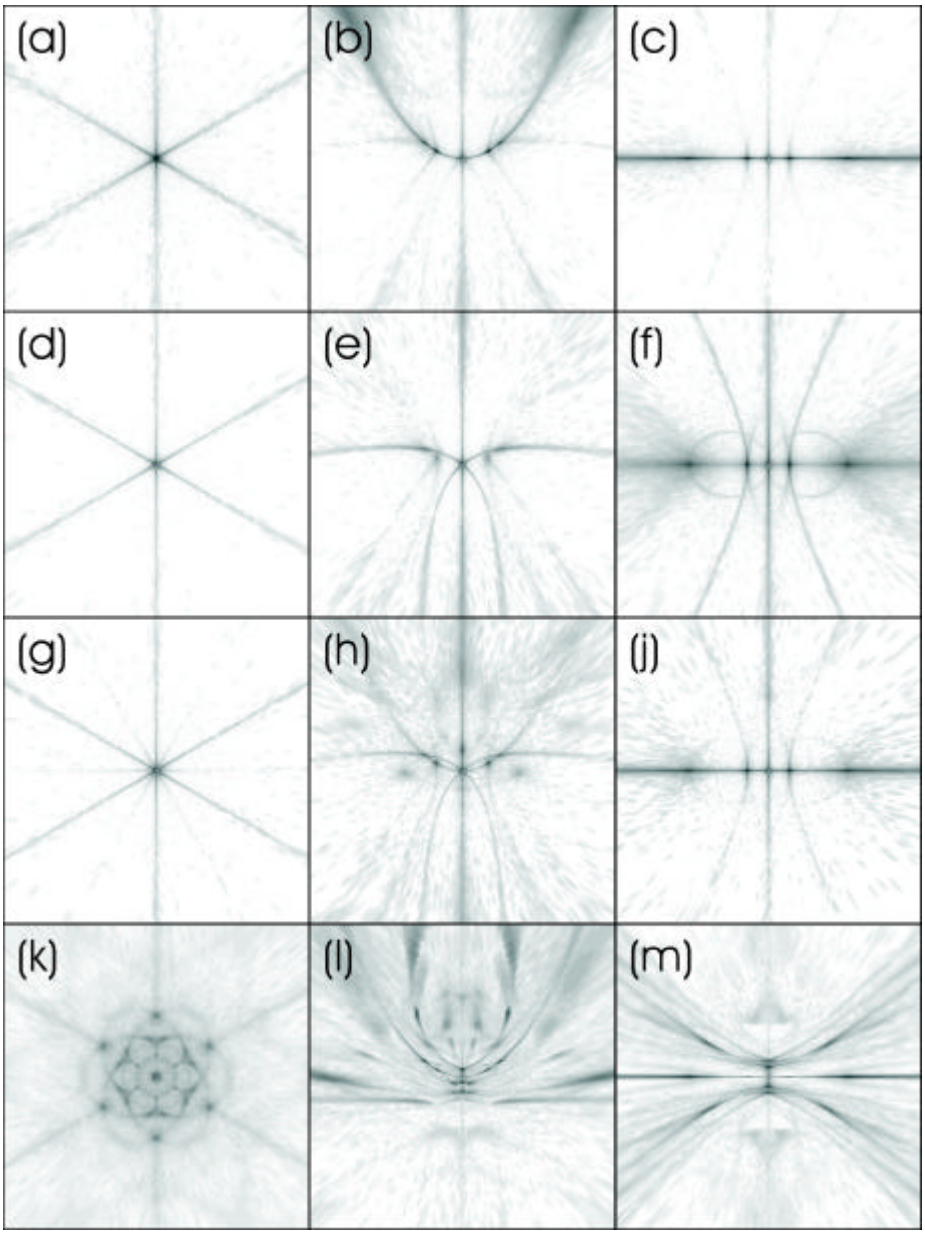

Figure 7.10: 2D scattering patterns for four geometries with three orientations shown for each (see text). All of the images are sections of the screen that are 100 mm square in size with the forward scattering point at the centre. The geometries are: Hexagonal column (a, b, c), hexagonal plate (d, e, f), capped column (g, h, j) and hollow column (k, l, m).

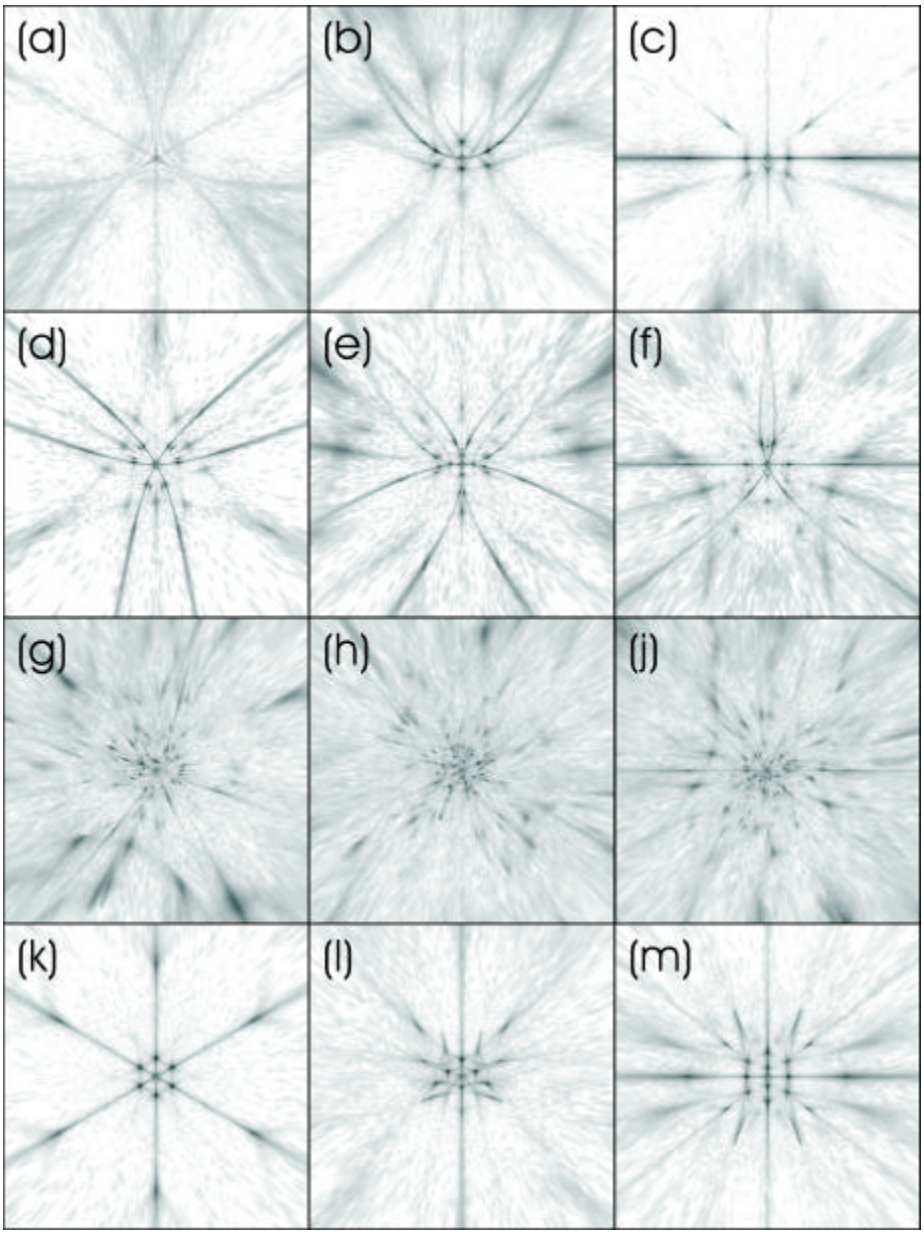

Figure 7.11: 2D scattering patterns for four geometries with three orientations shown for each (see text). All of the images are sections of the screen that are 100 mm square in size with the forward scattering point at the centre. The geometries are: Bullet (a, b, c), bullet rosette (d, e, f), reconstructed germ rosette Gros48 (g, h, j) and droxtal (k, l, m).

show the scattering patterns for a column identical in size to that used above capped with plates that have radii one and one and a half times the radius of the plate discussed in the last paragraph. The scattering patterns are an interesting combination of the patterns seen for the constituent geometries, most noticeable in figure 7.10h where both the column scattering arc and the plate six spoked star are visible.

Often observations show that columnar crystals contain hollow areas, particularly at the ends as discussed in section 5.3. The scattering patterns for a crystal exhibiting strongly indented ends are shown in figures 7.10k, 7.10l and 7.10m. The crystal is the same size as the column discussed above with inverted pyramids at the ends that meet at the crystal centre. Such a severe deformation of the crystal has a large effect on the scattering patterns created. Scattering features are closely packed while covering large areas of the screen, quite distinct from the other patterns in this study. This suggests that should an instrument with sufficient resolution be feasible in the future, it may be possible to identify degrees of crystal deformation in atmospheric ice. Clearly the degree of deformation will have a large effect on the scattering patterns and more importantly the reliability of this finding rests upon the accuracy of modelling hollow features using such inverted pyramids. This has already been discussed in section 5.3, where it was shown that there is evidence to support this modelling approach such as the observation of small angle halos, though how generally applicable it is to atmospheric ice remains unclear.

Many crystals observed in cirrus are considerably more complicated than columns and plates. One of the most common geometries is the rosette [124]. In this case, a 4-4 (four arm) pentagonal headed bullet rosette as defined by Iaquinta et al. [125] (discussed more thoroughly in section 5.6) will be considered. First consider the constituent bullet, the scattering patterns for which are shown in figures 7.11a, 7.11b and 7.11c. The bullet has the same radius and length (not including the head) as the column discussed above. The bullet scattering patterns are again distinct from a standard column, although it would be difficult to distinguish between a hollow column and a bullet given the closely packed features. It can be shown that a less severely deformed column than that considered above would produce scattering patterns that very closely resemble the bullet. This suggests that deformities at column ends, whether depressions or extensions, produce similar results for the purposes of particle characterisation. Note that the results for a bullet given in figures 7.11a and 7.11b would not be exactly the same if the bullet head faced the incident light, although the overall discussion would remain unchanged.

Figures 7.11d, 7.11e and 7.11f show the 2D scattering patterns for the 4-4 rosette where all four arms are identical, all being examples of the bullet that has just been considered. The crystal is shown in the three orientations in figure 7.9. The scattering patterns are significantly more complicated than for the column or the plate. The defining feature of the patterns created by the rosette are the multiple examples of scattering arcs that resemble those created by the column. These exist because each arm of the rosette can contribute such a scattering arc. For example, in figure 7.11e all four scattering arcs can be seen. This creation of the scattering arcs by a rosette is maintained as long as the arms are long enough for single scattering from the individual arms to dominate over multiple scattering between the arms. If the rosette arms appear parallel when viewed from the direction of incident light, it may not be possible to discriminate between the scattering arcs. The number of arcs may also not correspond to the number of arms if one or more of the arms is close to parallel to the incident light, as seen in figures 7.11d and 7.11f where only three distinct arms are visible. This means it would not immediately be possible to reliably identify the number of rosette arms from a single orientation in an in-situ instrument, but for broad crystal habit classification purposes this is not a significant concern. It would however be possible to easily distinguish between columns and rosettes purely from the complexity of the scattering pattern. There is the possibility that rosette scattering patterns could be confused for plates given the arcs predicted in figure 7.10d. However, to replicate the positions of the scattering arcs exactly a six arm rosette with the arms all coplanar and separated by 60° angles would be required. Other geometries may succeed in individual orientations through chance but no other geometry would succeed for all orientations. An interesting point to note is the significant difference between the 2D scattering for the rosette and its constituent geometry, the bullet. In section 5.6, it was shown that the RTDF model confirms the common finding that the phase function for a rosette resembles quite closely that of its constituent component. The 2D scattering patterns show that the similarity rests only with averaged random orientations, as one would intuitively expect.

It has been shown how scattering arcs can be created by each arm of a rosette if the arms are long enough for single scattering from the arms to dominate. Germ or budding rosettes are crystals where this is unlikely to be the case. They are also common in the atmosphere as they represent an earlier stage in the development of the longer arm rosettes. In section 6.2 Gros48 was introduced, a germ rosette geometry that was reconstructed from an ice analogue example. It is shown in the scattering orientations in figure 7.9. Figures 7.11g, 7.11h and 7.11j show the scattering patterns and as expected they are extremely compli-

cated. Single scattering arcs from individual arms do not have the ability to form as the majority of the scattering involves the central area of the crystal. Once again, such a complex pattern would potentially allow this type of geometry to be distinguished from those considered above. Note that the scattering patterns are essentially orientation independent. It is interesting to note that it is expected that a rosette with rough surfaces will create scattering patterns that are similar in nature to those created by Gros48. Distinguishing between smooth and rough crystals is an area that possibly requires future attention given the significantly reduced asymmetry parameters measured for rough ice analogue crystals in the laboratory [134].

As discussed in section 5.5, it is often the case that small crystals below 50 μm are classified as ice spheres when they may actually be small faceted objects such as droxtals. Figures 7.11k, 7.11l and 7.11m show 2D scattering patterns for a droxtal with a radius that ensures the hexagonal facets are the same size as those in the column case above. The sphericity has been maximised by volume to as closely simulate a sphere as possible. The first thing to notice is that the patterns are very different to the concentric rings one might expect from Mie theory calculations for a sphere, highlighting significantly more differences than can be seen with an equivalent phase function comparison (see section 5.5). A light scattering based probe can therefore distinguish between spherical and nonspherical particles, as has been shown in the field [12]. The droxtal scattering patterns are complicated, although the hexagonal nature of parts of the droxtal can be inferred from the patterns. The complexity of the droxtal patterns makes them reminiscent of the germ rosette patterns above. Given that Gros48 is an extreme case (the crystal has fifteen arms), the ability to distinguish between droxtals and germ rosettes on this evidence is likely to be limited unless instrument resolution is very high. However, it can be stated that it is possible to identify more complex, less spatial crystals such as droxtals and germ rosettes when compared to more expansive crystals such as the long armed rosettes with their clean pattern of clear scattering arcs.

In this short discussion it has been illustrated how the RTDF model can in principle be used to aid particle characterization. Broad crystal habit classification is possible by studying such 2D light scattering patterns and further investigation using the model will allow more sophisticated problems to be considered. The model allows rapid computation of such 2D scattering patterns for any crystal geometry. As well as broad classification considerations, it is theoretically possible to identify more in depth information. For example, the presence of crystal deformities such as hollow regions at column ends changes the 2D light

scattering predicted by the model. In practise, developing an instrument capable of utilising the model to achieve such detailed crystal classification would be a major challenge. It may also be possible to detect crystals with preferred orientations in the field, particularly for hexagonal columns and plates, if the natural orientation can be preserved by the instrument.

Chapter 8

Comparisons to Aircraft Radiance Measurements

This chapter presents work undertaken at the UK Met Office during an eight and a half week visit early in 2005. Some of the discussion and results have been included in a Met Office Technical Note [91].

Phase functions obtained from the RTDF model as well as from GO were used in conjunction with a Monte Carlo radiative transfer code to make comparisons with aircraft radiance measurements of cirrus held at the Met Office in Exeter. Calculations were initially performed for test geometries such as the hexagonal column, the droxtal and the polycrystal (which will be defined in section 8.3). These were followed by calculations for the reconstructed geometries of ice analogue crystals that were introduced in section 6.2. The method and results will be presented in the forthcoming sections. The chapter will address the suitability of the reconstructed geometries of ice analogue crystals as representative cirrus ice particle geometries in the cirrus cases considered. The candidature of the test geometries will also be considered. The effect of using size distribution functions for single geometries will be investigated. The combination of various geometries within size distribution functions to gain combined size and shape distributions will also be considered.

8.1 Radiative Transfer Modelling

All of the results presented in the preceding chapters have been single scattering results. Single scattering refers to the case where either an individual particle is being considered or a collection of identical particles whose concentration is low enough that each particle scatters light as if the other particles did not exist. This is also referred to as independent scattering. In most practical cases it is not possible to use the single scattering approximation because the scattered light from crystals does affect the scattering of other crystals. An exception to this is subvisual cirrus where the scattering medium can be considered thin enough to allow the application of the single scattering approximation.

A large collection of particles that interact are treated using *multiple scattering* techniques. The problem is often referred to as the problem of *radiative transfer*. Equation 8.1 is a simple form of the *radiative transfer equation* which can be used to describe a multiple scattering system formed from non-emitting media.

$$\frac{\mathrm{d}I\left(s,\theta,\phi\right)}{\mathrm{d}s} = -KI\left(s,\theta,\phi\right) + J \tag{8.1}$$

In equation 8.1, I is the intensity which is a function of path length (s) and direction (θ, ϕ) and ds is an element of the path length. Equation 8.1 is essentially a statement of conservation of energy. It describes the change in intensity per unit path length. The first term on the right hand side of the equation describes the attenuation of light travelling in a particular direction caused by extinction, K representing the extinction coefficient. The second term, J, is sometimes termed the *source function*. It is a sum of contributions from multiple scattering within the cloud, direct single scattering of solar radiation and thermal emission from the medium. In the following, it is assumed that there is no thermal emission. This is reasonable because for wavelengths shorter than 3.7 μm the solar component dominates over negligible thermal emission. The longest wavelength to be considered in this chapter is 1.61 μm. More information on the radiative transfer equation can be found in the literature, for example [38, Chapter 1] or more specifically related to cirrus [58, Chapter 13].

There are many computational methods available that solve the radiative transfer equation for atmospheric applications, for example [135]. In this study, a relatively simple Monte Carlo technique is used that considers a single cloud layer that is plane-parallel and homogeneous. A brief description of the method

follows. It is explained in more detail by Ley [136]. The code that implements the method was modified by Anthony Baran to run on VAX/Alpha machines and to provide support for multiple layers in 1992. In this method, radiances are calculated by tracing photon paths through the cloud. As a photon moves through the cloud, it can collide with the particles being considered and such an event may lead to it being scattered or absorbed. The single scattering albedo (defined using equation 2.11 in section 2.2.3) gives the probability that a photon will be scattered rather than absorbed as a result of a collision. This is considered in the extinction term in the radiative transfer equation. If the photon is not absorbed, it is scattered into an angle found using a probability density function calculated from the single scattering phase function of the particle. On escaping from the cloud the photon is collected into a detector, the orientation of which provides the overall scattering angle. This contributes to the resulting angular radiance distribution. By applying this method to many photons one can build the angular radiance distribution of the whole cloud.

In this study, all of the radiative transfer calculations use one million incident photons. In all cases, one scattering layer of particles is considered that is specified by an extinction optical depth value, τ. The extinction optical depth is a wavelength dependent dimensionless quantity, often referred to as just the optical depth. It is defined as the line integral of the sum of the scattering and absorption coefficients along a vertical path through the scattering layer. The sum of the absorption and scattering coefficients is equal to the inverse of the mean free path of a photon passing through a scattering medium. Consequently, in a uniform medium such as the cloud layer considered here the optical depth can be interpreted as a measure of the thickness of the scattering layer measured in units of mean free path.

In many cases in the results that follow, the radiative transfer result given is a best fit for the optical depth, τ. This retrieved optical depth is obtained using a χ^2 minimization technique to find the best agreement between calculated and observed angular radiance distributions. It will be quoted to the nearest 0.05. This degree of accuracy was chosen to reduce computer time and it gives acceptable results throughout. Using optical depth values retrieved from observations would be inappropriate because they would only be correct if the cloud model in terms of crystal geometries and cloud structure were accurate. In the case of the size distribution function work in section 8.6, the χ^2 minimization technique is also used to find the best fit value of the mean effective diameter, D_e, something that will be discussed in section 8.6.

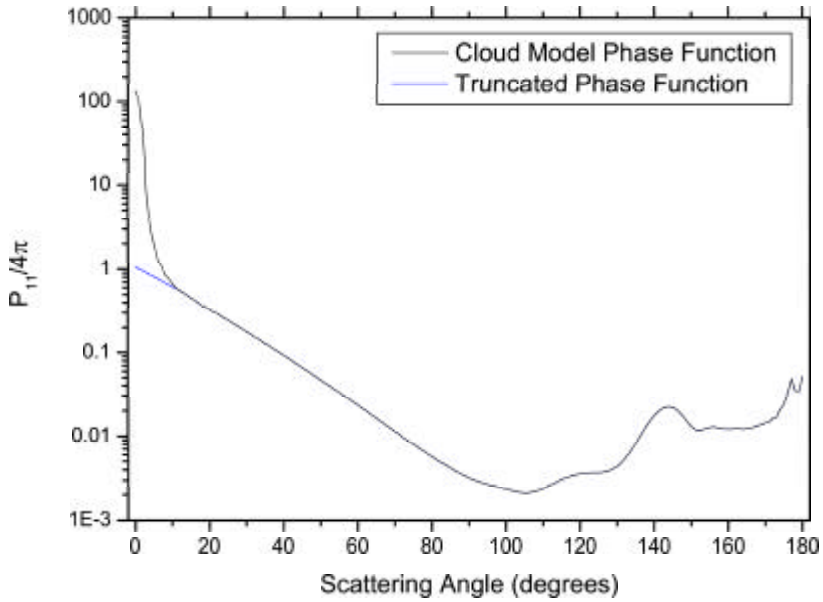

Figure 8.1: A reproduction of figure 1 from Potter 1970 illustrating the use of a truncated phase function.

The χ^2 minimization technique was made possible by obtaining the radiative transfer results for integer scattering angles only and then binning the radiance measurements into equivalent integer scattering angle bins. The radiance measurements will be represented here by a continuous line for ease of comparison to the model results.

8.2 Phase Function Truncation

A problem is sometimes encountered when solving a multiple scattering system using phase functions that exhibit large intensities at forward scattering due to diffraction. They can increase execution times significantly and in some cases lead to numerical instabilities in the calculations. To counter this, one can apply a delta function approximation as discussed in Potter [137]. The method removes the sharp diffraction peak at forward scattering. Photons scattered into the forward peak are scattered through only a very small scattering angle and so it is reasonable to assume that they are not scattered at all. This is implemented

by replacing the sharp forward diffraction peak with a Dirac delta function and then by considering the phase function without the delta function. Using this new truncated phase function simplifies the multiple scattering calculation. It is necessary when using the delta function approximation to adjust the single scattering albedo and the optical depth to match the truncated phase function, details of which are available in the referenced paper.

An example of a truncated phase function is shown in figure 8.1. The figure is a recreation of figure 1 from Potter [137]. The complete phase function shows the cloud model phase function calculated from Mie theory by H. Cheyney [138] at a wavelength of 0.554 μm. The phase function used in Potter [137] is slightly modified because it exhibits some smoothing of the back scattering region. Figure 8.1 may exhibit slightly different normalisation as a result of the back scattering differences. The modifications are discussed further in Arking and Potter [138]. In the same reference, the size distribution function that the phase function was generated from is given. It is reproduced in equation 8.2.

$$n\left(r\right) = \frac{6^6}{5!}\frac{1}{r_c}\left(\frac{r}{r_c}\right)^6 exp\left(\frac{-6r}{r_c}\right) \tag{8.2}$$

In equation 8.2, $n(r)$ is the fraction of particles with radii between r and $r + dr$. The radius at which n is a maximum is given by r_c, taken to be 4 μm here. This information was used to create the phase function in figure 8.1 using 1000 spheres of different radii over the size parameter range from 25 to 75 as detailed in Arking and Potter [138].

The truncated phase function was used in the Monte Carlo radiative transfer code to reproduce the case of Potter [137] figure 4 to ensure that it had been implemented correctly. The system is used in all of the forthcoming calculations.

8.3 Candidate Crystal Geometries

In the radiative transfer studies, a selection of crystal geometries are considered as candidate representative cirrus geometries. The hexagonal column (chapter 4), the droxtal (section 5.5) and the three reconstructed ice analogue geometries (section 6.2) have been encountered in the preceding chapters. In this case, the hexagonal column is taken to be have an aspect ratio $L/2r = 2$ with size

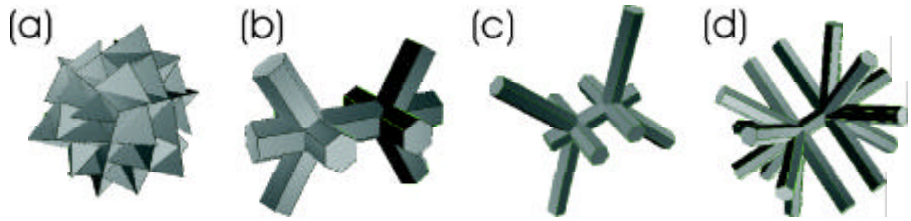

Figure 8.2: (a) An example of a polycrystal or Koch-fractal. (b) SDC_v1 (c) SDC_v2 (d) SDC_v4

parameter 50. The droxtal has its sphericity maximised by volume with a circumscribing sphere of size parameter 50. When size distribution functions are used (sections 8.6 and 8.7), the crystal dimensions are scaled appropriately.

There are two geometries that will be considered in this chapter that have not yet been discussed. The first is the polycrystal or Koch-fractal, built from a tetrahedral initial shape. The 25 μm example used here is shown in figure 8.2a and is a Koch-fractal of the second generation. The GO single scattering properties of the polycrystal have been investigated by Macke, for example [23]. The phase function of the polycrystal remains unchanged when investigating examples of different sizes. The polycrystal does not represent a realistic cirrus ice crystal but is normally used to model the very complicated and irregular ice particles that can be found in the lower regions of cirrus. Radiative transfer calculations using GO phase functions for this polycrystal have been previously published and so it doubles as a useful test case.

The second new geometry is that of the *Spatial Double Centred* (SDC) crystals. These crystals were constructed as the study progressed in a bid to increase scattering above 90° and to provide an alternative crystal geometry to be used to represent the larger more complex crystals within cirrus.

The three SDC crystals that were considered are shown in figures 8.2b, 8.2c and 8.2d. It was found that the first two cases did not have a significant effect when compared to a hexagonal column and were put to one side. The final case, SDC_v4, was introduced with so many arms specifically to increase scattering above 90° because when considering bullet rosettes, the increase in scattering above 90° compared to a single bullet is almost totally due to multiple external reflections from arms. This crystal produced very limited success but is included here to illustrate how very complex crystals do not necessarily change the scattering characteristics of a cloud as much as one might intuitively expect.

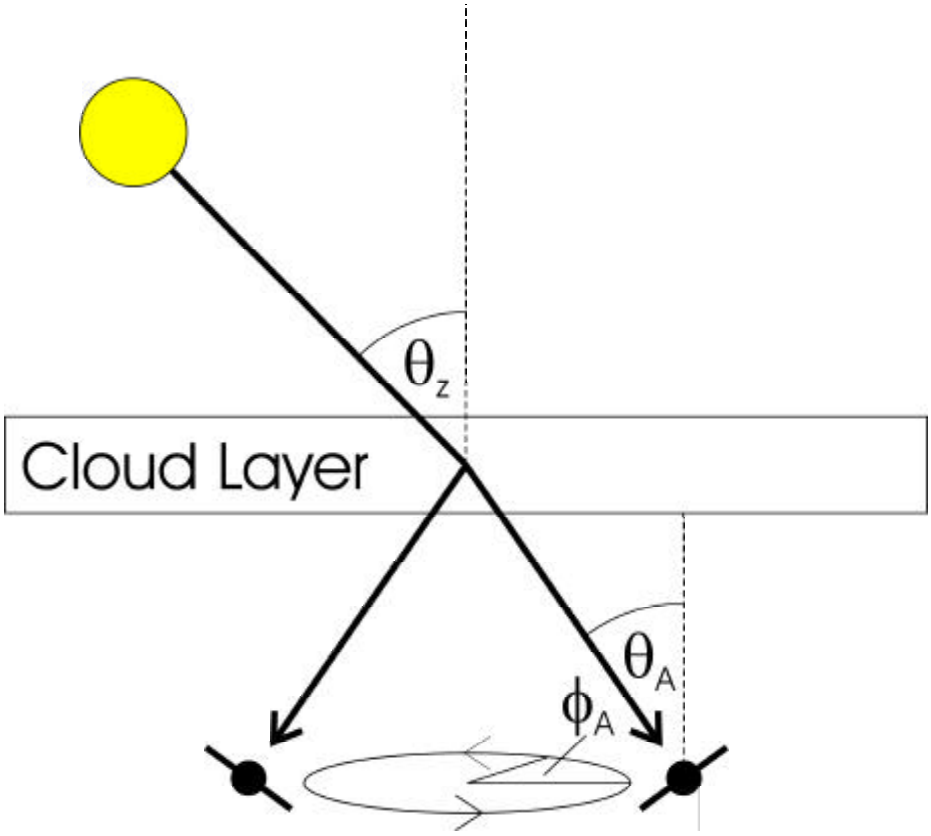

Figure 8.3: A diagram of an aircraft taking radiance measurements. Solar radiation is incident at a solar zenith angle of θ_z. The aircraft is banked at an angle of θ_A. The aircraft orbits below the cloud collecting measurements at azimuthal angles given by ϕ_A.

The *Analytic Phase Function* (APF) [90] will also be considered. The APF is based upon the Henyey-Greenstein phase function [139] with some modifications. The APF represents the scattering by an ensemble of nonspherical ice crystals. The APF is calculated using a set of of analytic expressions that depend on only one variable, the asymmetry parameter g. The APF is found to model the scattering of cirrus well and so can be used as a test case to which calculations from crystal geometries can be compared.

8.4 The Aircraft Radiance Measurements

Aircraft radiance measurements taken from three cases of cirrus will be considered in this chapter. All of the data have been provided by the Met Office

and were sampled using the Met Office C-130 aircraft. A schematic diagram of the aircraft taking the radiance measurements is shown in figure 8.3. In all of the cases considered in this chapter, the aircraft performed banked orbits below the target cloud. As the orbit proceeds, measurements are taken at a range of azimuthal angles, ϕ_A. The azimuthal angle is measured in a horizontal plane and represents the length of arc on the horizon. The azimuthal angles can be converted to scattering angles using the solar zenith angle θ_z and the aircraft orbit banking angle θ_A which also define the scattering angle range that can be considered.

In the following the flights will be referred to by their flight numbers. This section will provide a brief description of the three cirrus cases including the values of the solar zenith angle and the aircraft orbit banking angle for the specific sets of data that have been used. The data from flights A435 and A189 included in this chapter have been previously published in Baran et al. [90] (both flights), Francis et al. [89] (flight A435) and Francis [140] (flight A189). The flights are described in more detail in those references. The third flight, A802, is described in more detail in Baran and Francis [141]. The data included in this chapter from flight A802 are not the same as those published in [141] because they were sampled at a different time.

On 9th November 1995 radiance measurements were taken from a thin layer of frontal cirrus off the north-eastern coast of England. This flight is referred to as flight A435. The data made available from flight A435 to this study corresponds to an aircraft orbit banking angle of 53°. The solar zenith angle in this case was 74°, leading to sampled scattering angles between approximately 20° and 127°. This study considers radiance measurements taken during the flight at wavelengths of 0.87 μm and 1.61 μm. This is the flight studied in figures 4 and 7 of Baran et al. [90]. Cloud top was measured at 9.45 km with the cloud base at 7.10 km, although some variation was recorded. The data were sampled during orbit number 4.

Flight A189 occurred on 23rd April 1992 off the north-east coast of Scotland and took measurements from a layer of cirrus associated with a cold front that had passed over the UK the night before. The aircraft was banked at an angle of 30° with a solar zenith angle of 54.1°. This corresponds to sampled scattering angles between approximately 30° and 80°. The measurements considered here were taken at a wavelength of 0.55 μm during orbit number 1. This sample of cirrus had the cloud top at 9.9 km and the cloud base was at 7.0 km.

Flight A802 took radiance measurements on 17th October 2000 from a layer of cirrostratus over the Orkney Islands that was in advance of a warm front approaching the British Isles from the west. During the considered orbit below the cloud the aircraft banked at an angle of 60° with a solar zenith angle of 72.5°. This corresponds to scattering angles between approximately 16° and 131°, the largest angular range available in this study. Cloud top was measured to be at 9.75 km with cloud base at 8.5 km. This study considers measurements at wavelengths of 0.87 μm and 1.61 μm. The considered orbit was orbit number 1.

8.5 Single Crystal Clouds

In this section a single cloud layer will be modelled where all of the constituent crystals are identical in size and shape. This is not at all realistic but such a consideration will give a good indication of whether a single crystal geometry can be used as a representative geometry for a given set of radiance measurements. The dimensions of the crystals were given in section 8.3.

Three wavelengths are used in the calculations presented in this chapter, $\lambda = 0.55$ μm, $\lambda = 0.87$ μm and $\lambda = 1.61$ μm. The refractive indices for ice at these wavelengths are taken from Warren [110]. The values are $n_r = 1.3110$ and $n_i = 3.11 \text{ x } 10^{-9}$ for $\lambda = 0.55$ μm, $n_r = 1.3037$ and $n_i = 2.65 \text{ x } 10^{-7}$ for $\lambda = 0.87$ μm and $n_r = 1.2889$ and $n_i = 3.372 \text{ x } 10^{-4}$ for $\lambda = 1.61$ μm.

8.5.1 Flight A435: Comparisons at $\lambda = 0.87$ μm

Figure 8.4 shows the single crystal cloud calculations for the hexagonal column, the droxtal, the polycrystal and the APF compared to measured radiances from flight A435 at $\lambda = 0.87$ μm. Calculations for both GO and RTDF are shown for the crystal geometries. In the interests of clarity, the comparisons are offset for each case by a factor of ten. The best fit values for the optical depth τ for the GO and RTDF results are given in table 8.1. The APF result corresponds to a value of $\tau = 0.78$ which agrees with previously published work [90].

The first thing to notice is that the improvements that the RTDF model provides over GO are still apparent following a radiative transfer treatment. This justifies

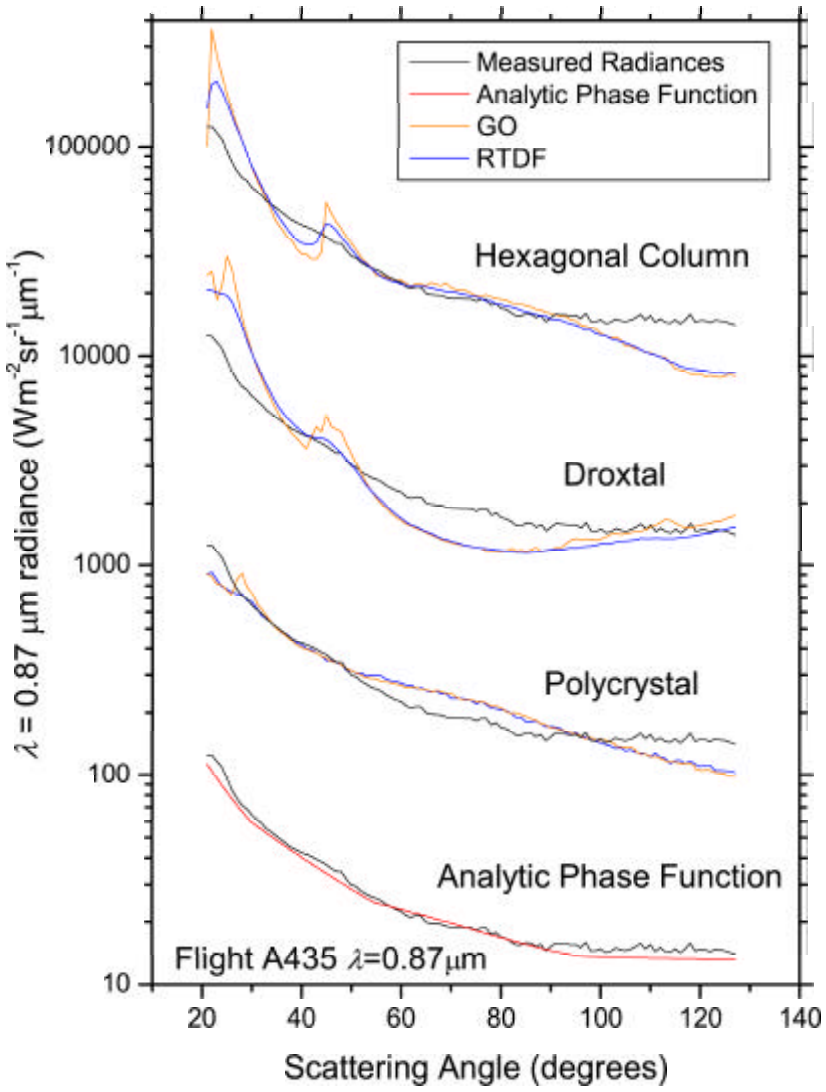

Figure 8.4: Radiative transfer calculations using GO and RTDF for the hexagonal column, the droxtal, the polycrystal and the analytic phase function compared to radiance measurements from flight A435 at $\lambda = 0.87$ μm. Model radiances are generated using best fit values of the optical depth, τ.

Crystal Geometry	τ (GO)	τ (RTDF)
Hexagonal Column	0.65	0.65
Droxtal	0.75	0.65
Polycrystal	0.49	0.49

Table 8.1: Best fit values for the optical depth τ found from the GO and RTDF results given in figure 8.4.

the use of the RTDF model in multiple scattering calculations and confirms that RTDF effects are not washed out.

The APF result in figure 8.4 is equivalent to the comparison shown in figure 4 of Baran et al. [90]. The result is near identical which verifies that the radiative transfer method used here, different from that used in [90], is functioning correctly. The comparison between the APF and flight A435 in this case is reasonably good across the angular range. Of particular interest is the constant radiance exhibited by the APF above a scattering angle of 95°. This same behaviour is clearly visible in the measured radiances from around 90° onwards and will be referred to repeatedly in the coming discussion.

The GO polycrystal result in figure 8.4 is equivalent to the comparison shown in figure 8 of Francis et al. [89]. The result compares well with the published work indicating that the procedures employed for handling phase functions generated using codes based upon the Macke GO code are correct. The GO polycrystal result does not compare well to the measured radiances except between 30° and 50°. The shape of the profile across the rest of the angular range is quite different. The RTDF polycrystal result smooths the halo totally, producing a more realistic featureless plot. The overall shape of the RTDF polycrystal profile still does not provide a very good fit, although it is much improved with the halo removed. The polycrystal produces high side scattering and underestimation of the measured radiances above 95°. This is in large contrast to the APF.

One might expect the hexagonal column to provide very good comparisons to measured radiances, given the prevalence of the geometry in cirrus and the fact that crystals based upon the geometry such as rosettes that are also very common scatter in a similar manner. The result in figure 8.4 shows that this is not the case. The halos are much too prominent in the calculated radiances, perhaps indicating that the chosen column is too large. The scattering above 90° does not become constant or show any movement towards such behaviour,

something that can also be seen in much smaller hexagonal columns (for example section 3.5.2 figure 3.14) which shows that a smaller hexagonal column would not improve the comparison across the angular range. There is reasonably good agreement between 50° and 90°. The result suggests that the hexagonal column on its own is not a good representative geometry for the present case.

A constant behaviour as seen in the APF above 95° is very difficult to reproduce using the types of crystal geometries that are found in cirrus in conjunction with GO based methods. The question of increasing scattering above 90° can be addressed in part using a droxtal. The droxtal result in figure 8.4 shows a steady rise in scattering above 80°. This provides the rare case of the phase function increasing in the scattering region immediately above 90°. This suggests that droxtal-like geometries may be useful in modelling cirrus. This will be discussed further in section 8.7. Overall, the droxtal does not compare well with flight A435 at this wavelength and is a worse fit than the hexagonal column when χ^2 values are compared. The discrepancy at side scattering is large, although the halo regions are likely to improve if the droxtal is used to represent very small crystals which exhibit much less pronounced halos.

Geometry	τ (GO)	τ (RTDF)	τ (RTDF dist=0.1)	τ (RTDF dist=0.2)
Gros48	0.70	0.55	0.55	-
Ros52	0.85	0.65	0.60	0.60
Ros172	0.60	0.70	0.65	0.65
SDC_v4	0.70	0.65	0.65	0.65

Table 8.2: Best fit values for the optical depth τ found from the GO and RTDF results given in figure 8.5.

Figure 8.5 is a continuation of figure 8.4, considering the same flight data but the geometries of Gros48, Ros52, Ros172 and SDC_v4. The best fit values of τ are given in table 8.2. The concept of distortion of crystal facets to simulate rough surfaces is introduced in this figure to illustrate the effect that it has in further smoothing halos and to investigate if such smoothing can assist in correcting the underestimation of scattering above 90°. During each ray-facet interaction, the facet normal is tilted randomly about its original direction. The tilt angle is calculated randomly to be between 0 and θ_d^{max} where θ_d^{max} is defined using equation 8.3. In this equation, d is the distortion value that is quoted in the figures and is always between 0 and 1. More information is available in Macke et al. [23].

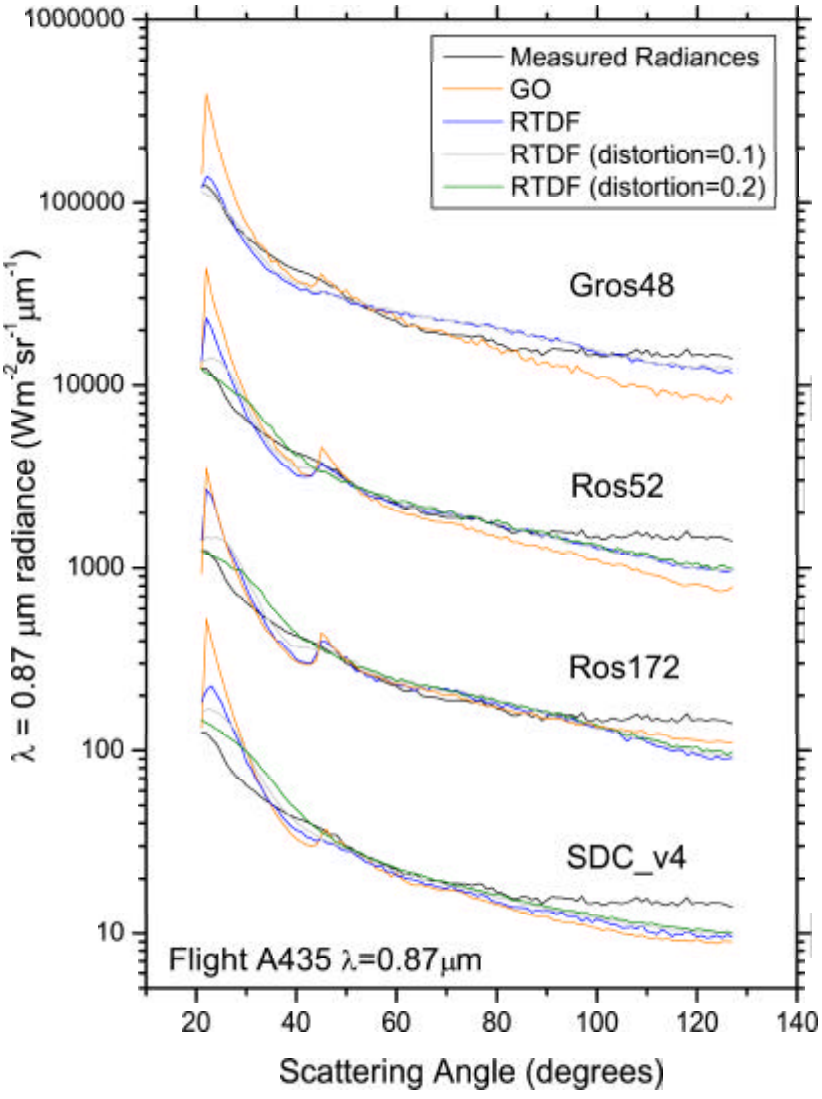

Figure 8.5: Radiative transfer calculations using GO and RTDF for Gros48, Ros52, Ros172 and SDC_v4 compared to radiance measurements from flight A435 at $\lambda = 0.87$ μm. Model radiances are generated using best fit values of the optical depth, τ.

$$d = \frac{\theta_d^{max}}{90^\circ} \tag{8.3}$$

The GO results in figure 8.5 are all similar. The clearest visible difference is in the strong 46° halo which is smallest for Gros48. The difference arises because the pure halo ray paths are less able to exist in the compact Gros48 structure. The large GO halos result in poor comparisons to the flight data, the χ^2 minimization treatment ensuring that the scattering at larger angles falls well below the measured radiances.

The RTDF results allow a more clear distinction between the geometries. The use of the RTDF model for Gros48 has a large effect on the GO profile. It exhibits a much improved 22° halo treatment with complete smoothing of the 46° halo. Side scattering is significantly increased and although this means that above 90° the result is close to that of the flight data, the shape of the profile across a wider angular range is incorrect. Although the results presented are best fit comparisons, to consider how appropriate a given phase function is to reproducing the radiance measurements over individual angular ranges the shape of the scattering in those regions is the main indicator. It should not go unnoticed then that the RTDF result for Gros48 reproduces the shape of the scattering above 110° reasonably well. Introducing mild distortion of 0.1 has some further effect on the 22° halo. However, the shape of the halo has passed at this level of distortion the shape of the radiance measurements, suggesting that further distortion would not improve the comparison. This was indeed found to be the case on further investigation but the increased distortion plots are omitted in the interests of clarity.

Ros52 is a less compact and larger crystal than Gros48. This means that the lengths of RTDF effective slits are likely to be longer and so deflections will be less pronounced. This is illustrated in the RTDF Ros52 result where the halos are still visible. However, the reduction in the halos results in a better balance compared to GO giving good agreement between 50° and 90°. The shape of scattering above 90° is still incorrect, not being strong enough compared to the measured radiances. The introduction of distortion does not affect the scattering above 50° at all. The halos are further smoothed, a distortion value of 0.2 reducing the 22° halo to a small hump and the 46° halo to nothing. The shape comparison in the halo regions is still not good but further distortion leads to poor shape agreement near 20°. In all of the RTDF cases for Ros52, above 90° the profile is similar to that of the polycrystal.

Ros172 is a large crystal of simple structure. The RTDF behaviour of the crystal is seen to be close to the GO result in figure 8.5. The overall shape of the profile differs little from the Ros52 results, particularly once facet distortion is introduced. One notable difference is the enhanced halos because of the increased crystal size and simplicity. The similarities to Ros52 result are to be expected given the similarity in the single scattering properties of the two crystals, as discussed in section 6.5.

The SDC crystal provides results that are very similar to Ros52 and Ros172. The aim of the SDC crystals was to create a 3D spatial crystal that would be a better fit than Gros48 and Ros52 above 90° by increasing side scattering. When comparing the SDC phase function to that of a hexagonal column, some increase in side scattering is seen but it does not translate to a significant change in profile shape in the radiative transfer results, as shown in figure 8.5. Given the similarity in the radiative transfer result, the SDC crystal can therefore be replaced by one of Ros52 or Ros172.

The results in figures 8.4 and 8.5 have shown that using crystals whose geometries are based upon hexagonal columns leaves two main problems in comparing to this flight data case. The first is the halo region, although this can be rectified to some extent using facet distortion or by using other methods for smoothing the halos which will be mentioned in section 8.6. The second problem is the underestimation of scattering above 90°. Referring back to the APF result, if one were able to introduce a constant radiance above 90° there would be a significantly improved comparison to flight A435. As will be shown in the coming sections, this feature is not restricted to this one cirrus case at this wavelength.

8.5.2 Flight A435: Comparisons at $\lambda = 1.61$ μm

The results in section 8.5.1 showed that the improvements offered by RTDF over GO persist following radiative transfer calculations. As a result, for the rest of this chapter the GO results will be omitted.

Figure 8.6 provides comparisons to flight A435 measured radiances at $\lambda = 1.61$ μm. The geometries considered are Gros48, Ros52, Ros172 and the droxtal. The best fit values of τ are given in table 8.3. Overall, the results are very similar to the $\lambda = 0.87$ μm results in the last section for each geometry. The absorption introduced at $\lambda = 1.61$ μm has a small effect in restricting the

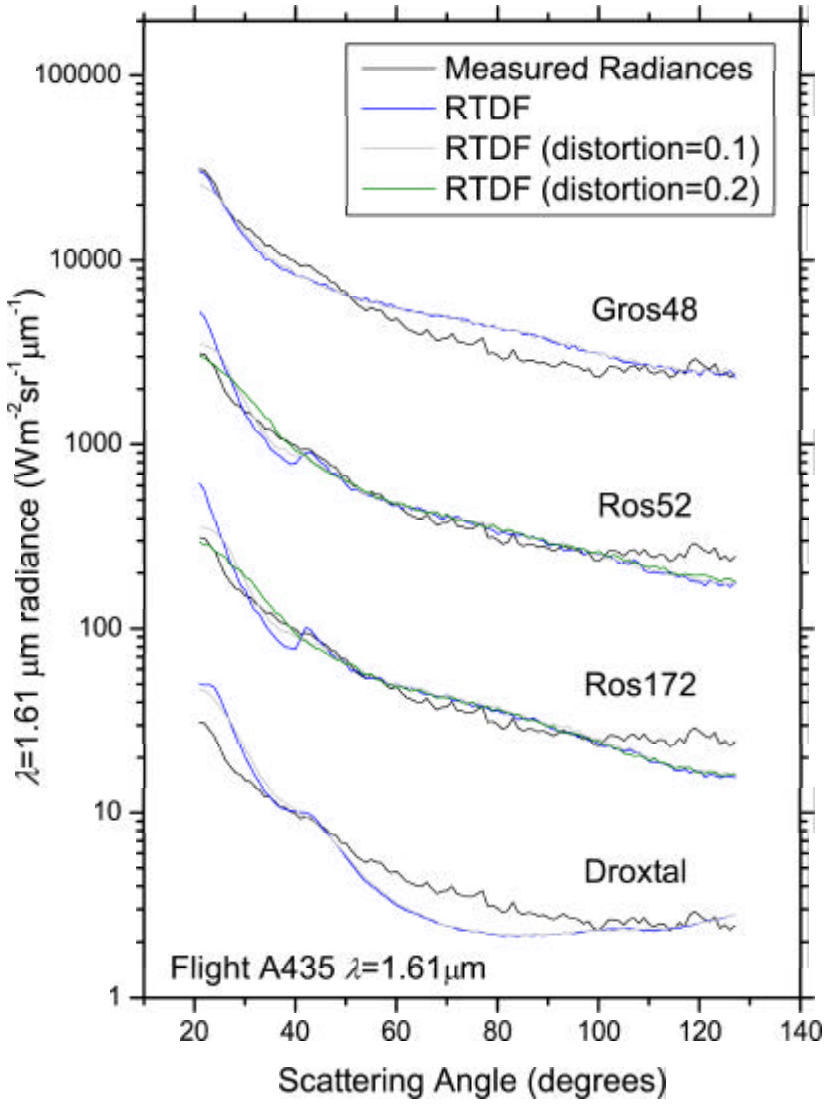

Figure 8.6: Radiative transfer calculations using the RTDF model for Gros48, Ros52, Ros172 and the droxtal compared to radiance measurements from flight A435 at $\lambda = 1.61$ μm. Model radiances are generated using best fit values of the optical depth, τ.

Crystal Geometry	τ (RTDF)	τ (RTDF dist=0.1)	τ (RTDF dist=0.2)
Gros48	0.50	0.50	-
Ros52	0.80	0.75	0.75
Ros172	0.80	0.75	0.70
Droxtal	0.55	0.55	-

Table 8.3: Best fit values for the optical depth τ found from the GO and RTDF results given in figure 8.6.

halo strength, most noticeable in the Gros48 result where the best fit RTDF result compares better across the angular range with the measured radiances in terms of absolute radiances. The undistorted RTDF Gros48 result gives good shape and scale agreement around the 22° halo and above 110°. After distortion, the halo smooths further and the agreement worsens. In both cases the scattering pattern is still clearly incorrect between 30° and 110°. The shape of the profiles do not improve significantly for any of the other three geometries with respect to the comparisons at $\lambda = 0.87$ μm. Distortion is used for the first time in the case of the droxtal but it does not improve the comparison and if taken to larger distortion levels actually harms the comparison.

The similarity between the results for Ros52 and Ros172 is again visible in these results. As a result of this, it is sensible to stop using Ros172 as a candidate crystal. The results will continue to closely resemble those from Ros52 so producing no scientific benefit.

8.5.3 Flights A189: Comparisons at $\lambda = 0.55$ μm

The calculations in the preceding sections assumed an input radiance of 1 and then used a calculated cloud top radiance as a scaling value. The given value was supplied with the data. Such a value was not available for all of the cases because when some of the measurements were taken it was not possible to produce a valid radiometric calibration for the radiometer. An alternative mechanism is employed in the remaining cirrus cases, as described in Francis [87]. A scattering angle is selected at which all of the model radiances are scaled to the measured value. At this scattering angle, an arbitrary value of unity is used for all radiances. The scattering angle is chosen by inspecting the model phase functions to be considered and identifying the scattering angle at which they exhibit the most agreement. This system means that the figures that follow

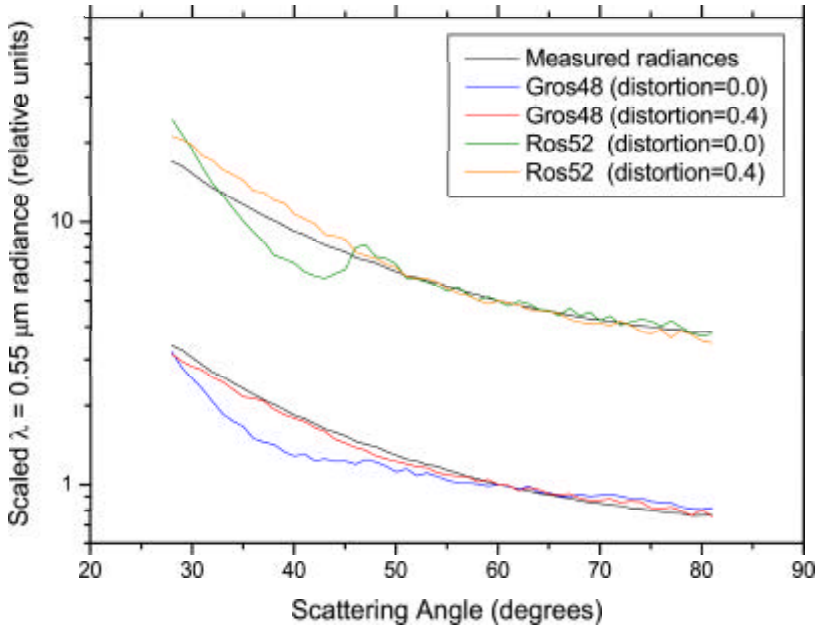

Figure 8.7: Radiative transfer calculations using the RTDF model for Gros48 and Ros52 compared to radiance measurements from flight A189 at $\lambda = 0.55$ μm.

investigate how the radiances change with scattering angle (the shape of the profiles) rather than comparing absolute radiances. The best fit optical depth is not as important a quantity in this system because the variation of radiance with scattering angle is not very sensitive to changes in the optical depth. Given clearly defined halos, a best fit optical depth will be unrealistically high compared to the values considered in the case of flight A435. In each figure that follows using this system, the optical depth is kept at a constant value. This will not hinder the search for answers to the questions raised in the previous sections.

Due to the solar zenith and aircraft orbit banking angles during the orbit in flight A189 that provides the available data, the scattering angle range is significantly lower when compared to the cirrus case discussed in the preceding sections. The data available from flight A189 were measured at a wavelength of $\lambda = 0.55$ μm. The radiances were scaled to unity at a scattering angle of 60°. Figure 8.7 shows comparisons to the measured radiances using RTDF for Gros48 and Ros52. The optical depth is kept constant at $\tau = 0.50$. Following strong facet distortion to a

value of 0.4, Ros52 gives reasonable agreement above 50°. The same strong facet distortion yields very good agreement for Gros48. However, further study was not pursued in this case because of the radiance measurements being confined to an angular range of approximately 30°-80°. It is highly likely that if a wider angular range were available the Gros48 result would fail above 90° as shown in earlier sections. Using such strong distortion, it is possible with Gros48 to gain similar best fit agreement to that shown in figure 8.7 over the same restricted angular range using flight A435 data. This emphasizes the need to study as wide a range of scattering angles as possible when studying observation data.

8.5.4 Flight A802: Comparisons at $\lambda = 0.87$ μm

Given the importance of studying wide angular ranges, the next cirrus case to consider is flight A802 which provides data with a wide angular range. It is important to note that the results from flight A802 are very similar to A435. This is shown in figure 8.8 where the $\lambda = 0.87$ μm and the $\lambda = 1.61$ μm data from the two flights are plotted together, scaled to unity at a scattering angle of 45°. The overall shape agreement is good for both wavelengths except in the halo regions, forward of 30°. It would appear that in contrast to flight A802, flight A435 had a small halo feature present. This is visible in the results from both wavelengths. Given that this indicates a difference in the cloud composition, it is interesting to note that the constant behaviour above 90° is present for both cirrus cases. One thing to note is the wide variability of the A802 $\lambda = 0.87$ μm plot. Though not desirable, this does not prevent the important trends being observed. As in the case of the A435 and A189 flights, the data is binned in 1° steps. It is possible to gain a much smoother trend using a larger bin step but for consistency the value of 1° is used throughout this chapter.

Figure 8.9 shows comparisons to flight A802 at $\lambda = 0.87$ μm for Gros48, Ros52, the droxtal and the APF. The results are scaled to unity at 45°. The optical depth is kept constant at $\tau = 0.90$. The distortion effects are not included here to enhance the figure clarity. The effect that facet distortion has is clear from the previous cases.

The comparisons of Gros48 and Ros52 differ little from the equivalent flight A435 comparison except that the lack of a halo signal in the flight data makes the model halos stand out. It is interesting to note that if the halos were sliced away, like the RTDF polycrystal result compared to equivalent GO result in figure 8.4,

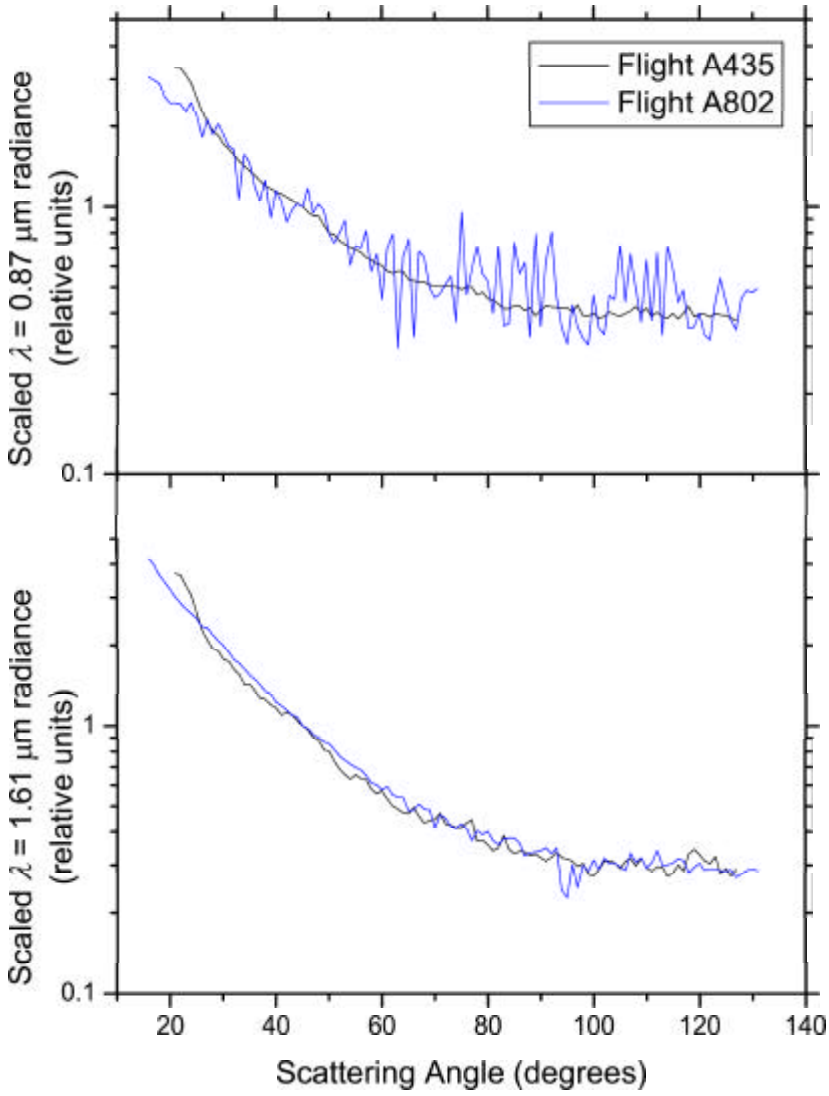

Figure 8.8: A comparison of the aircraft measured radiances from flights A435 and A802 at $\lambda = 0.87$ μm (top) and $\lambda = 1.61$ μm.

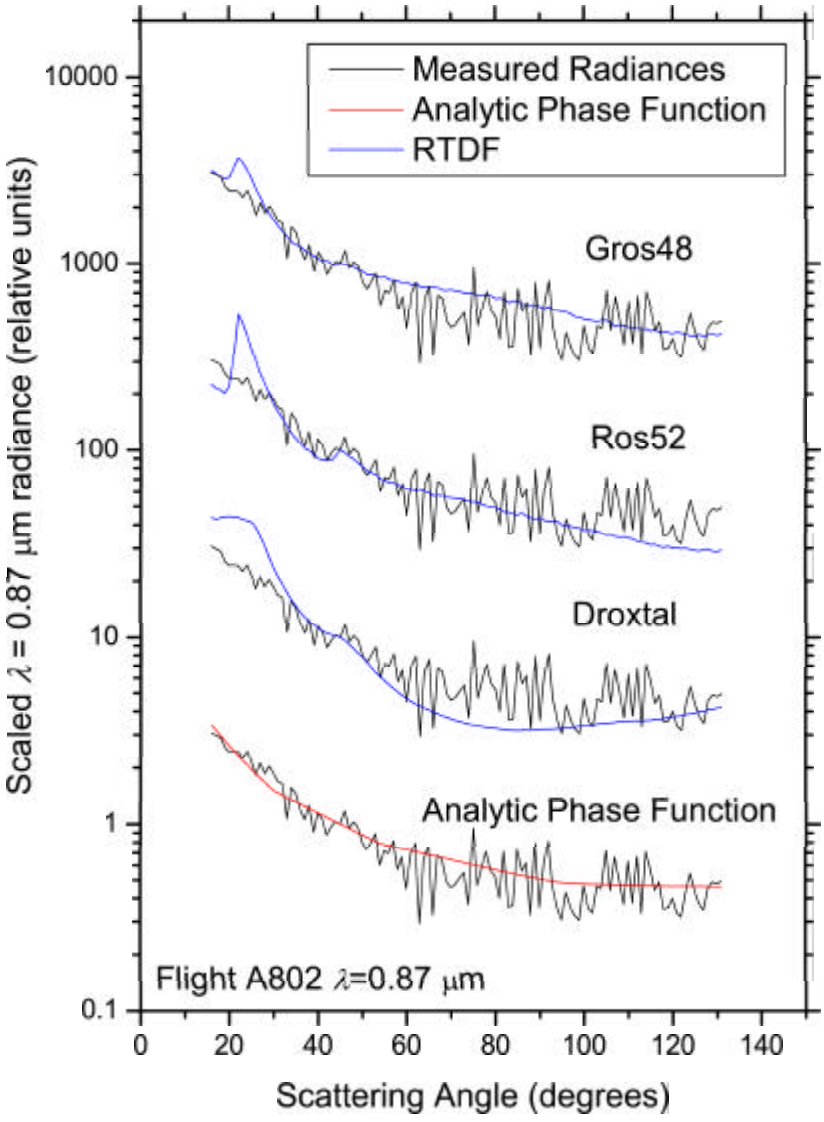

Figure 8.9: Radiative transfer calculations using the RTDF model for Gros48, Ros52, the droxtal and the analytic phase function compared to radiance measurements from flight A802 at $\lambda = 0.87$ μm. Radiances are scaled to unity at 45°.

then the comparison would be much improved. Strong distortion would help in this matter. The lack of constant behaviour above 90° persists. The droxtal comparison again differs little from the equivalent flight A435 comparison.

The APF result offers by far the best comparison and is a closer fit than in the equivalent flight A435 case. The asymmetry parameter in this APF result is taken to be $g = 0.70$ which is lower by 0.10 when compared to the flight A435 comparisons. The lack of the halo in the flight A802 data is the reason for the improved comparison, matching better the featureless APF.

8.5.5 Flight A802: Comparisons at $\lambda = 1.61$ μm

Figure 8.10 shows $\lambda = 1.61$ μm comparisons to flight A802 for Gros48, Ros52 and the droxtal. The radiances are scaled to unity at 45°. The optical depth is kept constant at $\tau = 0.50$. At this wavelength it is easier to see the that the A802 comparisons resemble the equivalent comparisons for flight A435 data and how the lack of any halo peak in the measured radiances harms the comparison with the hexagonal column based crystals.

It is clear from these results that none of the geometries that have been presented are good representative geometries for modelling the cirrus cases considered in this chapter. The indication from the results is that no single geometry will be able to model cirrus accurately using the single geometry cloud model.

Interestingly, a combination of the three geometries used in figure 8.10 would provide a reasonably good shape comparison across the angular range. Gros48 smooths the halos due to its compact nature and large RTDF deflections and the comparison below 50°, though not correct, is the best available without large amounts of facet distortion. Between 50° and 90° the result from Ros52 that so closely resembles an individual hexagonal column provides good shape comparison. Immediately above 90°, the only geometry that has been considered that provides a levelling or an increase above 90° is the droxtal. Although it exhibits a steady increase, a deviation from geometries that are based upon hexagonal columns such as a droxtal is essential in recreating this because even strong facet distortion does not alter the profile of a hexagonal column significantly in this angular range. Of course it is not possible to patch together phase functions to construct this ideal comparison but it may be that it is possible to use combinations of geometries and crystal sizes to better model the radiative

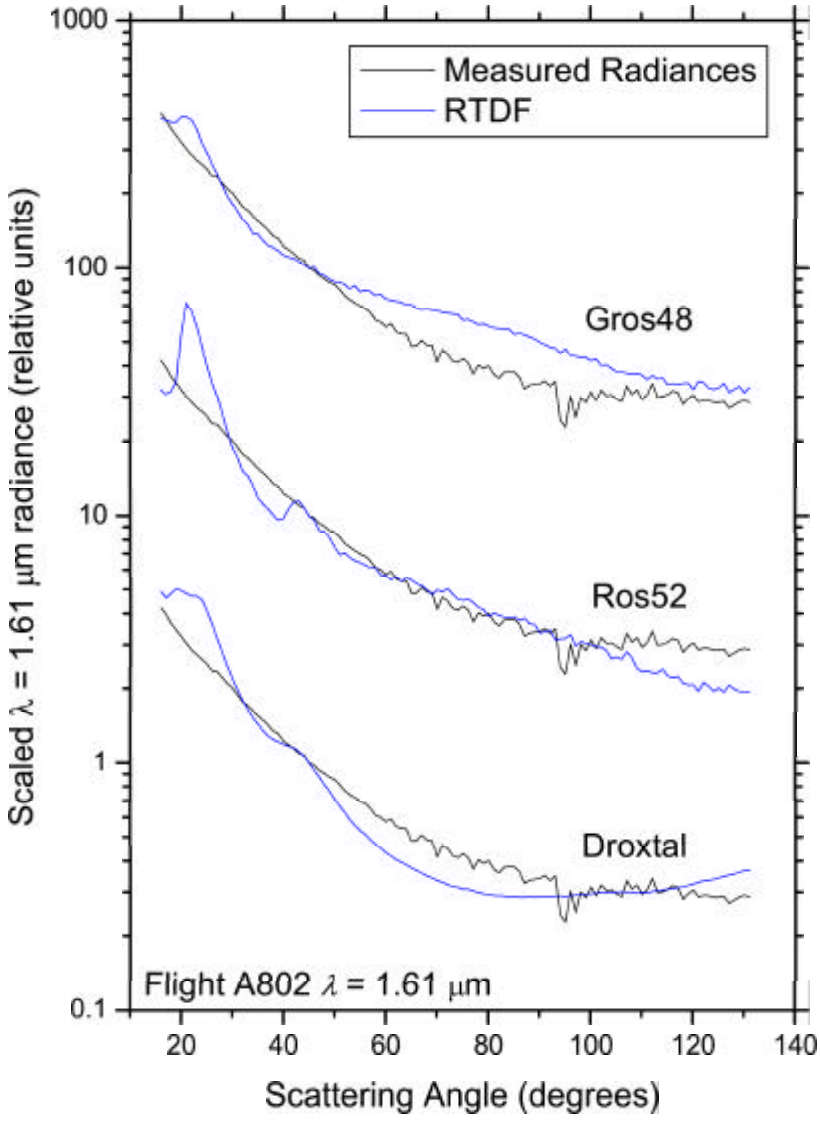

Figure 8.10: Radiative transfer calculations using the RTDF model for Gros48, Ros52, and the droxtal compared to radiance measurements from flight A802 at $\lambda = 1.61$ μm. Radiances are scaled to unity at 45°.

properties of cirrus. The first step towards this is to consider size distribution functions.

8.6 Size Distribution Functions

A cloud of ice particles where every constituent member is identical is not very realistic. Ideally, a range of geometries is required that covers a range of crystal sizes. This makes the cloud very complicated and introduces many variable factors. To maintain the simplicity of the case initially, this section will consider a cloud of crystals of identical geometry but that are scaled over a range of sizes using a *Size Distribution Function* (SDF).

The size distribution functions used in this study come from two sources. Fu [142] attempted to parameterize the solar radiative properties of cirrus by combining IGO results with 28 size distribution functions. Mitchell et al. [143] provide a further two size distribution functions.

To scale geometries over a range of sizes, it is necessary to define the crystal size in some way. This is achieved by using the maximum dimension. The concept originates from the maximum dimension possible in a 2D projection of the shape of the crystal in a given orientation. It is used to classify particles using images of crystals taken by in-situ probes. In this case where phase functions generated by randomly oriented crystals are being considered, the maximum dimension is taken to be the maximum distance within the crystal. This is the same as the definition that was used in section 6.2.

All 30 size distribution functions used in this chapter have 24 size bins considering values of the maximum dimension from $D = 3$ μm to $D = 3100$ μm. For each bin a value for the size distribution function is given indicating how strongly represented crystals of that particular size should be within the cloud.

In utilising the size distributions, the phase functions and accompanying data for all of the 24 crystal sizes need to be created. This information can then be integrated over the size distribution function giving a representative phase function for the cloud. This representative phase function can be used as the input for the radiative transfer method described in section 8.1.

It is possible using crystal geometries within a size distribution function to cal-

SDF	Ros52	Gros48
17	**5.413**	**13.051**
24	6.345	15.301
25	6.499	15.676
7	7.339	17.696
26	8.719	21.038
20	9.097	21.940
14	12.327	29.747
21	13.179	31.795
30	14.961	36.137
6	**15.168**	36.588
5	17.336	**41.818**
27	20.415	49.293
8	22.789	54.990
16	25.937	62.577
28	26.527	64.050
29	27.578	66.527
19	27.633	66.719
9	**30.421**	73.430
4	30.557	73.758
22	34.203	**82.548**
18	37.033	89.394
2	**39.412**	**95.142**
10	41.434	99.991
23	53.683	129.606
11	53.901	130.142
3	54.394	131.331
13	56.183	135.658
1	56.244	135.793
12	58.146	140.406
15	**66.099**	**159.664**

Table 8.4: Calculated values of D_e for the crystals considered over the 30 size distribution functions used in this study. The table has been sorted to give ascending values of D_e. Values shown in bold that are underlined are those chosen as representing a range of D_e values for the crystal in question and so considered as a candidate best fit D_e.

culate a value known as the mean effective diameter, D_e. It links the *Ice Water Content* (IWC) of the cloud to the geometry of the crystals. The definition used here is taken from Baran et al. [144]. An equivalent definition of a mean effective radius could be used that differs only by a factor of two [88]. The mean effective diameter is given by equation 8.4.

$$D_e = \frac{3}{2}\frac{\int V(D)n(D)\mathrm{d}D}{\int P(D)n(D)\mathrm{d}D} = \frac{3}{2}\frac{IWC}{\rho_{ice}A_c} \tag{8.4}$$

In equation 8.4, $V(D)$ is the volume of a given crystal, $P(D)$ is the projected area of a given crystal (in the case of random orientations, this is an average value), D is the maximum dimension of a crystal and $n(D)$ is the size distribution function as detailed above. The mass density of bulk ice is given by ρ_{ice} and is set to unity. It is included to ensure that the units in equation 8.4 are consistent. A_c is the total cross sectional area of ice crystals per unit volume.

Table 8.4 provides the values of the mean effective diameter, D_e, using Gros48 and Ros52 with the 30 size distribution functions considered in this section. Note that Gros48 gives higher values of D_e than Ros52. This is due to Gros48 being a more compact crystal. If one compact crystal and one open rosette with the same volume are considered, the open rosette will have a larger average projected area so leading to lower values of D_e as defined above.

In the following, the reconstructed ice analogue geometries Gros48 and Ros52 are considered in conjunction with the thirty size distribution functions. Five of the size distribution functions are chosen for each crystal to represent the full range of values calculated for D_e. A best fit value of the optical depth using the $\lambda = 0.87$ μm channel is found for all five size distribution functions applied to each crystal. These values are then applied to the $\lambda = 1.61$ μm channel to obtain the best fit value of D_e. There is no scientific reason for not iterating through all 30 size distribution functions to find the best fit D_e but the computer time involved could not be justified for this investigation.

Figure 8.11 shows the radiative transfer results for Ros52 (top) and Gros48 (bottom) using the selected size distribution functions at $\lambda = 0.87$ μm compared to flight A435. Each data set represents a best fit value of the optical depth.

In the case of Ros52, one can see that the size distribution function that is used has an impact upon the shape of the radiative transfer result. Most noticeable is the emergence of the halo features for SDF15, which corresponds to the largest effective mean diameter. This is not surprising because at larger crystal sizes the smoothing of halos by the RTDF model will begin to degrade so producing clearer sharper halos. In general, the halos are smoothed significantly when compared to the radiative transfer results from a cloud of original (single size) Ros52 crystals (compare to figure 8.5) and the general treatment in the halo

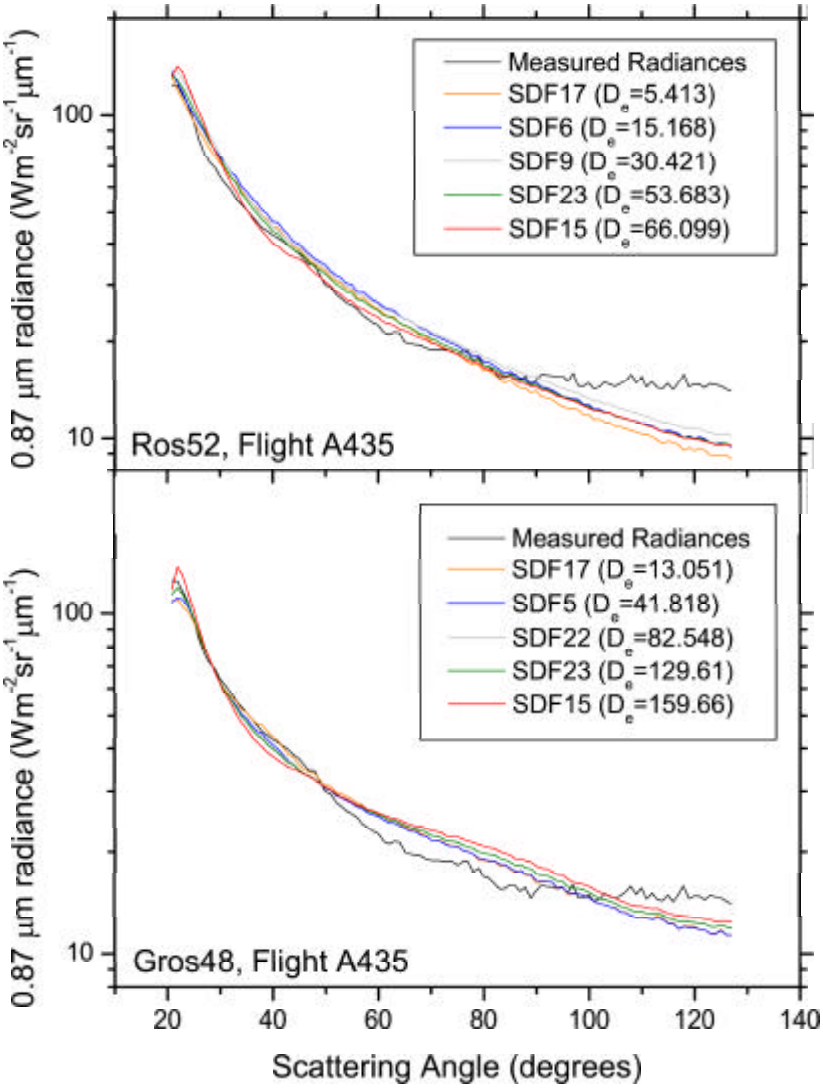

Figure 8.11: Radiative transfer results for a range of size distribution functions applied to the crystals Ros52 and Gros48 compared to radiance measurements from flight A435 at a wavelength of $\lambda = 0.87$ μm.

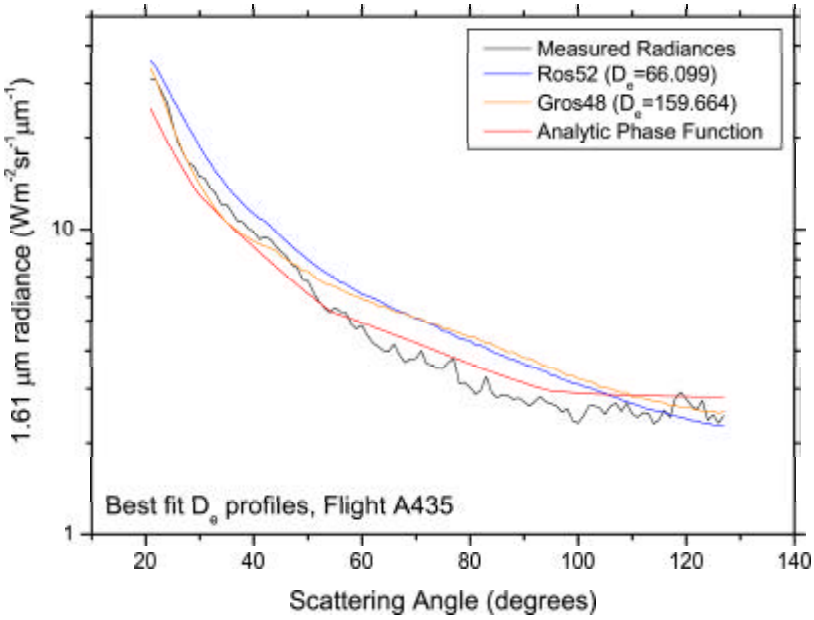

Figure 8.12: Best fit D_e radiative transfer calculations for flight A435 at a wavelength of $\lambda = 1.61$ μm.

region is much improved as a result. The greatest deviation from the radiance measurements comes above 90° as with the single size Ros52 results. The underestimation of scattering above this angle is clear and indicates that this crystal, if used in a scheme to represent the crystals within the cloud sampled by flight A435, must be used in conjunction with other crystal geometries.

In the Gros48 result the halos can again be seen to emerge as the effective mean diameter increases. Note however that for this crystal this only begins to really turn into a peak at a much larger value of D_e. Using the size distribution functions improves the shape comparison with the measured radiances below 50° (compare to, for example, figure 8.5). Above this angle the side scattering is still too high. Above 110° the profiles do level off somewhat but not as noticeably as in the cloud of one size Gros48 crystals. One could not say confidently that the shape of the profiles in this angular range do replicate the radiance measurements well without comparisons at higher scattering angles but the comparison does seem better in this range than for any of the Ros52 results.

The best fit values of the optical depth obtained in figure 8.11 have been applied

to the $\lambda = 1.61$ μm results. From this, a χ^2 minimization technique was applied to assess which size distribution function provides the best fit and hence find a best fit value of D_e. Figure 8.12 shows the best fit profiles for Gros48 and Ros52. An example APF result is plotted for comparison.

One finds from the information presented in figure 8.12 a best fit value of $D_e = 66.1$ μm for Ros52 and $D_e = 159.7$ μm for Gros48. Both these results correspond to size distribution function 15. Unfortunately, both these D_e values are the highest possible given the size distribution functions used for these two crystals. The value is therefore not reliable as a best fit because it cannot be proved that χ^2 is a minimum. A likely explanation for this behaviour is that if Gros48 and Ros52 are not good fits to the aircraft measurements, the value of D_e is likely to become as large as possible. This is because at $\lambda = 1.61$ μm, larger crystals will lead to greater absorption and increasingly featureless phase functions which are likely to provide a better fit.

The APF is seen to give a reasonable result above 60° for the shape of the angular distribution of the measured radiances. It is in this region that the shape of the Ros52 result begins to deteriorate, after appearing to be a reasonable fit to both the APF and the measured radiances up to 50°. In contrast, the shape of the Gros48 profile is poor up to 50° and acceptable between 50° and 90°. The intensity discrepancy seen between both profiles and the radiance measurements in regions where the shape appears reasonable can be due to the value of the optical depth used. More importantly, the intensity discrepancy shows that at this best fit value of the optical depth the balance of scattering is incorrect. If one had a result from radiative transfer calculations for a cloud model which gave better shape agreement across the whole angular range, the intensity discrepancy would disappear. As has been the case throughout this chapter, scattering above 90° does not level off for the ice analogue geometry reconstructions.

In this section it has been shown that using size distribution functions can change the shape of radiative transfer results and have a large effect on halo features, making them more realistic. Using Ros52, one can obtain a very good shape fit for flights A435 and A802 below a scattering angle of 90° but it is still not possible to resolve the problem of the underestimation of scattering above 90°.

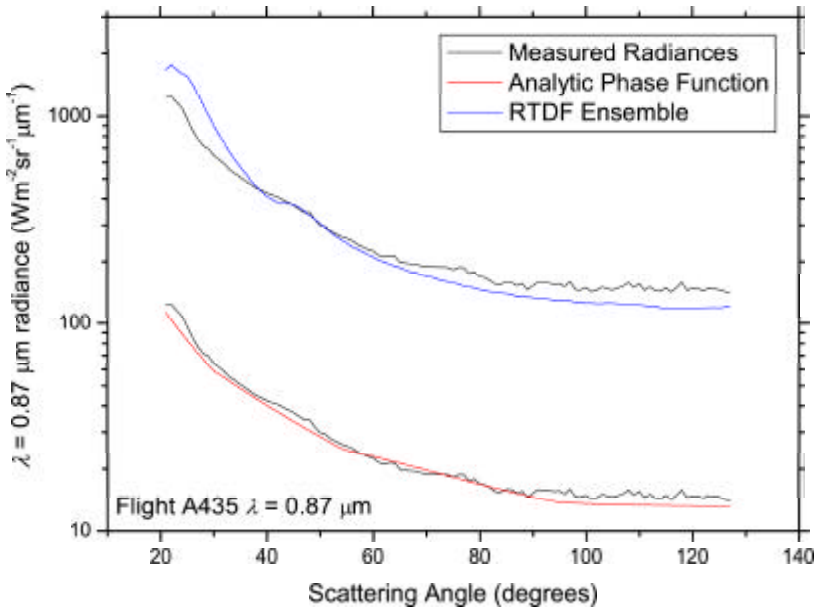

Figure 8.13: Radiative transfer calculations using the RTDF model for a geometry ensemble (see text for details) compared to radiance measurements from flight A435 at $\lambda = 0.87$ μm. Model radiances are generated using best fit values of the optical depth, τ.

8.7 A Combined Size and Shape Distribution Function

The preceding sections have failed to provide a cloud model that accurately represents the aircraft radiance measurements. It is not realistic to assume that the cloud represents a size distribution of only one particle shape that is equally distributed throughout the whole cloud. The next level of complexity is to utilise a size and shape distribution function. Ensembles of crystals were created by applying different geometries to the size distribution function bins. For example, due to Gros48 being compact in nature it could be used to represent smaller crystals. Ros52 being a more open rosette could represent intermediate sized crystals. Large crystals could be represented by the aggregate crystal proposed by Yang and Liou [127], SDCv4 or an 8-arm bullet rosette.

An example ensemble result is shown in figure 8.13 that was generated using

SDF15. In this case, the first four size distribution bins were represented by droxtals, the largest having a maximum dimension of 25 μm. The remaining twenty bins were represented by the geometry of Ros52. The introduction of the droxtal changes the profile at larger scattering angles significantly, helping to level off the profile above 90°. The shape agreement across the angular range is still not sufficient to state that this ensemble satisfactorily represents the crystals in the cirrus case considered but there is a significant improvement above 60° compared to, for example, the results in figures 8.4, 8.5 and 8.11. In figure 8.13, retrieved values of $\tau = 0.78$ for the APF and of $\tau = 0.60$ for the ensemble were found.

Many other combinations of crystals with different size distribution functions have been considered but it was not possible to improve significantly on the results presented in the preceding sections. The main problem remained flattening out the scattering above 90°. Using the droxtal to represent smaller crystals which provides a higher radiance contribution in this angular region was the only method found to address the issue. However, as shown in figure 8.13, use of the droxtal leads to discrepancies at smaller scattering angles.

There are two points that should be considered at this stage. The first point is that apart from the droxtal, all of the crystals studied here are based on pristine hexagonal columns. This leads to all those scattering patterns being related so that large variations in the radiative transfer results are unlikely, even using the RTDF model. Some variation in geometry, like the introduction of the droxtal to the ensembles, is required to model the scattering correctly at all scattering angles. This does not mean that the ice analogue crystals themselves are not realistic cirrus geometries necessarily. It is likely that the cloud modelling requires a more sophisticated approach, something that will be discussed in the next section.

The second point to make is that all of the size distribution functions are weighted by number towards smaller crystals. In the ensembles attempted in this investigation the radiative transfer results were seen to be dominated by the geometry that was used in the smallest size bins. In the case of figure 8.13, the ensemble is bound to fail if a droxtal is not a good representation of small crystals in all of the first four size bins. Further information regarding the nature of small crystals in cirrus is therefore most desirable.

8.8 Discussion

Perhaps the most important result from this chapter is that the improvements made by the RTDF model over the GO model in single scattering results are not smoothed out after the model is used in conjunction with a radiative transfer code. This is an important, although expected, result.

The results in section 8.5 show that a single representative geometry for cirrus is unlikely ever to be found. The examples selected were able to reproduce the aircraft radiances over limited ranges of scattering angles but were not suitable as generally representative geometries. This illustrates the importance of sampling as large an angular range as possible when conducting observations. More complex models of clouds need to be constructed to replicate flight data over wide angular ranges. The size distribution functions in section 8.6 have shown that unrealistically strong halos can be removed if the size distribution functions lean by number to the smaller size bins where halos are naturally smoothed out. Such size distribution functions, although realistic, cause further problems in the creation of clouds with varying crystal size and geometry because the scattering of the geometry in the smallest few bins tends to dominate. Unfortunately the values of the mean effective diameter D_e found using the ice analogue geometry reconstructions and the size distribution functions were not found to be reliable due to the value becoming very large, although it is likely that this was due to the fit to the aircraft data being unsatisfactory.

The main problem in modelling the aircraft radiances was the inability to obtain a correctly shaped scattering profile above 90° which, it would appear, cannot be rectified using crystals that use pristine hexagonal columns as their base. It should be noted that this finding relates only to the test and reconstructed geometries and should not be taken as any conclusion about the actual geometries of the ice analogue crystals. The constant radiance above 90° that is replicated well by the APF is seen in both flights A435 and A802 at two wavelengths and so is not isolated to an individual cirrus case. The formulation of the APF at these scattering angles is itself based upon POLDER [145] data which provide further observational evidence for such behaviour [90]. It is clear from the comparison of the two sets of aircraft data that the clouds in question were different in terms of structure or crystal content to some degree because of the differences in the 22° halo region. Despite this the constant radiance feature persists at scattering angles above 90°. The question of how this constant radiance occurs is important because it suggests a deviation, somewhere

in the single or multiple scattering processes, from the scattering expected from hexagonal based crystals. It is important to remember that the phase functions for hexagonal columns calculated using IGO do not exhibit constant radiance at these scattering angles, for example figure 4.6 in section 4.4. Given the results presented above, it does not seem sensible to speculate about the explanation for this discrepancy between observation and calculation at this stage.

The investigation in this chapter could have been expanded to fill a thesis by itself. There are many combinations of crystal sizes and geometries that could be worth exploring. If more time and resources were available specifically to expand the work in this chapter, there are some steps that would be taken to attempt to improve the comparisons to the measured radiances. For example, in all of the above modelling a single cloud layer has been used. Using multiple layers could help to create a more complete model of a cloud. Within each layer or size bin it may also be beneficial to consider a range of crystal geometries, particularly in the lower levels of a cloud where large complicated crystals are likely to be found. This could be easily achieved by adjusting the radiative transfer code to randomly select which geometry it should use from a list of appropriate geometries in a given section of the cloud for each photon-particle interaction.

Macke [23] suggested that discrepancies between the modelled and observed cirrus radiative properties are most likely due to an inaccurate treatment of the ice crystals single scattering properties. This is true, but it is clear from this chapter that it is necessary to combine accurate single scattering calculations for a wide range of representative geometries with well constructed cloud models to accurately replicate observations across a wide angular range.

It should be noted that facet distortion has been used in several of the figures in this chapter as a method of smoothing the halo regions. Halos can be smoothed in many ways such as simulating rough crystal surfaces by applying facet distortion (an approximation in itself), introducing hollow features to the crystals, distorting the geometries of the hexagonal columns and implementing size distribution functions. In reality, all of these are likely to exist in cirrus and so should be considered when modelling clouds.

Chapter 9

Conclusions

In the preceding chapters, a new model of light scattering applicable to dielectric faceted objects has been introduced. The new RTDF model combines ray tracing with diffraction on individual facets while maintaining the low computational expense of standard GO. The current 3D implementation is built upon a 2D test model for long columns [7, 8] and uses a system of effective slits to make it possible to consider a crystal facet of arbitrary shape. By introducing diffraction at individual facets, a physical optics correction is applied to standard GO that has been derived using exact theory calculations for diffraction at a half-plane.

The model is applicable to all crystals that fall in the size applicability range of the standard GO model. The introduction of a physical optics correction allows that size applicability range to be extended towards smaller crystals, although it is difficult to quantify a lower size limit. It has been shown that the model provides equally acceptable results when applied to crystals below the standard GO size range, although size parameters as low as twenty that would allow comparisons to near exact methods such as T-matrix are considered unreliable. It has also been shown that as the crystal size increases, the RTDF model approaches the GO result asymptotically.

Throughout this thesis, the focus has been the application of the model to the problem of the radiative properties of cirrus ice crystals. The hexagonal nature of ice crystal geometries coupled with the size applicability of the model makes it very difficult to verify the results that the model produces. However, the

model has been tested against SVM and shown to offer significant benefits over standard GO. Comparisons to IGO at visible and near infrared wavelengths have been favourable, especially considering the difference in the computational expense associated with the two models.

Comparisons to light scattering patterns created by an ice analogue hexagonal column in the laboratory have shown very good agreement. The RTDF model offers the possibility of creating 2D scattering patterns that represent scattering on a screen. Unlike GO, the new model can reproduce fixed crystal orientation results in this form as well as averaged random orientations. This makes the model potentially useful in particle characterization. It has been shown that different crystal geometries exhibit unique trends and characteristics that can be used to identify them. Interestingly, studying the RTDF model using this form of results highlighted that the new model not only spreads the direction of rays when compared to GO but it also allows some ray paths to exist that are not present in GO. It is important to note that possible particle characterization applications are not restricted to atmospheric science as there are many possible industrial applications.

The model has been applied to a range of crystal geometries, illustrating the flexibility of the model. Several interesting points arose from these geometry studies that are directly relevant to the study of cirrus. For example, it was shown that hexagonal columns with indentations at the ends, also referred to as hollow columns, can potentially explain rare small angle halos as well as act as a contributory factor to the lack of observed 22° and 46° halos. It was observed that the inner edge of the 22° halo exhibited a gradual change in the degree of linear polarization with increasing indentation. This indicates that polarimetry could potentially be used to identify levels of crystal deformation.

It has been suggested that small crystals in cirrus resemble the droxtal geometry [121]. Crystals below 50 μm are often classified as ice spheres because of a lack of resolution when using in-situ particle instruments. It was shown that not only does a droxtal exhibit large differences from a sphere in the phase function but that the degree of linear polarization bears little resemblance. This means that using ice spheres in models of cirrus clouds could harm the accuracy of climate modelling. It also provides scattering angles at which the two can be discerned.

Bullets and bullet rosettes were considered and the previously known result that a bullet rosette has averaged random orientation scattering properties that

are very close to its constituent bullet was confirmed. The dramatic difference created in the scattering properties of a bullet rosette adopting preferred orientations compared to averaged random orientations as it falls through a cirrus cloud was illustrated. Questions were posed over the modelling of ice aggregates, suggesting that further work in this area would be advantageous.

The model was also applied to three reconstructions of ice analogue geometries. The reconstruction of ice analogue geometries makes comparisons to laboratory measurements of more complex crystals a possibility. Although such comparisons have not yet been made, the reconstructions have allowed comparisons to maximum dimensions, projected areas and volumes determined from CPI data from the actual ice analogue crystals. It was observed that when the CPI was in good focus, the agreement was to within a few percent. Interestingly, the germ rosette Gros48 which is highly nonspherical appears quasi-spherical when photographed by the CPI. This further emphasises the need for better understanding of the geometries of small crystals in cirrus, especially given that the scattering properties of Gros48 were found to be quite different from a sphere or a droxtal.

The model was compared to aircraft radiance measurements provided by the Met Office. A series of crystal geometries including the ice analogue geometry reconstructions were assessed as to their suitability as representative cirrus crystal geometries. It was found that none agreed with the observation data over all scattering angles. A more sophisticated model of a cloud involving size distribution functions and multiple geometries was shown to be required but a successful model of this form was not obtained. Even so, it was seen that there were two main areas of disagreement between observations and crystals of a hexagonal nature. The first was the halo region which was overestimated in the model results. This is not of concern however because the use of realistic size distribution functions which are weighted towards smaller crystals where halos are less prominent smoothes the halo significantly. Several other possible explanations for the lack of halos were provided. The second area of disagreement was above 90° where two different cirrus cases exhibited a constant radiance. The phenomenon was observed in two wavelength channels for both cases. This constant radiance behaviour is commensurate with the analytic phase function which agrees with cirrus observations well. It was found that no hexagonal based crystal could replicate this behaviour, even by assuming rough facets. The same is true of results for hexagonal columns calculated using IGO. A droxtal was the only geometry that was found to offer anything other than a gradual decrease above 90° but its increase is too steep to offer the solution. By using a mixture

of crystals and a size distribution function it was shown that the behaviour could be replicated but at the expense of accuracy at lower scattering angles. The result still exhibited the best overall agreement from the investigation but there is room for further improvement. Avenues for extending the aircraft data investigation were discussed in section 8.8.

It should be noted that enhanced understanding of the radiative properties of cirrus may yet have unexpected implications in the future in solar system exploration, given the observation of very thin cirrus on Mars by NASA's Mars Exploration Rover *Opportunity* [146].

The project has thrown up many questions and possible project extensions. For example, there is nothing in principle preventing the 2D scattering pattern form of results being extended to linear polarization. Given the extra information that has been gained from the comparisons to experiment in chapter 7 this would be a worthwhile extension to the project, particularly if the linear polarization becomes a focus in the future.

A more complex addition to the project would be to extend the concept to curved surfaces. Although until now only crystal facets have been considered by the RTDF model, curved surfaces have long been treated by implementations of the GO model. It would be a substantial task because the model would need to be redefined in terms of the deflection angles used. A treatment of curved surfaces would allow the scattering of cirrus ice crystals in the lower portions of clouds that have suffered the rounding of facet edges through sublimation to be considered more accurately. Another possible application of such a treatment would be to allow calculations for spheres, ellipsoidal particles and long circular cylinders. A comparison to exact Mie theory could then be made. As a result, a better assessment of the size applicability of the model might be possible because the behaviour of Geometric Optics for a sphere and the size parameters for which it provides very good comparisons are well established.

Through Babinet's principle it is possible using RTDF to create external diffraction patterns by considering rays that pass by the crystal and are deflected towards it. Although in the implementation of the model described here there are currently no interference effects, the intensity distribution would broadly be correct given the agreement shown for diffraction at a slit in figure 3.3 of section 3.2.2. This would be an interesting investigation because it would allow external diffraction patterns for arbitrary crystal projections to be estimated and compared to the results obtained using the equal area circular aperture method

common to the Macke GO code. It would be time consuming in comparison to the Macke method but it would allow bounds of accuracy to be put on the use of Fraunhofer diffraction pattern, something that is inappropriate for use in applications such as the fixed orientation 2D scattering patterns. It is expected that this form of external diffraction modelling is essential for phase functions of small crystals in fixed orientations since then external and internal components would be added together using both amplitude and phase.

The lack of interference effects in the model has been raised several times in the preceding chapters. Most ray tracing programmes ignore interference effects between rays, though not all [27]. The introduction of interference effects by using a phase tracing method represents a significant undertaking. Some success has been gained by introducing phase tracing and a ray based far field approximation which includes physical optics effects into a two dimensional version of the RTDF model [108]. It was shown in reference [108] that scattering at forward and back scattering for fixed orientations was much improved when compared to exact SVM calculations for cylinders of infinite length. It has been highlighted in previous chapters that the phase function close to direct forward and back scattering for many averaged random orientations is an area that would benefit from the introduction of such a treatment. It is likely that the lack of interference effects is also responsible for the shape of RTDF halos not agreeing with those found using IGO. It is not yet clear if it is feasible to implement interference effects in a complete RTDF model implementation that provides meaningful results without increasing the computational expense unreasonably. Work in this area is ongoing at the University of Hertfordshire. An improvement in the scattering results in the back scattering would further enhance the value of the RTDF model in depolarization ratio studies, as discussed in section 2.6.3. There is a current collaboration exploiting results generated using the 3D implementation of the RTDF model [55].

The RTDF model uses a method whose basis is in classical physics yet provides opportunities to study light scattering calculations that are not yet possible with near exact or numerical methods due to computational restrictions. The results presented in the preceding chapters, particularly the comparisons to experiment, illustrate that the model has real promise in helping to fill the gap between the near exact methods and Geometric Optics. The model offers an impressive flexibility in terms of the geometries that can be considered combined with low computational overheads. The prospect of future improvements to the accuracy of the model and the many potential applications emphasises the need for further development, testing and application of the diffraction on facets model.

Bibliography

[1] A.J. Baran. On the scattering and absorption properties of cirrus cloud. *Journal of Quantitative Spectroscopy and Radiative Transfer*, 89(1-4):17–36, 2004.

[2] S. Havemann and A.J. Baran. Extension of T-matrix to scattering of electromagnetic plane waves by non-axisymmetric dielectric particles: Application to hexagonal ice cylinders. *Journal of Quantitative Spectroscopy and Radiative Transfer*, 70(2):139–158, 2001.

[3] T. Rother. Generalization of the separation of variables method for nonspherical scattering on dielectric objects. *Journal of Quantitative Spectroscopy and Radiative Transfer*, 60(3):335–353, 1998.

[4] S. Havemann, T. Rother, and K. Schmidt. Light scattering by hexagonal ice crystals. In M.I. Mishchenko, L.D. Travis, and J.W. Hovenier, editors, *Conference on Light Scattering by Nonspherical Particles 29th September - 1st October 1998, New York*, pages 253–256. American Meteorological Society, 1998.

[5] K. Muinonen. Scattering of light by crystals: A modified Kirchhoff approximation. *Applied Optics*, 28(15):3044–3050, 1989.

[6] P. Yang and K.N. Liou. Geometric-optics-integral-equation method for light scattering by nonspherical ice crystals. *Applied Optics*, 35(33):6568–6584, 1996.

[7] E. Hesse and Z. Ulanowski. Scattering from long prisms computed using ray tracing combined with diffraction on facets. *Journal of Quantitative Spectroscopy and Radiative Transfer*, 79-80:721–732, 2003. Preprint available from: http://strc.herts.ac.uk/ls/pubs.html.

[8] E. Hesse, Z. Ulanowski, and S. Havemann. Scattering from long prisms: A comparison between ray tracing combined with diffraction on facets and SVM. In *7th conference on Electromagnetic and Light Scattering by Non-Spherical Particles, Theory, Measurements and Applications, Bremen, Germany*, pages 119–122, Sept 8-12, 2003.

[9] Z. Ulanowski, E. Hesse, P.H. Kaye, A.J. Baran, and R. Chandrasekhar. Scattering of light from atmospheric ice analogues. *Journal of Quantitative Spectroscopy and Radiative Transfer*, 79-80:1091–1102, 2003. Preprint available from http://strc.herts.ac.uk/ls/pubs.html.

[10] Z. Ulanowski, P. Connolly, M. Flynn, M. Gallagher, A.J.M. Clarke, and E. Hesse. Using ice crystal analogues to validate cloud ice parameter retrievals from the CPI ice spectrometer data. In *International Conference on Clouds and Precipitation, Bologna*, pages 1175–1178, 2004. Poster available from: http://strc.herts.ac.uk/ls/pubs.html.

[11] P.H. Kaye. Spatial light-scattering analysis as a means of characterizing and classifying non-spherical particles. *Meas Sci Tech*, 9(2):141–149, 1998.

[12] E. Hirst, P.H. Kaye, R.S. Greenaway, P. Field, and D.W. Johnson. Discrimination of micrometer-sized ice and super-cooled droplets in mixed-phase cloud. *Atmospheric Environment*, 35(1):33–47, 2001.

[13] C.F. Bohren and D.R. Huffman. *Absorption and scattering of light by small particles.* Wiley, 1983.

[14] J.A. Stratton. *Electromagnetic Theory.* McGraw-Hill, 1941.

[15] P.W. Barber and S.C. Hill. *Light scattering by particles: Computational methods.* World Scientific Publishing, 1990.

[16] S. Asano and G. Yamamoto. Light scattering by a spheroidal particle. *Applied Optics*, 14(1):29–49, 1975.

[17] T. Rother, K. Schmidt, and S. Havemann. Light scattering on hexagonal ice columns. *Journal of the Optical Society of America A*, 18(10):2512–2517, 2001.

[18] P.C. Waterman. Symmetry, unitarity and geometry in electromagnetic scattering. *Physical Review D*, 3(4):825–839, 1971.

[19] K.S. Yee. Numerical solution of initial boundary value problems involving Maxwell's equation in isotropic media. *IEEE transactions on Antennas and Propagation*, AP-14(3):302–307, 1966.

[20] P. Yang and K.N. Liou. Finite-difference time domain method for light scattering by small ice crystals in three-dimensional space. *Journal of the Optical Society of America A*, 13(10):2072–2085, 1996.

[21] E.M. Purcell and C.R. Pennypacker. Scattering and absorption of light by non-spherical dielectric grains. *The Astrophysical Journal*, 186:705–714, 1973.

[22] B.T. Draine and P.J. Flatau. Discrete-dipole approximation for scattering calculations. *Journal of the Optical Society of America A*, 11(4):1491–1499, 1994.

[23] A. Macke, J. Mueller, and E. Raschke. Single scattering properties of atmospheric ice crystals. *Journal of the Atmospheric Sciences*, 53(19):2813–2825, 1996.

[24] J.E. Hansen and L.D. Travis. Light scattering in planetary atmospheres. *Space Science Reviews*, 16:527–610, 1974.

[25] A. Macke, M.I. Mishchenko, K. Muinonen, and B.E. Carlson. Scattering of light by large nonspherical particles: Ray-tracing approximation versus T-matrix method. *Optics Letters*, 20(19):1934–1936, 1995.

[26] J.I. Peltoniemi, K. Lumme, K. Muinonen, and W.M. Irvine. Scattering of light by stochastically rough particles. *Applied Optics*, 28(19):4088–4095, 1989.

[27] Q. Cai and K.N. Liou. Polarized light scattering by hexagonal ice crystals: Theory. *Applied Optics*, 21(19):3569–3580, 1982.

[28] P. Wendling, R. Wendling, and H.K. Weickmann. Scattering of solar radiation by hexagonal ice crystals. *Applied Optics*, 18(15):2663–2671, 1979.

[29] Y. Takano and K-N. Liou. Solar radiative transfer in cirrus clouds. Part I: Single-scattering and optical properties of hexagonal ice crystals. *Journal of the Atmospheric Sciences*, 46(1):3–19, 1989.

[30] K.D. Rockwitz. Scattering properties of horizontally oriented ice crystal columns in cirrus clouds. Part 1. *Applied Optics*, 28(19):4103–4110, 1989.

[31] A. Macke and M.I. Mishchenko. Applicability of regular particle shapes in light scattering calculations for atmospheric ice particles. *Applied Optics*, 35(21):4291–4296, 1996.

[32] Y-K. Lee, P. Yang, M.I. Mishchenko, B.A. Baum, Y.X. Hu, H-L. Huang, W.J. Wiscombe, and A.J. Baran. Use of circular cylinders as surrogates for hexagonal pristine ice crystals in scattering calculations at infrared wavelengths. *Applied Optics*, 42(15):2653–2664, 2003.

[33] A. Macke, M.I. Mishchenko, and B. Cairns. The influence of inclusions on light scattering by large hexagonal and spherical ice crystals. In Smith and Stamnes, editors, *IRS'96: Current Problems in Atmospheric Radiation*, pages 226–229, 1996.

[34] A. Macke. Scattering of light by polyhedral ice crystals. *Applied Optics*, 32(15):2780–2788, 1993.

[35] Y. Takano and K-N. Liou. Radiative transfer in cirrus clouds. Part III: Light scattering by irregular ice crystals. *Journal of the Atmospheric Sciences*, 52(7):818–837, 1995.

[36] K. Muinonen, K. Lumme, J. Peltoniemi, and W.M. Irvine. Light scattering by randomly oriented crystals. *Applied Optics*, 28(15):3051–3060, 1989.

[37] M. Born and E. Wolf. *Principles of optics: Electromagnetic theory of propagation, interference and diffraction of light.* Cambridge University Press, 7th (expanded) edition, 1999.

[38] M.I. Mishchenko, J.W. Hovenier, and L.D. Travis, editors. *Light Scattering by Nonspherical Particles.* Academic Press, first edition, 2000.

[39] S.B. Palmer and M.S. Rogalski. *Advanced University Physics.* Gordon and Breach, 1996.

[40] E. Hecht. *Optics.* Addison-Wesley, 1998.

[41] G.R. Fowles. *Introduction to Modern Optics.* Dover Publications (New York), 1989.

[42] J.D. Jackson. *Classical Electrodynamics.* John Wiley and sons, 3rd edition, 1999.

[43] E. Kreyszig. *Advanced Engineering Mathematics.* John Wiley, 1993.

[44] S.A. Schelkunoff. Kirchhoff's formula, its vector analogue, and other field equivalence theorems. *Communications on Pure and Applied Mathematics*, 4:43–59, 1951.

[45] J.B. Keller. Geometrical theory of diffraction. *Journal of the Optical Society of America*, 52(2):116–130, 1962.

[46] K.L. Coffey, K.J. Priestley, J.R. Mahan, and M.C. Sanchez. Diffraction models of radiation entering an aperture for use in a monte-carlo ray-trace environment. In *SPIE Conference on Current Developments in Optical Design and Engineering VII*, volume 3429, pages 213–219, 1998.

[47] B.K. Likeness. Stray light simulation with advanced Monte Carlo techniques. In *SPIE Stray light problems in optical systems*, volume 107, pages 80–88, 1977.

[48] E.R. Freniere, G.G. Gregory, and R.A. Hassler. Edge diffraction in Monte Carlo ray tracing. In *SPIE Conference on Optical Design and Analysis Software*, volume 3780, pages 151–157, July 1999.

[49] A.G. Borovoi and I.A. Grishin. Scattering matrices for large ice crystal particles. *Journal of the Optical Society of America A*, 20(11):2071–2080, 2003.

[50] A. Borovoi. Private communication.

[51] J.C. Ravey and P. Mazeron. Light scattering in the physical optics approximation; application to large spheroids. *Journal of Optics (Paris)*, 13(5):273–282, 1982.

[52] P. Yang and K.N. Liou. Light scattering by hexagonal ice crystals: Comparison of finite-difference time domain and geometric optics models. *Journal of the Optical Society of America A*, 12(1):162–176, 1995.

[53] A.J.M. Clarke, E. Hesse, Z. Ulanowski, and P.H. Kaye. A 3D implementation of ray tracing combined with diffraction on facets: Verification and a potential application. *Journal of Quantitative Spectroscopy and Radiative Transfer*, 100(1-3):103–114, 2006.

[54] H.C. van de Hulst. *Light Scattering by small particles.* Dover, 1981.

[55] S. Büttner, M. Schnaiter, O. Möhler, E. Hesse, A. Clarke, Z. Ulanowski, and P. Connolly. Influence of size and shape on the back-scattering linear depolarization ratio of ice crystals: Comparison of experimental and modelling results. *In preparation*, 2006.

[56] Y. Takano and K. Jayaweera. Scattering phase matrix for hexagonal ice crystals computed from ray optics. *Applied Optics*, 24(19):3254–3263, 1985.

[57] World Meteorological Organisation. *International Cloud Atlas.* World Meteorological Organisation, 1975.

[58] D.K. Lynch, K. Sassen, D. Starr, and G. Stephens, editors. *Cirrus*. Oxford University Press, 2002.

[59] Met Office Homepage: Cloud index, http://www.metoffice.com/bookshelf/clouds/cloudindex.html. Last accessed: 25/09/2005.

[60] G.L. Stephens, S-C. Tsay, P.W. Stackhouse, and P.J. Flatau. The relevance of the microphysical and radiative properties of cirrus clouds to climate and climatic feedback. *Journal of the Atmospheric Sciences*, 47(14):1742–1753, 1990.

[61] H.R. Pruppacher and J.D. Klett. *Microphysics of clouds and precipitation*. D. Reidel Publishing Company, 1978.

[62] M. Riikonen, M. Sillanpaa, L. Virta, D. Sullivan, J. Moilanen, and I. Luukkonen. Halo observations provide evidence of airborne cubic ice in the Earth's atmosphere. *Applied Optics*, 39(33):6080–6085, 2000.

[63] T. Kobayashi, Y. Furukawa, T. Takahashi, and H. Uyeda. Cubic structure models at the junctions in polycrystalline snow crystals. *Journal of Crystal Growth*, 35(3):262–268, 1976.

[64] A.J. Heymsfield and G.M. McFarquhar. High albedos of cirrus in the tropical pacific warm pool: Microphysical interpretations from CEPEX and from Kwajalein, Marshall Islands. *Journal of the Atmospheric Sciences*, 53(17):2424–2451, 1996.

[65] R.P. Lawson, A.J. Heymsfield, S.M. Aulenbach, and T.L. Jensen. Shapes, sizes and light scattering properties of ice crystals in cirrus and a persistent contrail during SUCCESS. *Geophysical Research Letters*, 25(9):1331–1334, 1998.

[66] D.J. Travis, A.M. Carleton, and R.G. Lauritsen. Contrails reduce daily temperature range. *Nature*, 418(6898):601, 2002.

[67] E.J. Jensen and O.B. Toon. The potential impact of soot particles from aircraft exhaust on cirrus clouds. *Geophysical Research Letters*, 24(3):249–252, 1997.

[68] K. Sassen. Contrail-cirrus and their potential for regional climate change. *Bulletin of the American Meteorological Society*, 78(9):1885–1904, 1997.

[69] P. Minnis, J.K. Ayers, R. Palikonda, and D. Phan. Contrails, cirrus trends and climate. *Journal of Climate*, 17(8):1671–1685, 2004.

[70] H. Weickmann. Die eisphase in der atmosphare. *Royal Aircraft Establishment, Farnborough, UK*, 1947.

[71] S. Kinne, T.P. Ackerman, A.J. Heymsfield, F.P.J. Valero, K. Sassen, and J.D. Spinhirne. Cirrus microphysics and radiative transfer: Cloud field study on 28 October 1986. *Monthly Weather Review*, 120:661–684, May 1992.

[72] S.L. Nasiri, B.A. Baum, A.J. Heymsfield, P. Yang, M.R. Poellot, D.P. Kratz, and Y. Hu. The development of midlatitude cirrus models for MODIS using FIRE-I, FIRE-II and ARM in situ data. *Journal of Applied Meteorology*, 41:197–217, 2002.

[73] S.Y. Matrosov, A.J. Heymsfield, J.M. Intrieri, B.W. Orr, and J.B. Snider. Ground-based remote sensing of cloud particle sizes during the 26 November 1991 FIRE II cirrus case: Comparisons with in situ data. *Journal of the Atmospheric Sciences*, 52(23):4128–4142, 1995.

[74] P.N. Francis, P. Hignett, and A. Macke. The retrieval of cirrus cloud properties from aircraft multi-spectral reflectance measurements during EUCREX'93. *Quarterly Journal of the Royal Meteorological Society*, 124:1273–1291, 1998.

[75] CRYSTAL-FACE homepage, http://cloud1.arc.nasa.gov/crystalface/index.html. Last accessed: 06/12/2005.

[76] R.P. Lawson, B.A. Baker, C.G. Schmitt, and T.L. Jensen. An overview of microphysical properties of arctic clouds observed in May and July 1998 during FIRE ACE. *Journal of Geophysical Research*, 106(D14):14989–15014, 2001.

[77] A.J. Heymsfield and J. Iaquinta. Cirrus crystal terminal velocities. *Journal of the Atmospheric Sciences*, 57(7):916–938, 2000.

[78] A.H. Auer and D.L. Veal. The dimension of ice crystals in natural clouds. *Journal of the Atmospheric Sciences*, 27(6):919–926, 1970.

[79] A.J. Heymsfield and C.M.R. Platt. A parameterization of the particle size spectrum of ice clouds in terms of the ambient temperature and the ice water content. *Journal of the Atmospheric Sciences*, 41(5):846–855, 1984.

[80] A. Macke, P.N. Francis, G.M. McFarquhar, and S. Kinne. The role of ice particle shapes and size distributions in the single scattering properties

of cirrus clouds. *Journal of the Atmospheric Sciences*, 55(17):2874–2883, 1998.

[81] M. Bailey and J. Hallett. Growth rates and habits of ice crystals between -20° and -70°c. *Journal of the Atmospheric Sciences*, 61(5):514–544, 2004.

[82] O. Möhler, O. Stetzer, S. Schaefers, C. Linke, M. Schnaiter, R. Tiede, H. Saathoff, M. Krämer, A. Mangold, P. Budz, P. Zink, J. Schreiner, K. Mauersberger, W. Haag, B. Karcher, and U. Schurath. Experimental investigation of homogeneous freezing of sulphuric acid particles in the aerosol chamber AIDA. *Atmospheric Chemistry and Physics*, 3(1):211–223, 2003.

[83] P. Connolly, P.R. Field, O. Möhler, S. Büttner, H. Saathoff, A.J. Heymsfield, M.W. Gallagher, and T.W. Choularton. Simulations of ice crystal nucleation and growth: Results from the AIDA cloud expansion chamber. In *14th International Conference on Clouds and Precipitation, Bologna, Italy*, pages 43–46, 19th-23rd July 2004.

[84] B. Barkey, M. Bailey, K.N. Liou, and J. Hallett. Light-scattering properties of plate and column ice crystals generated in a laboratory cold chamber. *Applied Optics*, 41(27):5792–5796, 2002.

[85] N.J. Bacon and B.D. Swanson. Laboratory measurements of light scattering by single levitated ice crystals. *Journal of the Atmospheric Sciences*, 57(13):2094–2104, 2000.

[86] A.J. Heymsfield, K.M. Miller, and J.D. Spinhirne. The 27-28 October 1986 FIRE IFO cirrus case study: Cloud microstructure. *Monthly Weather Review*, 118(11):2313–2328, 1990.

[87] P.N. Francis. Some aircraft observations of the scattering properties of ice crystals. *Journal of the Atmospheric Sciences*, 52(8):1142–1154, 1994.

[88] P.N. Francis, A. Jones, R.W. Saunders, K.P. Shine, A. Slingo, and Z. Sun. An observational and theoretical study of the radiative properties of cirrus: Some results from ICE'89. *Quarterly Journal of the Royal Meteorological Society*, 120(518):809–848, 1994.

[89] P.N. Francis, J.S. Foot, and A.J. Baran. Aircraft measurements of the solar and infrared radiative properties of cirrus and their dependence on ice crystal shape. *Journal of Geophysical Research*, 104(D24):31685–31695, 1999.

[90] A.J. Baran, P.N. Francis, L.-C. Labonnote, and M. Doutriaux-Boucher. A scattering phase function for ice cloud: Tests of applicability using aircraft and satellite multi-angle multi-wavelength radiance measurements of cirrus. *Quarterly Journal of the Royal Meteorological Society*, 127(577):2395–2416, 2001.

[91] A.J.M. Clarke. A new model of light scattering by ice crystals applied to aircraft radiance measurements using geometries that include examples reconstructed from ice analogue crystals. OBR Technical Note Number 54, Met Office, Exeter, UK, 2005.

[92] W. Tape. *Atmospheric Halos.* American Geophysical Union, 1994.

[93] R.G. Greenler. *Rainbows, Halos and Glories.* Cambridge University Press, 1980.

[94] K. Sassen and Y. Takano. Parry arc: A polarization lidar, ray-tracing and aircraft case study. *Applied Optics*, 39(36):6738–6745, 2000.

[95] W.F.J. Evans and R.A.R. Tricker. Unusual arcs in the Saskatoon display. *Weather*, 27:234–238, 1972.

[96] E.C.W Goldie, G.T. Meaden, and R. White. The concentric halo display of 14 April 1974. *Weather*, 31:304–311, 1976.

[97] R.A.R. Tricker. Arcs associated with halos of unusual radii. *Journal of the Optical Society of America*, 69(8):1093–1100, 1979.

[98] G.P. Konnen, S.H. Muller, and J. Tinbergen. Halo polarization profiles and the interfacial angles of ice crystals. *Applied Optics*, 33(21):4569–4579, 1994.

[99] G.P. Konnen, R.A. Wessels, and J. Tinbergen. Halo polarization profiles and sampled ice crystals: Observations and interpretation. *Applied Optics*, 42(3):309–317, 2003.

[100] K. Sassen, N.C. Knight, Y. Takano, and A.J. Heymsfield. Effects of ice-crystal structure on halo formation: Cirrus cloud experimental and ray-tracing modeling studies. *Applied Optics*, 33(21):4590–4601, 1994.

[101] M.G.J. Minnaert. *Light and color in the outdoors.* Springer-Verlag, 1993. Translated and revised by Len Seymour.

[102] Atmospheric Optics by Les Cowley, http://www.sundog.clara.co.uk/atoptics/phenom.htm. Last accessed: 22/09/2005.

[103] F. Pattloch and E. Trankle. Monte-Carlo simulation and analysis of halo phenomena. *Journal of the Optical Society of America A*, 1(5):520–526, 1984.

[104] Z. Ulanowski. Ice analog halos. *Applied Optics*, 44(27):5754–5758, 2005.

[105] M.I. Mishchenko and A. Macke. How big should hexagonal ice crystals be to produce halos? *Applied Optics*, 38(9):1626–1629, 1999.

[106] A. Heymsfield. Cirrus uncinus generating cells and the evolution of cirriform clouds. Part I: Aircraft observations of the growth of the ice phase. *Journal of the Atmospheric Sciences*, 32(4):799–808, 1975.

[107] F. Parungo. Ice crystals in high clouds and contrails. *Atmospheric Research*, 38(1-4):249–262, 1995.

[108] E. Hesse, Z. Ulanowski, A.J.M. Clarke, S. Havemann, and P.H. Kaye. Introducing phase tracing into a computational method which combines ray-tracing with diffraction on facets. In F. Moreno, J.J. López-Moreno, O. Muñoz, and A. Molina, editors, *8th conference on Electromagnetic and Light Scattering by Nonspherical Particles, Salobrena, Granada, Spain*, pages 112–115, 16th-20th May 2005. Extended abstract available from: http://strc.herts.ac.uk/ls/pubs.html.

[109] J.W. Hovenier and C.V.M. van der Mee. Fundamental relationships relevant to the transfer of polarized light in a scattering atmosphere. *Astronomy and Astrophysics*, 128(1):1–16, 1983.

[110] S.G. Warren. Optical constants of ice from the ultraviolet to the microwave. *Applied Optics*, 23(8):1206–1225, 1984.

[111] P. Yang, K.N. Liou, K. Wyser, and D. Mitchell. Parameterization of the scattering and absorption properties of individual ice crystals. *Journal of Geophysical Research - Atmospheres*, 105(D4):4699–4718, 2000.

[112] P.W. Stackhouse and G.L. Stephens. A theoretical and observational study of the radiative properties of cirrus: Results from FIRE 1986. *Journal of the Atmospheric Sciences*, 48(18):2044–2059, 1991.

[113] A. Macke. Modellierung der optischen eigenschaften von cirruswolken. Ph.D. thesis, Fachbereich Geowissenschaften der Universitaet Hamburg, Germany, 1994. Relevant sections translated by E. Hesse.

[114] K. Sassen. Remote sensing of planar ice crystal fall attitudes. *Journal of the Meteorological Society of Japan*, 58(5):422–429, 1980.

[115] C. Magono and C.W. Lee. Meteorological classifications of natural snow crystals. *Journal of the Faculty of Science, Hokkaido University*, Ser. VII(2):320–335, 1966.

[116] K.G. Libbrecht. The Physics of snow crystals. *Reports on Progress in Physics*, 68(4):855–895, 2005.

[117] R.T. Bruintjes, A.J. Heymsfield, and T.W. Krauss. An examination of double-plate ice crystals and the initiation of precipitation in continental cumulus clouds. *Journal of the Atmospheric Sciences*, 44(9):1331–1349, 1987.

[118] C. Liu, P.R. Jonas, and C.P.R. Saunders. Pyramidal ice crystal scattering phase functions and concentric halos. *Annales Geophysicae*, 14(11):1192–1197, 1996.

[119] W.P. Arnott, Y. Dong, J. Hallett, and M.R. Poellot. Role of small ice crystals in radiative properties of cirrus: A case study, FIRE II, November 22, 1991. *Journal of Geophysical Research*, 99(D1):1371–1381, 1994.

[120] T. Ohtake. Unusual crystal in ice fog. *Journal of the Atmospheric Sciences*, 27(3):509–511, 1970.

[121] P. Yang, B.A. Baum, A.J. Heymsfield, Y.X. Hu, H-L. Huang, S-C. Tsay, and S. Ackerman. Single-scattering properties of droxtals. *Journal of Quantitative Spectroscopy and Radiative Transfer*, 79-80:1159–1169, 2003.

[122] Z. Zhang, P. Yang, G.W. Kattawar, S-C. Tsay, B.A. Baum, Y. Hu, A.J. Heymsfield, and J. Reichardt. Geometrical-optics solution to light scattering by droxtal ice particles. *Applied Optics*, 43(12):2490–2499, 2004.

[123] M. Pekkola, M. Riikonen, J. Moilanen, and J. Ruoskanen. Halo arcs from airborne, pyramidal ice crystals falling with their c axes in vertical orientation. *Applied Optics*, 37(9):1435–1440, 1998.

[124] A.J. Heymsfield, S. Lewis, A. Bansemer, J. Iaquinta, and L.M. Miloshevich. A general approach for deriving the properties of cirrus and stratiform ice cloud particles. *Journal of the Atmospheric Sciences*, 59(1):3–29, 2002.

[125] J. Iaquinta, H. Isaka, and P. Personne. Scattering phase function of bullet rosette ice crystals. *Journal of the Atmospheric Sciences*, 52(9):1401–1413, 1995.

[126] M. Kajikawa and A.J. Heymsfield. Aggregation of ice crystals in cirrus. *Journal of the Atmospheric Sciences*, 46(20):3108–3121, 1989.

[127] P. Yang and K.N. Liou. Single-scattering properties of complex ice crystals in terrestrial atmosphere. *Contributions to Atmospheric Physics*, 71(2):223–248, 1998.

[128] E. Hesse, Z. Ulanowski, and P.H. Kaye. Stability characteristics of cylindrical fibres in an electrodynamic balance designed for single particle investigation. *Journal of Aerosol Science*, 33:149–163, 2002.

[129] Z. Ulanowski, R.S. Greenaway, P.H. Kaye, and I.K. Ludlow. Laser diffractometer for single-particle scattering measurements. *Measurement Science and Technology*, 13:292–296, 2002.

[130] CPI homepage, http://cloudbase.phy.umist.ac.uk/field/instruments/cpi.htm. Last accessed: 06/12/2005.

[131] E. Hesse. Private communication.

[132] A. Reisinger. Characteristics of optical guided modes in lossy waveguides. *Applied Optics*, 12(5):1015–1025, 1973.

[133] Z. Ulanowski. SID-2 data analysis and preliminary results from AIDA ice nucleation campaign IN5. Internal report, Science and Technology Research Institute, University of Hertfordshire, 2005.

[134] Z. Ulanowski, E. Hesse, P.H. Kaye, and A.J. Baran. Light scattering by complex ice-analogue crystals. *Journal of Quantitative Spectroscopy and Radiative Transfer*, 100(1-3):382–392, 2006.

[135] K.F. Evans and G.L. Stephens. A new polarized atmospheric radiative transfer model. *Journal of Quantitative Spectroscopy and Radiative Transfer*, 46(5):413–423, 1991.

[136] A. Ley. A Monte-Carlo model to simulate the multiple scattering of shortwave radiation. MRF Internal Note Number 15, Met Office, Exeter, UK, 1983.

[137] J.F. Potter. The delta function approximation in radiative transfer theory. *Journal of the Atmospheric Sciences*, 27(6):943–949, 1970.

[138] A. Arking and J. Potter. The phase curve of Venus and the nature of its clouds. *Journal of the Atmospheric Sciences*, 25(4):617–628, 1968.

[139] L. Henyey and J. Greenstein. Diffuse radiation in the galaxy. *The Astrophysical Journal*, 93:70–83, 1941.

[140] P.N. Francis. Some aircraft observations of the scattering properties of ice crystals. *Journal of the Atmospheric Sciences*, 52(8):1142–1154, 1995.

[141] A.J. Baran and P.N. Francis. On the radiative properties of cirrus cloud at solar and thermal wavelengths: A test of model consistency using high-resolution airborne radiance measurements. *Quarterly Journal of the Royal Meteorological Society*, 130(598):763–778, 2004.

[142] Q. Fu. An accurate parameterization of the solar radiative properties of cirrus clouds for climate models. *Journal of Climate*, 9(9):2058–2082, 1996.

[143] D.L. Mitchell, Y. Liu, and A. Macke. Modeling cirrus clouds. Part II: Treatment of radiative properties. *Journal of the Atmospheric Sciences*, 53(20):2967–2988, 1996.

[144] A.J. Baran, S. Havemann, P.N. Francis, and P.D. Watts. A consistent set of single-scattering properties for cirrus cloud: Tests using radiance measurements from a dual-viewing multi-wavelength satellite-based instrument. *Journal of Quantitative Spectroscopy and Radiative Transfer*, 79-80:549–567, 2003.

[145] POLDER homepage, http://smsc.cnes.fr/polder/. Last accessed: 12/12/2005.

[146] NASA Mars exploration rover *Opportunity*, images of cirrus-like clouds above the endurance crater captured on the rovers 290th and 291st sol. http://origin.mars5.jpl.nasa.gov/gallery/panoramas/opportunity/2004.html. Last accessed: 15/09/2005.

[147] A.J.M. Clarke, E. Hesse, Z. Ulanowski, and P.H. Kaye. A 3D implementation of ray tracing with diffraction on facets compared to SVM and experiment. In F. Moreno, J.J. López-Moreno, O. Muñoz, and A. Molina, editors, *8th conference on Electromagnetic and Light Scattering by Nonspherical Particles, Salobrena, Granada, Spain*, pages 60–63, 16th-20th May 2005. Extended abstract available from: http://strc.herts.ac.uk/ls/pubs.html.

Appendix A

Conventions

This appendix provides explanations of conventions that are applied in the preceding chapters to avoid confusion with other texts. Section A.1 outlines the use of the terms size and length parameter and section A.2 provides an explanation of Euler's rotation theorem and the convention for its use adopted during this project. Section A.3 will define some terms that may not be considered standard that are used throughout the thesis.

A.1 Size and Length Parameter

In the study of light scattering, the net size of a crystal has little importance. The key quantity is the size of the crystal with respect to the wavelength of the incident light. The size of a crystal with respect to the wavelength is defined by the *size parameter* χ_r, given by equation A.1 where r is a characteristic radius of the crystal and λ is the wavelength of the incident light.

$$\chi_r = \frac{2\pi r}{\lambda} \tag{A.1}$$

For elongated geometries such as hexagonal columns, one radius does not provide sufficient information. Occasionally, a similar definition for the length of a column, χ_l, can be used. This is shown in equation A.2, where l is the length

of the column.

$$\chi_L = \frac{2\pi L}{\lambda} \tag{A.2}$$

In this thesis, the size of a hexagonal column is always defined by the size parameter and a crystal aspect ratio, A, given in equation A.3 where L is the crystal length and r the crystal radius. When considering more complex geometries, dimensions are described in terms of constituent column-like crystals or the size of defining facets.

$$A = \frac{L}{2r} \tag{A.3}$$

A.2 Euler's Rotation Theorem

Euler's Rotation Theorem states that any arbitrary rotation can be described by only three parameters. The ray tracing codes used in this project use *Euler angles* to describe the orientation of a crystal. Each Euler angle is a rotation about a body centred axis and using three such rotations, any orientation can be achieved. There are many conventions for Euler angles used throughout the literature. The convention used here is shown in figure A.1. The first rotation is through an angle α about the z axis. The original axes move with the object and after the first rotation they are labelled x', y' and z'. The second rotation is through an angle β about the x' axis. After the second rotation, the new axes are labelled x'', y'' and z''. The final rotation is through an angle γ about the z'' axis. All three rotations are clockwise when looking in the positive direction of the axis of rotation. During the three rotations, the centre of mass of the crystal is positioned at the origin.

To understand the fixed orientations discussed in chapter 7 it is important to know the orientation of a crystal for $\alpha = \beta = \gamma = 0°$. An illustration of the crystal in the fixed orientation being considered will always be given. For a hexagonal column, an orientation of $\alpha = \beta = \gamma = 0°$ corresponds to the long axis aligned along the z-axis with two prism (rectangular) facets lying parallel to the y-z plane.

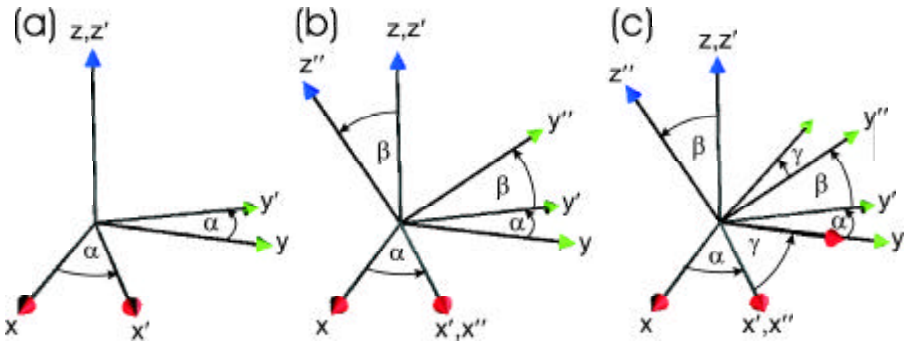

Figure A.1: A demonstration of the use of Euler angles. The rotations α, β and γ are about the z, x' and z'' axes respectively.

A.3 Miscellaneous Terms

In this section a selection of terms are defined that are used frequently throughout the thesis that may not be considered standard.

Basal Facet A facet acting as the 'base' of a crystal. In this thesis the term is used exclusively as referring to the hexagonal facets of a hexagonal column.

Prism Facet Used interchangeably with 'rectangular facet' when describing the six non-basal facets of a hexagonal column.

Forward Scattering Refers to a scattering direction. *Direct forward scattering* is located in the direction of the incident light at a scattering angle of $\theta = 0°$. The *forward scattering region* is a loose term referring to scattering angles within a few degrees of direct forward scattering.

Back Scattering Refers to a scattering direction. *Direct back scattering* is located in the direction opposite that of the incident light at a scattering angle of $\theta = 180°$. The *back scattering region* is a loose term referring to scattering angles within a few degrees of the back scattering point.

Perpendicular Incidence Used in connection with hexagonal columns and plates. Light approaches the crystal at perpendicular incidence if the cylinder axis of the crystal is perpendicular to the incident light. Note that the crystal can rotate around the cylinder axis and still be considered as being at perpendicular incidence as long as the perpendicular condition is true.

Basal Incidence Used in connection with hexagonal columns and plates. Light approaches the crystal at basal incidence if the cylinder axis of the crystal is parallel with the incident light. In other words, if light is normally incident on one of the basal facets.

Appendix B

Publications List

B.1 Journal Publications

- "A 3D implementation of ray tracing combined with diffraction on facets: Verification and a potential application" A.J.M. Clarke, E. Hesse, Z. Ulanowski and P.H. Kaye. Journal of Quantitative Spectroscopy and Radiative Transfer, 100(1-3) p.103-114, 2006. Reference: [53]. Reproduction provided in Appendix C.

- "Influence of size and shape on the back-scattering linear depolarization ratio of ice crystals: Comparison of experimental and modelling results" S. Büttner, M. Schnaiter, O. Möhler, E. Hesse, A.J.M. Clarke, Z. Ulanowski, and P. Connolly. In preparation for submission, 2006. Reference: [55].

B.2 Conference Publications

- "Using ice crystal analogues to validate cloud ice parameter retrievals from the CPI ice spectrometer data" Z. Ulanowski, P. Connolly, M. Flynn, M. Gallagher, A.J.M. Clarke, E. Hesse. In: Isaac G.A. (editor), 14th International Conference on Clouds and Precipitation, Bologna, 18th-23rd July 2004. IAMAS, p. 1175-1178. Reference: [10].

- "A new model of light scattering by ice crystals using ray tracing combined with diffraction on facets" A.J.M. Clarke, E. Hesse, Z. Ulanowski and P.H.

Kaye. In: Proceedings of the 16th annual Aerosol Society AGM, 14th-15th April 2005, Bristol, UK. p.71-74.

- "A 3D implementation of ray tracing with diffraction on facets compared to SVM and experiment" A.J.M. Clarke, E. Hesse, Z. Ulanowski and P.H. Kaye. In: F. Moreno, J.J. López-Moreno, O. Muñoz and A. Molina (editors), 8th Conference on Electromagnetic and Light Scattering by Nonspherical Particles: Theory, Measurements and Applications, 16th-20th May 2005, Salobreña, Spain. p. 60-63. Reference: [147].

- "Introducing phase tracing into a computational method which combines ray-tracing with diffraction on facets" E. Hesse, Z. Ulanowski, A.J.M. Clarke, S. Havemann and P.H. Kaye. In: F. Moreno, J.J. López-Moreno, O. Muñoz and A. Molina (editors), 8th Conference on Electromagnetic and Light Scattering by Nonspherical Particles: Theory, Measurements and Applications, 16th-20th May 2005, Salobreña, Spain. p. 112-115. Reference: [108].

B.3 Other Publications

- "A new model of light scattering by ice crystals applied to aircraft radiance measurements using geometries that include examples reconstructed from ice analogue crystals." A.J.M. Clarke. OBR Technical Note Number 54, Met Office, Exeter, UK. Reference: [91].

- "Diffraction on facets: A new model of light scattering." A.J.M. Clarke. The Aerosol Society Newsletter, Issue No. 43.

Appendix C

Reproduction of Journal Publication

In the forthcoming pages is a reproduction of Clarke et al. 2006 [53].